JSCSEN 73(8–9)771–935(2008)

Journal of the Serbian Chemical Society

Electronic version

VOLUME 73

NO 8–9

BELGRADE 2008

Available on line at

www.shd.org.rs/JSCS

The full search of JSCS is available through

DOAJ DIRECTORY OF OPEN ACCESS JOURNALS

www.doaj.org

Serbian Chemical Society
www.shd.org.yu

Journal of the Serbian Chemical Society
Electronic version
JSCS@tmf.bg.ac.yu • www.shd.org.yu/JSCS
ISSN 0352-5139

J. Serb. Chem. Soc. Vol. 73, No. 8–9 (2008)

CONTENTS

Organic Chemistry

O. Farsa, M. Dočkal, J. Kováčiková and *M. Benešová*: Synthesis of 2-{[2-(2-oxo-1-azacycloalkyl)acetamido]phenoxy}acetic acids and their activity as aminopeptidase M inhibitors 771

A. Husain, F. J. Ahmad, M. Ajmal and *P. Ahuja*: Synthesis of 1-(4-phenoxyphenyl)-3-[5-(substituted aryl)-1,3,4-oxadiazol-2-yl]propan-1-ones as safer anti-inflammatory and analgesic agents 781

Biochemistry

R. Masnikosa, A. J. Nikolić and *O. Nedić*: Lectin-induced alterations of the interaction of insulin and insulin-like growth factor 1 receptors with their ligands 793

L. Pitulice, A. Isvoran and *A. Chiriac*: Structural features of proteins as reflected by statistical scaling laws 805

Inorganic Chemstry

D. M. Mitić, Đ. U. Miodragović, D. M. Sladić, Ž. J. Vitnik, Z. M. Miodragović, K. K. Anđelković, M. Đ. Radulović and *N. O. Juranić*: Synthesis, NMR, DFT and antimicrobial studies of Zn(II) complexes with *N*-benzyloxycarbonyl-*S*-alanine 815

Physical Chemistry

J. J. Gulicovski, LJ. S. Čerović, S. K. Milonjić and *I. G. Popović*: Adsorption of itaconic acid from aqueous solutions onto alumina 825

R. Pode, E. Popovici, L. Cocheci, E. Reisz, E. M. Seftel and *V. Pode*: Sorption of phosphates and thiocyanates on isomorphic substituted Mg/Zn–Al-type hydrotalcites 835

Electrochemistry

S. Stevanović, D. Tripković, A. Kowal, D. Minić, V. M. Jovanović and *A. Tripković*: Influence of surface morphology on methanol oxidation at a glassy carbon-supported Pt catalyst 845

V. M. Maksimović, LJ. J. Pavlović, B. M. Jović and *M. G. Pavlović*: Electrodeposition of Fe powder from acid electrolytes 861

Analytical Chemistry

R. M. Džudović and *LJ. N. Jakšić*: Determination of relative acidity scales for some dipolar aprotic solvents by coulometry using a hydrogen–palladium electrode 871

S. S. Mitić, G. Ž. Miletić, A. N. Pavlović, B. B. Arsić and *V. V. Živanović*: Quantitative analysis of ibuprofen in pharmaceuticals and human control serum using kinetic spectrophotometry 879

Materials

S. N. Marinković: Carbon nanotubes (Review) 891

Polymers

L. Katsikas, M. Avramović, R. D. B. Cortés, M. Milovanović, M. T. Kalagasidis-Krušić and *I. G. Popović*: The thermal stability of poly(methyl methacrylate) prepared by RAFT polymerisation (Short communication) 915

Environmental

I. Gržetić and *R. H. A. Ghariani*: Potential health risk assessment for soil heavy metal contamination in the central zone of Belgrade (Serbia) 923

Errata (printed version only) 935

Published by the Serbian Chemical Society
Karnegijeva 4/III, 11000 Belgrade, Serbia
Printed by the Faculty of Technology and Metallurgy
Karnegijeva 4, P.O. Box 35-03, 11120 Belgrade, Serbia

Journal of the Serbian Chemical Society
JSCS@tmf.bg.ac.yu • www.shd.org.rs/JSCS
J. Serb. Chem. Soc. 73 (8–9) 771–780 (2008) UDC 547.466.1:547.538–32:547.233:66.097.8
JSCS–3760 *Original scientific paper*

Synthesis of 2-{[2-(2-oxo-1-azacycloalkyl)acetamido]phenoxy}acetic acids and their activity as aminopeptidase M inhibitors

OLDŘICH FARSA[1]*, MILAN DOČKAL[1], JANA KOVÁČIKOVÁ[2] and MÁRIA BENEŠOVÁ[2]

[1]*Institute of Chemical Drugs, Faculty of Pharmacy, University of Veterinary and Pharmaceutical Sciences Brno, Palackého 1/3, 612 42 Brno, Czech Republic and* [2]*Department of Cellular and Molecular Biology of Drugs, Faculty of Pharmacy, Comenius University, Kalinčiakova 8, 832 32 Bratislava, Slovak Republic*

(Received 21 February, revised 9 May 2008)

Abstract: A series of 9 phenoxyacetic acids substituted in the *o*-, *m*-, and *p*-position of benzene ring with 2-(2-oxo-1-azacycloalkyl)acetamidic moiety containing 5–7-membered *ω*-lactam ring was prepared by a 4-step synthetic procedure. Five selected substances of this series were tested *in vitro* for inhibition of porcine kidney aminopeptidase M. 2-{4-[2-(2-Oxoperhydroazepin-1-yl)acetamido]phenoxy}acetic acid exhibited the highest activity with K_i = 243.6 μM.

Keywords: *ω*-lactams; phenoxyacetic acids; aminopeptidase M; inhibition.

INTRODUCTION

Aminopeptidases are hydrolases cleaving *N*-terminal amino acid residue from a peptide chain. They are present in all organisms from bacteria to humans and play important roles in many metabolic pathways and regulatory processes.[1,2] Aminopeptidase M (EC 3.4.11.2, aminopeptidase N, membrane alanyl aminopeptidase, AP-M) is a metallo-dependent integral membrane protease. This enzyme belongs to the M1 family of the MA clan of peptidases, also called gluzincins.[3] At least nine different enzymes, five of which are integral membrane proteins, were recently discovered as members of the M1 family in mammals.[4] Aminopeptidase M has a molecular weight of about 110,000 and consists of 963––967 amino acids residues, depending on the species. It has a short *N*-terminal cytoplasmic domain, a single transmembrane part and a large cellular ectodomain containing the active site.[5] This enzyme was first isolated in 1963 by Pfleiderer and Celliers from pig kidney[6] and is also known as pseudo leucine aminopeptidase and under several other names originating from the processes in which it participates. This peptidase preferentially cleaves peptides with an *N*-terminal

* Corresponding author. E-mail: farsao@vfu.cz
doi: 10.2298/JSC0809771F

neutral or basic amino acid, although it possess a comparatively broad substrate specificity.[7] AP-M is present in many different tissues and cells, *e.g.*, in blood plasma and the vasculature, where AM-P, together with other exopeptidases, converts and/or inactivates various vasoactive peptides belonging to the kinin, angiotensin and bradykinin families.[8] AP-M is also involved in the inactivation of enkephalins.[9,10] In addition, this Zn metalloexopeptidase plays an important role in the degradation of the neuropeptide neuromedin N (NN), a hexapeptide of sequence H–Lys–Ile–Pro–Tyr–Ile–Leu–OH, which is synthesized together with the tridecapeptide neurotensin (NT), which has the same C-terminal sequence Pro–Tyr–Ile–Leu–OH and a similar pharmacological profile, from a common precursor. These peptides act almost at the same receptors, the main difference between them is that NT, being protected at its N-terminus, cannot be cleft by exopeptidases and is therefore degraded by Zn metallo-endopeptidases EC 3.4.24.11, EC 3.4.25.15 and EC 3.4.25.16, while unprotected NN is inactivated by AP-M.[11] Both NN and NT interact with NT_1 (NTRH) receptors, located on neurons, and NT_2 (NTRL) receptors, located on neurons and glia (NT_3 receptors, present in glia and adipocytes, are activated by NT only). There are various both biochemical and clinical evidence that a decrease of NT and NN levels in some regions of the brain participate in the pathophysiology of schizophrenia; even some potential antipsychotics, which can act as NT agonists, have been developed.[12] AP-M is also involved in memory facilitation mediated by the brain renin–angiotensine system.[13] It cleaves Arg at the *N*-terminal of angiotensine III to form the hexapeptide angiotensine IV, which is thought to be the main ligand at the AT_4 receptor. This receptor, which is in contradistinction to all other types of angiotensine receptors in that it is probably not coupled with G-protein, is considered responsible for the regulation of memory processes. On the other hand, AP-M was identified as an enzyme, which together with angiotensine convertase, is responsible for the degradation of hemorfine, a cationic decapeptide derived from β-, χ-, δ- or ε-chain of hemoglobin, which is also demonstrated to be a bioactive ligand of the AT_4 receptor[14] and can probably be useful for the enhancement of learning performance and treatment of Alzheimer disease.[15] For this reason, it was considered to be useful to test our newly prepared 2-{[2-oxo-1--azacycloalk-1-yl)acetamido]phenoxy}acetic acids for their ability to influence the activity of AP-M, because they were designed as candidate CNS therapeutic agents, potential cognitive enhancers*, as they contain fragments of 2-(2-oxopyrrolidin-1-yl)acetamide (classical nootropic piracetam) and phenoxyacetic acid,

* Some of these substances have been mentioned in literature in the context of the determination of their pK_a values by CZE.[16] We provided these compounds, prepared originally by us, to the authors of this paper, but they unfortunately published the results of their determinations with neither mentioning us in the Acknowledgements nor giving us notice of the publication.

which is present in the molecule of meclofenoxate (2-(dimethylamino)ethyl 4-chlorophenoxyacetate, a cognitive enhancer, Fig. 1).

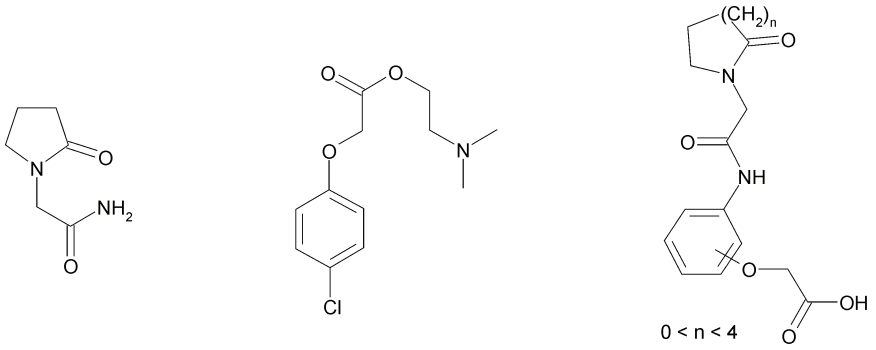

Fig. 1. Structures of piracetam, meclofenoxate and **7**–**15**.

EXPERIMENTAL

Chemistry

General. All melting points were determined on a Boetius PHMK apparatus (Nagema, Dresden, Germany) and are uncorrected. Elemental analyses (C, H, N) were performed with a Perkin–Elmer 2400 CHNS/O analyzer. The IR spectra were measured on a Nicolet Impact FTIR spectrometer. The ^{1}H- and ^{13}C-NMR spectra were recorded on a 200 MHz Gemini 2000 instrument (Varian, Palo Alto, CA, USA) using DMSO-d_6 as the solvent at 200 MHz or 50 MHz, respectively. The consequence of the synthetic steps is depicted in Scheme 1.

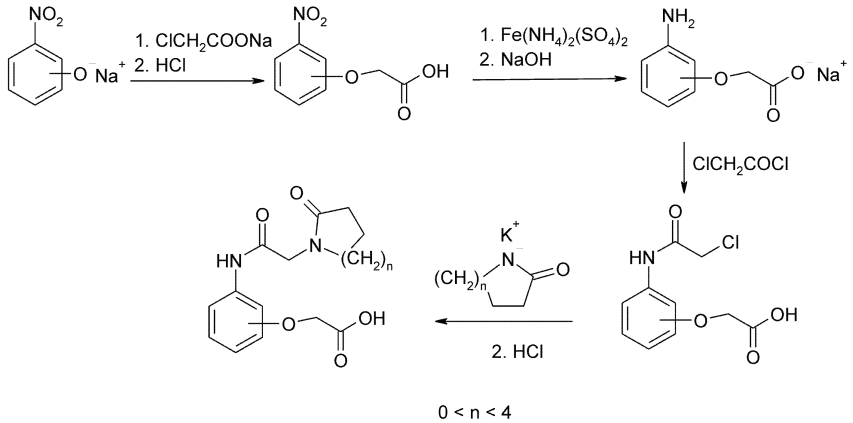

Scheme 1. Synthesis of 2-{[2-(2-oxo-1-azacycloalk-1-yl)acetamido]phenoxy}acetic acids **7**–**15**.

Nitrophenoxyacetic acids. Nitrophenol (50.0 g, 0.36 mol) was added to a solution of 27.8 g (0.70 mol) of sodium hydroxide in 280 ml of water. The resulting solution was heated to 80 °C and 34.0 g (0.36 mol) of chloroacetic acid was added. This mixture was refluxed for 24 h, then cooled and acidified with concentrated hydrochloric acid (≈ pH 0). This solution was let to crystallize in a refrigerator for several hours. The crude solid nitrophenoxyacetic acid was

filtered off and then recrystallized from boiling water. The crystals were filtered off again and dried at 60 °C under reduced pressure (0.93 kPa) for 4 h.

*2-(2-Nitrophenoxy)acetic acid (**1**)*. Yield: 50 %, m.p. 163–165 °C (lit.:[17] 158 °C). ^{1}H-NMR (200 MHz, DMSO-d_6, δ, ppm): 7.95–7.80 (1H, *m*, aromatic), 7.70–7.55 (1H, *m*, aromatic), 7.35–7.20 (1H, *m,* aromatic), 7.20–7.05 (1H, *m*, aromatic), 4.91 (2H, *s,* –OCH_2).

*2-(3-Nitrophenoxy)acetic acid (**2**)*. Yield: 99 %, m.p. 156–158 °C (lit.:[18] 156.4–156.7 °C). ^{1}H-NMR (200 MHz, DMSO-d_6, δ, ppm): 7.87–7.08 (1H, *m,* aromatic), 7.69 (1H, *t*, aromatic, J = 2.4 Hz), 7.58 (1H, *t*, aromatic, J = 8.2 Hz), 7.45–7.38 (1H, *m*, aromatic), 4.87 (2H, *s,* –OCH_2).

*2-(4-Nitrophenoxy)acetic acid (**3**)*. Yield: 78 %, m.p. 190–193 °C (lit.:[19] 195 °C). ^{1}H-NMR (200 MHz, DMSO-d_6, δ, ppm): 8.20 (2H, *d, o*-aromatic, J = 9.5 Hz), 7.14 (2H *d, m*-aromatic, J = 9.2 Hz), 4.88 (2H, *s,* –OCH_2).

Chloroacetamidophenoxyacetic acids. Nitrophenoxyacetic acid (10.0 g, 0.060 mol) was dissolved in 18 ml of *ca.* 13 % aqueous ammonia under heating. The resulting solution was added under stirring to a boiling solution of 100.0 g (0.360 mol) of ferrous sulfate heptahydrate in 200 ml of water and this mixture was refluxed for 25 min and, if the reaction of the liquid phase became neutral, it was alkalized with concentrated aqueous ammonia and then immediately filtered. An aqueous 10 % sodium hydroxide solution (36 ml) was added to the filtrate and the mixture was stirred for 10 min. Free ammonia and water were slowly distilled off on a rotary vacuum evaporator until a white precipitate of aminophenoxyacetic acid sodium salt appeared. Water was added until the precipitate dissolved and if this solution had no basic reaction, it was made alkaline with a saturated sodium hydroxide solution. Chloroacetyl chloride (6.1 ml, 0.080 mol) was added stepwise, in 4 parts over 20 min to the reaction mixture under vigorous stirring and cooling with water and ice; the stirring was continued for an additional 2 h. Then the mixture was acidified with concentrated hydrochloric acid (≈ pH 0) and the precipitated crude chloroacetamidophenoxyacetic acid was isolated by suction filtration and recrystalized from boiling water. The obtained crystals were dried at 60 °C under reduced pressure (0.93 kPa) for 4 h.

*2-[2-(2-Chloroacetamido)phenoxy]acetic acid (**4**)*. Yield 28 %, m.p. 137–140 °C (lit.:[20] 144.5–145.5 °C). ^{1}H-NMR (200 MHz, DMSO-d_6, δ, ppm): 9.2 (1H, *s,* –NH), 8.2–8.35 (2H, *m*, aromatic), 6.75–7.25 (2H, *m*, aromatic), 4.63 (2H, *s,* –OCH_2), 4.23 (2H, *s,* –$COCH_2Cl$).

*2-[3-(2-Chloroacetamido)phenoxy]acetic acid (**5**)*. Yield 32 %, m.p. 159–162 °C (lit.:[20] 159––162 °C). ^{1}H-NMR (200 MHz, DMSO-d_6, δ, ppm): 10.31 (1H, *s,* –NH), 7.1–7.3 (2H, *m*, aromatic), 6.6–6.7 (2H, *m*, aromatic), 4.64 (2H, *s,* –OCH_2), 4.24 (2H, *s,* –$COCH_2Cl$).

*2-[4-(2-Chloroacetamido)phenoxy]acetic acid (**6**)*. Yield 29 %, m.p. 166–169 °C (lit.:[20] 167––170 °C). ^{1}H-NMR (200 MHz, DMSO-d_6, δ, ppm): 10.19 (1H, *s,* δ-NH), 7.48 (2H, *d,* aromatic, J = 8.4 Hz), 6.87 (2H, *d,* aromatic, J = 8.1 Hz), 4.63 (2H, *s,* –OCH_2), 4.21 (2H, *s,* –$COCH_2Cl$).

2-{[2-(2-Oxo-1-azacycloalk-1-yl)acetamido]phenoxy}acetic acids. Finely powdered potassium hydroxide (11.2 g, 0.20 mol) was suspended in 12 ml of dimethyl sulfoxide under stirring and 0.040 mol of the required lactam (*i.e.*, 3.4 g of pyrrolidin-2-one, 4.0 g of piperidin-2-one and 4.5 g of azepan-2-one) were added. After stirring for 5 min, 2.4 g (0.010 mol) of the required chloroacetamidophenoxyacetic acid was added stepwise in 4–5 parts during 20 min under stirring. The mixture was stirred for an additional 2 h and then 140 ml of water was poured into it. The mixture was acidified with concentrated hydrochloric acid (≈ pH 0) and, after cooling to room temperature under stirring, it was left to crystallize in a refrigerator. After several days, the formed crystalline solid was filtered off and recrystallized from boiling water. The obtained crystals were dried at 60 °C under reduced pressure (0.93 kPa) for 4 h.

2-{2-[2-(2-Oxopyrrolidin-1-yl)acetamido]phenoxy}acetic acid (**7**), 2-{3-[2-(2-oxopyrrolidin-1-yl)acetamido]phenoxy}acetic acid (**8**), 2-{4-[2-(2-oxopyrrolidin-1-yl)acetamido]phenoxy}acetic acid (**9**), 2-{2-[2-(2-oxopiperidin-1-yl)acetamido]phenoxy}acetic acid (**10**), 2-{3-[2--(2-oxopiperidin-1-yl)acetamido]phenoxy}acetic acid (**11**), 2-{4-[2-(2-oxopiperidin-1-yl)acetamido]phenoxy}acetic acid (**12**), 2-{2-[2-(2-oxoperhydroazepin-1-yl)acetamido]phenoxy}acetic acid (**13**), 2-{3-[2-(2-oxoperhydroazepin-1-yl)acetamido]phenoxy}acetic acid (**14**) and 2-{4--[2-(2-oxoperhydroazepin-1-yl)acetamido]phenoxy}acetic acid (**15**) were synthesized using this procedure.

Enzyme assay

L-Leucine-*p*-nitroanilide, C.A.S. 4178-93-2, a substrate for AP-M, was purchased from Bachem, Switzerland, and AP-M, isolated from porcine kidneys,[21] from Calbiochem, U.S.A. The other chemicals used were of analytical or biochemical grade. The absorbance values at 405 nm, which is the absorption maximum of 4-nitroaniline, a product of substrate hydrolysis catalyzed by AP-M, were measured on an SP 1800 UV–Vis spectrophotometer (Pye Unicam, U.K.). The results of the assays were evaluated and K_i and IC_{50} values were calculated using GraFit biochemical software (Erichaus, U.S.A.). The colorimetric assay of enzyme inhibition was performed according to a previously described procedure,[22] which is considered a standard analytical method for such a purpose, although some alternative approaches including RP–HPLC with fluorescence detection have also been successfully tested.[23]

RESULTS AND DISCUSSION

A homological series of 2-{[2-(2-oxo-1-azacycloalk-2-yl)acetamido]phenoxyacetic acids containing a 5–7-membered ω-lactam ring was prepared using a conventional synthetic procedure, which can be shortly described as the alkylation of *o*-, *m*- or *p*-nitrophenol with chloroacetic acid (both reactants in the form of their sodium salts), reduction of the resulting nitrophenoxyacetic acids to aminophenoxyacetic acids with ferrous ammonium sulfate, *N*-acylation of these amino acids with chloroacetyl chloride and alkylation of ω-lactams (in form of their potassium salts) with the resulting chloroacetamidophenoxyacetic acids.

For the reduction of the nitro groups to amino moieties, both catalytic hydrogenation on a palladium catalyst and reduction with stannous chloride were tested but only the 'traditional' reduction with a ferrous salt according to the method of Jacobs and Heidelberger[20] led to the desired products. Hydrogenation under normal pressure proceeded very slowly and gave a mixture of products while reaction with stannous chloride resulted in hardly cleavable coordination compound of an amino acid with a stannic cation.

The final step of the synthesis, the alkylation of a metallic salt of ω-lactam with chloroacetamidophenoxyacetic acid, was successful only when the potassium salt of the lactame was used with an excess of potassium hydroxide. The use of the sodium salt of the ω-lactam, which can be easily generated by the action of metallic sodium on the lactam in an aromatic solvent, led exclusively to the piperazine-2,5-dione derivative, *i.e.*, 2,2'-[2,5-dioxopiperazine-1,4-diylbis-(4,1-phenyleneoxy)]bisacetic acid, which resulted from the mutual alkylation of

two molecules of chloroacetamidophenoxyacetic acid. This reaction is enabled due to comparable N–H acidity of ω-lactams and the chloroacetamidic moiety, expressed by the equilibrium at the top of Scheme 2. The successful *N*-alkylation of the potassium salts of ω-lactams with compounds containing a chloroacetamidic group is probably the result of the larger volume and solvation ability of potassium cations in comparison with sodium cations (Scheme 2).

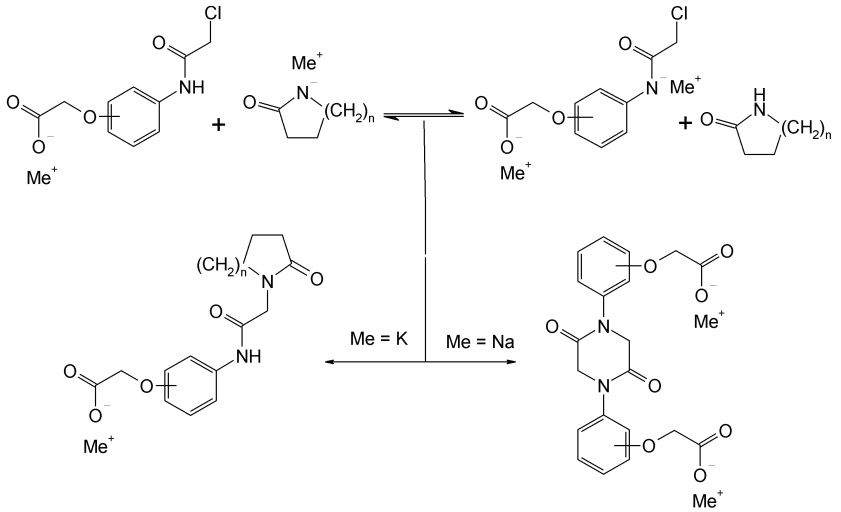

Scheme 2. Behaviour of chloroacetamidophenoxyacetic acids in the presence of metallic salts of ω-lactams.

The yields, melting points and spectral data of the prepared {[2-(2-oxo-1--azacycloalkyl)acetamido]phenoxy}acetic acids are given below.

*2-{2-[2-(2-Oxopyrrolidin-1-yl)acetamido]phenoxy}acetic acid (**7**)*. Yield: 93 %, m.p. 134–138 °C. Anal. Calcd. for $C_{14}H_{16}N_2O_5$: C, 57.53; H, 5.52; N, 9.58. Found: C, 57.61; H, 5.49; N 9.71. IR (KBr, cm^{-1}): 3329 (NH), 1753 (**CO**OH), 1689 (**CO**NH), 1607 (C=C aromatic), 1549 (NH), 1222 ($C_{aromatic}$–O–C). ^{1}H-NMR (200 MHz, DMSO-d_6, δ, ppm): 9.26 (1H, *s*, –NHCO), 8.0 (1H, *d,* aromatic, J = = 7.3 Hz), 6.80–7.35 (3H, *m,* aromatic), 4.76 (2H, *s,* –OCH_2), 4.07 (2H, *s,* –$COCH_2N$), 3.44 (2H, *t*, –N**H**$_2$$CH_2$, J = 7.0 Hz), 2.28 (2H, *t,* –CO**H**$_2$$CH_2$, J = = 8.0 Hz), 1.80–2.15 (2H, *m,* –CH_2C**H**$_2$$CH_2$). ^{13}C-NMR (50 MHz, DMSO-d_6, δ, ppm): 175.0, 170.6, 166.7, 148.2, 127.7, 124.5, 121.5, 120.9, 113,4, 66.2, 47.6, 46.2, 30.1, 17.7.

*2-{3-[2-(2-Oxopyrrolidin-1-yl)acetamido]phenoxy}acetic acid (**8**)*. Yield: 99 %, m.p. 86–89 °C. Anal. Calcd. for $C_{14}H_{16}N_2O_5$: C, 57.53; H, 5.52; N, 9.58. Found: C, 57.63; H, 5.43; N 9.75. IR (KBr, cm^{-1}): 3311 (NH), 2911 (CH_2), 1747 (**CO**OH), 1668 (**CO**NH), 1604 (C=C aromatic), 1552 (NH), 1220 ($C_{aromatic}$–O–C). ^{1}H-NMR (200 MHz, DMSO-d_6, δ, ppm): 10.09 (1H, *s*, –NHCO), 7.05–7.35 (3H, *m*, aro-

matic), 6.55–6.65 (1H, *m*, aromatic), 4.62 (2H, *s*, –OCH_2), 4.02 (2H, *s*,–$COCH_2N$), 3.43 (2H, *t*, –NCH_2CH_2, *J* = 6.8 Hz), 2.27 (2H, *t*, –$COCH_2CH_2$, *J* = 8.2 Hz), 1.85–2.10 (2H, *m*, –$CH_2CH_2CH_2$). ^{13}C-NMR (50 MHz, DMSO-d_6, δ, ppm): 174.8, 170.2, 166.8, 158.2, 140.0, 129.7, 112.0, 109.5, 105.6, 64.6, 47.6, 45.7, 30.1, 17.7.

*2-{4-[2-(2-Oxopyrrolidin-1-yl)acetamido]phenoxy}acetic acid (**9**)*. Yield: 99 %, m.p. 127–129 °C. Anal. Calcd. for $C_{14}H_{16}N_2O_5$: C, 57.53; H, 5.52; N, 9.58. Found: C, 57.59; H, 5.58; N 9.80. IR (KBr, cm^{-1}): 3273 (NH), 2935 (CH_2), 1751 (**CO**OH), 1666 (**CO**NH), 1616 (C=C aromatic), 1559 (NH), 1245 ($C_{aromatic}$–O–C). ^{1}H-NMR (200 MHz, DMSO-d_6, δ, ppm): 9.95 (1H, *s*, –NHCO), 7.46 (2H, *d*, aromatic CH=C–O, *J* = 8.1 Hz), 6.85 (2H, *d*, aromatic CH=C–N, *J* = 8.1 Hz), 4.62 (2H, *s*, –OCH_2CO), 3.99 (2H, *s*, –$COCH_2N$), 3.42 (2H, *t*, –NCH_2CH_2, *J* = 6.9 Hz), 2.26 (2H, *t*, –$COCH_2CH_2$, *J* = 7.9 Hz), 1.85–2.05 (2H, *m*, –$CH_2CH_2CH_2$). ^{13}C-NMR (50 MHz, DMSO-d_6, δ, ppm): 174.8, 170.4, 166.2, 153.9, 132.5, 120.9, 114.7, 64.9, 47.6, 45.6, 30.2, 17.7.

*2-{2-[2-(2-Oxopiperidin-1-yl)acetamido]phenoxy}acetic acid (**10**)*. Yield: 78 %, m.p. 155–160 °C. Anal. Calcd. for $C_{15}H_{18}N_2O_5$: C, 58.82; H 5.92; N 9.15. Found: C, 58.91; H, 6.01; 9.09. IR (KBr, cm^{-1}): 3372 (NH), 1708 (CO), 1604 (C=C aromatic), 1537 (NH), 1220 ($C_{aromatic}$–O–C). ^{1}H-NMR (200 MHz, DMSO-d_6, δ, ppm): 9.14 (1H, *s*, –NHCO), 8.05 (1H, *d*, aromatic, *J* = 7.3 Hz), 6.85–7.10 (3H, *m*, aromatic), 4.76 (2H, *s*, –OCH_2CO), 4.13 (2H, *s*, –$COCH_2N$), 3.2–3.4 (2H, *m*, –NCH_2CH_2), 2.15–2.40 (2H, *m*, –$COCH_2CH_2$), 1.60–1.85 (4H, *m*, –$CH_2CH_2CH_2CH_2$). ^{13}C-NMR (50 MHz, DMSO-d_6, δ, ppm): 170.5, 169.7, 167.3, 148.2, 127.9, 124.2, 121.5, 116.3, 113.2, 66.9, 50.8, 49.0, 31.9, 22.8, 21.2.

*2-{3-[(2-2-Oxopiperidin-1-yl)acetamido]phenoxy}acetic acid (**11**)*. Yield: 94 %, m.p. 96–99 °C. Anal. Calcd. for $C_{15}H_{18}N_2O_5$: C, 58.82; H 5.92; N 9.15. Found: C, 58.86; H, 9.06; N, 9.21. IR (KBr, cm^{-1}): 3303 (NH), 2942 (CH_2), 1756 (**CO**OH), 1671 (**CO**NH), 1601 (C=C aromatic), 1543 (NH), 1217 ($C_{aromatic}$–O–C). ^{1}H-NMR (200 MHz, DMSO-d_6, δ, ppm): 10.06 (1H, *s*, –NHCO), 7.05–7.30 (3H, *m*, aromatic), 6.50–6.65 (1H, *m*, aromatic), 4.62 (2H, *s*, –OCH_2CO), 4.07 (2H, *s*, –$COCH_2N$), 3.2–3.4 (2H, *m*, –NCH_2CH_2), 2.20–2.40 (2H, *m*, –$COCH_2CH_2$), 1.6–1.9 (4H, *m*, –$CH_2CH_2CH_2CH_2$). ^{13}C-NMR (50 MHz, DMSO-d_6, δ, ppm): 170.2, 169.3, 167.3, 158.2, 140.2, 129.7, 111.9, 109.4, 105.4, 64.6, 50.2, 49.1, 32.0, 22.9, 21.3.

*2-{4-[2-(2-Oxopiperidin-1-yl)acetamido]phenoxy}acetic acid (**12**)*. Yield: 99 %, m.p. 117–119 °C. Anal. Calcd. for $C_{15}H_{18}N_2O_5$: C, 58.82; H 5.92; N 9.15. Found: C, 58.93; H, 9.10; N, 9.05. IR (KBr, cm^{-1}): 3262 (NH), 2945 (CH_2), 1747 (**CO**OH), 1677 (**CO**NH), 1622 (C=C aromatic), 1555 (NH), 1229 ($C_{aromatic}$–O–C). ^{1}H-NMR (200 MHz, DMSO-d_6, δ, ppm): 9.89 (1H, *s*, –NHCO), 7.47 (2H, *d*, aromatic –CH=C–O, *J* = 9.2 Hz), 6.85 (2H, *d*, aromatic –CH=C–N, *J* = 9.2 Hz), 4.62 (2H, *s*, –OCH_2CO), 4.05 (2H, *s*, –$COCH_2N$), 3.2–3.4 (2H, *m*, –NCH_2CH_2), 2.1–2.4 (2H, *m*, –$COCH_2CH_2$), 1.6–1.9 (4H, *m*, –$CH_2CH_2CH_2CH_2$). ^{13}C-NMR

(50 MHz, DMSO-d_6, δ, ppm): 170.4, 169.3, 166.8, 153.8, 132.7, 120.7, 114.7, 64.9, 50.0, 49.1, 32.0, 22.9, 21.3.

2-{2-[2-(2-Oxoperhydroazepin-1-yl)acetamido]phenoxy}acetic acid ***(13)***. Yield: 57 %, m.p. 130–134 °C. Anal. Calcd. for $C_{16}H_{20}N_2O_5$: C, 59.99; H, 6.29; N, 8.74. Found: C, 59.84; H, 6.37; N, 8.82; IR (KBr, cm^{-1}): 3312 (NH), 2935 (CH_2), 1730 (**CO**OH), 1682 (**CO**NH), 1608 (C=C aromatic), 1541 (NH), 1200 ($C_{aromatic}$–O–C). ^{1}H-NMR (200 MHz, DMSO-d_6, δ, ppm): 9.07 (1H, *s*, –NHCO), 8.07 (1H, *d*, aromatic, J = 7.3 Hz), 6.8–7.2 (3H, *m*, aromatic), 4.75 (2H, *s*, –OCH_2CO), 4.15 (2H, *s*, –$COCH_2$N), 3.3–3.5 (2H, *m*, NC**H**$_2$$CH_2$), 2.51–2.58 (2H, *m*, COC**H**$_2$$CH_2$), 1.4–1.8 (6H, *m*, -C**H**$_2$C**H**$_2$C**H**$_2$). ^{13}C-NMR (50 MHz, DMSO-d_6, δ, ppm): 175.6, 170.5, 167.6, 148.2, 127.9, 124.2, 121.5, 120.9, 113.1, 65.9, 52.5, 50.4, 36.4, 29.4, 27.9, 23.0.

2-{3-[2-(2-Oxoperhydroazepin-1-yl)acetamido]phenoxy}acetic acid ***(14)***. Yield: 90 %, m.p. 84–87 °C. Anal. Calcd. for $C_{16}H_{20}N_2O_5$: C, 59.99; H, 6.29; N, 8.74. Found: C, 59.89; H, 6.37; N, 8.84. IR (KBr, cm^{-1}): 3437 (NH), 2930 (CH_2), 1744 (**CO**OH), 1686 (**CO**NH), 1613 (C=C aromatic), 1552 (NH), 1223 ($C_{aromatic}$– –O–C). ^{1}H-NMR (200 MHz, DMSO-d_6, δ, ppm): 9.96 (1H, *s*, –NHCO), 7.0–7.4 (3H, *m*, aromatic), 6.5–6.7 (1H, *m*, aromatic), 4.62 (2H, *s*, –OCH_2CO), 4.11 (2H, *s*, –$COCH_2$N), 3.2–3.6 (2H, *m*, –NC**H**$_2$$CH_2$), 2.4–2.6 (2H, *m*, –COC**H**$_2$$CH_2$), 1.4–1.9 (6H, *m*, –C**H**$_2$C**H**$_2$C**H**$_2$). ^{13}C-NMR (50 MHz, DMSO-d_6, δ, ppm): 175.3, 170.2, 167.8, 158.2, 140.3, 129.7, 112.0, 109.3, 105.5, 64.6, 52.0, 50.6, 36.5, 29.5, 27.8, 23.1.

2-{4-[2-(2-Oxoperhydroazepin-1-yl)acetamido]phenoxy}acetic acid ***(15)***. Yield: 83 %, m.p. 199–203 °C. Anal. Calcd. for $C_{16}H_{20}N_2O_5$: C, 59.99; H, 6.29; N, 8.74. Found: C, 59.81; H, 6.34; N, 8.81. IR (KBr, cm^{-1}): 3281 (NH), 2927 (CH_2), 1726 (**CO**OH), 1665 (**CO**NH), 1604 (C=C aromatic), 1549 (NH), 1229 ($C_{aromatic}$–O–C). ^{1}H-NMR (200 MHz, DMSO-d_6, δ, ppm): 9.82 (1H, *s*, –NHCO), 7.46 (2H, *d*, aromatic, J = = 8.8 Hz), 6.85 (2H, *d*, aromatic, J = 9.2 Hz), 4.75 (2H, *s*, –OCH_2CO), 4.15 (2H, *s*, –$COCH_2$N), 3.3–3.5 (2H, *m*, –NC**H**$_2$$CH_2$), 2.41–2.50 (2H, *m*, –COC**H**$_2$$CH_2$), 1.4–1.8 (6H, *m*, –C**H**$_2$C**H**$_2$C**H**$_2$). ^{13}C-NMR (50 MHz, DMSO-d_6, δ, ppm): 175.3, 170.4, 167.3, 153.8, 132.7, 120.8, 114.7, 64.9, 51.9, 50.5, 36.6, 29.8, 27.8, 23.1.

Five selected 2-{2-[2-(2-oxo-1-azacycloalkyl)acetamido]phenoxy}acetic acids underwent testing of their influence on activity of AP-M. Their inhibition abilities, expressed as IC_{50} and K_i values, are given in Table I.

Table I. Influence of selected prepared substances on the activity of AP-M

Compound	K_i / μM	IC_{50} / μM
7	514.3	948.5
10	636.6	1174.0
13	308.7	569.4
14	423.8	781.5
15	243.6	449.2

CONCLUSIONS

All the studied substances possessed inhibitory activity to AP-M. The highest inhibition, characterized by IC_{50} = 449.5 μM and K_i = 243.6 μM was exhibited by compound **15**, *i.e.*, 2-{4-[2-(2-oxoperhydroazepin-1-yl)acetamido]phenoxy}acetic acid. Comparison of the activities of the tested compounds indicates that the perhydroazepin-2-one ring is more advantageous than piperidin-2-one or pyrrolidin-2-one, while the position of the 2-(2-oxo-1-azacycloalkyl)acetamido moiety to carboxymethoxy group on the benzene ring has no clear influence on AP-M inhibition.

ИЗВОД

СИНТЕЗА 2-{[2-(2-ОКСО-1-АЗАЦИКЛОАЛКИЛ)АЦЕТАМИДО]ФЕНОКСИ}СИРЋЕТНИХ КИСЕЛИНА И ЊИХОВА АКТИВНОСТ КАО ИНХИБИТОРА АМИНОПЕПТИДАЗЕ М

OLDŘICH FARSA[1], MILAN DOČKAL[1], JANA KOVÁČIKOVÁ[2] и MÁRIA BENEŠOVÁ[2]

[1]Institute of Chemical Drugs, Faculty of Pharmacy, University of Veterinary and Pharmaceutical Sciences Brno, Palackého 1/3, 612 42 Brno, Czech Republic u [2]Department of Cellular and Molecular Biology of Drugs, Faculty of Pharmacy, Comenius University, Kalinčiakova 8, 832 32 Bratislava, Slovak Republic

Серија од девет феноксисирћетних киселина супституисаних у *o*-, *m*- и *p*-положају бензеновог прстена 2-(2-оксо-1-азациклоалкил)ацетамидним фрагментом који садржи пето- до седмочлани *ω*-лактамски прстен синтетизована је поступком који обухвата четири фазе. Тестирана је *in vitro* инхибиторна активност пет одабраних једињења на аминопептидазу М из бубрега свиње. Највишу активност поседује 2-{4-[2-(2-оксоперхидроазепин-1-ил)ацетамидо]феноксиј}сирћетна киселина са K_i = 243,6 μM.

(Примљено 21. фебруара, ревидирано 9. маја 2008)

REFERENCES

1. A. Taylor, *FASEB J.* **7** (1993) 290
2. M. Matsui, J. H. Fowler, L. L. Walling, *Biol. Chem.* **387** (2006)1535
3. N. M. Hooper, *FEBS Lett.* **354** (1994) 1
4. A. L. Albiston, S. Ye, S.-Y. Cha, *Protein Pept. Lett.* **11** (2004) 491
5. N. Luciani, C. Marie-Claire, E. Ruffet, A. Beaumont, B. P. Roques, M.-C. Fournié-Zaluski, *Biochemistry* **37** (1998) 686
6. G. Pfleiderer, P. G. Celliers, *Biochem. Z.* **339** (1963) 186
7. G. J. Sanderink, Y. Artur, G. Siest, *J. Clin. Chem. Clin. Biochem.* **26** (1988) 795
8. F. E. Palmieri, J. J. Petrelli, P. E. Ward, *Biochem. Pharmacol.* **34** (1985) 2309
9. C. Gros, B. Giros, J.-C. Schwartz, *Biochemistry* **24** (1985) 2179
10. F. Noble, B. Roques, *Expert Opin. Ther. Targets* **11** (2007) 145
11. P. Kitabgi, *Peptides* **27** (2006) 2515
12. E. B. Binder, B. Kinkead, M. J. Owens, C. B. Nemeroff, *Biol. Psychiatry* **50** (2001) 601
13. J. W. Wright, J. W. Harding, *Prog. Neurobiol.* **72** (2004) 263
14. A. L. Albiston, R. Fernando, S. Ye, G. R. Peck, S. Y. Chai, *Biol. Pharm. Bull.* **27** (2004) 765
15. H. John, S. Schulz, W.-G. Forssmann, *Biopharm. Drug Dispos.* **28** (2007) 73
16. A. Lišková, L. Křivánková, *Electrophoresis* **26** (2005) 4429
17. O. Behaghel, *J. Prakt. Chem.* **114** (1926) 287

18. B. R. Baker, W. T. Ashton, *J. Med. Chem*. **13** (1970) 1165
19. M. Kumar, U. Rao, *Z. Kristallogr. Kristallgeom. Kristallphys. Kristallchem*. **147** (1978) 113
20. W. A. Jacobs, M. Heidelberger, *J. Am. Chem. Soc.* **39** (1917) 2437
21. D. Wachsmuth, I. Fritze, G. Pfleiderer, *Biochemistry* **5** (1966)169
22. J. C. M. Hafkenscheid, in *Methods of Enzymatic Analysis; Vol. 5, Enzymes 3,* H. U. Bergmeyer, Ed., VCH Verlagsgesellschaft, Weinheim, 1984, p. 2
23. X. Xiong, A. Barathi, R. W. Beuermann, D. T. H. Tan, *J. Chromatogr. B* **796** (2003) 63.

www.shd.org.rs

Journal of the Serbian Chemical Society

JSCS@tmf.bg.ac.yu • www.shd.org.rs/JSCS

J. Serb. Chem. Soc. 73 (8–9) 781–791 (2008)
JSCS–3761

UDC 547.78:615.212:615.276:577.115–39
Original scientific paper

Synthesis of 1-(4-phenoxyphenyl)-3-[5-(substituted aryl)-1,3,4-oxadiazol-2-yl]propan-1-ones as safer anti-inflammatory and analgesic agents

ASIF HUSAIN[1]*, F. J. AHMAD[2], MOHD AJMAL[1] and PRIYANKA AHUJA[1]

[1]Department of Pharmaceutical Chemistry and [2]Department of Pharmaceutics, Faculty of Pharmacy, Jamia Hamdard (Hamdard University), New Delhi–110062, India

(Received 18 September 2007, revised 9 May 2008)

Abstract: A novel series of 1-(4-phenoxyphenyl)-3-[5-(substituted aryl)-1,3,4-oxadiazol-2-yl]propan-1-one was synthesized by reaction of 3-(4-phenoxybenzoyl)propionic acid with several aryl acid hydrazides in phosphorus oxychloride. The structures of the compounds were supported by IR, ^{1}H- and ^{13}C-NMR, MS data and elemental analysis results. These compounds were tested for their anti-inflammatory, analgesic, ulcerogenic and lipid peroxidation actions. A few compounds were found to have very good anti-inflammatory activity in the carrageenan-induced rat paw edema test, while a fair number of the compounds showed significant analgesic activity in the acetic acid-induced writhing test. These new compounds showed very low ulcerogenic action with reduced malondialdehyde content (MDA), which is one of the by-products of lipid peroxidation.

Keywords: 1,3,4-oxadiazole; anti-inflammatory; analgesic; ulcerogenic; lipid peroxidation.

INTRODUCTION

Non-steroidal anti-inflammatory drugs (NSAIDs) are used for the treatment of pain, fever and inflammation, particularly arthritis;[1,2] they are the most commonly prescribed medications in the world. The most prevalent side effects of the use of non-steroidal anti-inflammatory drugs are the occurrence of gastrointestinal side effects[3] (gastric upset, irritation and ulceration). The search for safer NSAIDs continues with the failure of the anticipated "ideal" anti-inflammatory agents, the coxibs, on long-term usage.[4,5] 3-(4-Phenoxybenzoyl)propionic acid is an example of the well known aroylpropionic acid class of anti-inflammatory drugs.[6] Aroylpropionic acids are good anti-inflammatory agents but suffer from inducing gastrointestinal side effects.[6,7] It is well known that structural modifica-

* Corresponding author. E-mail: drasifhusain@yahoo.com
doi: 10.2298/JSC0809781H

tions can improve the pharmacological profile of an active molecule. Synthetic approaches based on chemical modification have been taken with the aim of improving the safety profile of NSAIDs.[7–12] These studies showed that derivatization of the carboxylate function of some NSAIDs resulted in an increased anti-inflammatory activity with a reduced ulcerogenic effect.

During recent years, there has been extensive investigation of different classes of oxadiazole compounds, many of which were found to possess a wide spectrum of biological activities. In particular, compounds having 1,3,4-oxadiazole nucleus are known to exhibit good anti-edema and anti-inflammatory activity.[13–15] Differently substituted oxadiazole moieties have also been found to have other interesting activities, such as analgesic, antibacterial, bactericidal, antifungal, anticonvulsant, anticancer, *etc*.[16–20]

In our attempt to discover safer agents for the treatment of inflammatory conditions, the carboxylic acid group of 3-(4-phenoxybenzoyl)propionic acid was replaced with an additional heterocycle, *i.e.*, 1,3,4-oxadiazole, which was found to possess potential anti-inflammatory and analgesic activity with significant reduction in their ulcerogenic effect.

RESULTS AND DISCUSSION

Chemistry

The 1-(4-phenoxyphenyl)-3-[5-(substituted aryl)-1,3,4-oxadiazol-2-yl]propan--1-ones **4a**–**l** described in this study are shown in Table I and the reaction sequence for their preparation is outlined in Scheme 1. The required 3-(4-phenoxybenzoyl)propionic acid **3** was prepared by condensing diphenyl ether with succinic anhydride in the presence of anhydrous aluminum chloride, following the Friedel–Crafts acylation reaction conditions. The reaction between 3-(4-phenoxybenzoyl)propionic acid **3** and aryl acid hydrazides **2a**–**l** in phosphorous oxychloride (the reaction time varied from 2 to 5 h) afforded the title compounds **4a**–**l** in 48–66 % yield after recrystallization from methanol. The purity of compounds was controlled by TLC and elemental analysis. Both the analytical and spectral data (^{1}H-NMR, IR and mass spectra) of the synthesized compounds were in full agreement with the proposed structures.

*1-(4-Phenoxyphenyl)-3-(5-phenyl-1,3,4-oxadiazol-2-yl)propan-1-one (**4a**)*. Yield: 62 %, m.p. 142 °C; IR (KBr, cm^{-1}): 3050, 1650, 1420, 780; ^{1}H-NMR ($CDCl_3$, δ, ppm): 2.51 and 3.47 (each 2H, *t*, J = 6.6 Hz, 2×CH_2), 7.47 (6H, *m*, H-3,4,5, 2×phenyl), 7.63 (4H, *m*, H-2,6, 2×phenyl), 7.67 and 8.13 (each *d*, J = 8.1 Hz, 2×A_2B_2, *p*-disubstituted phenyl); ^{13}C-NMR ($CDCl_3$, δ, ppm): 26.8 (C_1), 34.3 (C_2), 191.8 (C_3), 161.7 ($C_{2''}$), 164.2 ($C_{5''}$), 129.8 (C_4), 130 ($C_{5,9}$), 118.3 ($C_{6,8}$), 155.8 (C_7), 155.1 (C_{10}), 119.7 ($C_{11,15}$), 133.1 ($C_{12,14}$), 124.2 (C_{13}), 130.2 ($C_{1'}$), 127.1 ($C_{2',6'}$), 129.1 ($C_{3',5'}$), 131.3 ($C_{4'}$); MS (*m*/*z*): 370 (M^+), 197, 170, 78, 77.

TABLE I. Anti-inflammatory, analgesic, ulcerogenic and lipid peroxidation activity of the compounds **4a**–**l**

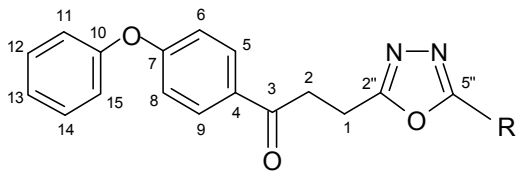

Compd.	R	Anti-inflammatory activity, % inhibition	Analgesic activity, % protection	Ulcerogenic activity (severity index)	Lipid peroxidation (nmol MDA content/100 mg tissue)
4a	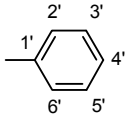	40.63	41.12	0.454	4.425
4b		43.75	56.35	0.523	5.733
4c	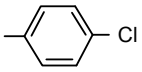	46.87	61.86	0.581	5.813
4d	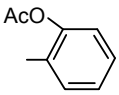	65.63	76.33	0.666	5.808
4e	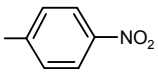	50.00	38.80	0.525	4.715
4f	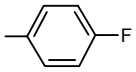	53.13	58.52	0.581	4.830
4g	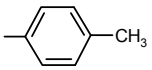	37.50	41.12	0.525	5.054
4h	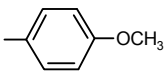	56.25	54.31	0.523	6.115
4i	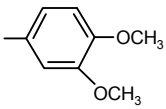	62.50	67.83	0.581	4.973
4j	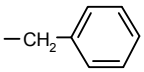	46.87	50.12	0.666	5.018

TABLE I. Continued

4k	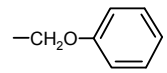	50.00	55.80	0.525	5.433
4l	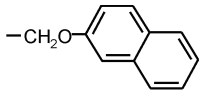	53.13	58.57	0.581	5.834
3	–	43.75	46.36	1.553	6.651
Indomethacin		68.75	72.44	2.332	8.133

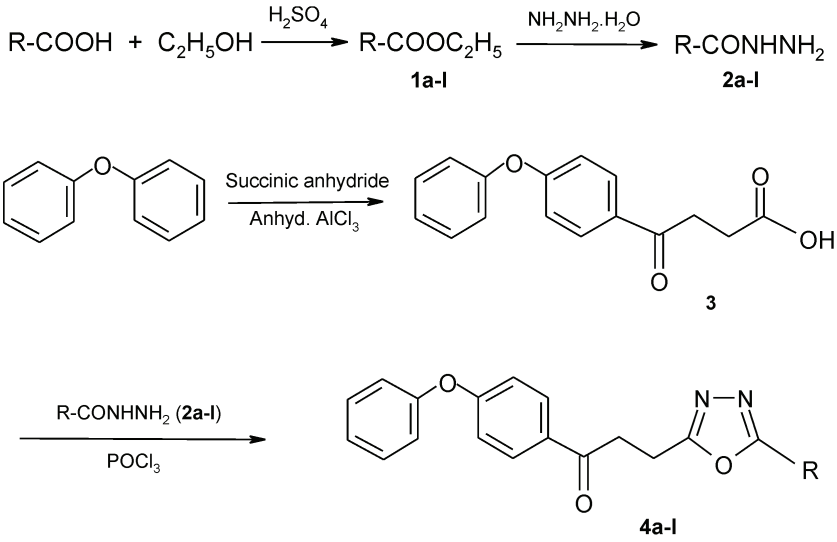

R=C_6H_5-, 2-Cl-C_6H_4-, 4-Cl-C_6H_4-, 2-OAc-C_6H_4-, 4-NO_2-C_6H_4-,4-F-C_6H_4-, 4-CH_3-C_6H_4-
-4-OCH_3-C_6H_4-,3,4-$(OCH_3)_2$-C_6H_3-, $C_6H_5CH_2$-, C_6H_5-OCH_2-, 2-$C_{10}H_7$-OCH_2-

Scheme 1.

*3-[5-(2-Chlorophenyl)-1,3,4-oxadiazol-2-yl]-1-(4-phenoxyphenyl)propan-1--one (**4b**)*. Yield: 56 %, m.p. 154–156 °C; IR (KBr, cm^{-1}): 3100, 1655, 1435, 820; ^{1}H-NMR ($CDCl_3$, δ, ppm): 2.55 and 3.43 (each 2H, *t*, *J* = 6.6 Hz, 2×CH_2), 7.29 (4H, *m*, H-3,4,5,6, *o*-chlorophenyl), 7.58 (5H, *m*, phenyl), 7.73 and 7.84 (each *d*, *J* = 8.1 Hz, 2×A_2B_2, *p*-disubstituted phenyl); ^{13}C-NMR ($CDCl_3$ δ, ppm): 27.4 (C_1), 34.3 (C_2), 192.5 (C_3), 159.8 ($C_{2''}$), 164.1 ($C_{5''}$), 129.7 (C_4), 130.6 ($C_{5,9}$), 117.6 ($C_{6,8}$), 155.6 (C_7), 155.2 (C_{10}), 119.8 ($C_{11,15}$), 132.6 ($C_{12,14}$), 124.1 (C_{13}), 127.4 ($C_{1'}$), 135.2 ($C_{2'}$), 128.7 ($C_{3'}$), 130.2 ($C_{4',6'}$), 127.8 ($C_{5'}$); MS (*m*/*z*): 404 (M^+), 197, 169, 77.

*3-[5-(4-Chlorophenyl)-1,3,4-oxadiazol-2-yl]-1-(4-phenoxyphenyl)propan-1--one (**4c**)*. Yield: 60 %, m.p 142 °C; IR (KBr, cm^{-1}): 3080, 1655, 1430, 810; ^{1}H-NMR ($CDCl_3$, δ, ppm): 2.51 and 3.57 (each 2H, *t*, *J* = 6.6 Hz, 2×CH_2), 7.33

(3H, *m*, H-3,4,5, phenyl), 7.38 (2H, *m*, H-2,6, phenyl), 7.46 and 7.65 (each, *d*, *J* = = 8.1 Hz, 2×A_2B_2, *p*-disubstituted phenyl; phenoxyphenyl), 7.15 and 7.83 (each, *d*, *J* = 8.4 Hz, 2×A_2B_2, *p*-chlorophenyl); ^{13}C-NMR ($CDCl_3$, δ, ppm): 27.3 (C_1), 34.3 (C_2), 193.1 (C_3), 159.2 ($C_{2''}$), 164.1 ($C_{5''}$), 129.2 ($C_{4,1'}$), 131.2 ($C_{5,9}$), 118.7 ($C_{6,8}$), 155.4 (C_7), 155.2 (C_{10}), 119.6 ($C_{11,15}$), 131.3 ($C_{12,14}$), 124.1 (C_{13}), 126.7 ($C_{2',6'}$), 129.9 ($C_{3',5'}$), 136.6 ($C_{4'}$); MS (*m*/*z*): 404 (M^+), 197, 169.

*3-[5-(2-Acetoxyphenyl)-1,3,4-oxadiazol-2-yl]-1-(4-phenoxyphenyl)propan-1-one (**4d**)*. Yield: 66 %, m.p. 136–138 °C; IR (KBr, cm^{-1}): 3100, 1660, 1425, 800; ^{1}H-NMR ($CDCl_3$, δ, ppm): 2.43 (3H, *s*, $OCOCH_3$), 2.61 and 3.54 (each 2H, *t*, *J* = 6.6 Hz, 2×CH_2), 7.46 (3H, *m*, H-3,4,5, phenyl), 7.67 (2H, *m*, H-2,6, phenyl), 7.25 (4H, *m*, H-3,4,5,6, *o*-disubstituted phenyl), 7.77 and 7.84 (each, *d*, *J* = = 8.1 Hz, 2×A_2B_2, *p*-disubstituted phenyl); ^{13}C-NMR ($CDCl_3$, δ, ppm): 26.9 (C_1), 34.1 (C_2), 191.7 (C_3), 160.6 ($C_{2''}$), 165.5 ($C_{5''}$), 130 (C_4), 129.8 ($C_{5,9}$), 122.4 ($C_{6,8,3'}$), 156.1 (C_7), 155.8 (C_{10}), 119.8 ($C_{11,15}$), 127.2 ($C_{12,14}$), 123.5 (C_{13}), 113.9 ($C_{1'}$), 147.2 ($C_{2'}$), 133.8 ($C_{4'}$), 124.3 ($C_{5'}$), 125.6 ($C_{-6'}$), 168.3 (C=O), 20.7 (–OAc); MS (*m*/*z*): M^+ not observed, 197, 169, 92, 78, 77.

*3-[5-(4-Nitrophenyl)-1,3,4-oxadiazol-2-yl]-1-(4-phenoxyphenyl)propan-1-one (**4e**)*. Yield: 54 %, m.p. 152 °C; IR (KBr, cm^{-1}): 3080, 1665, 1433, 815. ^{1}H-NMR ($CDCl_3$, δ, ppm): 2.63 and 3.57 (each 2H, *t*, *J* = 6.6 Hz, 2×CH_2), 7.44 (3H, *m*, H-3,4,5, phenyl), 7.66 (2H, *m*, H-2,6, phenyl), 7.73 and 7.85 (each, *d*, *J* = = 8.1 Hz, 2×A_2B_2, *p*-nitrophenyl), 7.77 and 7.98 (each, *d*, *J* = 8.1 Hz, 2×A_2B_2, *p*-disubstituted phenyl); ^{13}C-NMR ($CDCl_3$, δ, ppm): 26.8 (C_1), 34.3 (C_2), 192.3 (C_3), 158.8 ($C_{2''}$), 164.3 ($C_{5''}$), 129.6 (C_4), 129.8 ($C_{5,9}$), 123.5 ($C_{6,8}$), 157.3 (C_7), 155.1 (C_{10}), 118.4 ($C_{11,15}$), 128.6 ($C_{12,14,1'}$), 123.9 (C_{13}), 126.9 ($C_{2',6'}$), 119.6 ($C_{3',5'}$), 135.7 ($C_{4'}$). MS (*m*/*z*): 415 (M^+), 197, 169.

*3-[5-(4-Fluorophenyl)-1,3,4-oxadiazol-2-yl]-1-(4-phenoxyphenyl)propan-1-one (**4f**)*. Yield: 65 %, m.p. 146–148 °C; IR (KBr, cm^{-1}): 3020, 1655, 1430, 760; ^{1}H-NMR ($CDCl_3$, δ, ppm): 2.55 and 3.52 (each 2H, *t*, *J* = 6.6 Hz, 2×CH_2), 7.47 (3H, *m*, H-3,4,5, phenyl), 7.68 (2H, *m*, H-2,6, phenyl), 7.44 and 7.56 (each, *d*, *J* = = 8.1 Hz, 2×A_2B_2, *p*-fluorophenyl), 7.05 and 7.87 (each, *d*, *J* = 8.1 Hz, 2×A_2B_2, *p*-disubstituted phenyl); ^{13}C-NMR ($CDCl_3$, δ, ppm): 26.9 (C_1), 34.5 (C_2), 192.7 (C_3), 159.1 ($C_{2''}$), 164.5 ($C_{5''}$), 131.1 (C_4), 132.9 ($C_{5,9}$), 124.4 ($C_{6,8,13}$), 157.1 (C_7), 155.3 (C_{10}), 119.8 ($C_{11,15}$), 129.4 ($C_{12,14,1'}$), 127.3 (C_{13}), 127.3 ($C_{2',6'}$), 129.4 ($C_{3',5'}$), 143.6 ($C_{4'}$); MS (*m*/*z*): 388 (M^+), 197, 169, 77.

*3-[5-(4-Methylphenyl)-1,3,4-oxadiazol-2-yl]-1-(4-phenoxyphenyl)propan-1-one (**4g**)*. Yield: 57 %, m.p. 146 °C; IR (KBr, cm^{-1}): 3030, 1665, 1428, 805; ^{1}H-NMR ($CDCl_3$, δ, ppm): 2.13 (3H, *s*, CH_3), 2.55 and 3.49 (each 2H, *t*, *J* = 6.6 Hz, 2×CH_2), 6.68 and 7.77 (each, *d*, *J* = 8.1 Hz, 2×A_2B_2, phenyl), 7.43 (5H, *m*, phenyl), 6.91 and 7.64 (each, *d*, *J* = 8.1 Hz, 2×A_2B_2, *p*-methylphenyl); ^{13}C-NMR ($CDCl_3$, δ, ppm): 26.7 (C_1), 34.1 (C_2), 193.1 (C_3), 158.7 ($C_{2''}$), 163.9 ($C_{5''}$), 130.8 ($C_{4,1'}$), 133.7 ($C_{5,9}$), 124.3 ($C_{6,8}$), 157.6 (C_7), 156.2 (C_{10}), 118.4 ($C_{11,15}$), 129.9

($C_{12,14}$), 126.6 (C_{13}), 127.1 ($C_{2',6'}$), 128.3 ($C_{3',5'}$), 133.7 ($C_{4'}$), 22.4 (CH_3); MS (*m*/*z*): 384 (M^+), 197, 169, 91.

*3-[5-(4-Methoxyphenyl)-1,3,4-oxadiazol-2-yl]-1-(4-phenoxyphenyl)propan-1--one (**4h**)*. Yield: 58 %, m.p. 164–166 °C; IR (KBr, cm^{-1}): 3020, 1655, 1433, 780; ^{1}H-NMR ($CDCl_3$, δ, ppm): 3.84 (3H, *s*, OCH_3), 2.60 and 3.19 (each 2H, *t*, *J* = 6.6 Hz, 2×CH_2), 6.78 and 7.87 (each, *d*, *J* = 8.1 Hz, 2×A_2B_2, phenyl), 7.55 (5H, *m*, phenyl), 7.13 and 7.73 (each, *d*, *J* = 8.4 Hz, 2×A_2B_2, *p*-methoxy phenyl); ^{13}C-NMR ($CDCl_3$, δ, ppm): 26.1 (C_1), 34.3 (C_2), 194.4 (C_3), 158.9 ($C_{2''}$), 164.2 ($C_{5''}$), 130.8 (C_4), 132.4 ($C_{5,9}$), 123.3 ($C_{6,8}$), 157.8 (C_7), 156.6 (C_{10}), 118.1 ($C_{11,15}$), 130.2 ($C_{12,14}$), 125.8 (C_{13}), 126.5 ($C_{1'}$), 125.1 ($C_{2',6'}$), 129.4 ($C_{3',5'}$), 141.7 ($C_{4'}$), 52.6 (OCH_3). MS (*m*/*z*): 400 (M^+), 197, 169.

*3-[5-(3,4-Dimethoxyphenyl)-1,3,4-oxadiazol-2-yl]-1-(4-phenoxyphenyl)propan-1-one (**4i**)*. Yield: 62 %, m.p. 162 °C; IR (KBr, cm^{-1}): 3100, 1660, 1420, 810; ^{1}H-NMR ($CDCl_3$, δ, ppm): 3.96 (6H, two closely spaced singlets, 2×OCH_3), 2.58 and 3.44 (each, *t*, *J* = 6.6 Hz, 2×CH_2), 6.99 (1H, *d*, *J* = 7.8 Hz, H-5, dimethoxyphenyl), 7.15 (1H, *d*, *J* = 2 Hz, H-2, dimethoxy phenyl), 7.37 (1H, *dd*, *J* = 7.8 Hz, H-6, dimethoxyphenyl), 7.46 (3H, *m*, H-3,4,5, phenyl), 7.66 (2H, *m*, H-2,6, phenyl), 7.71 and 8.17 (each, *d*, *J* = 8.1 Hz, 2×A_2B_2, *p*-disubstituted phenyl); ^{13}C-NMR ($CDCl_3$, δ, ppm): 26.4 (C_1), 34.8 (C_2), 192.8 (C_3), 158.5 ($C_{2''}$), 164.1 ($C_{5''}$), 129.6 (C_4), 131.8 ($C_{5,9}$), 121.3 ($C_{6,8}$), 159.1 (C_7), 157.2 (C_{10}), 118.5 ($C_{11,15}$), 130.1 ($C_{12,14}$), 124.3 (C_{13}), 127.1 ($C_{1'}$), 119.8 ($C_{2',5'}$), 146.2 ($C_{3'}$), 143.7 ($C_{4'}$), 107.6 ($C_{6'}$), 54.7 (OCH_3); MS (*m*/*z*): 430 (M^+), 197, 169, 77.

*3-(5-Benzyl)-1,3,4-oxadiazol-2-yl]-1-(4-phenoxyphenyl)propan-1-one (**4j**)*. Yield: 54 %, m.p. 155 °C; IR (KBr, cm^{-1}): 3080, 1655, 1435, 805; ^{1}H-NMR ($CDCl_3$, δ, ppm): 2.37 and 3.58 (each 2H, *t*, *J* = 6.6 Hz, 2 x CH_2), 4.14 (3H, *s*, CH_2), 7.39 (6H, *m*, H-3,4,5, 2×phenyl), 7.61 (4H, *m*, H-2,6, 2×phenyl), 7.66 and 7.81 (each, *d*, *J* = 8.1 Hz, 2×A_2B_2, *p*-disubstituted phenyl); ^{13}C-NMR ($CDCl_3$, δ, ppm): 27.1 (C_1), 35.3 (C_2), 192.6 (C_3), 160.5 ($C_{2''}$), 159.8 ($C_{5''}$), 131.4 (C_4), 132.2 ($C_{5,9}$), 120.6 ($C_{6,8}$), 157.1 (C_7), 156.6 (C_{10}), 118.7 ($C_{11,15}$), 130.1 ($C_{12,14}$), 123.2 (C_{13}), 132.2 ($C_{1'}$), 128.6 ($C_{2',6'}$), 127.7 ($C_{3',5'}$), 127.5 ($C_{4'}$), 32.3 (CH_2); MS (*m*/*z*): 384 (M^+), 197, 169, 91, 77.

*3-[5-(Phenoxymethyl)-1,3,4-oxadiazol-2-yl]-1-(4-phenoxyphenyl)propan-1--one (**4k**)*. Yield: 64 %, m.p. 162 °C; IR (KBr, cm^{-1}): 3090, 1653, 1422, 790; ^{1}H-NMR ($CDCl_3$, δ, ppm): 2.52 and 3.48 (each 2H, *t*, *J* = 6.6 Hz, 2×CH_2), 4.56 (3H, *s*, OCH_2), 7.47 (6H, *m*, H-3,4,5, 2×phenyl), 7.65 (4H, *m*, H-2,6, 2×phenyl), 7.73 and 7.85 (each, *d*, *J* = 8.1 Hz, 2×A_2B_2, *p*-disubstituted phenyl); ^{13}C-NMR ($CDCl_3$, δ, ppm): 26.3 (C_1), 35.8 (C_2), 191.1 (C_3), 161.3 ($C_{2''}$), 157.1 ($C_{5''}$), 131.9 (C_4), 131.7 ($C_{5,9}$), 122.5 ($C_{6,8}$), 157.8 (C_7), 156.2 (C_{10}), 117.1 ($C_{11,15}$), 128.4 ($C_{12,14}$), 121.8 (C_{13}), 141.9 ($C_{1'}$), 121.5 ($C_{2',6'}$), 129.3 ($C_{3',5'}$), 123.6 ($C_{4'}$), 60.3 (OCH_2); MS (*m*/*z*): 400 (M^+), 197, 169, 135.

*3-[5-(2-Naphthyloxymethyl)-1,3,4-oxadiazol-2-yl]-1-(4-phenoxyphenyl)propan-1-one (**4l**)*. Yield: 48 %, m.p. 174 °C; IR (KBr, cm^{-1}): 3085, 1655, 1435, 785.; ^{1}H-NMR ($CDCl_3$, δ, ppm): 2.54 and 3.48 (each 2H, *t*, *J* = 6.6 Hz, 2×CH_2), 4.89 (3H, *s*, OCH_2), 7.21 (2H, *m*, H-1,3, naphthoxy), 7.47 (3H, *m*, H-3,4,5, phenyl), 7.67 (2H, *m*, H-2,6, phenyl), 7.76 and 8.13 (each, *J* = 8.1 Hz, 2×A_2B_2, *p*-disubstituted phenyl), 7.97 (5H, *m*, H-4,5,6,7,8, naphthoxy); ^{13}C-NMR ($CDCl_3$, δ, ppm): 26.8 (C_1), 36.1 (C_2), 192.3 (C_3), 160.7 ($C_{2''}$), 156.3 ($C_{5''}$), 130.9 (C_4), 132.3 ($C_{5,9}$), 121.8 ($C_{6,8}$), 156.1 (C_7), 155.8 (C_{10}), 118.2 ($C_{11,15}$), 128.7 ($C_{12,14}$), 122.8 (C_{13}), 144.2 ($C_{1'}$), 108.9 ($C_{2'}$), 135.3 ($C_{3'}$), 126.1 ($C_{4',5',6',7'}$), 129.3 ($C_{8',9'}$), 119.8 ($C_{10'}$), 61.6 (OCH_2); MS (*m*/*z*): 450 (M^+), 197, 169, 128.

In general, IR data revealed bands at 3100–3030 (C–H); 1650–1665 (C=O); 1440–1420 (C–N) and 750–830 cm^{-1} (aromatic). In the ^{1}H-NMR spectral data, the title compounds showed two triplets of two protons each at around δ 2.5 and 3.5, which could be assigned to the two methylene protons (–CH_2–CH_2–). Other peaks were observed at appropriate δ values. The mass spectra of the oxadiazoles showed acylium fragments containing phenoxyphenyl and aryl moieties as the major peaks, followed by peaks with the loss of CO, in addition to the molecular ion peaks in reasonable intensities. The elemental analysis results were within ±0.4 % of the theoretical values.

Biological screening

Anti-inflammatory activity. The tested compounds showed anti-inflammatory activity ranging from 37.50 to 65.63 % (Table I). Two compounds, 3-[5-(2-acetoxyphenyl)-1,3,4-oxadiazol-2-yl]-1-(4-phenoxyphenyl)propan-1-one **4d** and 3-[5-(3,4-dimethoxyphenyl)-1,3,4-oxadiazol-2-yl]-1-(4-phenoxyphenyl)propan-1-one **4i** showed very good anti-inflammatory activity with 65.63 and 62.50 %, respectively. The activity of these compounds (**4d** and **4i**) was comparable with that of indomethacin (68.75 %) and higher than that of the parent compound **3** (43.75 %).

These data show that the presence of 2-acetoxyphenyl, 3,4-dimethoxyphenyl or 4-methoxyphenyl substitution at position 5 of the oxadiazole ring caused a remarkable improvement in the anti-inflammatory activity.

Analgesic activity. The newly synthesized compounds showed activity ranging from 38.80 to 76.33 % (Table I). The activity showed that compound, 3-[5-(2-acetoxyphenyl)-1,3,4-oxadiazol-2-yl]-1-(4-phenoxyphenyl)propan-1-one **4d**, exhibited maximum analgesic activity (76.33 %) and its activity was better than that of standard drug indomethacin (72.44 %).

Acute ulcerogenesis. The tested compounds showed a significant reduction in ulcerogenic activity, ranging from 0.454 to 0.666, whereas the standard drug indomethacin and the parent drug **3** exhibited a high severity index, 2.332 and 1.553, respectively (Table I). The results indicate that the newly synthesized compounds are almost devoid of ulcerogenic action.

Lipid peroxidation study. It is evident that compounds showing less ulcerogenic activity also show a reduced malondialdehyde (MDA) content, a byproduct of lipid peroxidation.[21] Therefore, an attempt was made to correlate the low ulcerogenesis of the studied compounds with that of lipid peroxidation. Indomethacin and **3** (standard and parent compound) showed high lipid peroxidation, 8.133 and 6.842 nmol/100 mg of tissue, respectively, whereas the control group showed 3.788 nmol/100 mg of tissue (Table I). It was found that all the compounds showing low ulcerogenic activity also showed a reduction in lipid peroxidation. Therefore, the study indicated that these oxadiazole derivatives inhibited the induction of gastric mucosal lesions. The results further suggest that their protective effect might be related to the inhibition of lipid peroxidation in the gastric mucosa.

EXPERIMENTAL

Chemistry

Chemicals were procured from E. Merck (Germany & India) and S. D. Fine Chemicals (India). Melting points were determined in open capillary tubes and are uncorrected. Microanalysis of the compounds was done on Perkin-Elmer model 240 analyzer and the found values were within ±0.4 % of the theoretical values. ^{1}H- and ^{13}C-NMR spectra were recorded on Bruker spectrospin DPX-300 MHz and Bruker 400 Ultra Shield^{TM} instruments, with tetramethylsilane (TMS) as the internal standard. The splitting pattern abbreviations are as follows: *s*, singlet; *d*, doublet; *dd*, double doublet; *t*, triplet; *m*, multiplet. Mass spectra were recorded on a Jeol JMS-D 300 instrument fitted with a JMS 2000 data system at 70 eV. The spectral data are consistent with the assigned structures. The progress of the reactions was monitored on silica gel G plates using iodine vapor as the visualizing agent.

*Aryl acid ethyl esters and their hydrazides (**1a–l, 2a–l**)*

These compounds were obtained by the method reported in the literature.[22]

*3-(4-Phenoxy-benzoyl)propionic acid (**3**)*

Compound **3** was prepared according to a literature method.[8]

*General procedure for the synthesis of 1-(4-phenoxyphenyl)-3-[5-(supstituted phenyl)-1,3,4-oxadiazol-2-yl]propan-1-ones (**4a–l**)*

Compound **2a–l** (0.001 mol) was dissolved in phosphorus oxychloride (5 ml) and to it was added **3** (equimolar, 0.001 mol). The reaction mixture, after refluxing for 2–5 h, was cooled to room temperature and poured onto crushed ice. On neutralization of the contents with sodium bicarbonate solution (20 % w/v) a solid mass separated out which was filtered, washed with water, dried and recrystallized from methanol to give **4a–l**.

Biological screening

Anti-inflammatory activity. The newly synthesized compounds **4a–l** were evaluated for their *in vivo* anti-inflammatory activity by the carrageenan-induced rat paw edema method.[23] The protocol of the animal experiments was approved by the institutional animal ethics committee (IAEC). The compounds were tested at 20 mg/kg oral dose and were compared with the standard drug indomethacin and **3** at the same oral dose. The foot volume of the rats was measured before and after 4 h of carrageenan injection using a plethysmograph. The percentage inhibition of inflammation was calculated by applying the Newbould formula.[24]

Analgesic activity. The activity was carried out by acetic acid induced writhing method[25] on albino mice groups of six animals each. A 1.0 % aqueous acetic acid solution (i.p. injecttion, 0.10 ml) was used as writhing inducing agent. Test compounds and reference drugs (Indomethacin and compound **3**) were administered in the dose of 20 mg/kg as carboxymethylcellulose (CMC) suspension. One group was kept as control and received 1.0 % CMC. After 20 min of drug administration, 0.10 ml of 1.0 % acetic acid solution was given to mice intraperitoneally. The severity of writhing response was recorded for 20 min after administration of acetic acid solution. The analgesic activity was expressed in terms of percent protection $((n - n')/n)\times100$, where n is the mean number of writhes of control group and n' is the mean number of writhes of test group).

Acute ulcerogenesis. The title compounds were screened for their ulcerogenic activity in albino rats according to the method of Cioli.[26] The ulcerogenic activity was evaluated after p.o. administration of the test compounds or Indomethacin or **3** at a dose of 30 mg/kg.

Lipid peroxidation study. Lipid peroxidation of the synthesized compounds, as well of indomethacin and **3** (standard and parent compound) was determined according to the method of Ohkawa.[27] The lipid peroxidation was measured as nmol of MDA/100 mg of tissue.

CONCLUSIONS

To summarize, a novel class of 3-(4-phenoxybenzoyl)propionic acid derivatives, as safer anti-inflammatory and analgesic agents, was synthesized. Cyclization of the terminal carboxylic group of 3-(4-phenoxybenzoyl)propionic acid into the oxadiazole nucleus resulted in increased anti-inflammatory and analgesic activity, with a significant decrease of ulcerogenic activity, which is a common side effect with commonly used non steroidal anti-inflammatory agents (NSAIDs). These results make the novel 1,3,4-oxadiazoles interesting lead molecules for further synthetic and biological evaluation. It can be concluded that this class of compounds holds promise towards the pursuit to discover safer anti-inflammatory and analgesic agents. Further studies to acquire more information about structure–activity relationships are in progress.

Acknowledgements. The financial support provided by the Department of Science & Technology (D.S.T.), New Delhi, under the scheme SERC-fast track proposal for young scientists, is gratefully acknowledged. We are thankful to Mrs. Shaukat Shah, in-charge animal house, for providing the animals for the pharmacological studies.

ИЗВОД

СИНТЕЗА 1-(4-ФЕНОКСИФЕНИЛ)-3-5-(СУПСТИТУИСАНИ АРИЛ)-1,3,4-ОКСАДИАЗОЛ-2-ИЛ]ПРОПАН-1-ОНА КАО ПОГОДНИХ АНТИ-ИНФЛАМАТОРНИХ И АНАЛГЕТИЧКИХ АГЕНСА

ASIF HUSAIN[1], F. J. AHMAD[2], MOHD AJMAL[1] и PRIYANKA AHUJA[1]

[1]Department of Pharmaceutical Chemistry u [2]Department of Pharmaceutics, Faculty of Pharmacy, Jamia Hamdard (Hamdard University), New Delhi–110062, India

Реакцијом 3-(4-феноксибензоил)пропионске киселине и низа хидразида ароматичних карбоксилних киселина у фосфороксихлориду синтетисана је серија нових 1-(4-феноксифенил)-3-5-(супституисани арил)-1,3,4-оксадиазол-2-ил]пропан-1-она. Структуре једињења по-

тврђене су одговарајућим IR, NMR (^{1}H и ^{13}C) и MS подацима, као и резулататима елементалне анализе. Синтетисана једињења подвргнута су тестовима анти-инфламаторног, аналгетичког и улцерогеног дејства, као и тесту изазивања липидне пероксидације. Неколико једињења показало је врло високо анти-инфламаторно дејство на едем шапе пацова изазван карагенаном. Мањи број синтетисаних једињења показао је значајну аналгетичку активност према грчевима изазваним сирћетном киселином. Новосинтетисана једињења показала су слабу улцерогену активност и довела до појаве ниског садржаја малондиалдехида (MDA), једног од споредних производа липидне пероксидације.

(Примљено 18. септембра 2007, ревидирано 9. маја 2008)

REFERENCES

1. L. A. Sorbera, P. A. Lesson, J. Castanar, R. M. Castanar, *Drug Future* **26** (2001) 133
2. A. Palomer, F. Cabre, J. Pascual, J. Campos, M. A. Trugillo, A. Entrena, M. A. Gallo, L. Garcia, D. MacLeon, A. Espinosa, *J. Med. Chem.* **45** (2002) 1402
3. M. C. Allison, A. G. Howatson, C. J. Torrance, F. D. Lee, R. I. G. Russell, *N. Engl. J. Med.* **327** (1992) 749
4. M. M. Verrico, R. J. Weber, T. P. McKaveney, N. T. Ansani, A. L. Towers, *Ann. Pharmacother.* **37** (2003) 1203
5. F. A. Wollheim, *Lakartidningen* **100** (2003) 2927
6. B. Testa, P. Jenner, *Drug Metabolism, Chemical and Biochemical Aspect*, Marcel Dekker Inc., New York, 1976
7. M. S. Y. Khan, A. Husain, *Pharmazie* **57** (2002) 448
8. A. Husain, M. S. Y. Khan, S. M. Hasan, M. M. Alam, *Eur. J. Med. Chem.* **40** (2005) 1394
9. M. Amir, K. Shikha, *Eur. J. Med. Chem.* **39** (2004) 535
10. A. S. Kalgutkar, A. B. Marnett, B. C. Crews, R. P. Remmel, L. J. Marnett, *J. Med. Chem.* **43** (2000) 2860
11. A. S. Kalgutkar, B. C. Crews, S. W. Rowlinson, C. Garner, K. Seibert, L. J. Marnett, *Science* **280** (1998) 1268
12. M. Duflos, M. R. Nourrisson, J. Brelet, J. Courant, G. Le Baut, N. Grimaud, J. Y. Petit, *Eur. J. Med. Chem.* **36** (2001) 545
13. M. M. Burbuliene, V. Jakubkiene, G. Mekuskiene, E. Udrenaite, R. Smicius, P. Vainilavicius, *Farmaco* **59** (2004) 767
14. I. V. G. Nargund, G. R. N. Reddy, V. Hariprasad, *J. Pharm. Sci.* **83** (2006) 246
15. B. Narayana, K. K. Vijayaraj, B. V. Ashalatha, N. S. Kumari, *Arch. Pharm. (Weinheim)* **338** (2005) 373
16. A. Zarghi, S. A. Tabatabai, M. Faizi, A. Ahadian, P. Navabi, V. Zanganeh, A. Shafiee, *Bioorg. Med. Chem. Lett.* **15** (2005) 1863
17. T. M. Tan, Y. Chen, K. H. Kong, J. Bai, Y. Li, S. G. Lim, T. H. Ang, Y. Lam, *Bioorg. Med. Chem. Lett*. **16** (2006) 5036
18. R. M. Srivastava, L. A. Almeida, O. S. Vianna, M. J. Silva, M. T. Catanho, J. O. Morris, *Bioorg. Med. Chem.* **11** (2003) 1821
19. A. O. Maslat, M. Abussaud, H. Tashtoush, M. Al-Talib, *Pol. J. Pharmacol.* **54** (2002) 55
20. M. R. Yadav, S. T. Shirude, D. S. Puntambekar, P. J. Patel, H. B. Prajapati, A. Parmar, R. Balaraman, R. Giridhar, *Acta Pharm.* **57** (2007) 13
21. T. Pohle, T. Brzozowski, J. C. Becker, I. R. Vander Voort, A. Markmann, S. J. Konturek, A. Moniczewski, W. Domschke, J. W. Konturek, *Ailment Pharmacol. Ther.* **15** (2001) 677

22. B. Furniss, A. H. Hannaford, P. W. G. Smith, A. R. Tatchell, *Vogel's Textbook of Practical Organic Chemistry*, 5th Ed., Addison Wesley Longman, London, 1998, p. 1077
23. C. A.Winter, E. A. Risley, G. W. Nuss, *Proc. Soc. Exp. Biol. Med.* **111** (1962) 544
24. B. B. Newbould, *Br. J. Pharmacol.* **21** (1963) 127
25. E. Siegmund, R. Cadmus, G. Lu, *Proc. Soc. Exp. Biol.* **95** (1957) 729
26. V. Cioli, S. Putzolu, V. Rossi, P. S. Barcellona, C. Corradino, *Toxicol. Appl. Pharmacol.* **50** (1979) 283
27. H. Ohkawa, N. Ohishi, K. Yagi, *Anal. Biochem.* **95** (1979) 351.

www.shd.org.rs

Journal of the Serbian Chemical Society

JSCS@tmf.bg.ac.yu • www.shd.org.rs/JSCS

J. Serb. Chem. Soc. *73* (8–9) 793–804 (2008)
JSCS–3762

UDC 577.175.2:577.354
Original scientific paper

Lectin-induced alterations of the interaction of insulin and insulin-like growth factor 1 receptors with their ligands

ROMANA MASNIKOSA*#, ANNA J. NIKOLIĆ and OLGICA NEDIĆ#

INEP – Institute for the Application of Nuclear Energy, University of Belgrade, Banatska 31b, 11080 Belgrade, Serbia

(Received 16 October 2007, revised 15 January 2008)

Abstract: In order to study whether the carbohydrate moieties of the human placental IGF-I receptor (IGF1R), IGF-II receptor (IGF2R) and insulin receptors (IRs) play a role in ligand binding, solubilised cell membrane preparations were incubated with ^{125}I-labelled IGF-I, IGF-II and insulin in the presence of lectins with different sugar specificities. Three incubation procedures were tested: ligand-first, co-incubation and lectin-first incubation. Wheat germ agglutinin (WGA), concanavalin A (Con A) and phytohaemagglutinin (PHA) altered the binding of IGF-I and insulin to their high-affinity receptors in a lectin specific and dose-dependent manner, whereas these lectins did not affect the interaction of IGF-II with its receptor(s). Moreover, the same lectins either inhibited or enhanced IGF-I and insulin binding, depending on the incubation scheme. These results also suggest that IR-A and IR-B from human placenta might be differently glycosylated.

Keywords: IGF1R; IGF2R; IR; WGA; Con A; PHA.

INTRODUCTION

The insulin-like growth factor (IGF) system is a complex assemblage of peptide hormones (IGF-I and IGF-II), receptors and binding proteins.[1] The peptides IGF-I and IGF-II (IGFs) bind to the insulin/IGF family of cell surface receptors, namely, the insulin-like growth factor I receptor (IGF1R) and insulin receptors (IRs), and activate their intrinsic tyrosine kinase domains. These activated receptors initiate signalling cascades that ultimately result in the regulation of a number of biological responses.[1] The components of the IGF system act together to control several crucial biological outcomes, including cellular growth, proliferation, differentiation, survival against apoptosis and migration.[1,2]

The type 2 IGF receptor (IGF2R) is structurally dissimilar to IGF1R and IR, has no intrinsic signalling transduction capability and, in the context of the IGF

* Corresponding author. E-mail: romana@inep.co.yu
# Serbian Chemical Society member.
doi: 10.2298/JSC0809793M

system, primarily acts to sequester IGF-II from potential receptor activating interactions and to internalise and degrade IGF-II.[3] The IGF2R binds IGF-II with a high affinity but binds IGF-I with a very low affinity and does not bind insulin.[4]

It is known from earlier genetic experiments that IR mediates growth in response to IGF-II during foetal development of the mouse.[5] The homodimeric IR exists in two isoforms, which arise from the alternative splicing of exon 11 in the IR mRNA.[6] Exon 11 codes for twelve amino acids which are inserted upstream of the third last residue of the extracellular α-subunits of the IR-B isoform. The IR-A isoform lacks these twelve amino acids.[6] The presence or absence of the exon 11-encoded peptide yields two receptors with unique biochemical properties. IR-A and IR-B seem to be localised on different regions of the plasma membrane.[7] The IR-A has been identified as a high affinity receptor for IGF-II, which is preferentially expressed in foetal and cancer cells.[8]

Genetic evidence strongly suggests different roles for IGF1R and IR, despite their overall structural homology. The two receptors activate common intracellular pathways. In spite of attempts to elucidate the molecular basis of IGF1R *vs*. IR action, it is unclear what determines the signalling specificity *in vivo*.[9] Entingh-Pearsall and co-workers proposed that other factors could affect signalling, including the time course of stimulation of a cell with different ligands.[10] It is also believed that other molecules can influence the binding kinetics of the receptors.[11]

The hIR has eighteen potential sites for *N*-glycosylation, of which sixteen are glycosylated. The insulin binding α-subunit contains fourteen potential *N*-linked glycosylation sites.[12] The receptor is heavily glycosylated, as 22 % of its molecular mass is composed of carbohydrate.[13] Multiple potential sites for *N*-linked glycosylation (sixteen) are also found in the hIGF1R molecule.[14] IGF2R has nineteen potential *N*-glycosylation sites.[15]

Recently, *N*-glycans attached to human placental IGF and insulin receptors were characterised and multiple populations of the receptors, which bore different sugars at their termini, were observed.[16] The primary objective of the current study was to examine how lectins with different sugar specificities modify the interactions of IGFs and insulin with their glycoprotein receptors from human placenta.

EXPERIMENTAL

Materials

Porcine insulin was from Novo Nordisk (Bagsværd, Denmark). Human IGF-I and IGF-II were from GroPep Pty Ltd. (Adelaide, Australia). Hepes, poly(ethylene glycol) 8000 (PEG), bovine immunoglobulin G (IgG, technical grade), bovine serum albumin (BSA) and Triton X-100 were purchased from Sigma-Aldrich Chemie (Steinheim, Germany). $Na^{125}I$ for iodination was purchased from Isotope (Budapest, Hungary). Wheat germ agglutinin (WGA) was from Vector Laboratories (Burlingame, CA, USA). Concanavalin A (Con A) was from Amersham Biosciences (Little Chalfont, UK). The phytohaemagglutinin (PHA) used in this study (a mixture of E-PHA and L-PHA) was from INEP (Belgrade, Serbia).

Methods

^{125}I-IGF-I, ^{125}I-IGF-II and ^{125}I-insulin (tracers) were prepared using the chloramine T method.[17] Iodination was performed every three weeks and resulted in specific activities of $1.0-2.0\times10^8$ cpm μg^{-1}.

Human placental tissue was obtained from uncomplicated pregnancies at term, according to protocols approved by the local ethical committee. Solubilised placental membranes were prepared essentially as described previously.[16] The protein concentration in the solubilised membranes was determined by the method of Bradford.[18]

The lectins were dissolved according to the manufacturer's instructions to give stock solutions of a final concentration of 5 mg ml^{-1}. WGA was dissolved in 0.010 M HEPES buffered saline (HBS), pH 7.5; Con A in 0.050 M phosphate buffered saline (PBS), pH 6.5 and PHA in PBS, pH 7.5. Serial lectin dilutions were prepared, ranging from 0 to 2310 nmol L^{-1} for WGA, from 0 to 943 nmol L^{-1} for Con A and from 0 to 870 nmol L^{-1} for PHA in 0.050 M PBS buffer containing 0.25 % BSA.

The binding assays were performed with solubilised membranes diluted in assay buffer (0.050 M HBS, pH 7.5) to give a membrane protein concentration of 1.0 mg mL^{-1}. In the simplest lectin binding assays, solubilised membranes (100 μg of membrane protein per tube) were incubated with 0.10 pmol of ^{125}I-IGF-I, ^{125}I-IGF-II or ^{125}I-insulin (10^5 cpm) in the absence or presence of WGA, Con A or PHA solution (final concentration 20 μg mL^{-1}) in a fixed reaction volume of 0.50 mL containing assay buffer with BSA (final concentration 1.2 %). The second set of assays employed solubilised membranes, ^{125}I-ligands and increasing concentrations of plant lectins.

Three different incubation procedures were tested: 1) co-incubation, in which all three reactants (solubilised membranes, ^{125}I-ligand and plant lectin) were added simultaneously to the test tubes and incubated for 24 h at 4 °C, 2) lectin-first incubation, in which the solubilised membranes were first incubated with a lectin for 2 h, and then ^{125}I-ligand was added and 22 h at 4 °C was allowed for equilibration and 3) ligand-first incubation, in which the solubilised membranes were first incubated with ^{125}I-ligand for 22 h at 4 °C, then a plant lectin was introduced followed by a further 2 h incubation.

After incubation, the receptor/radioligand complexes were precipitated by the addition of bovine IgG (final concentration 0.050 %) and 1.5 ml of PEG solution (20 % in 0.050 M PBS, pH 7.5) to each tube. The tubes were vortexed, centrifuged (4500 x *g* for 45 min) and the supernatants were aspirated off. The precipitated ^{125}I-ligand radioactivity was measured in an automatic gamma counter (1470 Wallac Wizard, Perkin-Elmer, USA). Non-specific binding (NSB) was measured in reaction tubes which contained all reactants except solubilised membranes. The maximal binding (B_0), the quantity of ^{125}I-ligand bound to the receptors in the absence of lectin, was expressed as the percentage of the total available ^{125}I-ligand concentration (T). The specific binding in the presence of each lectin (B) was expressed as the percentage of that in its absence ($B/B_0\times100$). In each experiment, the specific binding was corrected for NSB. The data were plotted as a function of lectin concentration *vs*. B/B_0.

All curves were created and fitted using Origin Pro Version 7.5 (Origin Lab, Northampton, MA, USA). Statistical analyses were made using SPSS 10 software (SPSS Inc., Chicago, IL, USA). The B/B_0 data from the binding assays were subjected to one way Anova (with the independent variable being plant lectin or ^{125}I-ligand) followed by the LSD test. $P < 0.05$ was considered significant.

RESULTS

The tracer quantities of the ^{125}I-ligands used in this study corresponded to physiological concentrations of IGFs and insulin, thus ensuring that each ligand preferentially bound to the receptor of the highest affinity.[16] The interactions of ^{125}I-ligands with their receptors in the solubilised membranes were examined in the presence of increasing concentrations of lectins. The data obtained from the co-incubation experiments were grouped according to the employed ^{125}I-ligand and are presented in Figs. 1A to 1C.

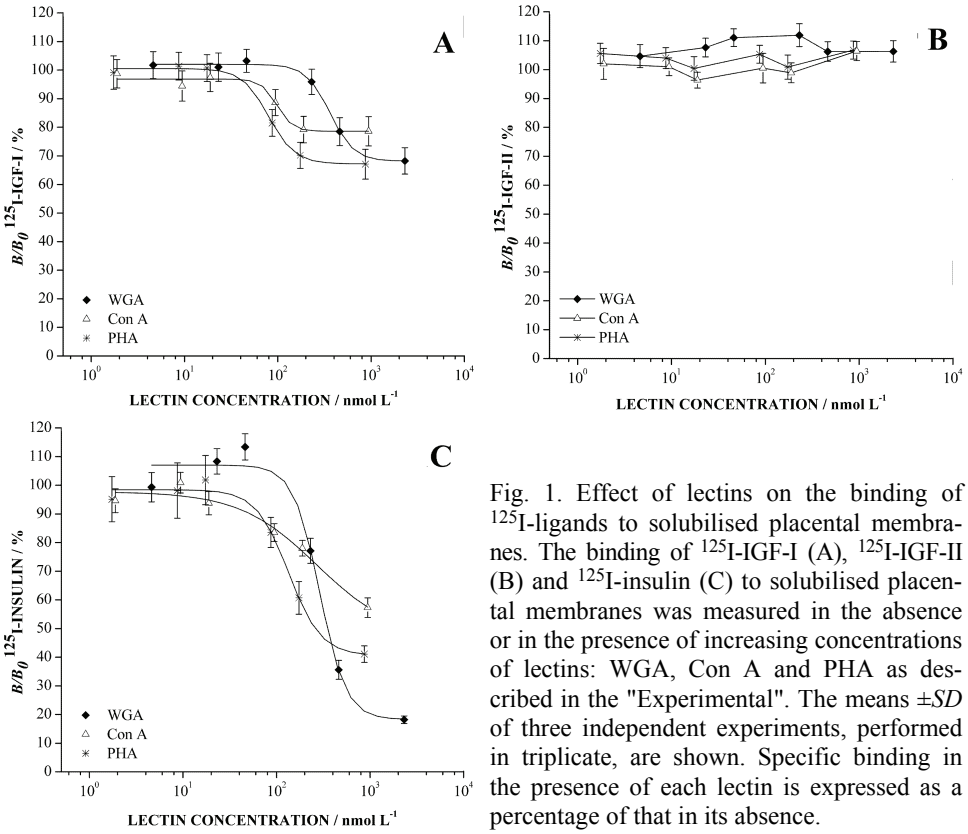

Fig. 1. Effect of lectins on the binding of ^{125}I-ligands to solubilised placental membranes. The binding of ^{125}I-IGF-I (A), ^{125}I-IGF-II (B) and ^{125}I-insulin (C) to solubilised placental membranes was measured in the absence or in the presence of increasing concentrations of lectins: WGA, Con A and PHA as described in the "Experimental". The means ±*SD* of three independent experiments, performed in triplicate, are shown. Specific binding in the presence of each lectin is expressed as a percentage of that in its absence.

Maximal binding (B_0) was 9.6±1.0 % for ^{125}I-IGF-I, 10.1±1.2 % for ^{125}I-IGF-II and 15.4±0.9 % for ^{125}I-insulin. The lectin dose-dependent binding curves for ^{125}I-IGF-I (Fig. 1A) and ^{125}I-insulin (Fig. 1C) were similarly shaped and they were mostly inhibitory throughout the examined lectin concentration range. The ^{125}I-IGF-II binding curves (Fig. 1B) did not reflect great changes in the tracer binding as a function of lectin concentration.

The most profound inhibition of ligand binding was observed after co-incubation of ^{125}I-insulin, IRs from solubilised membranes and WGA, when the B/B_0

value decreased to 18.2±1.3 % (Fig. 1C). This resembled the degree of displacement of ^{125}I-insulin bound to placental IRs by unlabelled insulin.[16] At the largest employed concentration of lectin, Con A and PHA demonstrated weaker inhibitory effects on the ^{125}I-insulin–IR interaction, than did WGA. The effect seemed to be receptor-specific, as the same lectins showed weaker inhibitory effects on ^{125}I-IGF-I binding to IGF1R (Fig. 1A). Thus, WGA and PHA lowered the specific binding of ^{125}I-IGF-I to 68.2±4.6 and 67.1±5.2 % of the initial values, respectively, whereas the specific binding of this tracer reached 78.6±5.1 % in the presence of the maximally effective Con A concentration.

In the second set of binding assays, the effect of three different types of incubation: ligand-first incubation, co-incubation and lectin-first incubation on the specific binding of ^{125}I-labelled ligands to their receptors was examined. The final lectin concentration of 20 μg mL^{-1} was chosen as it initiated a significant inhibition of the ^{125}I-ligand–receptor binding (the penultimate points on the graphs in Figs. 1A and 1C). The B/B_0 values obtained from three independent experiments performed in triplicate were subjected to statistical analysis. The results are given in Table I.

TABLE I. Effects of lectins on the displacement of ^{125}I-ligand binding to solubilised placental cell membranes. Solubilised membranes (100 μg of membrane protein per tube) were incubated with 0.10 pmol of ^{125}I-IGF-I, ^{125}I-IGF-II or ^{125}I-insulin (105 cpm) in the absence or presence of WGA, Con A or PHA solution (final concentration 20 μg mL^{-1}) in a fixed reaction volume of 0.50 ml containing assay buffer with BSA (final concentration 1.2 %). Specific binding in the presence of each lectin ($B/B_0\times100$) is expressed as the percentage of that in its absence (no lectins present; the binding normalised to 100 %). The effect of three different types of incubation: ligand-first incubation, co-incubation and lectin-first incubation on the specific binding of ^{125}I-labelled ligands to their receptors was tested. B/B_0 values obtained from three independent experiments performed in triplicate (means ±*SD*) were subjected to statistical analysis

^{125}I-Ligand		B/B_0 / %		
		Ligand-first	Co-incubation	Lectin-first
^{125}I-IGF-I	No lectins	100	100	100
	+WGA	120.7±5.5[a]	78.5±4.9[a]	65.4±4.2[a]
	+Con A	97.1±7.1[b]	79.2±4.6[a]	73.2±1.3[a]
	+PHA	123.4±5.8[a]	70.1±4.6[a]	53.9±4.9[a]
^{125}I-IGF-II	No lectins	100	100	100
	+WGA	97.0±3.6[b]	106.2±3.4[c]	99.0±2.6[b]
	+Con A	95.3±4.2[b]	98.9±3.4[b]	95.7±4.5[b]
	+PHA	103.3±3.0[b]	100.8±4.2[b]	92.3±3.2[c]
^{125}I-Insulin	No lectins	100	100	100
	+WGA	167.8 ± 3.8[a]	35.6±3.3[a]	39.1±3.2[a]
	+Con A	128.5 ± 7.8[a]	78.0±2.7[a]	65.9±2.4[a]
	+PHA	144.9 ± 6.0[a]	60.7±2.9[a]	59.7±4.8[a]

[a]Significant at $P \le 0.001$; [b]not significant, as compared to control binding (no lectins); [c]significant at $P < 0.05$

The order of reagent addition substantially affected the specific binding of ^{125}I-IGF-I and ^{125}I-insulin (Figs. 2A and 2C), whereas the specific binding of ^{125}I-IGF-II was, generally, not changed (Fig. 2B). The co-incubation and lectin-first incubation schemes resulted in inhibition of the specific binding of ^{125}I-IGF-I and ^{125}I-insulin. However, in the ligand-first incubation scheme, the binding of ^{125}I-IGF-I and ^{125}I-insulin presented completely different patterns, as inhibition was replaced by enhancement of the binding (Figs. 2A and 2C).

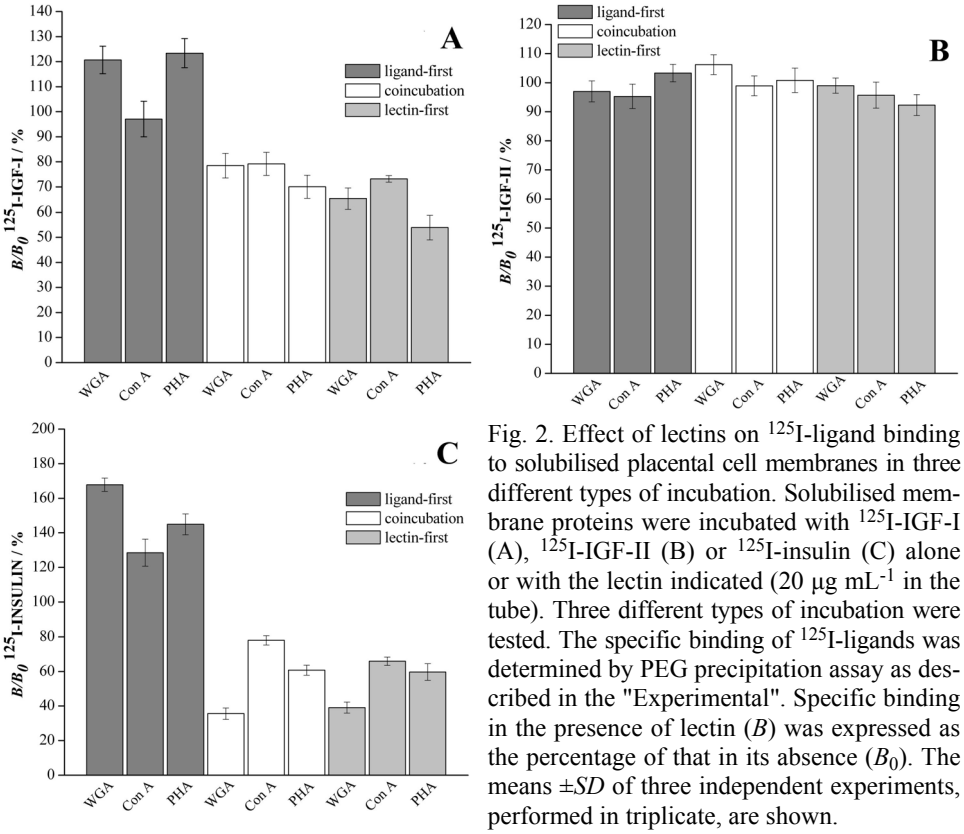

Fig. 2. Effect of lectins on ^{125}I-ligand binding to solubilised placental cell membranes in three different types of incubation. Solubilised membrane proteins were incubated with ^{125}I-IGF-I (A), ^{125}I-IGF-II (B) or ^{125}I-insulin (C) alone or with the lectin indicated (20 μg mL^{-1} in the tube). Three different types of incubation were tested. The specific binding of ^{125}I-ligands was determined by PEG precipitation assay as described in the "Experimental". Specific binding in the presence of lectin (B) was expressed as the percentage of that in its absence (B_0). The means ±SD of three independent experiments, performed in triplicate, are shown.

Compared to the control experiment (no lectins present; the binding normalised to 100 %), all three lectins provoked significant changes in the specific binding of ^{125}I-IGF-I to its receptor ($P \leq 0.001$), the only exception being the combination of ^{125}I-IGF-I and Con A in the ligand-first type of incubation (Table I). The most prominent inhibition of ^{125}I-IGF-I binding to IGF1R occurred when PHA was added to the solubilised receptors prior to the radioligand (B/B_0 = = 53.9±4.9 %).

In general, the binding of ^{125}I-IGF-II to its placental receptor(s) was not changed in the presence of lectins (Fig. 2B). The presence of WGA in co-incubation or PHA in the lectin-first incubation scheme was of minor statistical signi-

ficance ($0.001 < P < 0.05$, Table I), compared to the control binding. These findings led to the omission of ^{125}I-IGF-II from the third set of experiments.

As for the B/B_0 values obtained with ^{125}I-insulin, the presence of all three lectins potently altered the magnitude of the tracer binding. Of all the tested lectins, WGA exerted the greatest influence on ^{125}I-insulin binding to the placental IRs, causing the corresponding B/B_0 values to increase to 167.8±3.8 % in the ligand-first type of incubation or to decrease to 35.6±3.3 % in the co-incubation assays (Table I).

When the lectin was set as the independent variable, statistical analysis of the binding data showed that WGA and PHA exerted different effects on ^{125}I-ligand binding to their receptors, regardless of the type of incubation ($P \leq 0.001$). Statistically significant differences between the binding of ^{125}I-IGF-I and ^{125}I-IGF-II to the placental receptors were not observed in the presence of Con A in the ligand-first ($P = 0.752$) and lectin-first type of incubation ($P = 0.740$). The binding of ^{125}I-IGF-I and ^{125}I-insulin was not different in the presence of the same lectin ($P = 0.549$).

In the third set of experiments, the interactions of ^{125}I-IGF-I and ^{125}I-insulin with their receptors from the solubilised membranes were examined in the presence of increasing concentrations of lectins in two different incubation schemes, *i.e.*, ligand-first and lectin-first incubation. The obtained data are presented in Figs. 3A and 3B.

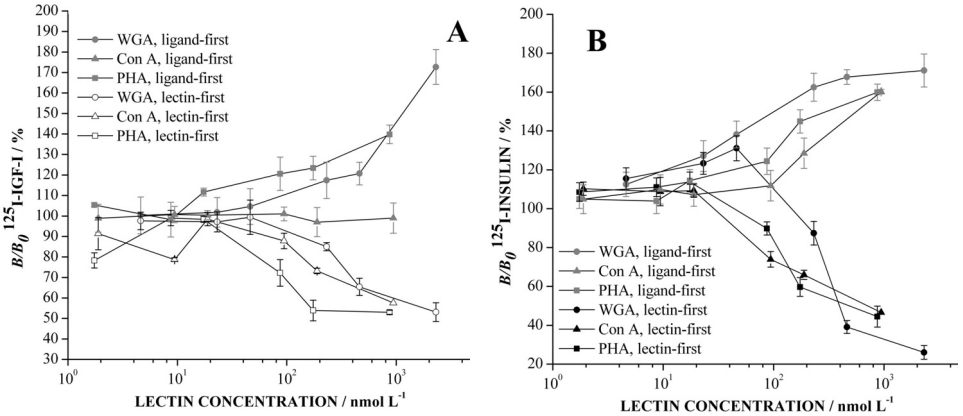

Fig. 3. Effect of lectins on the binding of ^{125}I-IGF-I and ^{125}I-insulin to solubilised placental membranes. Solubilised placental membranes were incubated with ^{125}I-IGF-I (A) or ^{125}I-insulin (B) and increasing concentrations of WGA, Con A or PHA. Ligand-first and lectin-first incubation schemes are shown. See legend for Fig. 1.

The binding curves obtained for the two radioligands were similar in shape for each lectin, both for the ligand-first and the lectin-first incubation scheme. The lectin-first incubation curves lay mostly in the inhibitory range, whereas their ligand-first counterparts lay mostly in the "activatory" range (Figs. 3A and 3B).

The B/B_0 values of ^{125}I-IGF-I binding in ligand-first incubation with Con A were close to 100 % throughout the studied lectin concentration range (Fig. 3A), suggesting that this lectin had no influence on the interaction of the tracer with IGF1R. These data confirmed those obtained in the binding assays using a fixed concentration of lectin (Fig. 2A). The statistical analysis also showed that Con A had no significant effect on the interaction of ^{125}I-IGF-I with the placental IGF1R (Table I). As for ^{125}I-insulin, all lectins tested in the lectin-first type of incubation displaced the tracer bound to the IR and caused the B/B_0 values to decrease significantly, but not until a concentration of 10 μg mL^{-1} was attained (Fig. 3B).

In general, the experiments described above suggest that the affinity of the solubilised placental IGF1R and IR towards their ligands was affected by interaction with plant lectins.

DISCUSSION

IGF1R and IR share a high degree of homology. Their functions are physiologically distinct but overlapping.[9] Each receptor, however, encroaches on the others domain, suggesting that they have an intrinsic ability to mediate other functions.[9] Some investigators believe that the differences between IGF1R and IR can be ascribed to extrinsic factors[19] or that the cellular environment may alter signalling.[11] Thus the search for putative affinity modulators that can bind to IGFR and IR is becoming increasingly attractive.

In a previous study, the differences in glycosylation between IGFRs and IR from human placenta were analysed.[16] The pattern of binding to five different immobilised lectins indicated that the glycosylation of these receptors differed. Several populations of the receptors were found, with various types of sugar branches. In the work presented here, binding assays were used to characterise more extensively the interactions of the oligosaccharide branches of IGFRs and IR of human placenta with lectins.

It was observed that WGA, Con A and PHA caused the specific binding of ^{125}I-IGF-I and ^{125}I-insulin to change in a lectin specific and dose-dependent manner, whereas the same lectins did not alter the binding of ^{125}I-IGF-II to its receptor(s). The effect of lectins on the binding of ^{125}I-labelled peptides to their receptors was ligand specific, as concluded after careful statistical analysis of the binding data. In other words, IGF1R, ^{125}I-IGF-II binding receptor(s) and IR responded differently to particular plant lectins. The same lectins were able either to inhibit or enhance the specific binding, depending on the scheme of incubation. Inhibition of ^{125}I-ligand binding to solubilised placental IGF1R or IR occurred when the lectin was added to IGF1R or IR either simultaneously or before the ligand. Enhancement of the specific binding occurred when the lectins were added after the ligand had been equilibrated with its receptor.

The inhibition, most probably, originated from an overlapping of the ligand binding sites and the lectin binding sites on the receptors or because of a conformational change in the receptor molecule after lectin binding. WGA provoked the most prominent inhibition of insulin binding to IR in the present experimental system. This lectin promotes insulino-mimetic effects.[20] The strongest inhibition of ^{125}I-IGF-I binding to IGF1R was observed when PHA was added to the receptor prior to the tracer. Given the sugar binding specificity of WGA[21] and PHA,[22] their potent inhibitory effects may be attributed to the interaction with complex type *N*-glycans, with repeating *N*-acetyllactosamines at their termini, attached to the molecules of IGF1R and IR. These results are consistent with those published previously, where strong adsorption of ^{125}I-IGF-I/IGF1R complexes and ^{125}I-insulin/IR complexes to agarose-immobilised WGA and PHA was found.[16] Poly--*N*-acetyllactosamine chains were detected in the carbohydrate branches of the human lymphocyte IR.[23] Moreover, both high-mannose type and bi-, tri- and tetra-antennary complex type oligosaccharide structures were recently found on IR molecules from mouse liver.[24] Despite these findings, the roles of the saccharide chains in the functions and metabolism of the IR are not fully elucidated. The types of glycans attached to IGF1R have so far received little attention of researchers.

The first three domains of the IR α-subunit differ from those of the IGF1R in the sequences governing ligand specificity.[25] *N*-Linked carbohydrates are attached at the Asn residues 16, 25, 111, 215, 255, 337, 397 and 418 in the L1-CR-L2 fragment of IR. Interestingly, a residue analogous to Asn16 of the IR is missing in the sequence of the IGF1R, as is Asn255. IR residue Asn15 is one of the most important residues for the high-affinity binding of insulin.[25] The high-affinity binding of IGF-I to IGF1R involves a specific sequence in the CR domain of the receptor, which is positioned seven residues away from a residue analogous to Asn255.[25] Thus, the main differences in glycosylation between IGF1R and IR seem to lie near the amino acid sequences which participate in the high affinity ligand binding to the receptors. The different effects of the different plant lectins on the interactions of IGF-I and insulin with their receptors, observed here, can be explained in light of these data. This might also suggest a role for the saccharides attached to IGF1R and IR in interactions with other proteins, possibly placental lectins.

The alteration of the specific binding of certain hormones and growth factors to their receptors in the presence of plant lectins has already been described in the literature. Thus, Vale and Shooter reported that of eight tested plant lectins, only WGA significantly inhibited (50 %) the binding of ^{125}I-labelled nerve growth factor (NGF) to cells.[26] Buxser and co-workers described increased binding of ^{125}I-NGF to human melanoma cell membranes in the presence of WGA. In order to inhibit binding, these authors added WGA 30 min before ^{125}I-NGF, whereas

WGA added after the binding of ^{125}I-NGF had equilibrated did not affect the total amount of ^{125}I-NGF specifically bound.[27] An increase in the human placental IR affinity was reported after elution from lectin columns, which was speculated to be a consequence of the removal of a putative IR inhibitor during lectin affinity chromatography.[28]

In contrast to IGF1R and IR, the binding of ^{125}I-IGF-II to its receptor(s) was generally not susceptible to lectin inhibition and/or enhancement under the employed experimental conditions. This finding strongly suggests differences in glycosylation between the high-affinity receptor(s) for IGF-II and the receptors that bind IGF-I and insulin from human placental membranes. ^{125}I-labelled IGF-II was reported to bind to three types of receptors in human placental membranes: IGF1R, IGF2R and IR.[29] Besides IGF1R and IR, a significant quantity of immunoreactive IGF2R was detected in the soluble placental membrane preparations using western immunoblot.[16] Despite this, the results of other experiments strongly suggested preferential binding of ^{125}I-IGF-II to the IR. Unlabelled IGF-II was a potent competitor of tracer levels of ^{125}I-insulin binding to the IR from solubilised placental cell membranes.[16] The receptor population eluted from an insulin–agarose column bound ^{125}I-IGF-II and ^{125}I-insulin equally well (unpublished results). The tracer concentrations of ^{125}I-IGF-II, which were used in all our experiments, allowed it to bind preferably to the receptor with the highest affinity for this ligand. The candidate receptor for this role is IR-A, which binds IGF-II with a K_d of 0.9 nM,[30] whereas the K_d for the IGF-II-IGF2R interaction is approximately 1.3 nM.[31] Taken together with the literature data, the present findings might imply that the IR population from human placenta which binds ^{125}I-IGF-II and the IR population which binds ^{125}I-insulin are differently glycosylated. It was reported that the glycosylation state of the IR alters insulin and IGF-II binding to this receptor,[32] which is in accordance with the present data. Although all cell types express both isoforms of the IR to various degrees (placenta expresses equal levels of the two IR isoforms),[33] little is known about the mechanisms that underlie IR isoform-specific signalling.[7]

The potential differences in glycosylation between IR-A and IR-B might imply different interactions of the two isoforms with different placental proteins, which could in turn result in different effector pathways. *N*-Glycans attached to IR-A and IR-B could be the signal for targeting the two isoforms to different membrane compartments, which is in accordance with the finding that IR-A and IR-B localise to different regions of the plasma membrane.[7]

Many authors have suggested that the sugar moieties covalently attached to receptors play no significant role in ligand binding, but instead function to direct the transportation of the *de novo* synthesised receptors to the cell surface.[34–36] In contrast, the requirement of carbohydrate moieties for high affinity binding of somatostatin,[37] cholecystokinin[38] and VIP receptors[39] was observed as an inherent property of these receptors.

CONCLUSIONS

In summary, several aspects of this study are noteworthy. First, lectins modulate the binding of IGF-I and insulin to their receptors, but not the interactions of IGF-II with its receptor(s). Second, different lectins have significantly different effects on the ligand binding to human placental IGF1R and IRs, which is in accordance with differences in the glycosylation of the receptors. Moreover, the sequence of interactions (ligand-first to lectin-first) has great influence on the outcome of the binding reaction (enhancement or inhibition). Finally, the obtained results suggest that IR-A and IR-B from human placenta might be differently glycosylated.

Acknowledgement. The authors are grateful to the Ministry of Science of the Republic of Serbia for financial support (Project No. 143019).

И З В О Д

УТИЦАЈ ЛЕКТИНА НА ИНТЕРАКЦИЈЕ РЕЦЕПТОРА ЗА ИНСУЛИН И ИНСУЛИНУ СЛИЧНЕ ФАКТОРЕ РАСТА СА ЊИХОВИМ ЛИГАНДИМА

РОМАНА МАСНИКОСА, ANNA J. NIKOLIĆ и ОЛГИЦА НЕДИЋ

ИНЕП – Институт за примену нуклеарне енергије, Универзитет у Београду, Банатска 31б, 11080 Београд

У циљу утврђивања значаја угљенохидратне компоненте типа 1 IGF рецептора (IGF1R), типа 2 IGF рецептора (IGF2R) и инсулинског рецептора (IR) пореклом из хумане плаценте у везивању лиганада за ове рецепторе, солубилизоване ћелијске мембране су инкубиране са ^{125}I-обележеним IGF-I, IGF-II и инсулином у присуству лектина различитих шећерних специфичности. Тестирана су три типа инкубације: прво-лиганд, коинкубација и прво-лектин тип инкубације. Под дејством лектина из пшеничних клица (WGA), конканавалина А (Con A) и фитохемаглутинина (PHA), мења се специфично везивање IGF-I и инсулина за одговарајуће рецепторе високог афинитета на лектин-специфичан и дозно-зависан начин, док ти исти лектини не утичу на интеракцију IGF-II са његовим рецептором (-има). Штавише, исти лектини су инхибирали или поспешивали везивање лиганада за IGF и инсулинске рецепторе, што је зависило искључиво од типа инкубације. Резултати овог рада такође сугеришу да би изоформе инсулинског рецептора IR-A и IR-B из хумане плаценте могле бити различито гликозиловане.

(Примљено 16. октобра 2007, ревидирано 15. јануара 2008)

REFERENCES

1. A. Denley, L. J. Cosgrove, G. W. Booker, J. C. Wallace, B. E. Forbes, *Cytokine Growth Factor Rev.* **16** (2005) 421
2. M. N. Pollak, E. S. Schernhammer, S. E. Hankinson, *Nat. Rev. Cancer* **4** (2004) 505
3. C. D. Scott, S. M. Firth, *Horm. Metab. Res.* **36** (2004) 261
4. S. Kornfeld, *Annu. Rev. Biochem.* **61** (1992) 307
5. A. Louvi, D. Accili, A. Efstratiadis, *Dev. Biol.* **189** (1997) 33
6. S. Seino, G. I. Bell, *Biochem. Biophys. Res. Commun.* **159** (1989) 312
7. S. Uhles, T. Moede, B. Leibiger, P.-O. Berggren, I. B. Leibiger, *J. Cell Biol.* **163** (2003) 1327
8. F. Frasca, G. Pandini, P. Scalia, L. Sciacca, R. Mineo, A. Costantino, I. D. Goldfine, A. Belfiore, R. Vigneri, *Mol. Cell. Biol.* **19** (1999) 3278

9. J. J. Kim, D. Accili, *Growth Horm. IGF Res.* **12** (2002) 84
10. A. Entingh-Pearsall, C. R. Kahn, *J. Biol. Chem.* **279** (2004) 38016
11. D. R. Clemmons, L. A. Maile, *Endocrinology* **144** (2003) 1664
12. T. C. Elleman, M. J. Frenkel, P. A. Hoyne, N. M. McKern, L. J. Cosgrove, D. R. Hewish, K. M. Jachno, J. D. Bentley, S. E. Sankovich, C. W. Ward, *Biochem. J.* **347** (2000) 771
13. L. J. Cosgrove, G. O. Lovrecz, A. Verkuylen, L Cavaleri, L. A. Black, J. D. Bentley, G. J. Howlett, P. P. Gray, C. W. Ward, N. M. McKern, *Protein Express. Purif.* **6** (1995) 789
14. A. Ullrich, A. Gray, A. W. Tam, T. Yang-Feng, M. Tsubokawa, C. Collins, W. Henzel, T. Le Bon, S. Kathuria, E. Chen, S. Jacobs, U. Francke, J. Ramachandran, Y. Fujita-Yamaguchi, *EMBO J.* **5** (1986) 2503
15. T. Braulke, *Horm. Metab. Res.* **31** (1999) 242
16. R. Masnikosa, I. Baričević, D. R. Jones, O. Nedić, *Growth Horm. IGF Res.* **16** (2006) 174
17. W. M. Hunter, F. C. Greenwood, *Nature* **194** (1962) 495
18. M. M. Bradford, *Anal. Biochem.* **72** (1976) 248
19. P. De Meyts, B. Urso, C. T. Christoffersen, R. M. Shymko, *Ann. N. Y. Acad. Sci.* **766** (1995) 388
20. J. D. Smith, A. Y. Liu, *Science* **214** (1981) 799
21. J. T. Gallagher, A. Moris, T. M. Dexter, *Biochem. J.* **231** (1985) 115
22. I. E. Liener, N. Sharon, I. J. Goldstein, *The lectins: properties, functions and applications in biology and medicine*, Academic Press Inc., New York, 1986, p. 46
23. A. S. B. Edge, C. R. Kahn, R. G. Spiro, *Endocrinology* **127** (1990) 1887
24. S. Parry, D. Hadaschik, C. Blancher, M. K. Kumaran, N. Bochkina, H. R. Morris, S. Richardson, T. J. Aitman, D. Gauguier, K. Siddle, J. Scott, A. Dell, *Biochim. Biophys. Acta* **1760** (2006) 652
25. M. Lou, T. P. J. Garrett, N. M. McKern, P. A. Hoyne, V. C. Epa, J. D. Bentley, G. O. Lovrecz, L. J. Cosgrove, M. J. Frenkel, C. W. Ward, *Proc. Natl. Acad. Sci. USA* **103** (2006) 12429
26. R. D. Vale, E. M. Shooter, *J. Cell Biol.* **94** (1982) 710
27. S. E. Buxser, D. J. Kelleher, L. Watson, P. Puma, G. L. Johnson, *J. Biol. Chem.* **258** (1983) 3741
28. J. A. Hedo, L. C. Harrison, J. Roth, *Biochemistry* **20** (1981) 3385
29. R. Rebourcet, F. de Ceuninck, S. Deborde, J. Willeput, F. Ferre, *Biol. Reprod.* **58** (1998) 37
30. L. E. Diaz, Y.-C. Chuan, M. Lewitt, L. Fernandez-Perez, S. Carrasco-Rodríguez, M. Sanchez-Gomez, A. Flores-Morales, *Mol. Hum. Reprod.* **13** (2007) 567
31. J. F. Perdue, J. K. Chan, C. Thibault, P. Radaj, B. Mills, W. H. Daughaday, *J. Biol. Chem.* **258** (1983) 7800
32. J. M. Podskalny, D. G. Rouiller, G. Grunberger, R. C. Baxter, A. McElduff, P. Gorden, *J. Biol. Chem.* **261** (1986) 14076
33. H. Benecke, J. S. Flier, D. E. Moller, *J. Clin. Invest.* **89** (1992) 2066
34. C. J. van Koppen, N. M. Nathanson, *J. Biol. Chem.* **265** (1990) 20887
35. D. G. Sawutz, S. M. Lanier, C. D. Warren, R. M. Graham, *Mol. Pharmacol.* **32** (1987) 565
36. K. R. Jarvie, H. B. Niznik, P. Seeman, *Mol. Pharmacol.* **34** (1988) 91
37. S. Rens-Domiano, T. Reisine, *J. Biol. Chem.* **266** (1991) 20094
38. R. Santer, Y. K. Leung, P. Alliet, E. Lebenthal, P. C. Lee, *Biochim. Biophys. Acta* **1051** (1990) 78
39. J. Chochola, C. Fabre, C. Bellan, J. Luis, S. Bourgerie, B. Abadie, S. Champion, J. Marvaldi, A. El Battari, *J. Biol. Chem.* **268** (1993) 2312.

www.shd.org.rs

Journal of the Serbian Chemical Society

JSCS@tmf.bg.ac.yu • www.shd.org.rs/JSCS

J. Serb. Chem. Soc. 73 (8–9) 805–813 (2008)
JSCS–3763

UDC 577.112:54.02:519.2
Original scientific paper

Structural features of proteins as reflected by statistical scaling laws

LAURA PITULICE, ADRIANA ISVORAN* and ADRIAN CHIRIAC

Department of Chemistry, West University of Timisoara, 16 Pestallozi, 300115, Timisoara, Romania

(Received 31 December 2007, revised 28 March 2008)

Abstract: Within this paper, statistical scaling laws for the radius of gyration with the residues number, the surface area with the probe radii and the backbone length with the interval of residues for a set of 60 proteins are revealed. The proteins belong to three different structural classes: *alpha*, *beta* and *alpha* plus *beta* class (20 proteins for each) according to the SCOP database classification, which takes into account the composition in the elements of their secondary structure. The shape and the surface roughness of proteins seem to be independent of the protein content in the secondary structure elements. On the contrary, the protein packing density shows a strong correlation with this composition.

Keywords: protein; backbone; fractal dimension; radius of gyration; scaling law.

INTRODUCTION

Even though the general nature of the interatomic forces involved in the building the spatial structures of proteins is already known, there is still a necessity for further research to be performed in the field in order to reveal the details of the folding processes of proteins. In this respect, the application of the concepts of fractal geometry would be useful. These concepts have been widely applied for the study of the structural and dynamical properties of proteins.[1–17]

With regards to the structure of proteins, the fractal aspects refer either to the protein surface or to its backbone length. Protein surfaces have been shown to be fractal with different fractal dimensions on the micro and macro scale.[3–11] The fractal properties of 5526 tertiary structures of different proteins were investigated and a mean fractal dimension of their surface of about 2.47 was obtained.[15]

Protein backbones show two fractal dimensions, one corresponds to local folding and the other to global folding, suggesting that different molecular features are responsible for the two different spatial organizations.[2,6,12–14,16,17]

The surface of a protein is generated from the van der Waals radii of the component atoms. The surface area of proteins has been shown to be fractal,

* Corresponding author. E-mail: aisvoran@cbg.uvt.ro
doi: 10.2298/JSC0809805P

having a scaling behavior with the probe radius rolled onto it.[3–11,16,17] To determine the accessible surface (*AS*) of a protein, the ball-rolling model[18] may be applied. It uses a sphere of radius *R*, which is rolled onto the surface of the protein maintaining contact with the van der Waals surface. As a result, the following scaling law is obtained:

$$AS \approx R^{2-D_S} \tag{1}$$

where D_S is the surface fractal dimension that can be determined from the slope of the line of the plot log *AS versus* log *R*.

To reveal the fractal aspects of protein backbone, the concept of backbone length was employed. The length (*L*) of the backbone is determined by connecting step by step the carbon-alpha (C^{α}) atoms of the protein for different sequence intervals and summing these distances:

$$L_m = \sum_{i \neq m}^{j} \sqrt{(x_{i+m} - x_i)^2 + (y_{i+m} - y_i)^2 + (z_{i+m} - z_i)^2} \tag{2}$$

where x_i, y_i and z_i refer to the spatial coordinates of the i^{th} carbon-alpha atom, *j* is the integer part of the ratio *N*/*m* with *N* the total number of amino acids in sequence and *m* is the interval of the residues (Fig. 1). The scaling law is given by Eq. (3):

$$L \approx m^{\frac{1}{D}-1} \tag{3}$$

where *D* is also a non-integer value, named the backbone fractal dimension. Similarly, *D* may be calculated from the plot log *L versus* log *m*.

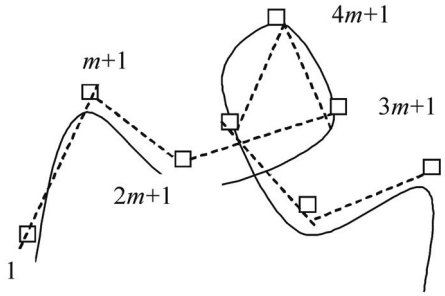

Fig. 1. Schematic representation of the algorithm to determine the backbone length (*L*) of a protein for different intervals of amino acids (*m*) (adapted from Dewey[6]).

Another fractal feature of the structure of a protein may be revealed through the dependence of its radius of gyration on the number of amino acids in the protein sequence. It has been demonstrated that the radius of gyration scales with the residue number for different types of proteins.[1,6–11,17] The radius of gyration, R_g, is defined as the root mean squared distance of the mass constituents of a polymer from the center of its mass. It scales with the residue number (*N*) according to the Eq. (4):

$$R_g \approx N^{\frac{1}{D_f}} \quad (4)$$

where D_f is a non-integer value that may be obtained as the slope of the line of the plot log R_g *versus* log N. The scaling properties of the radius of gyration with the residue number have been demonstrated for globular proteins,[6] proteases and non-proteases,[10] and for *O*-glycosidases.[11]

The above-mentioned scaling laws (Eqs. (1), (3) and (4)) have usually been used to study and describe the shape, surface roughness and packing compactness of different proteins. In the present study, an attempt was made to show if these dependences correlate with the composition in the secondary structural elements of proteins. Thus, the scaling laws for the above-mentioned properties were examined considering 60 proteins belonging to three different structural classes, as given by the SCOP database,[19] *i.e.*, all *alpha* (essentially formed by α-helices), all *beta* (dominated by β-sheets) and *alpha* plus *beta* class (in which α-helices and β-strands are largely segregated).

EXPERIMENTAL

For this study, three unbiased sets of 20 proteins for each considered structural class were randomly chosen. The structural data necessary for the calculations were retrieved from the Protein Data Bank of the RCSB (http://www.rcsb.org/pdb/home/home.do)[20]and the following files were considered:

− 1MOH, 19GS, 1A56, 1A59, 1A7W, 1AEW, 1AH7, 1AIN, 1A6G, 1A7D, 1DAV, 1TZV, 1BKR, 1NOL, 1AD6, 1ALU, 1B1B, 1C20, 1CMZ, 2UTG for all *alpha* class;

− 2AVG, 1A42, 1A18, 1A3K, 1A1X, 1A3Z, 1AG6, 1AMX, 9ILB, 1A21, 1A25, 1A3Y, 1A9V, 1AAC, 1AG4, 1AQB, 1B8E, 4PEP, 43C9, 2SOD for all *beta* class;

− 1A0K, 1A4V, 1A6F, 1A70, 1APS, 1RLO, 1ABA, 4YAS, 16PK, 1A8Q, 1AJZ, 1ARL, 1B0J, 1B7E, 1BAM, 1BCO, 1CEX, 1CJC, 1CP7, 5ULL for *alpha* plus *beta* class.

In order to avoid a reduction of the statistical significance of the results due to the analysis of similar sequences, sequences alignment of these proteins was performed using the Clustalw software accessible on-line.[21] The similarity in the sequences was predicted to be lower than 35 %, which is considered as satisfactory.

The radius of gyration was calculated using the on-line facilities provided by the Protein Dipole Moments Server under the Weizman Institute web page (http://bioportal.weizmann.ac.il/dipol/dipol2.html)[18] and the molecular weights were calculated using the ProtParam tool under the Swiss Prot web page.[22]

The proteins backbone lengths were determined using an in-house Pascal 7.0 program. It uses the spatial coordinates of carbon-alpha atoms as they are given in Protein Data Bank in order to calculate the distances between them for different intervals of amino acids. On summing these distances, the length of the backbone is obtained for every interval, according to Eq. (2).

Finally, the molecular surface was calculated using the Getarea on-line free software[18] (http://www.pauli.utmb.edu/cgi-bin/get_a_form.tcl), for which probe radii of 1.0, 1.2, 1.4, 1.6, 1.8 and 2.0 Å were used.

RESULTS

In order to assess the manner in which the shapes of the investigated proteins from the three distinct structural classes compare with each other, the radius of

gyration of each protein was computed and represented *versus* the residue number in a double logarithmical plot, as shown in Fig. 2.

A linear dependence of log R_g *versus* log N was obtained for each structural class of proteins. The global fractal dimensions obtained by fitting linearly the points according to Eq. (3) are: 1.272±0.087 for the *alpha* class, 1.161±0.074 for the *beta* class and 1.172±0.023 for the *alpha* plus *beta* class. The exponent values obtained in this study are in the same range as those previously reported[6,9–11,16] and indicate a structure of the proteins closer to that of an extended ideal polymer.[6]

The fractal diagrams for the backbone of the studied proteins were obtained according to the algorithm presented by Dewey.[6] As an example, the fractal diagram for the bacteriophage T4 glutaredoxin (code entry 1ABA) is presented in Fig. 3.

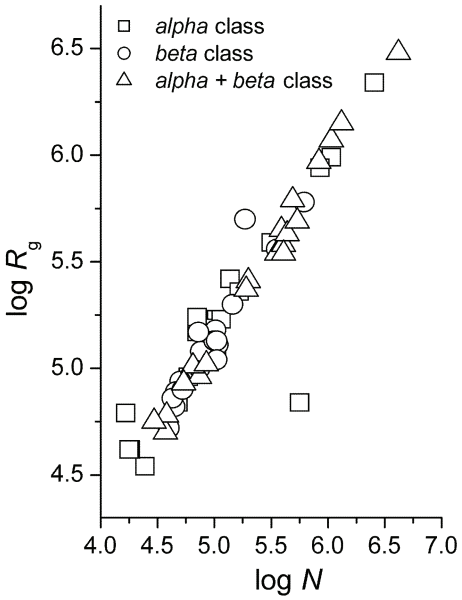

Fig.2. The double logarithmical plot of the radius of gyration *versus* the residue number (□ – *alpha* class; ○ – *beta* class; △ – *alpha* + *beta* class).

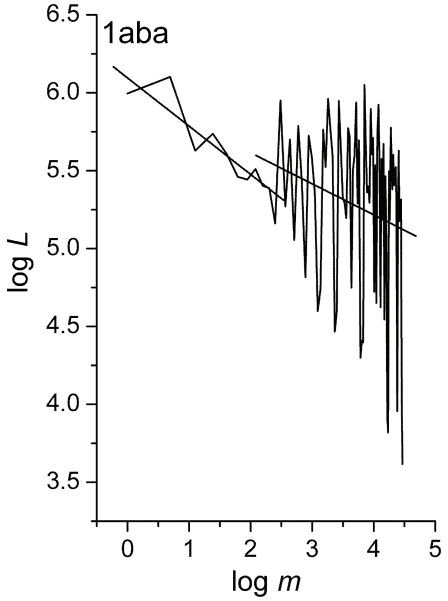

Fig.3. The fractal diagram for bacteriophage T4 glutaredoxin showing the linear fits for the two regions.

Within this plot, two regions can be seen, as reported in the literature for many others proteins.[2,6,12–14,16,17] For each region, an automatic linear fitting was performed. The first region is clearly linear (linear correlation coefficient, R^2, is 0.9516) and is associated with local folding of the protein.[2,6,10–14,16,17] The slope of this line enabled the local fractal dimension (D_l) for the protein backbone to be calculated according to Eq. (2). The values obtained for the studied proteins are presented in Table I. The mean values are: 1.687±0.102 for the

alpha class, 1.367±0.130 for the *beta* class and 1.506±0.119 for the *alpha* plus *beta* class. The Student t-test, implemented under the Origin 7.0 package, showed that these values are significantly different, with only a 0.05 probability that the differences may be caused by chance. The second region of the fractal diagram contains a lot of noise and the errors are high; the R^2 value for the linear fit was 0.4218 in this case. Thus, it was decided not to use this part of the graph in the analysis for accuracy reasons.

Table I also contains the values of the surface fractal dimensions for the investigated proteins, calculated according to Eq. (1). The mean values are: 2.221± ±0.009 for the *alpha* class, 2.184±0.005 for the *beta* class and 2.234±0.004 for the *alpha* plus *beta* class; these values are not significantly different.

As it is to be expected that the protein surface (*AS*) should be dependent on the molecular weight, *M*, of the protein, this relation is presented in Fig. 4 for the three classes of studied proteins.

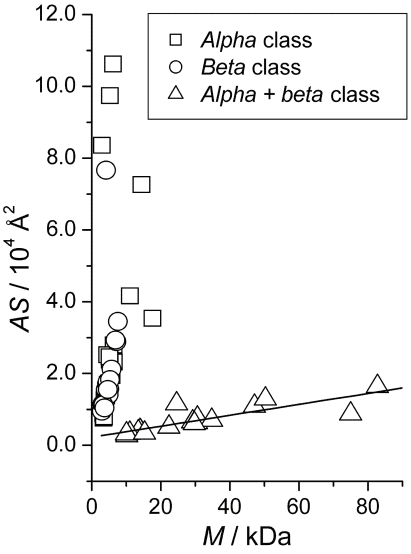

Fig. 4. The dependence of the surface area of proteins on their molecular weight.

From Fig. 4, it can be can observed that for the proteins belonging to *alpha* plus *beta* class, the dependence between the two parameters is linear (R^2 = = 0.8437) and the slope of the line is 0.152±0.024. With regard to the *alpha* and *beta* classes of proteins, linear fitting does not offer an accurate description as some data are scattered around the line. Even though the errors might be high, a slope 0.208±0.039 for the *alpha* class dependence and of 0.186±0.013 for the *beta* class was retrieved for comparison purposes.

TABLE I. The values of the local fractal dimensions and those of the surface fractal dimensions for the investigated proteins

Alpha class			*Beta* class			*Alpha* + *beta* class		
PDB code	D_1	D_S	PDB code	D_1	D_S	PDB code	D_1	D_S
1moh	1.774±0.036	2.253±0.013	2avg	1.430±0.129	2.163±0.019	1a0k	1.392±0.178	2.165±0.013
19gs	1.669±0.028	2.198±0.018	1a42	1.422±0.016	2.180±0.015	1a4v	1.402±0.245	2.169±0.018
1a56	2.107±0.162	2.372±0.024	1a18	1.307±0.014	2.238±0.022	1a6f	1.478±0.207	2.200±0.024
1a59	1.381±0.162	2.233±0.021	1a3k	1.070±0.249	2.157±0.015	1a70	1.580±0.166	2.201±0.016
1a7w	1.674±0.059	2.065±0.017	1a1x	1.092±0.168	2.167±0.011	1aps	1.428±0.139	2.180±0.021
1aew	1.614±0.091	2.207±0.016	1a3z	1.472±0.035	2.101±0.006	1rlo	1.609±0.189	2.291±0.017
1ah7	1.954±0.172	2.218±0.025	1ag6	1.293±0.186	2.071±0.013	1aba	1.448±0.049	2.127±0.025
1ain	1.283±0.139	2.190±0.025	1amx	1.325±0.016	2.118±0.026	4yas	1.489±0.022	2.194±0.025
1a6g	1.889±0.103	2.340±0.005	9ilb	1.597±0.183	2.149±0.023	16pk	1.369±0.168	2.306±0.005
1a7d	1.629±0.044	2.163±0.021	1a21	1.185±0.194	2.167±0.007	1a8q	1.603±0.022	2.284±0.021
1dav	1.380±0.259	2.166±0.013	1a25	1.310±0.019	2.156±0.015	1ajz	1.532±0.020	2.304±0.013
1tzv	1.934±0.075	2.298±0.021	1a3y	1.472±0.155	2.311±0.011	1arl	1.445±0.157	2.301±0.021
1bkr	1.686±0.029	2.124±0.023	1a9v	1.390±0.185	2.352±0.013	1b0j	1.740±0.146	2.350±0.023
1nol	1.588±0.152	2.397±0.014	1aac	1.338±0.028	2.147±0.015	1b7e	1.514±0.031	2.267±0.014
1ad6	1.489±0.173	2.179±0.004	1ag4	1.394±0.145	2.243±0.032	1bam	1.567±0.107	2.250±0.004
1alu	1.966±0.102	2.252±0.012	1aqb	1.393±0.175	2.215±0.010	1bco	1.371±0.163	2.189±0.012
1b1b	1.791±0.053	2.113±0.017	1b8e	1.463±0.130	2.237±0.021	1cex	1.388±0.163	2.154±0.017
1c20	1.462±0.068	2.300±0.007	4pep	1.526±0.138	2.244±0.013	1cjc	1.710±0.161	2.285±0.007
1cmz	1.899±0.101	2.319±0.024	43c9	1.333±0.288	2.086±0.014	1cp7	1.558±0.018	2.236±0.024
2utg	1.572±0.031	2.043±0.012	2sod	1.534±0.147	2.178±0.017	5ull	1.400±0.034	2.226±0.012

DISCUSSION

By analyzing unrelated proteins belonging to three distinct structural classes, consistent structural similarities regarding their shape and surface roughness were noticed. On the contrary, their packing density seems to be a unique feature of each protein class.

Shape and compactness are critical properties characterizing the folding process. On the one hand, the shape of a protein may be quantitatively interpreted by its radius of gyration. In this study, very similar values of the exponent of the scaling law log R_g *versus* log N were obtained for each studied class of proteins (see Fig. 2). On the other hand, the calculated surface fractal dimension (D_S), which measures the surface roughness of a protein, does not differ significantly from one class to another (see Table I). These results suggest a weak dependence of the global folding of these proteins on their composition in the elements of the secondary structure. The rationale of this observation might be that even hard proteins from the same structural class share a similar secondary structure packing, the arrangement of these secondary structural units along the polypeptide chain is different. Moreover, the proteins shape and surface roughness are not dependent on their secondary structure composition. For EF-hand calcium binding proteins, which have the same secondary structure arrangements, the shape and surface roughness are significantly different for those adopting dissimilar spatial conformations: extended and compact, respectively.[17] This indicates that there are other factors responsible for the global folding of a protein, in addition to the composition of the secondary assembly, such as electrostatic and/or hydrophobic interactions. This may bring arguments for the fact that some mutations, which alter the secondary arrangement, do not have important consequences on the function of the protein.

With reference to the protein compactness, its analysis was performed using the local fractal dimension of the backbone of the proteins and the surface area per residue. These parameters should be regarded on a local and global level. The obtained data for the average local fractal dimension of the proteins backbone indicate the highest local packing density for the *alpha* class and the lowest for *beta* class of proteins. This result is not unexpected because a *beta*-strand is the local conformation in which the backbone is extended as much as possible. Also, lattice model studies indicated that compactness could induce polymer chains to develop protein-like secondary structures and lead to a considerable stabilization of them.[22] On the global level, the values of the average surface area per residue show that the highest packing density corresponds to the *alpha* plus *beta* class and the lowest to the *alpha* class. This information is corroborated by the slope of the line $AS = f(M)$ for *alpha* plus *beta* class, the value of which is lower than those corresponding to the other two classes of proteins (see Fig. 4). Thus, the packing compactness seems to be in strong correlation with the composition of the se-

condary structure of the proteins. A similar result was obtained for proteases and non-proteases, which showed the same surface fractal dimensions (2.17) but with clearly different packing densities due to their distinct composition in the elements of their secondary structures.[10]

CONCLUSIONS

In summary, this study supports the fact that statistical scaling laws may be employed in describing structural features of proteins on both the local and global levels. Moreover, it suggests that the protein shape and surface roughness do not depend on the composition of the secondary structure elements but the packing density strongly depends on it. This is thus an appropriate tool to distinguish proteins possessing distinct secondary structures.

ИЗВОД

СТРУКТУРНЕ КАРАКТЕРИСТИКЕ ПРОТЕИНА ДОБИЈЕНЕ НА ОСНОВУ СТАТИСТИЧКИХ РАЗМЕРНИХ ЗАКОНИТОСТИ

LAURA PITULICE, ADRIANA ISVORAN и ADRIAN CHIRIAC

Department of Chemistry, West University of Timisoara, 16 Pestallozi, 300115, Timisoara, Romania

У овом раду су приказане статистичке размерне законитости за везу средњег полупречника са бројем остатака, површине и пробних полупречника и дужине протеинског ланца са интервалом остатака за 60 протеина. Ови протеини припадају трима различитим структурним класама: *алфа*, *бета*, и *алфа* плус *бета* класи (по 20 протеина од сваке класе) према SCOP класификационој бази података, која узима у обзир састав елемената њихове секундарне структуре. Облик и површинска храпавост протеина изгледа да не зависи од састава протеинских секундарних структурних елемената. С друге стране, густина паковања протеина показује изразиту зависност од овог састава.

(Примљено 31. децембра 2007, ревидирано 28. марта 2008)

REFERENCES

1. M. Lewis, D. C. Rees, *Science* **230** (1985) 1163
2. C. X. Wang, F. H. Huang, *Phys. Rev. A* **41** (1990) 7043
3. D. Fushman, *J. Biomol. Struct. Dynam.* **7** (1990) 1333
4. T. Goetze, J. Brickman, *Biophys. J.* **61** (1992) 109
5. A. M. Tamburro, A. De Stradis, L. D'Alessio, *J. Biomol. Struct. Dynam.* **12** (1995) 1161
6. G. T. Dewey, *Fractals in molecular biophysics,* Oxford University Press, New York, 1997
7. A. A. Timchenko, O. V. Galzitskaya, I. N.Serdyuk, *Proteins Struct. Funct. Genet.* **28** (1997) 194
8. R. Fraczkiewicz, W. Braun, *J. Comput. Chem.* **19** (1998) 319
9. M. Daniel, S. Baskar, M. M. Latha, *Phys. Scripta* **60** (1999) 270
10. E. W. Stawiski, A. E. Baucom, S. C. Lohr, L. M. Gregoret, *Proc. Natl. Acad. Sci. U.S.A.* **97** (2000) 3954
11. E. W. Stawisky, Y. Mandel-Gutfreund, A. C. Lowenthal, L. M.Gregoret, *Pacific Symp. Biocomput.* **7** (2002) 637
12. A. Isvoran, A. Licz, L. Unipan, V. V. Morariu, *Chaos, Solitons & Fractals* **12** (2001) 757

13. A. Isvoran, A. Licz, V. V. Morariu, *Rev. Roum. Chim.* **46** (2001) 857
14. A. Isvoran, *Chaos Solitons Fractals* **19** (2004) 141
15. M. A. Moret, J. G. V. Miranda, Jr., E. Nogueira, M. C. Santana, G. F. Zebende, *Phys. Rev. E* **71** (2005) 012901
16. A. Isvoran, L. Pitulice, C. T. Craescu, A. Chiriac, *Chaos Solitons Fractals* **35** (2008) 960
17. L. Pitulice, A. Isvoran, G. T. Craescu, A. Chiriac, *Chaos Solitons Fractals* (2007), doi:10.1016/j.chaos.2007.08.016
18. H. M. Berman, J. Westbrook, Z. Feng, G. Gilliland, T. N. Bhat, H. Weissig, I. N. Shindyalov, P. E. Bourne, *Nucleic Acids Res.* **28** (2000) 235
19. A. G. Murzin, S. E. Brenner, T. Hubbard, C. Chothia, *J. Mol. Biol.* **247** (1995) 536
20. E. Gasteiger, C. Hoogland, A. Gattiker, S. Duvaud, M. R. Wilkins, R. D. Appel, A. Bairoch, *The proteomics protocols handbook*, Humana Press, Hatfield, 2005, p. 571
21. R. Chenna, H. Sugawara, T. Koilee, R. Lopez, T. J. Gibson, D. G. Higgins, J. D. Thompson, *Nucleic Acids Res.* **31** (2003) 3497
22. L. M. Gregoret, *J. Mol. Biol.* **219** (1991) 109.

Journal of the Serbian Chemical Society
JSCS@tmf.bg.ac.yu • www.shd.org.rs/JSCS
J. Serb. Chem. Soc. 73 (8–9) 815–824 (2008) UDC 546.472+547.466.23:543.422.25:615.28–188
JSCS–3764 *Original scientific paper*

Synthesis, NMR, DFT and antimicrobial studies of Zn(II) complexes with *N*-benzyloxycarbonyl-*S*-alanine

DRAGANA M. MITIĆ[1#], ĐENANA U. MIODRAGOVIĆ[1*#], DUŠAN M. SLADIĆ[1#], ŽELJKO J. VITNIK[1], ZORAN M. MIODRAGOVIĆ[1#], KATARINA K. ANĐELKOVIĆ[1#], MILANKA Đ. RADULOVIĆ[2#] and NENAD O. JURANIĆ[3]

[1]*Faculty of Chemistry, University of Belgrade, Studentski trg 12–16, 11001 Belgrade,* [2]*Centre of Chemistry, Institute of Chemistry, Technology and Metallurgy, Njegoševa 12, 11000 Belgrade, Serbia and* [3]*Mayo Clinic and Foundation, Rochester, 59905 Minnesota, USA*

(Received 23 January, revised 1 April 2008)

Abstract: In this study, the first complexes of Zn(II) with the *N*-benzyloxycarbonyl-*S*-alaninato ligand (*N*-Boc-*S*-ala) were synthesized. The new complexes were characterized by elemental analysis, conductometric measurements, IR, ^{1}H-NMR, ^{13}C-NMR and 2D-NMR spectroscopy. On the basis of the experimental data, tetrahedral geometry of the Zn(II) complexes was proposed. A very good agreement between the NMR and DFT calculated data was obtained. Investigation of antimicrobial activity of the newly synthesized complexes was also performed. It was established that [Zn(*N*-Boc-*S*-ala)$_2$] was selective and acts only on *Candida albicans*.

Keywords: antimicrobial activity; DFT; *N*-benzyloxycarbonyl-*S*-alanine; NMR; Zn(II) complexes.

INTRODUCTION

It is well known that metal complexes with aromatic amino acids can serve as model systems for the study of various interactions in which aromatic amino acids residues participate.[1–3] In our previous articles, metal complexes containing aromatic amino acids were described.[4–6] As a continuation, new metal complexes with *N*-benzyloxycarbonyl (*N*-Boc) protected amino acids were examined.[7] It is interesting to note that the *N*-benzyloxycarbonyl amino acids and their derivates were reported as anti-convulsant, anti-inflammatory and anti-neoplastic agents.[8–11] *N*-Protected amino acids have abilities to function as cholecystokinin receptor antagonists[12] and derivates of *N*-Boc amino acids also show a good degree of inhibition of the gastric proton pump.[13]

* Corresponding author. E-mail: dmiodrag@chem.bg.ac.yu
# Serbian Chemical Society member.
doi: 10.2298/JSC0809815M

In spite of interesting biological activities, only a few complexes with *N*-Boc amino acids have hitherto been described.[14–18] As *N*-benzyloxycarbonylglycine has favorable membrane penetration properties,[19,20] neutral complexes of it with various metal ions were prepared in a previous study.[7] Since in the literature there are no data concerning the antimicrobial activities of these compounds, the antimicrobial activities of the obtained metal complexes were also determined. It was established that among the investigated strains, the Zn(II) and Co(II) complexes were selective, acting only against the fungus *Candida albicans*.

The elaboration of new types of antifungal agents is presently a very urgent task.[21] As a result of this, the aim of this work was to synthesize new neutral zinc(II) complexes with the *N*-benzyloxycarbonyl-*S*-alaninato ligand (*N*-Boc-*S*--ala), with or without bipyridine as an additional ligand, and to investigate and compare the antimicrobial activity of the Zn(II) complexes with *N*-Boc-*S*-ala and *N*-Boc-gly ligands with mixed complexes containing 2,2'-bipyridine.

EXPERIMENTAL

Materials and measurements

All the employed reagents and solvents were of analytical grade. *N*-Boc-Glycine, *N*-Boc--*S*-alanine, 2,2'-bipyridine and the metal salts were obtained from Aldrich and used without further purification. Elemental analyses for C, H, N were performed on a Vario III CHNOS Elemental analyzer, Elementar Analysensysteme GmbH. The solid state IR spectra (KBr pellets) were performed on a Perkin-Elmer FT-IR 1726X spectrometer.

The molar conductivity of a methanolic solution of the complexes (c = 10^{-3} mol dm^{-3}) was measured at room temperature on a Jenway-4009 digital conductivity meter.

The ^{1}H-NMR (200 MHz) spectra were recorded using a Varian Gemini 2000 spectrometer at room temperature in DMSO-d_6 solution. The ^{13}C-NMR (50.3 MHz) spectra were recorded using the same instrument in DMSO-d_6 solution. The solvent peak at 39.7 ppm was used to calibrate the scale of chemical shifts. 2D-NMR spectra: DQF–COSY, TOCSY (mixing time 40 ms), ROESY (mixing time 80 ms) and {^{1}H-^{13}C}-HSQC, were recorded on a Bruker 700 MHz instrument.

N-*Boc*-S-*Alanine (Scheme 1)*. ^{1}H-NMR (δ, ppm): 12.3 (1H, *bs*, H(1)), 7.62 (1H, *d*, J = = 7.4 Hz, H(NH)), 7.36 (5H, *m*, H (6,6',7,7',8)), 5.03 (2H, *s*, H(4)), 4.02 (1H, *quintet*, J = 7.4 Hz, H(2)), 1.27 (3H, *d*, J = 7.4 Hz, H(9)); ^{13}C-NMR (δ, ppm): 174.8 (C1), 156.2 (C3), 137.3 (C5), 128.7 (C7,C7'), 128.1 (C8), 128.1 (C6,C6'), 65.7 (C4), 49.5 (C2), 17.3 (C9).

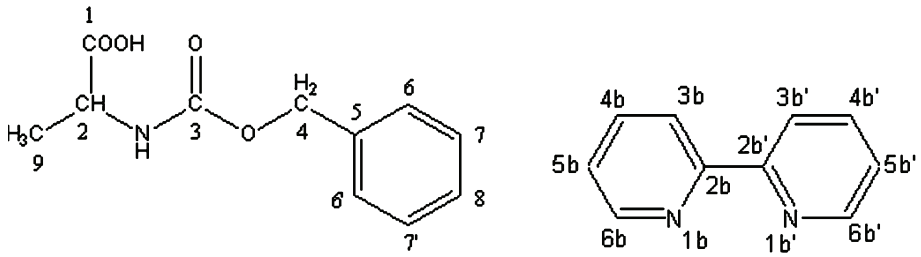

Scheme 1. Numbering of the C atoms in *N*-benzyloxycarbonyl-*S*-alanine and in 2,2'-bipyridine.

*Synthesis of [Zn(*N-*Boc*-S-*ala)$_2$]·1.5H$_2$O (**1**)*

To a solution of *N*-benzyloxycarbonyl-*S*-alanine (0.20 g, 0.90 mmol) in ethanol–water (1:1) mixture (5.0 cm^3), $ZnCl_2$ (0.060 g, 0.44 mmol) dissolved in a minimal volume of water was added. The resulting solution was allowed to reflux for 30 min, with constant stirring. The pH value of the obtained system was then adjusted to 6.0 using NaOH solution (0.20 mol dm^{-3}).

The resulting suspension was stirred for one hour at room temperature. The reaction mixture was then filtered and the obtained filtrate left at room temperature. After a few days, the obtained white crystals were separated by suction and then air-dried. Yield: 0.90 g (40 %).

*Synthesis of [Zn(*N-*Boc*-S-*ala)$_2$(bipy)]·2H$_2$O (**2**)*

To a 50-cm^3 flask, containing 0.18 g (0.34 mmol) of [Zn(*N*-Boc-*S*-ala)$_2$]·1.5H$_2$O in 2.5 cm^3 of acetonitrile, 0.060 g (0.38 mmol) of 2,2'-bipyridine in 2.0 cm^3 of acetonitrile was added. The obtained suspension was stirred for one hour without heating. The transparent reaction mixture was filtered by suction and the filtrate was left at room temperature. After a few days, white-yellow crystals were obtained. Yield: 0.19 g (81 %).

*Synthesis of [Zn(*N-*Boc-gly)$_2$(bipy)]·H$_2$O (**3**)*

To a solution of [Zn(*N*-Boc-gly)$_2$][7] (0.10 g, 0.21 mmol) dissolved in chloroform (15 cm^3), 0.032 g (0.20 mmol) of 2,2'-bipyridine dissolved in chloroform (2.5 cm^3) was added dropwise during 60 min with stirring at room temperature. The mixture was then continuously stirred for about 120 min. The filtrate was concentrated in a vacuum evaporator and left in a refrigerator. White crystals were obtained two days later. Yield: 0.80 g (61 %).

Density functional method calculation

The studied compounds **1** and **2** were subjected to geometry optimization using the density functional theory (DFT) with the Becke three-parameter exchange functional (B3)[22] and the Lee–Yang–Parr (LYP) correlation functional.[23] The DFT method was used as it gives good results for all 3d-metal complexes.[24-26] These B3LYP calculations were performed with the Gaussian03 program.[27] Various rotamers of compounds **1** and **2** were computed. As the starting point for the calculation, the conformation of the *N*-Boc residue obtained by the single crystal X-ray method was used.[15,18] The DFT calculation was performed for several conformations of the *N*-Boc-*S*-ala residuals. The conformation search was performed by variation of the Zn–O–C–N torsion angles. The geometries of conformers of the complexes were fully optimized using the LANL2DZ basis set. The optimized geometry of the most stable conformers of complexes **1** and **2** are given in Figs. 1 and 2, respectively.

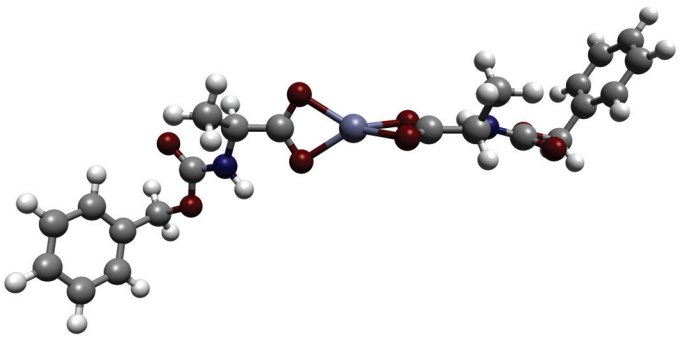

Fig. 1. Proposed tetrahedral geometry of the [Zn(*N*-Boc-*S*-ala)$_2$] complex (**1**) (structure optimized using B3LYP//LANL2DZ).

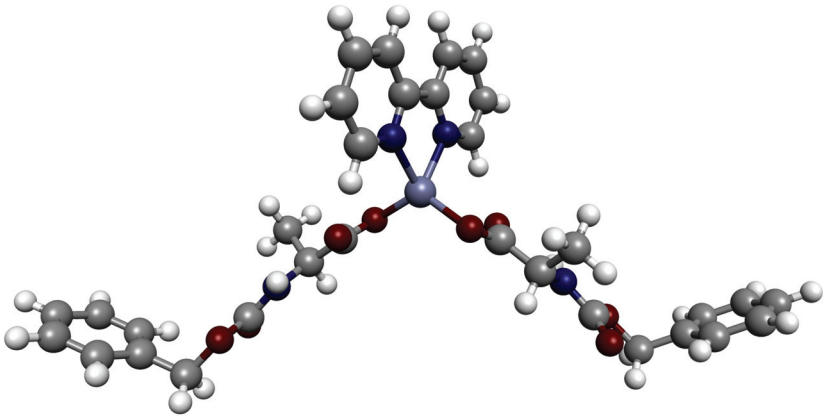

Fig. 2. Proposed tetrahedral geometry of the [Zn(*N*-Boc-*S*-ala)$_2$bipy] complex (**2**) (structure optimized using B3LYP//LANL2DZ).

Microbiological assay

N-Benzyloxycarbonyl-*S*-alanine and its Zn(II) complexes were screened for their *in vitro* antifungal activity against *Candida albicans* (ATCC 24433) and *Aspergillus niger* and their antibacterial activity against: *Escherichia coli* (ATCC 25922, Gram negative), *Staphylococcus aureus* (ATCC 25923, Gram positive) and *Micrococcus lysodeikticus* (ATCC 4698, Gram positive). The antifungal and antibacterial activity of these complexes was determined using the minimal inhibitory concentration (MIC) test.[28] The MIC test was performed by making serial dilutions in the appropriate medium with the investigated substances dissolved in DMSO in a predetermined range of concentration (5000–625 μg ml^{-1}). After plating, the bacteria were incubated at 37 °C and the growth was observed after 24 h, while fungi were incubated at 27 °C and growth was observed after 72 h. The media for the growth of the bacteria and fungi were Mueller-Hinton agar and Sabouraud dextrose agar, respectively. The experiments were performed in triplicate. The control was DMSO.

RESULTS AND DISCUSSION

Synthesis

One of the goals of this work was the synthesis of neutral (because of facilitated transport through cell membranes) complexes of zinc(II) ion with the *N*-benzyloxycarbonyl-*S*-alaninato ligand with or without 2,2'-bipyridine as an additional ligand. Compound **1** was obtained by direct synthesis by the reaction of $ZnCl_2$ with the *N*-Boc-*S*-ala ligand in the mole ratio 1:2. Complex **2** was obtained by reaction of compound **1** with 2,2'-bipyridine in the mole ratio 1:1. Compound **3** was obtained by the reaction of the previously synthesized [Zn(*N*-Boc-gly)$_2$] complex[7] with 2,2'-bipyridine. This complex was synthesized to compare the antimicrobial activities of the mixed complexes **2** and **3**. The values of the molar conductivity of the synthesized complexes in methanol (c = 10^{-3} mol dm^{-3}), *i.e.*, Λ_M = 49.15, 42.24 and 43.5 Ω^{-1} cm^2 mol^{-1} for complexes **1**, **2** and **3**, respectively, confirmed their non-electrolyte type.

Analytic and spectroscopic characterization

*[Zn(*N-*Boc*-S-*ala)$_2$]·1.5H$_2$O* (***1***). Anal. Calcd. for $C_{22}H_{25}O_{9.5}N_2Zn$: C, 49.22; H, 5.03; N, 5.22. Found: C, 49.40; H, 4.79; N, 5.43. ^{1}H-NMR (δ, ppm): 3.96 (1H, *quintet*, J = 7.4 Hz, H(2)), 7.12 (1H, *d*, J = 7.8 Hz, H(NH)), 5.01 (2H, *s*, H(4)), 7.35 (5H, *m*, H (6,6',7,7',8)), 1.25 (3H, *d*, J = 7.2 Hz, H(9)). ^{13}C-NMR (δ, ppm): 178.1 (C1); 155.9 (C3); 137.5 (C5); 128.6 (C7,C7'); 128.6 (C8); 128.0 (C6,C6'); 65.4 (C4); 50.5 (C2); 18.8 (C9).

*Zn(*N-*Boc*-S-*ala)$_2$(bipy)]·2H$_2$O* (***2***). Anal. Calcd. for $C_{32}H_{36}O_{10}N_4Zn$: C, 54.74; H, 5.13; N, 7.98. Found: C, 54.63; H, 5.03; N, 8.14. ^{1}H-NMR (δ, ppm): 8.75 (2H, *d*, J = 4.6 Hz, H(6b,6b')), 8.55 (2H, *d*, J = 8 Hz, H(3b,3b')), 8.16 (2H, *t*, J = 7.6 Hz, H(4b,4b')), 7.65 (2H, *t*, J = 5.9 Hz, H(5b,5b')), 7.34 (5H, *m*, H (6,6',7,7',8)), 6.97 (1H, *d*, J = 7.6 Hz, H(NH)), 4.98 (2H, *s*, H(4)), 3.89 (1H, *quintet*, J = 7.4 Hz, H(2)), 3.49 (H_2O), 1.19 (3H, *d*, J = 6 Hz, H(9)). ^{13}C-NMR (δ, ppm): 177.6 (C1), 155.7 (C3), 151.0 (C2b,2b'), 149.3 (C6b,6b'), 140.0 (C4b,4b'), 137.5 (C5), 128.5 (C7,C7'), 128.6 (C8), 127.8 (C6,C6'), 126.0 (C5b,5b'), 121.6 (C3b,3b'), 65.2 (C4), 50.8 (C2), 19.0 (C9).

*[Zn(*N-*Boc-gly)$_2$(bipy)]·H$_2$O* (***3***). Anal. Calcd. for $C_{30}H_{30}O_9N_4Zn$: C, 54.93; H, 4.58; N, 8.54. Found: C, 54.63; H, 4.52; N, 8.50. ^{1}H-NMR (δ, ppm): 8.68 (2H, *d*, J = 8 Hz, H(6b,6b')), 8.58 (2H, *d*, J = 4.4 Hz, H(3b,3b')), 8.19 (2H, *t*, J = 7.6 Hz, H (4b,4b')), 7.68 (2H, *t*, J = 6.1 Hz, H(5b,5b')), 7.33 (5H, *s*, H (6,6',7,7',8)), 7.13 (1H, *t*, J = 5.5 Hz, H(NH)), 4.99 (2H, *s*, H(4)), 3.51 (2H, *d*, J = 6 Hz, H(2)). ^{13}C-NMR (δ, ppm): 174.8 (C1), 156.5 (C3), 151.0 (C2b,C2b'), 149.3 (C6b,C6b'), 140.3 (C4b, C4b'), 137.5 (C5), 128.6 (C7,C7'), 128.6 (C8), 127.9 (C6,C6'), 126.2 (C5b, C5b'), 121.8 (C3b,C3b'), 65.4 (C4), 43.8 (C2).

*IR spectroscopy of complexes **1**–**3***

On the basis of the differences in the frequencies of the asymmetric and symmetric skeletal vibration of the carboxylic group (1600–1350 cm^{-1} region) in free ($\Delta\nu$ = 182 cm^{-1}) and coordinated *N*-Boc-*S*-ala it can be concluded that the modes of coordination of the carboxylic group in the complexes of zinc(II) with *N*-Boc-*S*-ala (**1** and **2**) are different.[29] Namely, in the case of complex **1** ($\Delta\nu$ = = 146 cm^{-1}), chelate bidentate coordination of the carboxylic group occurs. These findings are in agreement with the coordination mode of the carboxylic group in the previously described [Zn(*N*-Boc-gly)$_2$] complex.[7] In the case of the mixed complex **2** ($\Delta\nu$= 208 cm^{-1}), monodentate coordination of the carboxylic group seems likely, *i.e.*, the introduction of 2,2'-bipyridine into the coordination sphere of the metal ion changes the coordination mode of carboxylic group from bidentate to monodentate.

The complexes **1**–**3** crystallize with 1–2 water molecules. Since in the IR spectra of the new compounds, bands that could be assigned to vibration of coordinated water are missing,[29] tetrahedral geometry around the Zn(II) ion in all complexes was proposed.

DFT calculation

Since all attempts to obtain a single crystal suitable for X-ray crystallography failed, DFT calculation was applied to check the hypothesis that the new zinc(II) complexes with *N*-benzyloxycarbonyl-*S*-alaninato ligands adopt tetrahedral geometry (Figs. 1 and 2).

Another goal was to determine which geometry of the complex of stoichiometric composition [Zn(*N*-Boc-*S*-ala)$_2$bipy] (**2**) is more stable, the tetrahedral one with monodentate coordination of the carboxylic groups (as assumed) or the octahedral one with bidentate coordination of the carboxylic group. DFT calculation was performed for several conformations of the *N*-Boc-*S*-ala residuals. The conformation search was performed by variation of the Zn–O–C–N torsion angle. Each starting geometry was allowed to be fully optimized. The DFT calculation revealed that the most stable geometry is tetrahedral with monodentate coordination of carboxylic groups (Fig. 2). The most stable octahedral geometry is higher in energy by 2.6877 kJ mol^{-1} than the most stable tetrahedral geometry. The results of the DFT calculations confirmed the assumption based on IR spectroscopy that coordination of 2,2'-bipyridine caused a change in the coordination mode of the carboxylic groups of the *N*-Boc-*S*-ala ligands, from bidentate to monodentate. Monodentate coordination of *N*-Boc-*S*-ala through carboxylate oxygen atom is also in accordance with monodentate coordination of *N*-benzoylalaninato and DL-alaninato ligands in mixed Zn(II)-complexes, the structures of which were determined by single crystal X-ray analysis.[30,31]

In the case of complex **3** ($\Delta\nu$ = 211 cm^{-1}), coordination of 2,2'-bipy causes a change in the coordination mode of the carboxylic group from bidentate (in the previously synthesized [Zn(*N*-Boc-gly)$_2$] complex)[7] to monodentate. Tetrahedral geometry is proposed for this complex, as in the case of complex **2**.

*NMR spectroscopy of complexes **1**–**3***

Assignment of ^{1}H- and ^{13}C-NMR chemical shifts was obtained from analysis of DQF–COSY, TOCSY and {^{1}H-^{13}C}-HSQC spectra.

In the ^{1}H-NMR spectra of complexes **1**–**3**, a signal assignable to carboxylic group protons was absent, indicating that deprotonation of carboxylic group occurred and that coordination through this group took place.

The complexes **1**–**3** were also characterized by means of ^{13}C-NMR spectroscopy. The higher values of the chemical shift of C(1), C(2) and C(9) atom signals in complexes **1**–**3** in comparison with those of the signals in the respective non-coordinated ligands,[7] strongly suggest that coordination through the carboxylate groups had occurred. On the other hand, the absence of a change of the chemical shift of the carbamate carbon C(3) indicates that the carbamate group does not participate in the coordination. The assumption that coordination through nitrogen atom does not occur (except in complexes of Pb(II), Cd(II) and Cu(II) with

N-sulfonylamino acids) is in accordance with the data concerning the coordination abilities of other *N*-acylated amino acids.[15,18,32–34] The NMR spectra of the 2,2'-bipyridine complexes show that both pyridine nitrogen atoms participate in the coordination.

The most direct evidence for the DFT calculated geometry is the close contacts between the protons seen in the 2D-ROESY spectrum of **2** (Fig. 3). Thus, the proton at position 6b of the 2,2'-bipyridine ligand is close in space to the methyl protons at position 9 of the *N*-benzyloxycarbonyl-*S*-alaninato ligand. The data presented in Fig. 3 give a good example of how theoretical and experimental data can fit.

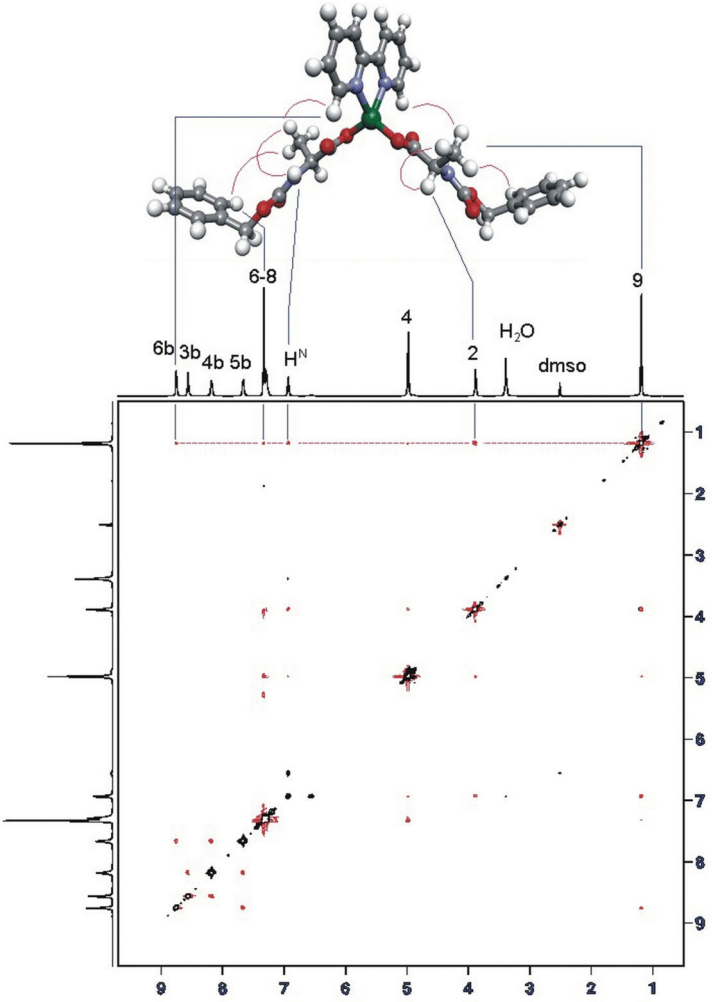

Fig. 3. ROESY spectrum of [Zn(*N*-Boc-*S*-ala)$_2$bipy] complex (**2**) exhibits inter-proton close contacts in agreement with the DFT calculated structure. ^{1}H spectral axis is in ppm relative to TMS.

Microbiological assay

The complexes **1**–**3** and *N*-benzyloxycarbonyl-*S*-alanine were screened for their *in vitro* antifungal and antibacterial activity against representative strains. The investigated complex **1** was inactive against bacterial and fungal strains, except against *Candida albicans*. The complex was more efficient in suppressing the growth of this pathogen than both the ligand and a simple zinc salt. The MIC value (625 μg ml^{-1}) was the same as that obtained for the analogue complex with the *N*-Boc-gly ligand.[7] The small increase in lipophilicity caused by the introduction of a methyl group did not change the MIC value.

Mixed complexes **2** and **3** suppressed the growth of neither *C. albicans* nor of any other investigated strains. These results are in agreement with those of recently *in vitro* performed antimicrobial studies of Cu(II) and Mn(II) complexes with 2,2'-bipy, which also did not suppress the growth of clinical isolates of *Candida* species, although their complexes with 1,10-phenanthroline were extremely toxic to the cells.[35–37] Although the MIC values for the present complexes were higher in comparison to those obtained, for example, for the Ag(I) complex with *N*-acetylglycine,[38] complexes of Zn(II) with *N*-Boc-gly and *N*-Boc-*S*-ala ligands were selective in suppressing the growth of *C. albicans*. Only the established selectivity of zinc(II) complexes with *N*-benzyloxycarbonylamino acids against one of the investigated strains may be of interest for further studies on antimicrobial activities of similar compounds.

Acknowledgement. This work was supported by the Serbian Ministry of Science, Grants Nos. 142062 and 142010.

ИЗВОД

СИНТЕЗА, NMR И DFT ПРОРАЧУНАВАЊА И ИСПИТИВАЊЕ АНТИМИКРОБНЕ АКТИВНОСТИ Zn(II) КОМПЛЕКСА СА *N*-БЕНЗИЛОКСИКАРБОНИЛ-*S*-АЛАНИНОМ

ДРАГАНА М. МИТИЋ[1], ЂЕНАНА У. МИОДРАГОВИЋ[1], ДУШАН М. СЛАДИЋ[1], ЖЕЉКО Ј. ВИТНИК[1], ЗОРАН М. МИОДРАГОВИЋ[1], КАТАРИНА К. АНЂЕЛКОВИЋ[1], МИЛАНКА Ђ. РАДУЛОВИЋ[2] и НЕНАД О. ЈУРАНИЋ[3]

[1]Хемијски факултет, Универзитет у Београду, Студентски трг 12–16, 11001 Београд, [2]Центар за хемију, Институт за хемију, технологију и металургију, Његошева 12, 11000 Београд и [3]Mayo Clinic and Foundation, Rochester, 59905 Minnesota, USA

У овом раду су синтетизовани први комплекси Zn(II) са *N*-бензилоксикарбонил-*S*-аланинато лигандом (*N*-Boc-*S*-ala). Комплекси су окарактерисани елементалном анализом, кондуктометријским мерењем, IR, ^{1}H-NMR, ^{13}C-NMR и 2D-NMR спектроскопијом. Тетраедарска геометрија Zn(II) комплекса претпостављена је на основу експерименталних података. Добијено је веома добро слагање између NMR и DFT података. Испитивана је антимикробна активност новосинтетизованих комплекса. Установљено је да је [Zn(*N*-Boc-*S*-ala)$_2$] комплекс селективан и да делује само на гљиву *Candida albicans*.

(Примљено 23. јануара, ревидирано 1. априла 2008)

REFERENCES

1. T. Yajima, R. Takamoto, A. Shimazaki, A. Odani, Y. Nakabayashi, O. Yamauchi, *J. Chem. Soc., Dalton Trans.* (2007) 299
2. N. Niklas, A. Zahl, R. Alsfasser, *J. Chem. Soc*., *Dalton Trans.* (2003) 778
3. S. Novokmet, F. W. Heinemann, A. Zahl, R. Alsfasser, *Inorg. Chem*. **44** (2005) 4796
4. D. U. Miodragović, Ž. J. Vitnik, S. M. Milosavljević, M. J. Malinar, I. O. Juranić, *Eur. J. Inorg. Chem.* (2005) 3172
5. G. A. Bogdanović, D. U. Miodragović, M. J. Malinar, *Acta Cryst. C* **58** (2002) 338
6. D. U. Miodragović, S. M. Milosavljević, M. J. Malinar, M. B. Ćelap, N. Todorović, N. Juranić, *Enantiomer* **7** (2002) 375
7. D. U. Miodragović, D. M. Mitić, Z. M. Miodragović, G. A. Bogdanović, Ž. J. Vitnik, M. D. Vitorović, M. Đ. Radulović, B. J. Nastasijević, I. O. Juranić, K. K. Anđelković, *Inorg. Chim. Acta* **361** (2008) 86
8. M. Geurts, J. H. Poupaert, G. K. E. Scriba, D. M. Lambert, *J. Med. Chem*. **41** (1998) 24
9. S. Sussan, A. Dagan, M. Bialer, *Epilepsy Res.* **33** (1999) 11
10. Z. Sajadi, M. Almahmood, L. J. Loeffler, I. H. Hall, *J. Med. Chem*. **22** (1979) 1419
11. W. Koch, M. Scheer, U. Wolke, A. Kaiser, US Patent App. No. 189 (1971) 371
12. P. N. Maton, V. E. Sutliff, R. T. Jensen, J. D. Gardner, *Am. J. Physiol.* (1985) 248
13. P. Sharma, S. Singh, T. I. Siddiqui, V. S. Singh, B. Kundu, P. Prathipati, A. K. Sawena, D. K. Dikshit, L. Rastogi, C. Dixit, M. B. Gupta, G. K. Patrik, M. Dikshit, *Eur. J. Med. Chem.* **42** (2007) 386
14. Y.-S. Kim, R. Song, H. C. Chung, M. J. Jun, Y. S. Sohn, *J. Inorg. Biochem.* **98** (2004) 98
15. L. Antolini, L. Menabue, M. Saladini, M. Sola, L. P. Battaglia, A. B. Corradi, *Inorg. Chim. Acta* **93** (1984) 61
16. L. Antolini, L. Menabue, G. C. Pellacani, M. Saladini, L. P. Battaglia, A. B. Corradi, *J. Chem. Soc., Dalton Trans*. (1984) 2325
17. L. Antolini, L. Menabue, G. C. Pellacani, M. Saladini, M. Sola, L. P. Battaglia, A. B. Corradi, *J. Chem. Soc., Dalton Trans.* (1984) 2319
18. L. Antolini, L. Menabue, M. Saladini, P. Prampolini, M. Saladini, *J. Chem. Soc., Dalton Trans*. (1982) 2109
19. D. M. Lambert, G. K. E. S. Sriba, J. H. Poupaert, P. Dumont, *Eur. J. Pharm. Sci.* **4** (1996) 159
20. D. M. Lambert, M. Geurts, G. K. E. Scriba, J. H. Poupaert, P. Dumont, *J. Pharm. Belg*. **150** (1995) 294
21. N. V. Loginova, T. V. Koval'chuk, R. A. Zheldakova, A. A. Chernyavskaya, N. P. Osipovich, G. K. Glushonok, G. I. Polozov, V. N. Povalishev, V. L. Sorokin, O. I. Shadyro, *Polyhedron* **25** (2006) 3603
22. A. D. Becke, *J. Chem. Phys*. **98** (1993) 5648
23. C. Lee, W. Yang, R. G. Parr*, J. Chem. Phys. Rev.* **B 37** (1988) 785
24. N. J. Henson, P. J. Hay, A. Redondo, *Inorg. Chem.* **38** (1999) 1618
25. L. A. Berben, J. R. Long, *Inorg. Chem*. **44** (2005) 8459
26. P. E. M. Siegbahn, R. H. Crabtree, *J. Am. Chem. Soc*. **119** (1997) 3103
27. M. J. Frisch, G. W. Trucks, H. B. Schlegel, G. E. Scuseria, M. A. Robb, J. R. Cheeseman, V. G. Zakrzewski, J. A. Montgomery, Jr., R. E. Stratmann, J. C. Burant, S. Dapprich, J. M. Millam, A. D. Daniels, K. N. Kudin, M. C. Strain, O. Farkas, J. Tomasi, V. Barone, M. Cossi, R. Cammi, B. Mennucci, C. Pomelli, C. Adamo, S. Clifford, J. Ochterski, G. A. Petersson, P. Y. Ayala, Q. Cui, K. Morokuma, D. K. Malick, A. D. Rabuck, K.

Raghavachari, J. B. Foresman, J. Cioslowski, J. V. Ortiz, A. G. Baboul, B. B. Stefanov, G. Liu, A. Liashenko, P. Piskorz, I. Komaromi, R. Gomperts, R. L. Martin, D. J. Fox, T. Keith, M. A. Al-Laham, C. Y. Peng, A. Nanayakkara, C. Gonzalez, M. Challacombe, P. M. W. Gill, B. Johnson, W. Chen, M. W. Wong, J. L. Andres, C. Gonzalez, M. Head-Gordon, E. S. Replogle, J. A. Pople, *Gaussian 98, Revision A. 7*, Gaussian, Inc., Pittsburgh PA, 1998
28. K. Nomiya, K. Tsuda, T. Sudoh, M. Oda, *J. Inorg. Biochem.* **68** (1997) 39
29. K. Nakamoto, *Infrared and Raman Spectra of Inorganic and Coordination*, Wiley, Toronto, 1997
30. A.-Y. Fu, Y.-L. Sun, D.-Q. Wang, W.-S. Zhang, A.-K. Ren, *Acta Crystallogr., Sect. E, Struct. Rep. Online* (2004) m701
31. M. S. Nandhini, R. V. Krishnakumar, S. Natarajan, *Acta Crystallogr., Sect. E: Struct. Rep. Online* (2002) m127
32. M. Saladini, D. Iacopino, L. Menabue, *J. Inorg. Biochem.* **78** (2000) 355
33. M. Borsari, L. Menabue, M. Saladini, *J. Chem. Soc., Dalton Trans*. (1996) 4201
34. G. Battistuzzi, M. Borsari, L. Menabue, M. Saladini, M. Sola, *Inorg. Chem.* **35** (1996) 4239
35. M. McCann, M. Geraghty, M. Devereux, D. O'Shea, J. Mason, L. O'Sullivan, *Metal Based Drugs* **7** (2004) 185
36. M. Devereux, M. McCann, D. O'Shea, R. Kelly, D. Egan, C. Deegan, K. Kavanagh, V. McKee, G. Finn. *J. Inorg. Biochem*. **98** (2004) 1023
37. M. Devereux, M. McCann, V. Leon, M. Geraghty, V. McKee, J. Wikaira, *Polyhedron* **19** (2000) 1205
38. N. C. Kasuga, R. Yamamoto, A. Hara, A. Amano, K. Nomiya, *Inorg. Chim. Acta* **359** (2006) 4412.

www.shd.org.rs

Journal of the Serbian Chemical Society

JSCS@tmf.bg.ac.yu • www.shd.org.rs/JSCS

J. Serb. Chem. Soc. 73 (8–9) 825–834 (2008)
JSCS–3765

UDC 547.462.3+541.183:661.183.8
Original scientific paper

Adsorption of itaconic acid from aqueous solutions onto alumina

JELENA J. GULICOVSKI[1#], LJILJANA S. ČEROVIĆ[1#], SLOBODAN K. MILONJIĆ[1*#] and IVANKA G. POPOVIĆ[2#]

[1]*The Vinča Institute of Nuclear Sciences, P.O. Box 522, 11001 Belgrade and* [2]*Faculty of Technology and Metallurgy, P.O. Box 3503, 11120 Belgrade, Serbia*

(Received 18 February 2008)

Abstract: Itaconic acid, IA ($C_5H_6O_4$), was investigated as a potential flocculant for the aqueous processing of alumina powders. The adsorption of IA, as a function of its concentration and pH value of the solution, onto the alumina surface was studied by the solution depletion method. The stability of the suspensions in the presence of itaconic acid was evaluated in light of the surface charge of the alumina powder used, the degree of dissociation of IA, as well as the sedimentation behavior and rheology of the suspensions. It was found that the adsorption process is extremely pH dependent; the maximum adsorption of IA onto alumina surface occurring at a pH close to the value of the first IA dissociation constant, pK_{a1}. Also, IA does not influence the value of the point of zero charge of alumina. It was shown that IA represents an efficient flocculant for concentrated acidic alumina suspensions.

Keywords: alumina; itaconic acid; adsorption; stability; flocculation; suspension.

INTRODUCTION

The preparation and transformation of concentrated aqueous ceramic suspensions are of paramount importance in the manufacture of ceramic parts. The key element in the colloidal processing of ceramic powders is maintaining control over the interparticle forces within the suspension during all stages; certain steps depend on repulsive forces between the particles, whereas other steps may require attractive ones.[1–3] Stable suspensions can be prepared if the repulsive potential between the particles is of sufficient magnitude that the attractive van der Waals potentials are counterbalanced or exceeded. The consolidation stage can be very slow due to the high fluidity of suspensions; and the formed green body can be rather brittle and difficult to handle. Many methods have been developed in recent years to improve ceramic processing by transforming the homogeneous suspension into a near net-shaped solid green body. This can be achieved either by

* Corresponding author. E-mail: smiloni@vin.bg.ac.yu
# Serbian Chemical Society member.
doi: 10.2298/JSC0809825G

consolidating the dispersion medium as in gel casting,[4] or by flocculating or coagulating the powder particles in suspension, *i.e.,* direct coagulation casting, *etc*.[5–7]

Polymers can induce either stabilization or flocculation of the suspension, depending on many factors, such as the nature of the particle surface, chemical structure and concentration of the polymer, dispersion medium, *etc*.[8–9]

Numerous and different kinds of organic molecules, *i.e.*, dispersants, have been used to prepare stable ceramic suspensions. Contrary to other adsorbing polymers having a charged species at only one end of the molecule, polyelectrolytes possess a charge that is present along the length of the chain, imparting electrosteric stabilization.[10,11] The use of small electrolyte molecules has gained in interest, as they enable the preparation of high solid content suspensions without a steric barrier. Their efficiency is determined by their ability to be adsorbed onto the powder surface and by a large number of functional groups which can dissociate and act as surface charge modifiers.[12] Graule *et al.*[1] investigated the potential of phenols and low-molecular aromatic carboxylic acids as alumina dispersants. A number of aliphatic organic acids were tested to study the effect of chain length, localization of double bond, number of –COOH groups, *trans*/*cis* isomery, *etc*., on the stability of Al_2O_3 suspensions.[13]

Non-adsorbing polymers usually induce depletion flocculation, or phase separation, but if added in larger concentrations they lead to depletion (re)stabilization. In the case of adsorbing polymers, different types of effects can be identified. If one polymer molecule adsorbs more than one particle simultaneously, then the polymer holds the particles together. This effect is called bridging flocculation and is usually a result of strong adsorption of low concentrations of high molecular weight polymers. If, instead, the polymer forms a layer on each particle, this can lead to a repulsive force, *i.e.*, steric stabilization. However, if the adsorbed layer is thin, the effect of short range van der Waals attraction may lead to weak flocculation and the suspension becomes more viscous. When a polyelectrolyte of opposite charge to that of the particles is added, flocculation occurs by charge neutralization.[8,9]

Itaconic acid (IA), $C_5H_6O_4$, (3-carboxy-3-butanoic, propylenedicarboxylic acid), is an unsaturated dicarbonic acid. IA is soluble in ethanol, acetone and water; it dissociates in aqueous solutions (pK_{a1} = 3.85 and pK_{a2} =5.55).[14] It is a small molecular weight monomer, obtained by distillation of citric acid (CA). CA and its salts are commonly used as alumina dispersants. However, unlike citric acid, IA does not possess any additional functionality, which would contribute to the charging of the alumina particles.

IA is an environmentally friendly substance with a large variety of industrial applications, *e.g*., as a comonomer in resins and in the manufacture of synthetic fibers, coatings, adhesives, thickeners and binders.

The intent of the present work was to investigate the efficiency of itaconic acid as a potential flocculant for the aqueous processing of alumina. The interactions of IA and alumina surface were studied in more detail to characterize the effect of this molecule on the stability of Al_2O_3 suspensions. The adsorption of IA was studied as a function of its concentration and solution pH. The suspension stability with and without IA addition was studied and evaluated in terms of the point of zero charge of alumina, the ionization chemistry of IA, and the sedimentation behavior and rheology of the suspensions.

EXPERIMENTAL

Alpha-alumina (CT 3000 SG) with an average particle size of d_{50} = 0.6 μm and a BET specific surface area, S_p = 6 m^2 g^{-1}, was produced by Alcoa, Germany. The itaconic acid was purchased from Aldrich-Chemie. The adsorption behavior of IA onto alumina was studied using a batch method. Fractions of alumina (5.0 g) were added to separately prepared 50 ml KNO_3 solutions of set pH values (initial, pH_i values) with different amounts of IA, up to 0.20 g l^{-1}. PVC vessels containing the samples were agitated mechanically for 24 h at room temperature. High-speed centrifugation allowed the separation of the supernatant for analysis. The quantity of IA adsorbed was determined by the solution depletion method, using UV spectrophotometry (Uvicon 810/820, Kontron Instruments, Austria). In order to assess quantitatively the amount of IA remaining in the supernatant, calibration curves were constructed for each measurement, *i.e.*, each pH after 24 h of equilibration, pH_e. The absorbance of IA solutions was recorded in the range from 190 to 330 nm. The calibration curves were obtained from the absorbance at the wavelength of maximum absorbance, 242 nm. The calibration is linear for the IA concentration range from 0 to 0.14 g l^{-1} for all pH_e values. The point of zero charge of alumina with and without the addition of IA was also determined by applying the batch equilibration method.[15] The suspension stability at different pH, with and without IA, was evaluated *via* gravity sedimentation tests, by pouring 50 ml of the given suspension into a graduated glass cylinder. The sediment heights were recorded as a function of time. The viscosity of the suspensions was measured using a Brookfield Synch instrument.

RESULTS AND DISCUSSION

Adsorption of itaconic acid onto α-Al_2O_3

The adsorption of IA onto alumina was studied in the pH_e interval from 3.00 to 8.50. Adsorption isotherms obtained for the suspension with pH_e set at 3.85 and 3.15, *i.e.*, at pH ≤ pK_{a1}, are presented in Fig. 1. The related adsorption curves, given as the dependence of the adsorbed amount of IA per g of alumina *vs.* the IA equilibrium concentration in the supernatant,[16] were constructed based on the difference between the initial IA concentration, c_0, and that remaining in the supernatant, c_e, according to the mass balance in the batch:

$$\Gamma = \frac{V(c_0 - c_e)}{m} \tag{1}$$

where: Γ is the amount of adsorbed IA ($g_{IA}\ g^{-1}_{alumina}$), m (g) the amount of alumina powder and V (ml) the volume of the solution.

Although the adsorption of IA at both the examined pH values increased with increasing IA concentration until a plateau was attained, the shape of the curve obtained at pH_e 3.15 indicates a rather small amount of IA adsorbed. However, the given isotherm exhibits at pH_e 3.85 a much steeper initial slope, with a plateau attained at a much higher level, indicating the greater affinity of itaconic acid for α-Al_2O_3 surfaces at $pH_e = pK_{a1}$. After 24 h, about 60 % of the initial amount was adsorbed.

The effect of the different pH_e values studied on the amount of IA adsorbed onto the alumina is summarized in Fig. 2. The observed differences in adsorption will be discussed later in the text.

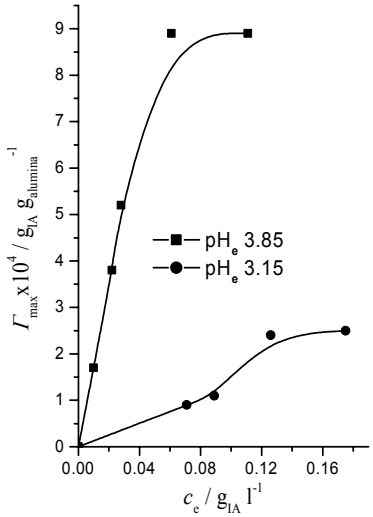

Fig. 1. Adsorption isotherms of itaconic acid onto alumina at various pH_e values.

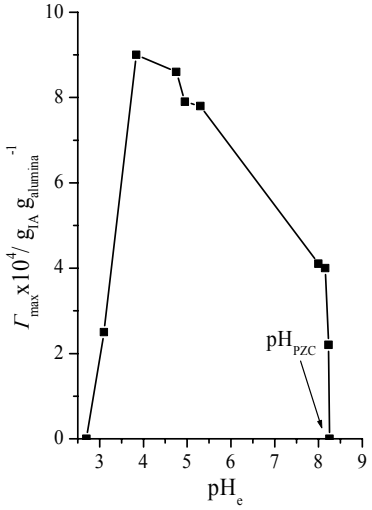

Fig. 2. The adsorption of itaconic acid as a function of suspension pH_e.

The effect of the addition of IA on the pH_{PZC} of the alumina powder

It is well-known that the point of zero charge, pH_{PZC}, together with the iso-electric point, pH_{iep}, and the surface charge of the particles, σ_0, is an important guide to the interfacial properties of a ceramic powder. Following the approach of Davis *et al*. on the dissociation-association of the amphoteric surface groups present on alumina, the reactions that occur and cause particle charge at pH_s below and above pH_{PZC} can be defined by Eqs. (2) and (3), respectively:[17]

$$AlOH_2^+ \rightleftharpoons SOH + H_s^+ \quad (2)$$

$$AlOH \rightleftharpoons SO^- + H_s^+ \quad (3)$$

where $AlOH_2^+$, SOH, and SO^- denote the positive, neutral and negative sites on an Al_2O_3 surface.

The result obtained for the pH_{PZC} of the as-received Al_2O_3 powder, given as the dependence of the pH value of filtered KNO_3 solutions after 24 h equilibration of the alumina, pH_f, on the initial pH values, pH_i, is presented in Fig. 3. The plateau observed at pH 8.3 corresponds to the point of zero charge of the investigated powder. This value is in good agreement with previous results.[18,19]

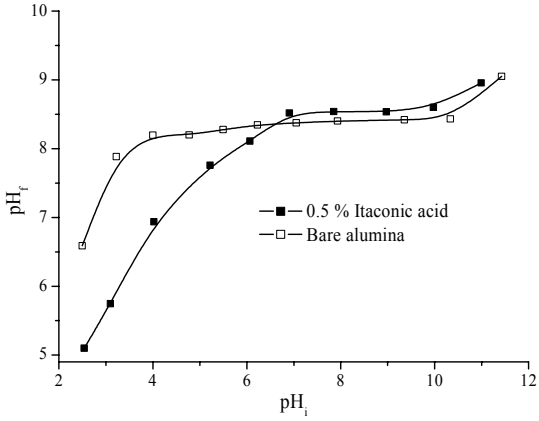

Fig. 3. Determination of the pH_{PZC} of alumina and the effect of itaconic acid addition on it.

The influence of IA addition on the pH_{PZC}, also evident from the dependence of pH_f *vs.* pH_i, was found to be somewhat different with respect to the interval of pH_i values, also presented in Fig. 3. In the range of pH_i values above pK_{a2}, *i.e.*, pH ≥ 6.00, the position of the plateau was unaffected by the presence of IA, indicating no specific IA adsorption onto alumina occurred. A change in the plateau length and shape was observed for $pH_i \leq 6.00$, *i.e.*, below the dissociation constant of IA. This can be explained either by the screening effect caused by the presence of IA, or by its non-specific adsorption onto the alumina surface. Consequently, the reaction responsible for the positive charging of alumina particles at $pH_s < pH_{PZC}$ was suppressed.

From the presented insight in the surface charging of alumina and taking into consideration the dissociation of itaconic acid ($pK_{a1} = 3.85$ and $pK_{a2} = 5.55$), the differences in IA adsorption, measured at various suspension pH_s, can be easily understood. It is evident, Fig. 2, that a maximum in the IA adsorption onto alumina occurs around pH 3.80, *i.e.*, close to the value of pK_{a1}. As the pH decreases, the positive charge of the alumina increases but the number of negatively charged IA sites continually decreases, leading to reduced (pH 3.15) or suppressed adsorption (pH 2.70). Still appreciable adsorption occurs at pH values near the value of the second dissociation constant. However, IA adsorption decreases with increasing pH, as the attraction between the positively charged alumina surface and the negatively charged IA anion decreases with increasing pH, becoming negligible in the vicinity of the pH_{PZC} value of alumina. At pH > > pH_{PZC}, no measurable adsorption occurs, confirming the mutual repulsion be-

tween the negatively charged adsorbent (alumina) and adsorbate (IA). This trend indicates the electrostatic mechanism of the adsorption process.

The result agrees well with the literature data.[13] Tomasik *et al.* confirmed the electrostatic nature of the adsorption mechanism for a series of aliphatic carboxylic acids onto alumina, including succinic acid.[13] It is worth noting that itaconic acid can also be regarded as methylene succinic acid.

Studart *et al.*[20] also claimed that the adsorption process is pH dependent, and significantly influenced by the dissociation constants (pK_a values) of the functional groups that constitute the adsorbing molecule. It was observed that the maximum adsorption occurred in a pH range near the pK_a values of the dissociating groups in the molecule. Less adsorption was expected to occur at pH ≤ pK_a due to the absence of dissociated anchoring groups on the molecule. At pH ≥ pK_a, although the functional groups are expected to be fully dissociated, the lower density of the positively charged sites on the alumina surface limits the adsorption of anionic molecules.[21]

Hidberg *et al.*[12] studied the adsorption of citric acid (CA) onto alumina powder over a wide pH range. The amount of CA varied from 0.1 to 0.6 wt. %. Almost complete adsorption was observed at pH values between 3.0 and 7.0, with values of 0.52 and 1.02 μmol CA m^{-2} Al_2O_3 measured for 0.1 and 0.2 wt. % CA, respectively. In general, with increasing pH, the adsorption of citric acid decreased. The maximum in the adsorption occurred at pH 3.0, a value close to the value of pK_{a1} of CA. The citric acid molecule has four functionalities: three COOH and one OH group (pK_{a1} = 3.13, pK_{a2} = 4.76 and pK_{a3} = 6.40).

In this study, the maximum adsorption of itaconic acid (0.20 wt. % IA added) was also registered at pH = pK_{a1}, with the value of 8.8 10^{-4} g IA/g Al_2O_3, *i.e.*, 1.13 μmol IA/m^2 Al_2O_3. Variation from this pH value had a negative impact on the adsorption process.

Contrary to itaconic acid, the adsorption of CA was also registered at pH values > pK_{a3}, which was attributed to the formation of an inner-sphere complex between the citrate ion and the alumina surface. This mechanism is most often described by the ligand (L)-exchange model,[22] where, in the case of CA, two COO^- groups in the molecule participate in the complex formation, while the third one and the hydroxyl group contribute to an increase in the negative surface charge, thus leading to electrostability of alumina suspensions. However, unlike CA, IA has neither additional functionalities, which would render charge to the particles, nor a negative incremental charge, due to the presence of a double bond of sufficient magnitude to create a negative charge on the alumina particles upon adsorption.

Stability of alumina suspensions in the presence of IA

The stabilities of alumina suspensions with different pH values, both without and with IA addition, were compared and judged *via* sedimentation velocities,

expressed as the change in the suspension height with time, Figs. 4–7. The suspension height was calculated by subtracting the top interface height separating the supernatant from the rest of the suspension.

The alumina suspension prepared in the acidic region, around pH 4, exhibited stability over a long period of time, due to simple electrostability, as seen, Fig. 4. The addition of IA in an amount of 0.50 wt. %, did not significantly influence the stability. A slight decrease in acidity (pH 4.3) resulted in a faster particle settling, Fig. 5.

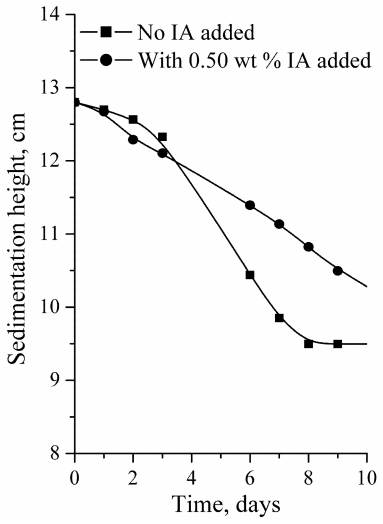

Fig. 4. Change in the alumina suspension height with time at pH 3.8 with and without IA addition.

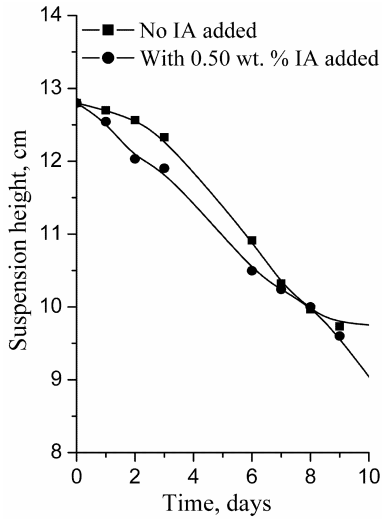

Fig. 5. Change in the alumina suspension height with time at pH 4.3 with and without IA addition.

The suspension stability at pH values above the second dissociation constant of itaconic acid, pK_{a2} = 4.55, is shown in Fig. 6. As can be seen, the stability decreased with increasing pH, so that at ≈ pH 6, the particles settled during one hour. More basic pH values promoted suspension instability. For comparison, the change of the suspension height with time with no IA added at pH ≥ pH_{PZC} of Al_2O_3 is illustrated in Fig. 7. In the vicinity of pH_{PZC}, the alumina suspensions settled completely within the first 20 min, as the powder particles were subjected to the strongest attraction without electrostatic repulsion from the surface charge. A pH increase to pH 10.0 was not sufficient to impart stability to the suspension.

The flock diameters in suspensions prepared at pH > pK_{a2} were calculated using the experimental results (Figs. 6 and 7) and the Stoke law:

$$v = \frac{d^2 g(\rho - \rho_0)}{18\eta} \tag{3}$$

where d is the particle diameter, g the acceleration of free fall, ρ and ρ_0 the particle and liquid densities, respectively, and η the viscosity of the liquid.

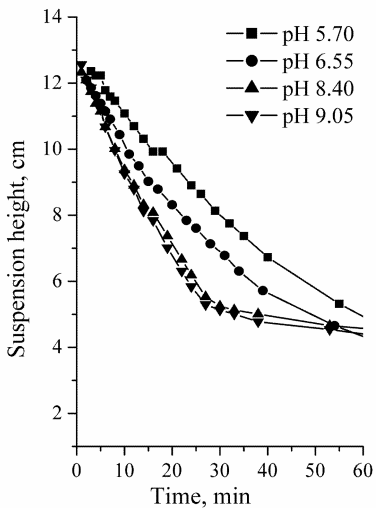

Fig. 6. Change in the alumina suspension height in time with 0.50 wt. % IA added.

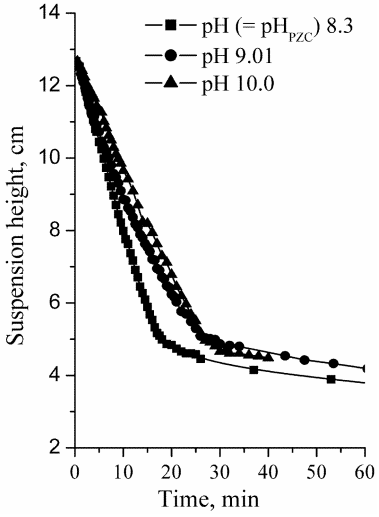

Fig. 7. Change in the alumina suspension height in time with no IA added.

The related flock diameters in the IA suspensions ranged from 4.25 to 5.0 μm at neutral pH values, while they were about 6 μm in the alkaline region. The flock diameters calculated for suspensions without IA at pH ≈ pH$_{PZC}$ were somewhat larger, probably due to the fact that in the presence of IA, the attraction of particles was screened and they settled slightly slower. The settling velocities were the same for both suspensions at pH 9.00, confirming that the addition of 0.50 wt. % IA to the dilute Al_2O_3 suspension at pH > pK_{a2} has no impact on its stability.

Rheological behavior of the alumina suspensions in the presence of IA

Alumina suspensions with a high solid content, 70 wt. %, were prepared without and with IA at pH 3.85, *i.e.*, at the pH where the maximum amount of itaconic acid was adsorbed. The low viscosity (< 4 Pa s, at a shear rate of 1.0 cm^{-1}) measured for the suspension without IA indicated that its stability was imparted *via* electrostabilization. The addition of IA in the amounts of 0.50, 1.0 and 1.5 wt. % led to an increase in the suspension viscosity, which was not possible to be measured by the available instrument. However, the suspensions appeared to be very smooth and paste-like, with no visible phase segregation. They easily regained fluidity upon the slightest addition of acid. Such behavior suggests that partially negatively charged IA molecules at pH 3.85 interact with positively charged alumina surface sites patch wise and flocculation occurs by charge neutralization.

To achieve further progress in the application of IA in gel casting or other near-net forming methods, a detailed study of the optimum surface coverage for flocculation, the influence of temperature, catalyst, effect of other monomer addition, *etc.*, is required for a clearer understanding of the flocculation mechanism and its potentialities.

A superior strength improvement in an acrylamide–IA system for the manufacture of paper was reported recently. The authors, who used this system in the presence of inorganic particles, also stated that an increase in the amount of IA increased significantly the water swelling, as well as the gel strength.[23]

CONCLUSIONS

The adsorption process of itaconic acid, IA, onto alumina, at various pH values, was investigated. It was found that the adsorption is strongly governed by the pH of the suspension and increases with increasing IA concentration. The maximum adsorption occurs at a pH close to the pK_{a1} of IA. At lower and higher pH values, the adsorption decreases, confirming its electrostatic mechanism. The pH_{PZC} of alumina was determined by the batch equilibration technique and was found to be 8.3. The presence of IA does not cause a shift in the pH_{PZC} value.

Sedimentation data showed that the addition of 0.50 wt. % IA has no significant influence on the stability of a dilute alumina suspension. However, the rheological behavior of concentrated (70 wt. %) suspensions confirmed that IA is very efficient in the flocculation of acidic (pH ≈ pK_{a1}) suspensions; the flocculation mechanism involved is charge neutralization.

Acknowledgements. This work was partially supported by the Ministry of Science of the Republic of Serbia, (Projects No. 142004 and 142023).

И З В О Д

АДСОРПЦИЈА ИТАКОНСКЕ КИСЕЛИНЕ ИЗ ВОДЕНИХ РАСТВОРА НА АЛУМИНИЈУМ-ОКСИДУ

ЈЕЛЕНА Ј. ГУЛИЦОВСКИ[1], ЉИЉАНА С. ЧЕРОВИЋ[1], СЛОБОДАН К. МИЛОЊИЋ[1] и ИВАНКА ПОПОВИЋ[2]

[1]Институт за нуклеарне науке "Винча", п. пр. 522, 11001 Београд и [2]Технолошко–металуршки факултет, п. пр. 3503, 11120 Београд

Изучавана је примена итаконске киселине, ИК ($C_5H_6O_4$), као потенцијалног флокуланта, за водено процесирање прахова алуминијум-оксида. Адсорпција итаконске киселине на површини алуминијум-оксида изучавана је у функцији концентрације и pH раствора. Стабилност суспензија алуминијум-оксида у присуству итаконске киселине објашњена је узимајући у обзир површинско наелектрисање алуминијум-оксида, степен дисоцијације итаконске киселине, седиментационо понашање и реолошка својства суспензија. Нађено је да адсорпција ИК јако зависи од pH. Максимална адсорпција ИК на површини алуминијум-оксида дешава се при pH вредности блиској вредности прве константе дисоцијације ИК, pK_{a1}. Додатак итаконске киселине не утиче на вредност тачке нултог наелектрисања алуминијум-оксида. Показано је да је ИК ефикасан флокулант за концентроване, киселе суспензије алуминијум-оксида.

(Примљено 18. фебруара 2008)

REFERENCES

1. P. C. Hidber, T. J. Graule, L. J. Gauckler, *J. Eur. Ceram. Soc.* **17** (1997) 239
2. L. Guo, Y. Zhang, N. Uchida, K. Uematsku, *J. Am. Ceram. Soc.* **81** (1998) 549
3. J. Davies, J. G. P. Binner, *J. Eur. Ceram. Soc.* **20** (2000) 1555
4. A. C. Young, O. O. Omatete, M. A. Janney, P. A. Menchhofer, *J. Am. Ceram. Soc.***743** (1991) 612
5. L. J. Gauckler, Th. Graule, F. Baader, *Mater. Chem. Phys.* **61** (1999) 78
6. R. Laucournet, C. Pagnoux, T. Chartier, J. F. Baumard, *J. Am. Ceram. Soc.* **83** (2000) 2661
7. W. M. Sigmund, N. S. Bell, L. Bergstrom, *J. Am. Ceram. Soc.* **83** (2000) 1557
8. E. Dickinson, L. Erikson, *Adv. Colloid Interface Sci.* **34** (1991) 1
9. L. Bergstrom, in *Surface and Colloid Chemistry in Advanced Ceramic Processing, Surfactant Sciences Series, 51*, R. Pugh, L. Bergstrom, Eds., Marcel Dekker, New York, 1994, pp. 193
10. J. Cesarano, I. A. Aksay, *J. Am. Ceram. Soc.* **71** (1998) 1062
11. P. C. Hidberg, T. J. Graule, L. J. Gauckler, *J. Am. Ceram. Soc.* **79** (1996) 1857
12. P. Tomasik, C. Schilling, R. Jankowiak, J. C. Kim, *J. Eur. Ceram. Soc.* **23** (2003) 913
13. T. Willke, K. D. Vorlop, *Appl. Microbiol. Biotechnol.* **56** (2001) 289
14. S. K. Milonjić, A. Ruvarac, M. Šušić, *Thermochim. Acta* **11** (1975) 261
15. S. K. Milonjić, *J. Serb. Chem. Soc*. **72** (2007) 1363
16. J. A. Davis, R. O. James, J. O. Leckie, *J. Colloid Interface Sci.* **63** (1978) 480
17. Ž. N. Todorović, S. K. Milonjić, V. T. Dondur, *Mater. Sci. Forum* **453–454** (2004) 361
18. J. J. Gulicovski, Lj. S. Čerović, S. K. Milonjić, *Ceram. Int.* **34** (2008) 23
19. A. R. Studart, V. C. Pandolfelli, E. Tervoort, L. J. Gauckler, *J. Eur. Ceram. Soc.* **23** (2003) 997
20. A. R. Studart, J. Gallo, V. C. Pandolfelli, *Am. Ceram. Soc. Bull.* **81** (2002) 36
21. R. Kummert, W. Stumm, *J. Colloid Interface Sci.* **75** (1980) 373
22. M. A. Hubbe, O. J. Rojas, D. S. Argyropoulos, Y. Wang, J. Song, N. Sulic, T. Sezaki, *Colloids Surfaces A* **301** (2007) 23.

www.shd.org.rs

Journal of the Serbian Chemical Society

JSCS@tmf.bg.ac.yu • www.shd.org.rs/JSCS

J. Serb. Chem. Soc. 73 (8–9) 835–843 (2008)
JSCS–3766

UDC 546.185+546.268.5:541.183:549.525.2
Original scientific paper

Sorption of phosphates and thiocyanates on isomorphic substituted Mg/Zn–Al-type hydrotalcites

RODICA PODE[1]*, EVELINE POPOVICI[2], LAURA COCHECI[1], ERIKA REISZ[1], ELENA MIHAELA SEFTEL[2] and VASILE PODE[1]

[1]*Faculty of Industrial Chemistry and Environmental Engineering, University "Politehnica" of Timisoara, Victoriei Sq. 2, 300006 Timisoara and* [2]*Faculty of Chemistry, "Al. I. Cuza" University of Iasi, Carol I Blvd. 11, 700506 Iasi, Romania*

(Received 15 April 2007, revised 15 March 2008)

Abstract: The sorption equilibriums of phosphate and thiocyanate anions on isomorphic substituted Mg/Zn–Al-type hydrotalcites were investigated in this study. Langmuir and Freundlich isotherms were used to interpret the equilibrium data for phosphate. The sorption equilibriums of phosphate on Mg_3Al, Mg_2ZnAl and $Mg_{1.5}Zn_{1.5}Al$ hydrotalcites were well described by the Langmuir isotherm. The highest maximum sorption capacities for these adsorbents were as follows: 111, 101 and 95 mg g^{-1}. The equilibrium constant and standard Gibbs energy changes were also calculated from the sorption data. Standard Gibbs energy changes of about –20 kJ mol^{-1} indicated that the process might be considered as physical adsorption. The sorption equilibriums of phosphate on isomorphic substituted samples of $MgZn_2Al$ and Zn_3Al were well described by the Freundlich isotherm. Thiocyanate showed a relative low affinity for the studied materials, as indicated by both the "S"-shaped isotherms and low sorption capacities. The sorption of phosphate and thiocyanate on the investigated hydrotalcites showed a continuous decrease of the sorption capacity in the following order: $Mg_3Al > Mg_2ZnAl > Mg_{1.5}Zn_{1.5}Al > MgZn_2Al > Zn_3Al$.

Keywords: Mg/Zn–Al-type hydrotalcites; sorption; equilibrium; phosphate; thiocyanate.

INTRODUCTION

Layered double hydroxides (LDHs), hydrotalcite-type solids or anionic clays, are described by the general formula $[M^{2+}_{1-x}M^{3+}_{x}(OH)_2]^{x+}(A^{n-}_{x/n})\cdot mH_2O$, where M is a divalent or trivalent metals and A^{n-} charge-compensating group.[1] The general formula underlines the possibility of obtaining a large number of compounds with different stoichiometry.

Many studies have considered the synthesis and characterization of LDHs with a variety of divalent (Mg and/or Ni, Zn, Co, Zr) or trivalent (Al and/or Fe,

* Corresponding author. E-mail: rodicapode@yahoo.com
doi: 10.2298/JSC0809835P

Ga, Cr) metal cations within the layers of an LDH. Several kinds of charge--compensating group, mono- or multivalent (HO^-, CO_3^{2-}, NO_3^-, Cl^-, SO_4^{2-}) were intercalated at the interlayer of the LDH because the volume of the interlayer gallery is variable and the interlayer distance between adjacent layers is enhanced or reduced in proportion to the molecular size of the anion.[2]

There are numerous studies on synthesis, structure and physico–chemical characteristics of these compounds.[3–5]

The layered double hydroxides, particularly anionic hydrotalcite compounds, have gained a large importance for pollution abatement due to their sorption and catalytic properties.[6–11]

The anion exchange properties of LDHs and the anion sorption ability under the LDHs reconstruction process have been investigated for the removal of environmentally undesirable anions. Among oxyanions, the sorption of phosphate species by LDHs has been the subject of many studies because of its consequences for water pollution.[12–15] The presence of phosphate anions in surface water leads to the serious problems of eutrophication, which requires a decrease of the phosphate concentration to stipulated limits. Thiocyanate-containing wastewaters result from a variety of industrial processes, such as, herbicide and insecticide production, acrylic fibre production, manufacturing of thiourea, electroplating, *etc*. The removal of thiocyanates from wastewater is a necessity since this anion is well-known as a priority dangerous pollutant.[16]

The aim of this work was to investigate the influence of the isomorphic substitution ratio Mg/Zn on the sorption equilibriums of phosphate and thiocyanate on Mg/Zn-Al-type hydrotalcites.

EXPERIMENTAL

A series of hydrotalcite-type solids with various compositions were synthesized in order to obtain various substitution ratios ($r_{Mg(II)}$ = 0.065 nm; $r_{Zn(II)}$ = 0.074 nm). The M(II)/Mg mole ratios were 0:3, 1:2, 1.5:1.5, 2:1 and 3:0.

The synthesis was performed by a classic procedure, the co-precipitation method, under conditions of low supersaturation.[7] An aqueous 1.0 mol l^{-1} solution of nitrates, *i.e.*, $Zn(NO_3)_2{\cdot}6H_2O$, $Mg(NO_3)_2{\cdot}6H_2O$ and $Al(NO_3)_3{\cdot}9H_2O$ (Sigma), was slowly added to a solution of NaOH, under magnetic stirring. The pH was maintained between 7.0 and 7.5 (Hanna HI 991003 pH-meter).

The mixing step was performed under stirring for 1 h at room temperature and then on an oil bath at 60 °C under reflux for 18 h. The hydrotalcite powders were isolated by centrifugation and washed several times with demineralised water until pH 7.0. This step was followed by drying at 80 °C overnight. Then the dried samples were ground and sieved. The fraction between 0.060 and 0.125 mm was used as an adsorbent. The sample activation was performed in an oven at 500 °C in air and a heating rate of 1.0 °C min^{-1} for 4 h.

All sorption experiments were performed on activated Mg/Zn–Al hydrotalcite samples. To study the retention capacity at equilibrium, identical quantities of synthesized solids were contacted with identical volumes of aqueous solutions containing phosphate and thiocyanate, the initial concentrations of which ranged from 10 to 500 mg l^{-1} for phosphate and from 5.0 to

100 mg l^{-1} for thiocyanate. The solution pH was 7.0±0.2 and the solid/liquid ratio was 1.0 g l^{-1}. The samples were maintained at a constant temperature (25±1 °C) in a thermostated shaker bath for 12 h to reach sorption equilibrium. The kinetic studies preceded the determination of the equilibrium isotherm in order to determine the time demand for attaining thermodynamic equilibrium.

At equilibrium, the solid was separated by centrifugation and the phosphate and thiocyanate concentration in the supernatant was analysed by using a Varian Carry 50 UV–Vis spectrophotometer. The phosphate concentration in the aqueous solution was determined at 450 nm in line with the vanado-molybdate method.[17] The concentration of thiocyanate was also determined spectrophotometrically at 475 nm.[18]

X-Ray diffractions patterns were recorded on a Philips PW 1830 power diffractometer (45 kV, 25 mA) using Ni filtered Cu_α (0.154 nm) radiation.

The thermal analysis was performed under an inert atmosphere (nitrogen), from 20 to 990 °C, at a heating rate of 10 °C min^{-1} using a TG 209 analyzer (Netzsch, Germany). A Proteus Analysis (Netzsch) program was used for data processing.

RESULTS AND DISCUSSION

Samples characterization

The X-ray diffraction analysis enabled the computation of the unit cell parameters *a* and *c*, which highlighted the rhombohedric symmetry of the synthesized hydrotalcite-like compounds (Table I).

TABLE I. Parameters of the cell unit, *a* and *c*, for the synthesized samples

M(II)/Mg mole ratio	Sample	*a* / Å	*c* / Å	Symmetry
3	Zn_3Al	3.03	22.94	3R
2	Zn_2MgAl	3.03	23.06	3R
1	$Zn_{1.5}Mg1_{1.5}Al$	3.03	23.20	3R
0.5	$ZnMg_2Al$	3.04	23.25	3R
0	Mg_3Al	3.04	23.37	3R

The *a* parameter corresponds to the cation–cation gap within the brucite layer and the $c = 3c'$ parameter is the thickness of the layer made of a brucite-like film and an interlayer. The numbers are characteristic of a rhombohedric symmetry and they were calculated using the following relationships:

$$1/d^2 = 4/3(h^2+hk+k^2)/a^2 + l^2/c^2 \quad (1)$$

where:

$$d = \lambda/2 \sin\theta \text{ and } \lambda = 1.54051 \text{ Å} \quad (2)$$

The influence of the degree of isomorphic substitution on the thickness of the layer can be seen.

In addition, the thermal behaviour of the samples was influenced by the degree of isomorphic substitution, indicating changes in the hydroxyl surface structure (Table II). Firstly, dehydration occurred due to the loss of adsorbed water molecules in one minor step at 100 °C. The second step was caused by the loss of interlayer water molecules in the Mg_3Al sample at about 212 °C. For the Zn-sub-

stituted samples, the temperature of this step was lower. In addition, the dehydroxylation of the Mg/Zn/Al hydroxide sheets and decarbonisation decreased with increasing Zn content.

TABLE II. Thermal analysis results

Stage	Mg/Zn mole ratio									
	3:0		2:1		1.5:1.5		1:2		0:3	
	t / °C	Mass loss %	t / °C	Mass loss %	t / °C	Mass loss %	t / °C	Mass loss %	t / °C	Mass loss %
1	100.0	2.35	100.0	2.29	89.4	2.04	100.0	2.17	100.0	1.40
2	212.2	12.67	175.8	8.16	100.0	2.61	183.1	9.85	176.5	9.01
3	379.0	31.85	302.3	15.56	182.6	9.01	270.5	17.80	216.6	14.62
4	–	–	363.2	23.89	261.0	17.01	372.1	28.42	–	–

Sorption equilibrium of phosphate on Mg/Zn–Al-type hydrotalcites

The results showed that for the Mg_3Al sample, at the upper limit of the equilibrium concentration range, the sorption capacity for phosphate remained practically constant (Fig. 1). Thus, the equilibrium was well described by the Langmuir isotherm (Eq. (3)):

$$q_e = q_{max} K_L c_e / (1 + K_L c_e) \quad (3)$$

where q_e is the quantity of anion sorbed at equilibrium (mg g^{-1}), q_{max} is the maximum sorbed quantity (mg g^{-1}), c_e is the equilibrium concentration (mg l^{-1}) and K_L is the equilibrium constant (l mg^{-1}).

The Henry domain was also well defined for this situation.

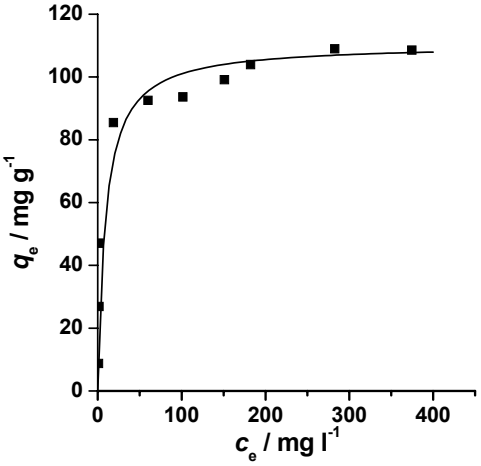

Fig. 1. Sorption isotherm of phosphate on Mg_3Al hydrotalcite.

The experimental data obtained from the sorption of phosphate on Mg/Zn––Al-type hydrotalcites (Figs. 2–5) were interpreted by means of the Langmuir (full line) and Freundlich (dotted line) isotherms (Eqs. (3) and (4)):

$$q_e = \alpha c_e^{\beta} \quad (4)$$

where q_e and c_e have the same meaning as previously mentioned; and α and β are constants.

The isotherms for the sorption of phosphate on Mg_2ZnAl and $Mg_{1.5}Zn_{1.5}Al$ hydrotalcites (Figs. 2 and 3) displayed a typical Langmuir plateau, while those for Mg_2ZnAl and Zn_3Al hydrotalcites (Figs. 4 and 5) did not reach the plateau at up to 450 mg l^{-1}, the maximum equilibrium concentration employed in this study.

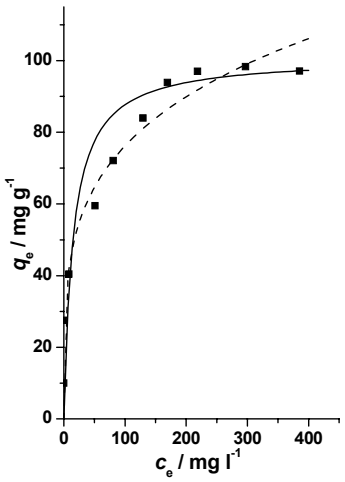

Fig 2. Sorption isotherm of phosphate on Mg_2ZnAl hydrotalcite: full line – Langmuir isotherm; dotted line – Freundlich isotherm.

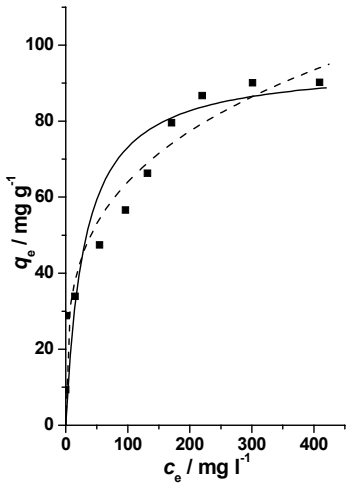

Fig. 3. Sorption isotherm of phosphate on $Mg_{1.5}Zn_{1.5}Al$ hydrotalcite.

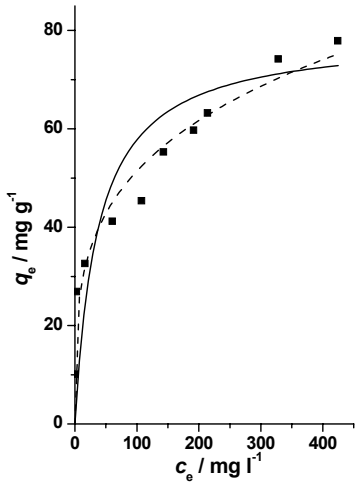

Fig. 4. Sorption isotherm of phosphate on $MgZn_2Al$ hydrotalcite.

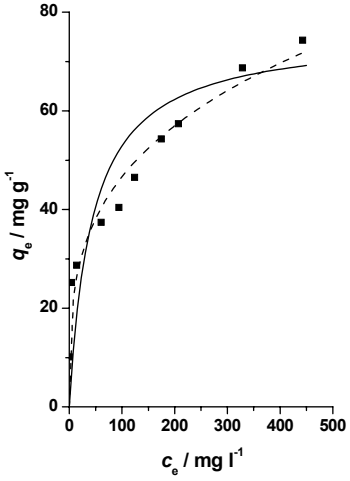

Fig.5. Sorption isotherm of phosphate on Zn_3Al hydrotalcite.

On analysing the results, it followed that the Mg_3Al sample had the best sorption behaviour. The maximum sorption capacity of phosphate on this adsorbent was 111 mg g^{-1}. In addition, as the isomorphic substitution degree increased, the sorption capacity decreased continuously. This finding is in agreement with the low values of cell unit parameters, which impeded the access of phosphate ions to the space between the brucite layers (Table III).

TABLE III. The sorption equilibrium characteristics of phosphate on Mg/Zn–Al-type hydrotalcites

Sample	Langmuir isotherm				Freundlich isotherm	
	q_{max} mg g^{-1}	Equilibrium constant, K_L		$\Delta_{ads}G^{\ominus}$ (298 K) kJ mol^{-1}	α	β
		l mg^{-1}	10^3 l mol^{-1}			
Mg_3Al	111	0.107	10.1	–22.9	–	–
Mg_2ZnAl	101	0.066	6.25	–21.7	25.4	0.239
$Mg_{1.5}Zn_{1.5}Al$	95	0.033	3.14	–20.0	18.2	0.273
$MgZn_2Al$	79	0.027	2.56	–19.4	15.3	0.263
Zn_3Al	76	0.023	2.19	–19.1	12.3	0.290

For all samples, in the low concentration range, a decrease in the slope of the Langmuir isotherm with increasing degree of substitution of Mg^{2+} by Zn^{2+} could be seen. This decrease might be attributable to the decrease of the phosphate affinity of the hydrotalcites within the Mg/Zn–Al series. Both the decrease of the isotherm slope and the maximum sorption capacities led to the following order for phosphate affinity for the studied hydrotalcites:$Mg_3Al > Mg_2ZnAl > Mg_{1.5}Zn_{1.5}Al > > MgZn_2Al > Zn_3Al$.

The Langmuir model allowed the computation of the sorption equilibrium constant, K_L, and standard Gibbs energy change, $\Delta_{ads}G^{\ominus}$ (298 K). The equilibrium constant decreased by a factor of 1.4 from Mg_3Al to Zn_3Al, showing that the sorption process was not favoured as the degree of substitution of Mg^{2+} by Zn^{2+} increased. In accordance with the calculated standard Gibbs energy changes, about –20 kJ mol^{-1}, the process could be considered as physical adsorption.[15]

An examination of the Langmuir isotherms showed that there was deviation from the experimental data at higher isomorphic substitution ratios ($MgZn_2Al$ and Zn_3Al). The sorption equilibrium of phosphate on these samples followed the Freundlich isotherm closely. In addition, the interpretation of experimental results using the Freundlich isotherm can be justified by the fact that advanced wastewater treatment does not assume operation at the quite high concentrations used in this study.

In all cases, both the subunit β (Table III) and the $\Delta_{ads}G^{\ominus}$ (298 K) values underlined that the interaction forces between phosphate and the studied adsorbents were weak and thus the process was physical adsorption.[15]

Sorption equilibrium of thiocyanate on Mg/Zn–Al -type hydrotalcites

The experimental sorption isotherms for thiocyanate are shown in Fig. 6

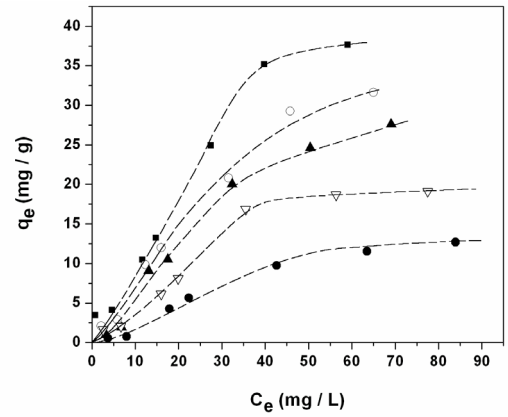

Fig. 6. Sorption isotherms for thiocyanate on: Mg_3Al (■); Mg_2ZnAl (○); $Mg_{1.5}Zn_{1.5}Al$ (▲); $MgZn_2Al$ (∇); Zn_3Al (●). Lines are drawn to guide the eye.

By analysing the sorption isotherms, their "S" shape is immediately obvious, which suggests low affinity of thiocyanate for the studied hydrotalcites. This finding was also highlighted by the values of the sorption capacities, *e.g.* 38 mg g^{-1} for Mg_3Al and 13 mg g^{-1} for Zn_3Al, at the maximum equilibrium concentration employed in this study (60 mg l^{-1}). These results are in accordance with the literature,[15,19] concerning the affinity of monovalent ions for hydrotalcites as opposed to polyvalent ions, which showed a lower affinity. In addition, the values obtained for the sorption capacity of thiocyanate anion are comparable with those reported by other authors.[14]

For a given equilibrium concentration, there was a 3-times continuous decrease of the sorption capacity in the following order: Mg_3Al > Mg_2ZnAl > > $Mg_{1.5}Zn_{1.5}Al$ > $MgZn_2Al$ > Zn_3Al, which emphasizes the negative influence of the isomorphic substitution by Zn^{2+} within the brucite layer on the retention of thiocyanate.

By comparing the sorption of the two anions on Mg/Zn–Al-type hydrotalcites, it follows that phosphate sorption occurred with good results, highlighted by the values of the maximum sorption capacities, while thiocyanate sorption was ineffective; the affinity of the studied adsorbents for this anion was poor. The results are in accordance with literature data,[19] which reported that the affinity of hydrotalcites for monovalent anions was modest. Another finding referred to the negative influence of zinc substitution into the brucite-like layer.

CONCLUSIONS

The equilibrium of phosphate and thiocyanate sorption on Mg/Zn–Al-type hydrotalcites was studied under various Zn/Mg substitution ratios.

Langmuir and Freundlich models were applied to characterize the equilibrium of phosphate sorption on Mg/Zn–Al hydrotalcites.

The Langmuir isotherm can be used to describe all adsorption equilibriums but with increasing substitution of Mg^{2+} by Zn^{2+}, the deviation of the experimental points from the theoretical curve increased. For $MgZn_2Al$ and Zn_3Al hydrotalcites, the experimental data were better described by Freundlich isotherms.

The highest sorption capacity for phosphate was attained with the Mg_3Al sample (111 mg g^{-1}). Phosphate adsorption on hydrotalcites within the Mg/Zn–Al series indicated a decrease of the maximum sorption capacity as the Zn/Mg substitution ratio increased.

Expressing the equilibrium data using the Langmuir model allowed the computation of the sorption equilibrium constant, K_L, and the standard Gibbs energy change, $\Delta_{ads}G^{\ominus}$ (298 K). Based on results, the process can be considered as physical adsorption.

This finding was confirmed with the assessment of the constant β, which was determined based on the Freundlich isotherm for $MgZn_2Al$ and Zn_3Al.

The experimental sorption isotherms of thiocyanate showed a lower affinity for Mg/Zn–Al series as compared to phosphate. For a given equilibrium concentration, there was a continuous decrease of the sorption capacity in the following order: $Mg_3Al > Mg_2ZnAl > Mg_{1.5}Zn_{1.5}Al > MgZn_2Al > Zn_3Al$.

Acknowledgments. The results were obtained as part of the activities of Project CEEX No.1/S1-2005, under the auspices of the MATNANTECH Scientific Authority.

ИЗВОД

СОРПЦИЈА ФОСФАТА И ТИОЦИЈАНАТА НА ИЗОМОРФНИМ СУПСТИТУИСАНИМ ХИДРОТАЛЦИТИМА ТИПА Mg/Zn–Al

RODICA PODE[1], EVELINE POPOVICI[2], LAURA COCHECI[1], ERIKA REISZ[1], ELENA MIHAELA SEFTEL[2] и VASILE PODE[1]

[1]Faculty of Industrial Chemistry and Environmental Engineering, University "Politehnica" of Timisoara, Victoriei Sq. 2, 300006 Timisoara и [2]Faculty of Chemistry, "Al. I. Cuza" University of Iasi, Carol I Blvd. 11, 700506 Iasi, Romania

У овом раду су испитиване сорпционе равнотеже фосфата и тиоцијаната на изоморфним супституисаним хидроталцитима типа Mg/Zn–Al. За тумачење равнотежних података за фосфате коришћене су Ленгмирова и Фројндлихова изотерма. Сорпционе равнотеже за фосфате на Mg_3Al-, Mg_2ZnAl- and $Mg_{1.5}Zn_{1.5}Al$-хидроталцитима добро су описане Ленгмировом изотермом. Највећи максимални сорпциони капацитети износили су 111, 101 и 95 mg g^{-1}. Такође су израчунати и константа равнотеже и промена стандардне Гибсове енергије сорпције. Промена стандардне Гибсове енергије сорпције од око –20 kJ mol^{-1} указује на то да процес треба сматрати као физичку адсорпцију. Сорпционе равнотеже фосфата на изоморфним супституисаним хидроталцитима $MgZn_2Al$ and Zn_3Al добро су описане Фројндлиховом изотермом. Тиоцијанати су показали релативно мали афинитет према испитиваним материјалима, на шта указују изотерме облика "S" криве и мали сорпциони капацитети. Сорпција фосфата и тиоцијаната на испитиваним хидроталцитима показала је континуално опадање сорпционог капацитета према следећем низу: $Mg_3Al > Mg_2ZnAl > Mg_{1.5}Zn_{1.5}Al > MgZn_2Al > Zn_3Al$.

(Примљено 15. априла 2007, ревидирано 15. марта 2008)

REFERENCES

1. S. M. Auerbache, K. A. Corrado, P. K. Dutta, *Handbook of Layered Materials*, Marcel Dekker Inc., New York, NY, 2004, p. 373
2. E. Kanezaki, in *Clay Surfaces. Fundamentals and Applications*, F. Wypych, K. G. Satynarayana, Eds., Elsevier, New York, 2004, p. 346
3. L. Châtelet, J. Y. Bottero, J. Yvon, A. Bouchelaghem, *Coll. Surf. A* **111** (1996) 167
4. E. M. Seftel, E. Dvininov, D. Lutic, E. Popovici, C. Ciocoiu, *J. Optoelectron. Adv. Mater.* **7** (2005) 2869
5. W. Yang, Y. Kim, P. K. T. Liu, M. Sahini, T. T. Tsotsis, *Chem. Eng. Sci.* **57** (2002) 2945
6. C. Forano, E. Gèraut, V. Prevot, F. Leroux, T. Alekseeva, M. Bouhent, Z. Derriche, S. Rafqah, M. Sarakha, in *Proceedings of the 43rd Annual Meeting of CMS – 4eme Colloque du GFA*, (2006), Abstracts, 2006, p. 95
7. A. Vaccari, *Catal. Today* **41** (1998) 53
8. H. Curtius, Z. Kattilparampil, *Clay Miner.* **40** (2005) 455
9. A. E. Palomares, J. G. Prato, F. Rey, A. Corma, *J. Catal.* **221** (2004) 62
10. D. P. Das, J. Das. K. Parida, *J. Colloid Interf. Sci.* **261** (2003) 213
11. V. K. Gupta, *Ind. Eng. Chem. Res.* **37** (1998) 192
12. G. K. Morse, J. N. Lester, *Sci. Total Environ.* **212** (1998) 69
13. A. Dimirkou, A. Ioannou, M. Doula, *Advan. Coll. Interface Sci*. **97** (2002) 37
14. N. K. Lazaridis, *Water Air Soil Poll.* **146** (2003) 127
15. C. Forano, in *Clay Surfaces. Fundamentals and Applications*. F. Wypych, K. G. Satynarayana, Eds., Elsevier, New York, 2004, p. 426; p. 430
16. C. H. Hung, S. G. Pavlostathis, *Wat. Res.* **31** (1997) 2761
17. A. D. Eaton, L. S. Clesceri, E. W. Rice, A. E. Greenberg, *Standard Methods for the Examination of Water and Wastewater*, 21st Ed., American Public Health Association, Washington, DC, 2005, p. 4151
18. *Die Untersuchung von Wasser*, E. Merck, Darmstadt, 1974, p. 206
19. W. T. Reichle, S. Y. Kang, D. S. Everhardt, *J. Catal.* **101** (1986) 352.

www.shd.org.rs

Journal of the Serbian Chemical Society

JSCS@tmf.bg.ac.yu • www.shd.org.rs/JSCS

J. Serb. Chem. Soc. 73 (8–9) 845–859 (2008)
JSCS–3767

UDC 546.26–033.5+547.261+
+66.094.3:546.92+544.478
Original scientific paper

Influence of surface morphology on methanol oxidation at a glassy carbon-supported Pt catalyst

S. STEVANOVIĆ[1#], D. TRIPKOVIĆ[1#], A. KOWAL[2], D. MINIĆ[3], V. M. JOVANOVIĆ[1#] and A. TRIPKOVIĆ[1*#]

[1]*ICTM – Center for Electrochemistry, University of Belgrade, Njegoševa 12, P. O. Box 473, 1100 Belgrade, Serbia,* [2]*Institute of Catalysis and Surface Chemistry, Polish Academy of Science, Krakow, Niezapominajek 8, 30-239, Poland and* [3]*Faculty of Physical Chemistry, University of Belgrade, Studentski trg 12, 1100 Belgrade, Serbia*

(Received 20 December 2007, revised 14 March 2008)

Abstract: Platinum supported on glassy carbon (GC) was used as a model system for studying the influence of the surface morphology of a Pt catalyst on methanol oxidation in alkaline and acidic solutions. Platinum was deposited by the potential step method on GC samples from $H_2SO_4 + H_2PtCl_6$ solution under the same conditions with loadings from 10 to 80 μg cm^{-2}. AFM and STM images of the GC/Pt electrodes showed that the Pt was deposited in the form of 3D agglomerates composed of spherical particles. Longer deposition times resulted in increased growth of Pt forms and a decrease in the specific area of the Pt. The real surface area of Pt increased with loading but the changes were almost negligible at higher loadings. Nevertheless, both the specific and mass activity of platinum supported on glassy carbon for methanol oxidation in acidic and in alkaline solutions exhibit a volcanic dependence with respect to the platinum loading. The increase in the activity can be explained by the increasing the particle size with the loading and thus an increase in the contiguous Pt sites available for adsorption and decomposition of methanol. However, the decrease in the activity of the catalyst with further increase of loading and particle size after reaching the maximum is related to the decrease of active sites available for methanol adsorption and their accessibility as a result of more close proximity and pronounced coalescence of the Pt particles.

Keywords: glassy carbon; methanol oxidation; electrochemical Pt deposition; surface morphology.

INTRODUCTION

Methanol is one of the most extensively investigated small organic molecules, both from a fundamental and practical point of view. Considered as a poten-

* Corresponding author. E-mail: amalija@tmf.bg.ac.yu
# Serbian Chemical Society member.

doi: 10.2298/JSC0809845S

tial fuel for fuel cells, studies of its oxidation on Pt and supported Pt catalysts have intensified during the last decades. The overall reaction:

$$CH_3OH + H_2O \rightarrow CO_2 + 6H^+ + 6e^- \quad (1)$$

occurs in several steps[1–3] but the two main processes are adsorption followed by dehydrogenation of methanol and oxidation of CO_{ad}.[1] Oxidation of CO_{ad} commences when oxygen-containing species are produced in the interaction of water with platinum.[1] Studies of this reaction at Pt poly and single crystal electrodes showed that the adsorption of methanol as well as its oxidation exhibit strong surface sensitivity, which is reflected in the amount and rate of surface coverage by CO_{ad}.[1,4,5] Ren *et al.*[6] examined methanol oxidation at smooth, mildly rough (roughness factor ≈ 50) and highly rough (roughness factor ≈ 200) Pt electrodes prepared by electrochemical treatment and found a difference in the potential of the peak current which indicated an effect of the surface roughness. Raman spectroscopy showed that CO oxidation becomes slower on a highly rough surface, *i.e.*, a surface with more defects, such as edges, kinks and step sites, than on a less rough surface. Beden *et al.*[3,7] studied the electroadsorption and oxidation of methanol on smooth and rough polycrystalline, single crystalline and preferentially oriented Pt electrodes using electromodulated infrared spectroscopy (EMIRS). They found that poisoning by CO was reduced on electrodispersed Pt (roughness factor ≈ 20) in comparison to smooth Pt, indicating that the structure of the surface plays an important role in diminishing the phenomena of CO_{ad} poisoning.

Chemical or electrochemical deposition of platinum on a substrate with a high surface area results in a Pt catalyst with a roughness which depends on the Pt particle size, *i.e.*, on the Pt loading. Mikhaylova *et al.*[8] deposited Pt on glassy carbon by cyclic voltammetry with loadings from 10 to 540 μg cm^{-2} and obtained electrodes with a roughness factor < 20. The catalytic effect on methanol oxidation in acid increased with increasing loading up to 60 μg cm^{-2} (roughness factor ≈ 6) and remained unchanged with further growth of the deposit. At higher loadings, the specific activities were close to that of smooth platinum, which was explained by the similar coverage of Pt with organic particles on those surfaces with a roughness factor from 6 to 20 and on smooth Pt. They concluded that the catalytic effect is connected with the change in the bond strength of methanol adsorbates with Pt particles, caused by the structural properties of the deposits. Umeda *et al.*[9] used porous-microelectrodes prepared by the chemical deposition of Pt on carbon black for methanol electro-oxidation. The activity of the catalyst first increased and then decreased with loading. As the potential of Pt oxide formation also shifted anodically with increasing loading, their results showed that the peak potential of methanol oxidation strongly depends on the formation of Pt oxide. Hence, they concluded that the maximum activity is determined by the properties of the Pt surface. Tang *et al.*[10] investigated the effect of loading of Pt deposited

on a graphite electrode and on graphitic nanofibers by cyclic voltammetry. The mass activity for methanol oxidation on Pt on nanofibers increased up to a loading of 180 μg cm^{-2} and then decreased for higher loadings. They explained such results by the accumulation of Pt and a decrease of the valuable Pt surface for methanol oxidation. However, for the same range of loadings, the mass activity for methanol oxidation on Pt deposited on a graphite electrode only increased. According to the authors, the particle size and dispersion of Pt deposits are important factors determining the activity of a catalyst. Duarte *et al.*[11] used the potential step method to deposit Pt on glassy carbon, graphite fibers and graphite cloth. Pt on glassy carbon exhibited the highest activity for methanol oxidation. On these electrodes, a pronounced increase of the Pt surface area with loading up to 30 μg cm^{-2} was observed, while loadings higher than 50 μg cm^{-2} had a small effect on the surface area of Pt. The increase of activity with increasing mass specific surface area was explained by the reduction of the particle size. The effect of particle size on the activity for methanol oxidation was pointed out also by Frelink *et al.*[12] These authors used different methods as well as variations of a single method to prepare Pt catalysts supported on carbon black with loading of 3.5 to 5.5 % of platinum with a particle size in the range 1.2 to 7.8 nm. They found a decrease of the activity for methanol oxidation activity with decreasing particle size from 4.5 to 1.2 nm but for particles larger than 4.5 nm, the activity remained almost constant. According to the authors, the dependence of the activity on the size of the Pt particles could be explained either by the particle size effect on the formation of adsorbed hydroxyl species or its effect on the number of methanol adsorption sites. Yahikozawa and coworkers[13] studied methanol oxidation on a Pt catalyst vacuum evaporated on glassy carbon with a particle size of 3.8 and 5.3 nm. The decrease of the activity for methanol oxidation with decreasing particle size was related to the existence of some oxide layer on the surface closely related to the exposed crystal planes. Examining methanol oxidation on carbon black supported Pt catalyst with 10 and 60 wt. % of platinum and particles of 2.0 and 8.8 nm respectively, Park *et al.*[14] also observed a particle size dependent electrocatalytic effect. The decrease of the activity on decreasing the particle size to below 4 nm, was explained by a decrease of contiguous Pt sites ("ensemble effect") needed for dehydrogenation of methanol to form CO. Scheijan *et al.*[15] also attributed the decrease of activity with decreasing particle size to a decrease in the number of Pt ensemble sites available for adsorption and decomposition of methanol. However, they examined this reaction using Pt catalysts with particles ranging from 10–20 and 10–120 nm and also a full monolayer of Pt and concluded that the shape and the morphology rather than size of the particles played predominant roles in the reaction kinetics.

Despite the differences in the hitherto reported results, all the authors suggested that the change of activity of the catalyst is mainly based on the particle size.

In this work, the influence of surface morphology of platinum deposited on glassy carbon support by the potential step method on methanol oxidation was studied.

EXPERIMENTAL

Platinum was deposited on two glassy carbon (GC) (Sigradur–Sigri, Elektrographite, GmbH, Germany) disc electrodes with different geometric area (A_{GC}): 0.21 (GC_I) and 0.39 cm^2 (GC_{II}).

The GC electrode surfaces were refreshed before each deposition of platinum, by abrasion with emery paper of decreasing grain size followed by polishing with alumina of 1, 0.3 and 0.05 μm particle size. The final cleaning of the electrodes was performed in high purity water (Millipore 18 MΩ cm) in an ultrasonic bath.

Before each deposition of platinum, a cyclic voltammogram of the GC electrode was recorded in 0.10 M NaOH solution or in 0.50 M H_2SO_4 (potential range –0.20 V to 1.4 V, sweep rate 50 mV s^{-1}), to ensure that the GC surface was clean and free of Pt from the previous experiment.

Platinum was electrodeposited on glassy carbon by the potential step method in deoxygenated 0.50 M H_2SO_4 + 6.0 mM H_2PtCl_6. A potential perturbation from 0.06 V to 0.36 V was applied after 0.5 s at the initial potential. Platinum was deposited under the same conditions in each experiment but with loadings (W_{Pt}) from 10 to 80 μg cm^{-2}. The amount of platinum deposited was estimated from the charge calculated by integrating the *I–t* transient. After deposition, the electrode was thoroughly rinsed with high-purity water and transferred to the cell containing 0.10 M NaOH or 0.50 M H_2SO_4. The real surface area of platinum deposited, A_{Pt} (cm_R^2), was estimated from the hydrogen adsorption/desorption region of the basic voltammogram (integrated part of the CV was in the potential range from 0.06 V to 0.45 V with a correction for a double layer charging). The specific catalyst area S_{Pt} (m^2 g^{-1}) was calculated from the equation: $S_{Pt} = 100A_{Pt}/(A_{GC}W_{Pt})$.[16]

The electrocatalytic activity of the GC/Pt electrodes for methanol oxidation was studied in 0.10 M NaOH + 0.50 M CH_3OH and in 0.50 M H_2SO_4 + 0.50 M CH_3OH solutions. Methanol was added to the solution while holding the electrode potential at 0.06 V. The potential was cycled between 0.06 V and 1.3 V with sweep rates of 50 and 1.0 mV s^{-1}.

The employed reagents were of p.a. purity, and the solutions were prepared with high purity water (18 MΩ cm). The electrolytes were purged with purified nitrogen prior to each experiment.

All electrochemical experiments were performed at room temperature in a standard three-electrode/three-compartment glass cell. The counter electrode was a Pt wire while a bridged saturated calomel electrode (SCE) was used as the reference electrode. However, all potentials are given *versus* the reversible hydrogen electrode (RHE). The electronic equipment in all of the experiments consisted of a PAR Model 273 potentiostat and Philips Model 8033 *X–Y* recorder.

GC_{II}/Pt electrodes with different loadings were characterized at room temperature in air by atomic force (AFM) and scanning tunneling microscopy (STM) techniques. The structural characterization was performed with a NanoScope III A (Veeco, USA) microscope. The AFM observations were performed in the contact mode using NanoProbes silicon nitride cantilevers with a force constant 0.06 N m^{-1}. The STM images were obtained in the height mode using a Pt–Ir tip (set-point current, i_t: from 1 to 2 nA; bias voltage, V_b: –300 mV).

RESULTS

AFM and STM

The AFM and STM techniques were used for the characterization of GC/Pt electrodes with different loadings. The AFM images (Fig. 1) reveal the topography of the glassy carbon electrodes with platinum deposited on the surface in the form of large 3D agglomerates of lateral size ranging from 100 to 700 nm. Increasing the loading leads to an increase in the number and predominant size of the agglomerates, their closer proximity and pronounced coalescence. Agglomerates composed of Pt particles were also observed in STM images by Duarte *et al.*[11] and Gloaguen *et al.*[16] Their formation can be explained by nucleation and growth of the Pt electrodeposits. According to Gloaguen *et al.,*[16] at very beginning of the electrodeposition process (t < 0.3 s), a large number of nano-sized

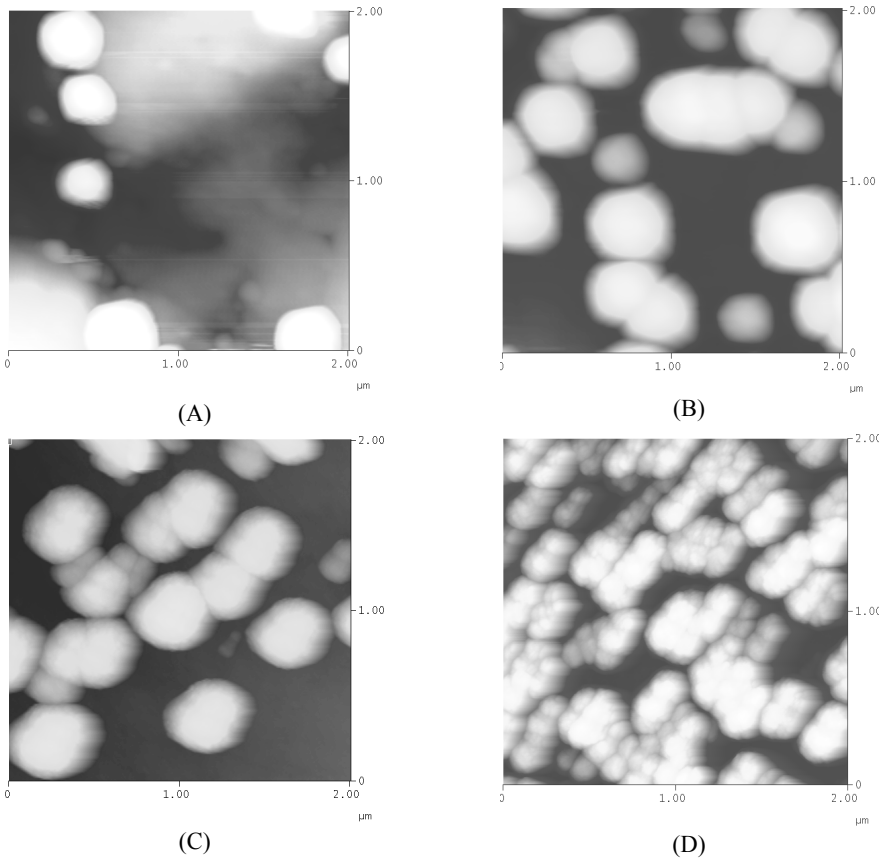

Fig. 1. AFM Images (2.00×2.00 µm^2) of the GC/Pt, with low loadings of 11.9 (A), 28.9 (B), 49.8 (C) and 72.3 µg cm^{-2} (D).

particles is formed and they might be mobile and assemble in Pt agglomerates. The number as well as the size of the particles increases during deposition. The first process is predominant at short times of deposition, while the other prevails at longer times.

The STM images of the Pt agglomerates (Fig. 2) show that they consisted of spherical nanoparticles of platinum. The size distributions of the particles for the examined loadings, ascertained from the STM images,[17] are given in Table I. Increasing the Pt loading led to an increase of the particle size, their distribution and density. The Pt particles were rather loose at the lowest loading, becoming closely packed at the highest one.

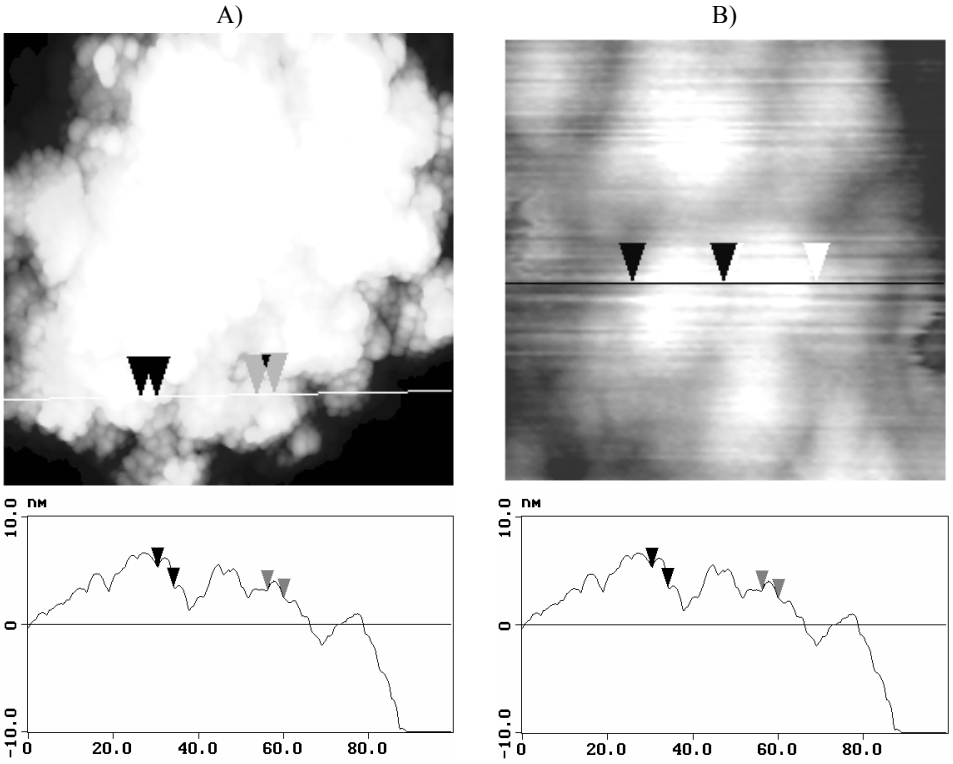

Fig. 2. STM Images (125×125 nm^2) of the GC/Pt with a low loading of 11.9 μg cm^{-2} (A) and a high loading of 49.8 μg cm^{-2} (B).

TABLE I. Pt particle size for GC_{II}/Pt electrodes with different Pt loadings

Loading, W_{Pt} / μg cm^{-2}	11.9	21.1	28.9	49.8	72.3
Particle size, d / nm	4.4±0.7	8.9±1.6	10.6±2.3	36.1±5.3	52.4±11.1

Electrochemical characterization

Platinum was deposited on two samples of glassy carbon (GC_I and GC_{II}) under the same conditions with loading ranging from 10–80 μg cm^{-2}. Typical cyclic voltammograms of a GC_I/Pt electrode in 0.10 M NaOH and of a GC_{II}/Pt in 0.50 M H_2SO_4 are shown in Figs. 3A and 3B, respectively. They resemble the corresponding voltammograms for smooth platinum with well defined hydrogen adsorption/desorption region (from 0.06 V to 0.40 V), separated in sulfuric acid (Fig. 3B) from the region of surface oxide formation at higher potentials by a double layer charging/discharging region. In alkaline solution (Fig. 3A) the hydrogen desorption is followed by reversible OH^- adsorption (0.40 V < E < 0.75 V) and irreversible oxide formation at potentials higher than 0.75 V. The potentials of all the anodic and cathodic peaks remained the same regardless of the loading. The ratio between the peak heights for strongly (h_{Ps}) and weakly (h_{Pw}) bound hydrogen, remained almost constant for all the examined electrodes (inserts in Fig. 3).

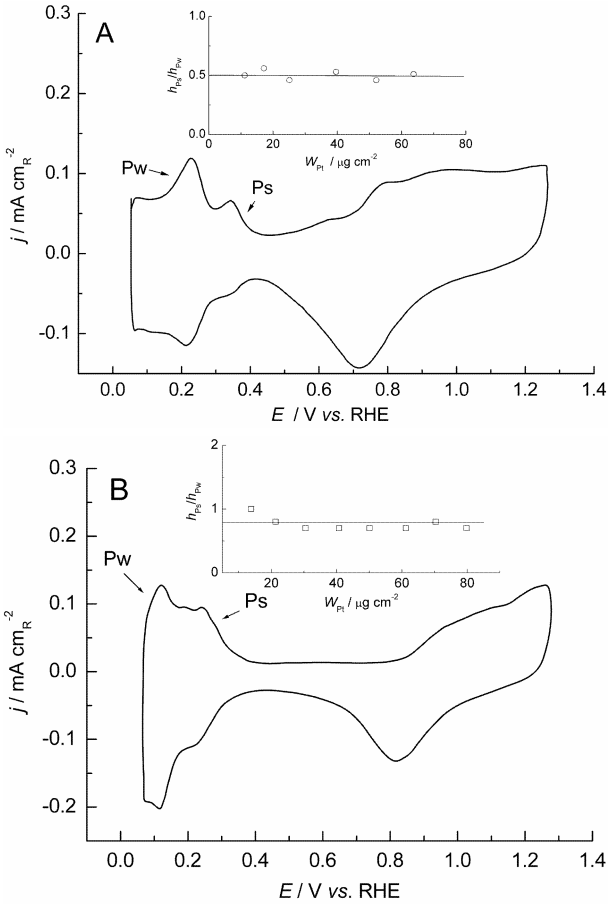

Fig. 3. Cyclic voltammograms of GC/Pt electrodes in 0.10 M NaOH (A) and 0.50 M H_2SO_4 (B), sweep rate 50 mV s^{-1}. Insets: the dependence of the ratio of the peak heights, h_{Ps}/h_{Pw}, on the loading for all the GC/Pt electrodes.

The real surface area of the platinum catalysts (A_{Pt}), determined from the hydrogen adsorption/desorption charge, is plotted *versus* the loading in Fig. 4. The Pt real surface area initially increased with loading but at higher loadings remained nearly constant. A similar dependence of the Pt surface area with loading was found by Duarte *et al.*[11] The difference in the surface areas of the Pt particles deposited on the GC_I and GC_{II} supports arises from the different geometric area of the glassy carbon substrates and the non-homogeneity of this material and is in accordance with literature data.[18]

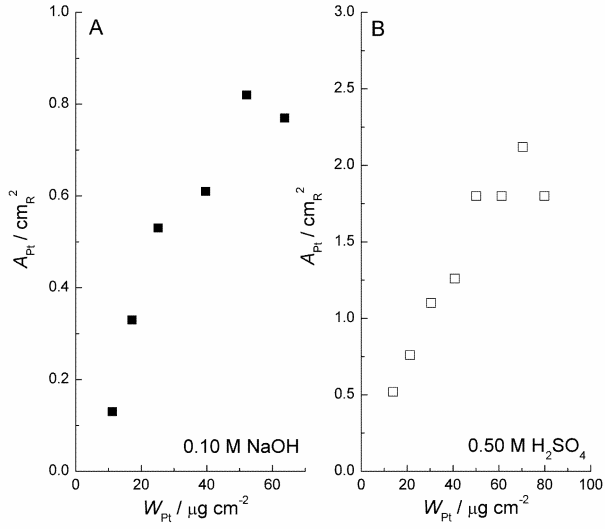

Fig. 4. The dependence of the real surface area (A_{Pt}) on the loading of Pt deposited on the smaller GC_I (A) and larger GC_{II} (B) substrate.

The dependence of the specific catalyst area (S_{Pt}) on the loading is depicted in Fig. 5. The specific catalyst area generally decreases with the loading. This trend is more pronounced at the higher loadings (Figs. 5A and 5B), which is in accordance with reported data.[8,9,11,19] However, for the electrode with the support of smaller geometric area examined in alkaline solution (Fig. 5A), the dependence attained a maximum at ≈ 25 μg cm^{-2}, was followed by decrease in S_{Pt}. An initial increase in S_{Pt} at low loadings was shown by Mikhaylova *et al.*[8] and considered as deviations from the regularity attributed to inaccuracies in the determination of the real surface area, A_{Pt}, of small deposits. Although this possibility cannot be neglected, based on the presented results, we are of the opinion that this initial increase in S_{Pt} of the studied GC/Pt electrodes might be related to the conditions of the Pt electrodeposition. In the region of small loadings, *i.e.*, short deposition times, the Pt agglomerates were smaller, well separated and their number increased with the amount of Pt, resulting in the increase of the specific surface. Longer times of deposition favor the growth of Pt crystals relative to nuclei formation. Consequently, the deposition of Pt at higher loadings results in the increased growth of the Pt forms, their higher concentration and closer pro-

ximity at the same geometric surface and in a decrease of the specific area of Pt because the ratio of the surface to bulk atoms decreases. This might be the reason why the dependence of the specific area on the loading exhibited a maximum.

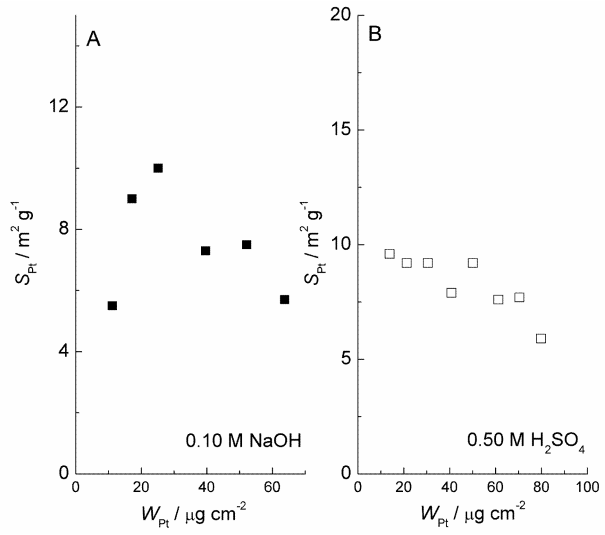

Fig. 5. The dependence of the specific catalyst area (S_{Pt}) upon the loading of Pt deposited on the smaller GC_I (A) and larger GC_{II} (B) substrate.

Methanol oxidation

The influence of the loading, *i.e.*, surface morphology, of the GC/Pt electrodes on their electrocatalytic activity for methanol oxidation was studied in 0.10 M NaOH and in 0.50 M H_2SO_4.

Methanol oxidation under potentiodynamic conditions at GC/Pt electrodes with a loading of ≈ 30 μg cm^{-2} in 0.10 M NaOH and 0.50 M H_2SO_4 is shown in Figs. 6A and 6B, respectively. Methanol oxidation commences at the onset of OH anion adsorption (Fig. 3A) and proceeds on the surface covered by reversible OH_{ad} species. The maximum of the current is attained at potentials (E ≈ 0.85 V) where the rate of methanol dehydrogenation and the rate of oxidation of the dehydrogenated product by OH_{ad} species are in balance.[20]

The coverage of the GC_{II}/Pt electrode with adsorbed organic species, calculated from the hydrogen adsorption/desorption region in the presence and in the absence of methanol, given as the covered area is depicted in Fig. 7. As can be seen, the coverage initially increases with increasing loading, reaches a maximum and then decreases at higher Pt loadings. It should be mentioned here that such a dependence was not obtained for the GC_I/Pt electrode with a smaller geometric surface used in alkaline solution because of the scattered data for the calculated area. This might be explained by the possibility that OH adsorption, to a certain extent, overlaps with H adsorption in alkaline solutions.[21]

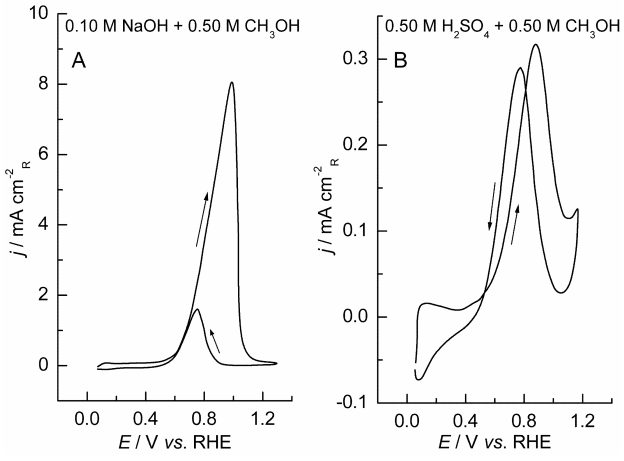

Fig. 6. Cyclic voltammograms of the GC/Pt electrodes in 0.10 M NaOH + 0.50 M CH_3OH (A) and 0.50 M H_2SO_4 + 0.50 M CH_3OH (B); sweep rate 50 mV s^{-1}.

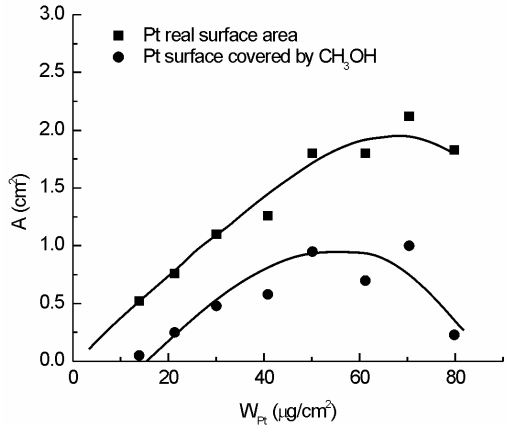

Fig. 7. The dependence of Pt surface area covered by adsorbed organic particles in 0.50 M H_2SO_4 + 0.50 M CH_3OH on the loading. The real Pt surface area, A_{Pt}, is given for comparison.

The electrocatalytic activity of the GC/Pt electrodes for methanol oxidation was considered under potentiostatic conditions, as the activities observed under potentiodynamic measurements are transient in nature. Tafel plots, recorded using linear sweep voltammetry at 1.0 mV s^{-1}, are presented in Fig. 8. Well defined straight lines with the Tafel slopes of approximately 100 mV dec^{-1} in NaOH (Fig. 8A) and 80 mV dec^{-1} in H_2SO_4 (Fig. 8B) were obtained at all loadings. However, a decrease of activity of the GC/Pt electrode with higher Pt loadings was clearly observed in both cases.

The dependences of the specific and mass activity (at 0.62 V) on the loading of the GC/Pt electrodes are shown in Figs. 9 and 10, respectively. Inspection of these figures revealed that the activity increased, reached a maximum and then decreased as the loading increased. A maximum activity for this reaction in acid solution at supported platinum catalysts *versus* the specific catalyst area was also described by Umeda *et al.*[9] and Attwood *et al.*[18] The results of Frelink *et al.*[12]

for the same reaction showed a slight maximum of the specific activity with particle size but when the mass activity of the same electrode was plotted *versus* the particle size such a maximum was not found. Comparing their results with those of Attwood and coworkers,[18] the authors concluded that the preparation method could have a considerable influence on the behavior of the Pt catalysts. It should be mentioned that all these authors used different methods for the chemical deposition of Pt. On the other hand, the activity of Pt electrodeposited on GC either increased with loading[8] or showed a maximum at much higher loadings if the Pt was deposited on nanofibers.[10]

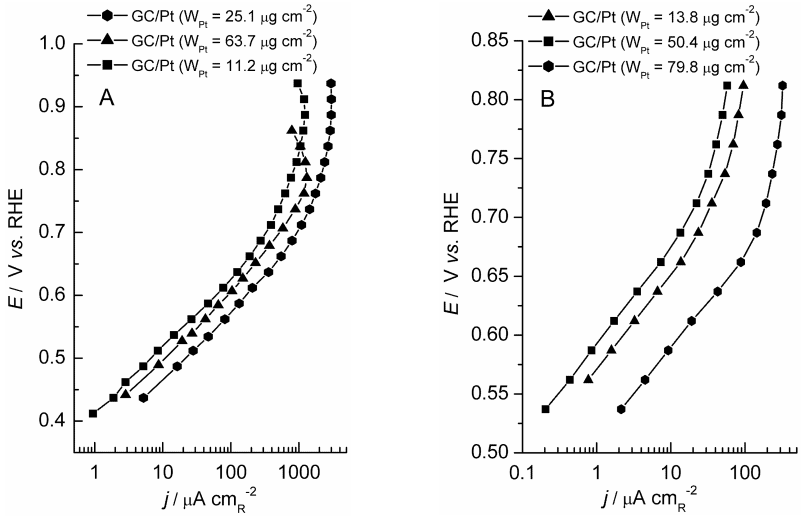

Fig. 8. Tafel plots for the oxidation of 0.50 M CH_3OH on the GC/Pt electrodes in 0.10 M NaOH (A) and 0.50 M H_2SO_4 (B).

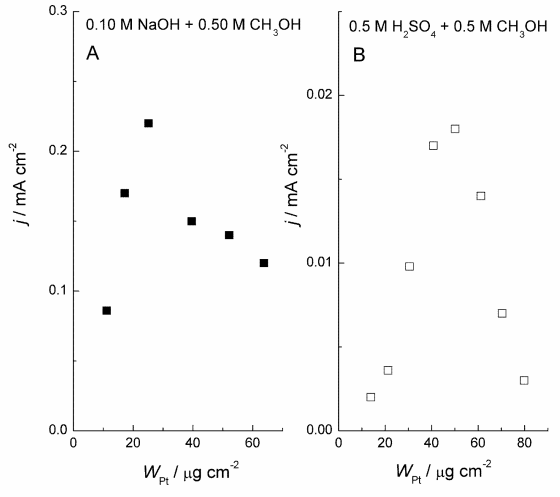

Fig. 9. The specific activity for methanol oxidation *versus* loading of the GC/Pt electrodes in 0.10 M NaOH (A) and 0.50 M H_2SO_4 (B).

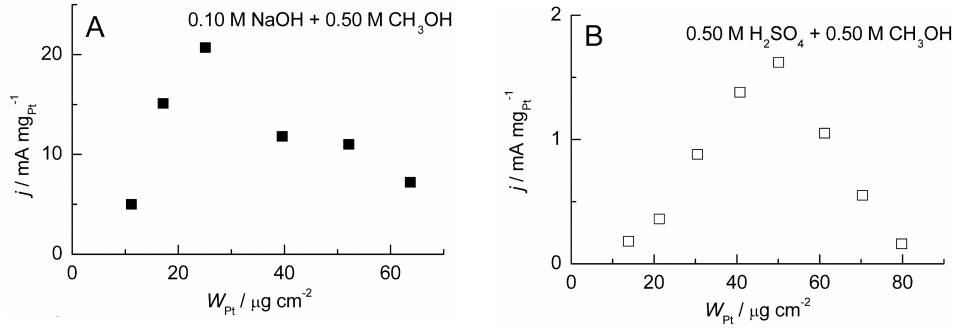

Fig. 10. The mass activity for methanol oxidation *versus* loading of the GC/Pt electrodes in 0.10 M NaOH (A) and 0.50 M H_2SO_4 (B).

DISCUSSION

The activity of the GC/Pt electrodes depended generally on the Pt loading in both solutions (Figs. 8–10), increasing at lower loadings, reaching a maximum at ≈ 30 and ≈ 50 μg Pt cm^{-2} in alkaline and acidic solutions, respectively, and then decreasing rapidly with further increase of the loading.

Activity of GC/Pt catalysts in methanol oxidation has mostly been related to the particle size effect and discussed in the numerous papers.[9–25] Basically, the particle size effect assumes that the activity of the electrode is determined by the number of contiguous sites available for methanol adsorption.[14] In this sense, the higher the number of correspondingly arranged sites is, the higher is the activity. Accordingly, the increase of activity up to the maximum value (Figs. 8–10) could be attributed to the increase of the Pt particle size. However, further increase of loading leading to a decrease of the activity of the catalyst, being not in accordance with the particle size effect, clearly indicates to the importance of the surface morphology.

AFM and STM images of GC/Pt electrodes obtained under conditions of lower loadings (Figs. 1A, 1B and 2A) show that the Pt was deposited in the form of randomly distributed, mostly well separated agglomerates consisting of small, rather loose particles. This surface morphology remains unaffected significantly by increasing of particle size with loading (Fig. 1B). In the range of lower loadings, the real surface area increases (Fig. 4) as well as the specific catalyst area of Pt deposited on the smaller support (Fig. 5A), while the specific catalyst area of Pt on the larger support remains almost unchanged, probably due to the non-homogeneity of the glassy carbon with different geometric areas. The maximum activity for methanol oxidation in both solutions (Figs. 8–10) was exhibited by electrodes with a high value of the real surface area and the maximum value of the specific catalyst area (Figs. 4 and 5), suggesting clearly that the corresponding surface morphology provides the high number of contiguous sites available

for the reaction. On the other hand, it suggests also that particle size effect, operative under the conditions of lower loadings should be related to the surface morphology.

It should be noted that any significant changes concerning the hydrogen adsorption/desorption or Pt oxide formation/reduction on the basic voltammograms, as well as the peak position on the cyclic voltammograms for methanol oxidation, usually observed with a change of particle size,[9,12,13,20,21] were not detected (Figs. 3 and 6). Most likely this was caused by the rather wide particle size distribution in each loading and the overlapping of the same particle sizes in two loadings (Table 1).

Increasing of Pt loading altered the surface morphology leading to the deposition of predominantly larger agglomerates with increased particle size, their higher density, closer proximity and even coalescence (Figs. 1C, 1D and 2B). Simultaneously, the real surface area remained almost constant due to the saturation of the substrate with Pt. Consequently, the specific catalyst area decreased due to the diminishing ratio of surface to bulk atoms. Such a change of the parameters cannot explain the decrease of the catalytic activity. However, the surface morphology under conditions of high loadings, which indicates the existence of different defects caused by the close proximity and coalescence of agglomerates and particles, could help in the solution of this problem.

The presence of defect sites related to steps and grain boundaries which interconnect nanoparticles into complex structure was postulated by Millard *et al.*[26] and Cheristiouk *et al.*[27] As the number of defects increases with the enhancement of Pt loading, due to the increase of particle coalescence, the ratio between facets, *i.e.*, flat surface domains, and defects increases in favor of defects, leading to a diminishing of the Pt contiguous sites available for methanol adsorption. This view is supported by the fact that the coverage of GC_{II}/Pt electrode with adsorbed organic species increased parallel with increasing real surface area up to a loading corresponding to the maximum activity and then decreased (Fig. 7), while the real surface area remained practically constant.

CONCLUSIONS

The activities of GC/Pt electrodes in the oxidation of methanol in both acidic and alkaline solutions exhibit an volcano dependence with respect to the platinum loading.

The activity increases in the range of lower loadings following the particle size effect as the Pt particles are distributed in mostly well separated agglomerates, which provides for a high number of contiguous sites for methanol adsorption. The activity decreased in the range of high loadings when different defects were formed due to the close proximity and coalescence of the Pt particles. Decreasing of the ratio between the flat surface domains and the defects in favor of

the defects with increasing Pt loading leads to a diminishing number of contiguous sites for methanol adsorption.

Finally, it could be concluded that the activity of the catalyst cannot be explained exclusively by particle size effect without relating this effect to surface morphology.

Acknowledgements. The authors are pleased to acknowledge the financial support provided by Ministry of Science and Ecology of Serbia (project No. 142056).

ИЗВОД

УТИЦАЈ ПОВРШИНСКЕ МОРФОЛОГИЈЕ НА ОКСИДАЦИЈУ МЕТАНОЛА НА ПЛАТИНСКИМ КАТАЛИЗАТОРИМА СА ПОДЛОГОМ ОД СТАКЛАСТОГ УГЉЕНИКА

С. СТЕВАНОВИЋ[1], Д. ТРИПКОВИЋ[1], А. KOWAL[2], Д. МИНИЋ[3], В. М. ЈОВАНОВИЋ[1] и А. ТРИПКОВИЋ[1]

[1] ИХТМ – Центар за електрохемију, Универзитет у Београду, Његошева 12, п. пр. 473, 1100 Београд,
[2]Institute of Catalysis and Surface Chemistry, Polish Academy of Science, Krakow, Niezapominajek 8, 30-239, Poland и [3]Факултет за физичку хемију, Универзитет у Београду, Студентски трг 12, 1100 Београд

Платина исталожена на стакласти угљеник (GC) коришћена је као модел систем за испитивање утицаја морфологије површине Pt катализатора за реакцију оксидације метанола у алкалним и киселим растворима. Платина је таложена потенциостатском пулсном методом на GC подлогу из $H_2SO_4 + H_2PtCl_6$ раствора под истим условима у количини од 10 то 80 μg cm^{-2}. АФМ и СТМ слике GC/Pt електрода показују да је Pt исталожена у облику 3D агломерата који се састоје од сферних честица. Дуже време таложења доводи до повећаног раста Pt форми и смањења специфичне површине наталожене платине. Реална површина исталожене платине расте са повећањем количине исталожене платине достижући плато. Без обзира на ово, специфична и масена активност платине исталожене на стакласти угљеник за оксидацију метанола како у киселим тако и у алкалним растворима показује вулканску зависност од количине исталожене платине. Повећање активности се може објаснити преко повећања величине честица са количином исталожене платине, односно преко повећања суседних Pt места доступних за адсорбцију и декомпозицију метанола. Међутим, смањење каталитичке активности са даљим повећањем количине исталожене платине и величине њених честица након постигнутог максимума је повезано са смањењем броја активних места доступних за адсорпцију метанола и резултат је смањења растојања и израженог стапања Pt честица.

(Примљено 20. децембра 2007, ревидирано 14. марта 2008)

REFERENCES

1. T. Iwasita, *Electrochim. Acta* **47** (2002) 3663
2. M. W. Breiter, *Electrochemical Processes in Fuel Cells*, Springer-Verlag, Berlin, 1969
3. B. Beden, F. Hahn, C. Lamy, J. M. Leger, N. R. Tacconi, R. O. Lezna, A. J. Arvia, J. *Electroanal. Chem.* **261** (1989) 401
4. X. H. Xia, T. Iwasita, F. Ge, W. Vielstich, *Electrochim. Acta* **41** (1996) 711
5. R. Adzić, A. V. Tripković, W. O'Grady, *Nature* **296** (1982) 137
6. B. Ren, X. Q. Li, C. X. She, D. Y. Wu, Y. Q. Tian, *Electrochim. Acta* **46** (2000) 193
7. B. Beden, F. Hahn, C. Lamy, J. M. Leger, C. L. Perdriel, N. R. De Tacconi, R. O. Lezna, A. J. Arvia, *J. Electroanal. Chem.* **301** (1991) 129

8. A. A. Mikhaylova, O. A. Khazova, V. S. Bagotzky, *J. Electroanal. Chem.* **480** (2000) 225
9. M. Umeda, M. Kokubo, M. Mohamedi, I Uchida, *Electrochim. Acta* **48** (2003) 1367
10. H. Tang, J. Chen, L. Nie, D. Liu, W. Deng, Y. Kuang, S. Yao, *J. Colloid Interface Sci.***269** (2004) 261
11. M. M. E. Duarte, A. S. Pilla, J. M. Sieben, C. E. Mayer, *Electrochem. Commun*. **8** (2005) 159
12. T. Frelink, W. Visscher, J. A. R. van Veen, *J. Electroanal .Chem.* **382** (1995) 65
13. K. Yahikozawa, Y. Fujii, Y. Matsuda, K. Nishimura, Y. Takasu, *Electrochim. Acta* **36** (1991) 973
14. S. Park, Y. Xie, M. Weaver, *Langmuir* **18** (2002) 5792
15. F. J. E. Scheijen, G. L. Beltramo, S. Hoeppener, T. H. M. Housmans, M. T. M. Koper, *J. Solid State Electrochem.* **12** (2008) 483
16. F. Gloaguen, J. M. Leger, C. Lamy, A. Marmann, U. Stimming, R. Vogel, *Electrochim. Acta* **44** (1999) 1805
17. D. Tripković, S. Stevanović, A. Tripković, A. Kowal, V. M. Jovanović, *J. Electrochem. Soc.* **155** (2008) B281
18. P. A. Attwood, B. D. McNicol, R. T. Short, *J. Appl. Electrochem.* **10** (1980) 213
19. Y. M. Maksimov, B. I. Podlovchenko, T. L. Azarchenko, *Electrochim. Acta* **43** (1998) 1053
20. A. V.Tripković, K. Dj. Popović, J. D. Lović, V. M. Jovanović, A.Kowal, *J. Electroanal. Chem.* **572** (2004) 119
21. J. S. Spendelow, J. D. Goodpaster, P. J. A. Kenis, A. Wieckowski, *Langmuir* **22** (2006) 10457
22. A. Stoyanova, V. Naidenov, K. Pertov, I. Nikolov, T. Vitanov, E. Budevski, *J. Applied Electrochem*. **29** (1999) 1197
23. Y. Takasu, T. Iwazaki, W. Sugimoto, Y. Murakami, *Electrochem. Commun*. **2** (2000) 671
24. S. Terzić, D. Tripković, V. M. Jovanović, A. Tripković, A. Kowal, *J. Serbian Chem. Soc.* **72** (2007) 165
25. A. V. Tripković, S. Lj. Gojković, K. Đ. Popović, J. D. Lović, *J. Serb. Chem. Soc.* **71** (2006) 1333
26. F. Millard, S. Schreier, M. Hanzlik, E. R. Savinova, S. Weinkauf, U. Stimming, *Phys. Chem. Chem. Phys.* **7** (2005) 385
27. V. Cheristiouk, P. A. Simonov, E. R. Savinova, *Electrochim. Acta* **48** (2003) 3851.

www.shd.org.rs

Journal of the Serbian Chemical Society

JSCS@tmf.bg.ac.yu • www.shd.org.rs/JSCS

J. Serb. Chem. Soc. 73 (8–9) 861–870 (2008)
JSCS–3768

UDC 669.1–492.2+66.087:541.135–32
Original scientific paper

Electrodeposition of Fe powder from acid electrolytes

VESNA M. MAKSIMOVIĆ[1]*, LJUBICA J. PAVLOVIĆ[2#], BORKA M. JOVIĆ[3#] and MIOMIR G. PAVLOVIĆ[2#]

[1]*Institute of Nuclear Sciences Vinča, University of Belgrade, P.O. Box 522, 11000 Belgrade,* [2]*Institute of Electrochemistry ICTM, University of Belgrade, Njegoševa 12, 11000 Belgrade, and* [3]*Institute for Multidisciplinary Research, P.O. Box 33, 11030 Belgrade, Serbia*

(Received 17 December 2007, revised 27 February 2008)

Abstract: Polarization characteristics of the electrodeposition processes of Fe powders from sulfate and chloride electrolytes and the morphology of the obtained powders were investigated. The morphology depended on the anion presence in the electrolyte but not on the current density in the investigated range. A characteristic feature of the dendritic powder with cauliflower endings obtained from sulfate electrolyte is the presence of cone-like cavities and the crystallite morphology of the powders surface. On the other hand, Fe powders electrodeposited from chloride electrolyte appear in the form of agglomerates. A soap solution treatment applied as a method of washing and drying provides good protection from oxidation of the powders.

Keywords: Fe powder; morphology; polarization diagrams.

INTRODUCTION

By the electrochemical classification of metals, transition metals such as Fe, Ni and Co belong to the "inert metal" group, with a small exchange current density, j_0, and a high overpotential of electrodeposition, η.[1,2] All polarization diagrams recorded during the electrochemical deposition of metals and alloy powders of the Fe group are distinguished through the following phenomena: a) the deposition of powders (as well as compact metal) is accompanied by the simultaneous evolution of hydrogen from the very beginning of metal deposition. In this situation, a plateau corresponding to the limiting current density cannot be registered on the polarization diagram, as is the case with copper,[3] b) all of the polarization diagrams corrected for the *IR* drop are characterized by the presence of two inflexion points, *i.e.*, the first inflection corresponds to the beginning of metal deposition, which is then followed by a rapid rise of the current density, where-

* Corresponding author. E-mail: vesnam@vin.bg.ac.yu
# Serbian Chemical Society member.
doi: 10.2298/JSC0809861M

as the second inflection characterizes the start of a linear change of current density with potential. This deviation from linearity demonstrates a change of the mechanism of metal deposition.[4,5]

Fe powder is an important raw material, which is widely used in the manufacture of porous metallo–ceramic bearings, friction materials, parts for machinery, for production of various alloys, in the chemical industry for the fabrication of rechargeable batteries, *etc*.[6] The physical and chemical characteristics of Fe determine its peculiar electrochemical behavior. Almost all data concerning the electrodeposition of Fe powders were summarized by Calusaru.[6] A literature survey of the electrodeposition of Fe powders shows that mainly two types of electrolytes were investigated and these were based on sulfate[6–11] and chloride electrolytes.[6,12] In all the reported cases, the morphology of the deposited powders was dendritic.[8,13] With increasing duration of electrolysis, the dendrites merge, which is unacceptable for the further application of such deposits as they must be ground in order to obtain powders. However, in the range of lower acidity, the deposits become powdery and, in some cases, may be spongy and sticky. Generally, the hitherto research indicates that there are two steps in the electrodeposition of Fe powders, deposition of a fragile film followed by grinding.[14–16] It should be emphasized that we successfully attempted to obtain powdery Fe powders without the grinding process.

Fe powders have a very high tendency to corrosion. The wet electrolytic product contains over 99 % Fe, while the washed and dried powders may contain several percent of oxide.[8] Kuzmin and Kiseleva[8] demonstrated a marked influence of pH on the content of oxide in Fe powders electrodeposited from sulfate electrolytes. Fe(II)-based electrolytes were investigated within the pH range 1.5–4.2. The oxide content depended not only on the amount of hydroxides formed during deposition, but also on the amount of powder oxidized during washing and drying. It is noteworthy that the lower the pH, the much lower was the oxide content.

The aim of this work was to investigate the polarization characteristics of the processes of the electrodeposition of Fe powders from sulfate and chloride electrolytes and the morphologies of the obtained powder as a function of the type of electrolyte and current density. X-Ray diffraction analysis was performed in order to check the quality of the selected way of stabilization of the Fe powders.

EXPERIMENTAL

Polarization diagrams were recorded in a three-compartment standard electrochemical cell at room temperature. The Pt-foil counter electrode and the reference saturated silver|silver chloride (Ag|AgCl) electrode were placed in separated compartments. All solutions were prepared from analytical grade chemicals and distilled water. Polarization measurements were performed using a computer-controlled potentionstat (PAR M273A) and corrosion software (PAR M352/252, Version 2.01) at a sweep rate of 1.0 mV s^{-1}. To obtain polarization curves corrected for the *IR* drop, the current interrupt technique was used with a current interruption time of 0.5 s.

All powder samples were electrodeposited at the room temperature in a cylindrical glass cell of total volume 3 dm^3 with a cone-shaped bottom for the collection of the powder particles. The working electrode was a glassy carbon rod with a total surface area of 1.45 cm^2 immersed in the solution and placed in the middle of the cell.

Pure metal powders were electrodeposited from solutions containing either 70 g dm^{-3} $FeSO_4$ + 133 g dm^{-3} $(NH_4)_2SO_4$ or 50 g dm^{-3} $FeCl_2$ + 105 g dm^{-3} NH_4Cl. The deposition time was 5.0 min. The pH of the investigated solutions was varied from 1.3 to 1.6.

The wet powder was washed several times with a large amount of demineralized water until the wet powder was free from traces of acid. All the time, the powder was submersed in water to prevent oxidation. To inhibit oxidation in air, sodium soap Sap G-30, which contains 78 % of total fatty acids, was added as an additive to the water used for washing the Fe powder. The powder was then dried in the a furnace under a controlled nitrogen atmosphere at 100 °C.[17]

The morphology of the electrodeposited powders was examined using a Jeol T-20 scanning electron microscope, SEM.

The phase structure of the powders was investigated using a Philips PW 1050 X-ray powder diffractometer.

RESULTS AND DISCUSSION

It is well-known that the deposition of powders (as well as compact metal) of the Fe group is accompanied by the simultaneous evolution of hydrogen from the very beginning of metal deposition. A selection of the polarization diagrams for the process of electrodeposition of Fe powders from chloride electrolyte, the polarization curve for the electrodeposition of Fe powder measured with correction for the *IR* drop (Fe + H_2), the polarization curve for hydrogen evolution (H_2) and the polarization curve for Fe powder electrodeposition after subtraction of j_{H_2} (Fe) are shown in Fig. 1a. The current for hydrogen evolution was obtained using the equation for the Faraday law[18] applied to the process of gas evolution:

$$I_{H_2} = \frac{nFV_0}{tV_n} \tag{1}$$

where V_0 is the experimentally determined volume of evolved hydrogen at p_{at} and T = 298 K corrected to normal conditions ($p^{\ominus}$ and T = 273 K), t the time of hydrogen evolution at a constant current, V_n the volume of 1 mol of hydrogen at normal conditions (22.4 dm^3 mol^{-1}), n the number of exchanged electrons and F is the Faraday constant. After subtracting the obtained values from the total current densities (Fe + H_2), the values corresponding to the deposition of pure iron (Fe) were obtained. All polarization diagrams are characterized by the presence of two inflection points.

The current efficiency for the electrodeposition process was obtained from the relation:

$$\eta_j(\%) = 100\frac{j_{Fe/SO_4^{2-}}}{j_{tot}} = 100\frac{j_{tot} - j_{H_2}}{j_{tot}} \tag{2}$$

The corresponding values of the current efficiency are shown in Fig. 1b. As can be seen at the beginning of the electrodeposition process significant amount of hydrogen is evolving, causing the value of the current efficiency of about 30 %. At more negative potentials this value increases to about 55 % and further the sharp decrease is taking place in the region of the sharp increase in current density to about more then 30 %.

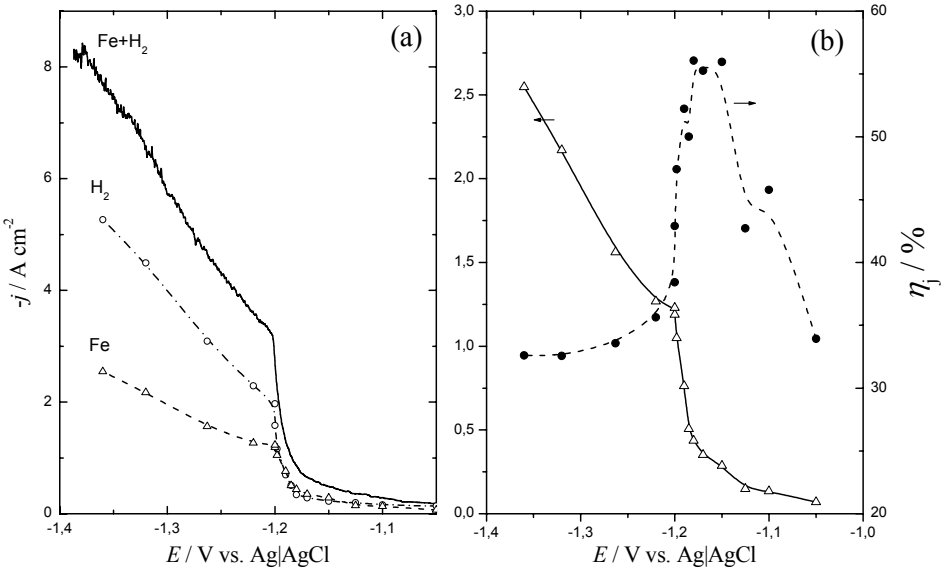

Fig. 1. (a) Polarization curve for the electrodeposition of Fe powder from the chloride electrolyte measured with *IR* drop correction (solid line Fe + H_2), (○) polarization curve for hydrogen evolution (dashed–dotted line, H_2) and (Δ) polarization curve for Fe powder electrodeposition after subtraction of j_{H_2} (dashed line, Fe); (b) polarization curve for Fe powder electrodeposition and the corresponding η_j *vs.* E curve (●).

The polarization diagrams (Fe + H_2) for the processes of electrodeposition of Fe powders from sulfate and chloride electrolytes are illustrated in Fig. 2. A sharp increase of the current occurred at about –1.0 V during the deposition from sulfate electrolyte, while for the deposition from chloride electrolyte, this phenomenon moved to more negative potentials (at about –1.2 V), indicating that the overpotential for the deposition from chloride electrolyte is by about 0.20 V negative than that from the sulfate electrolyte. The shape of the diagrams suggests that intensive hydrogen evolution occurred during the deposition process. According to the polarization diagrams, three current densities for each electrolyte were selected for analysis (see Fig. 2).

The morphology of the obtained powders depended on the anion presence in the electrolyte. The typical morphology of the powder electrodeposited from sulfate and chloride electrolytes is shown in Figs. 3a and 3b, respectively. The Fe

powder electrodeposited from the sulfate electrolyte was characterized by dendrite, coral-like particles, while the powder electrodeposited from the chloride electrolyte contained one type of agglomerates.

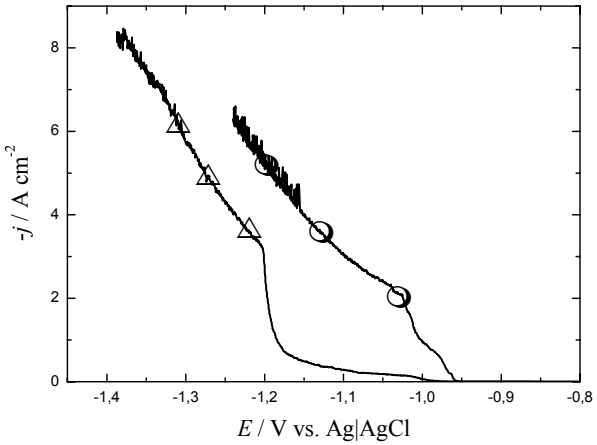

Fig. 2. Polarization curves for the electrodeposition of Fe powders from the sulfate and chloride electrolytes measured with *IR* drop correction at selected current densities; (Δ) chloride (j = 3.6, 4.8 and 6.0 A cm^{-2}) and (○) sulfate (j = 2, 3.5 and 5.0 A cm^{-2}) electrolytes.

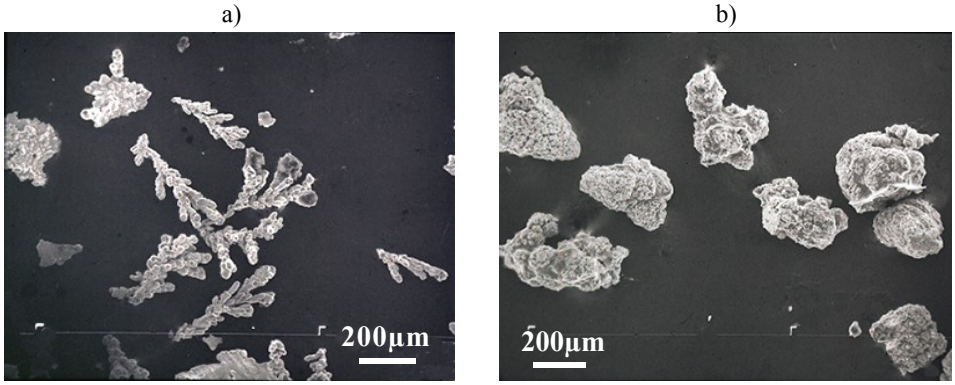

Fig. 3. Typical powder particle morphology; sulfate, j = 5.0 cm^{-2} (a), and (b) chloride electrolyte, j = 6.0 A cm^{-2}.

The morphologies of the Fe powders and their surfaces deposited from the sulfate electrolyte at current densities j = 2, 3.5 and 5.0 A cm^{-2} are shown in Figs. 4a–4f. The morphology of the Fe powders deposited at all the investigated current densities is dendritic of the coral type. There is no significant difference in size and shape of particles with increasing current density in the range from 2.0 to 5.0 A cm^{-2}. Only primary ramification of the dendrites occurred without a clear crystallographic orientation and further ramification was hindered. It is a characteristic for the primary branch of dendritic particles that only one type of cavity, *i.e.*, cone-shaped, could be detected on all the particles: (Fig. 4b). The appearance of such cavities is most probably the result of bubble formation due to

hydrogen evolution.[4,5,19] Such a kind of cavities was found and explained in previous papers on alloy powders.[4,5] At higher magnification, which enabled detailed observation of the morphology of the dendrite, insufficiently developed cauliflower endings with crystallites were noticed regardless of the applied current density. These crystallites represent potential places for further growth of dendrites. The morphology of the endings depends on the moment of detachment of the particles from the electrode.[4]

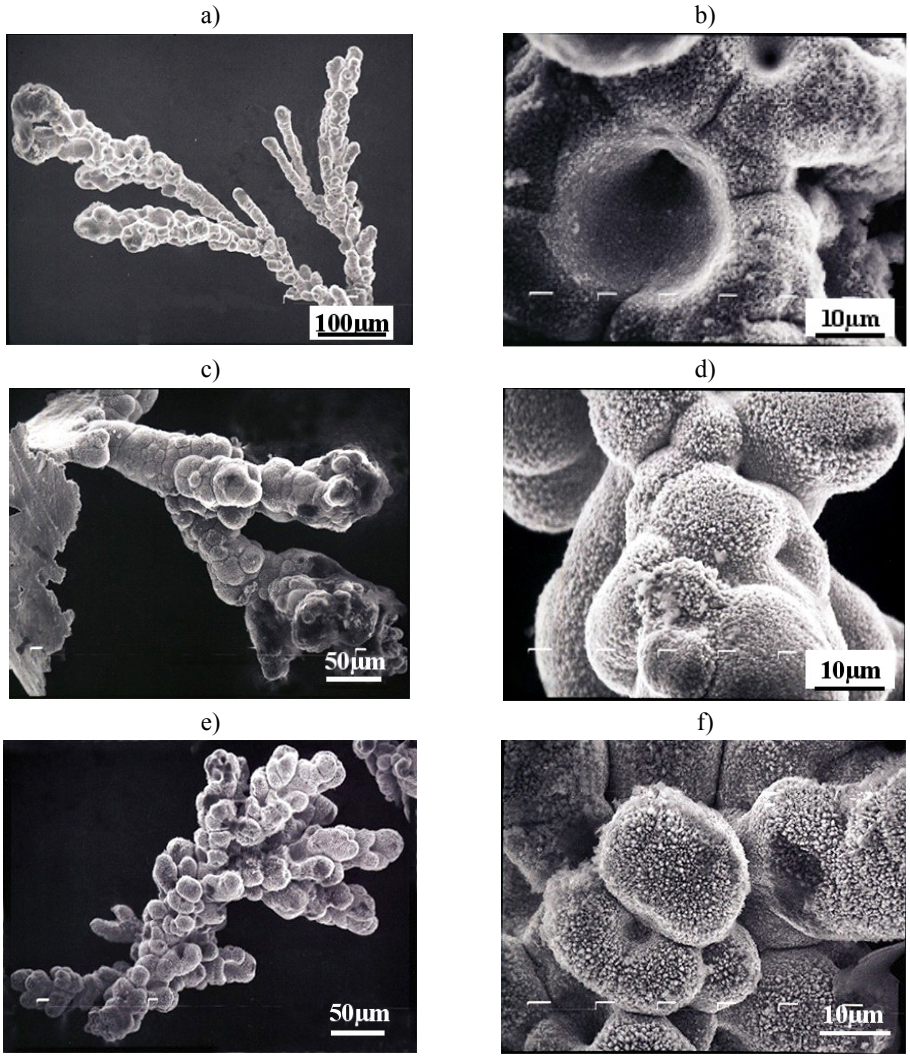

Fig. 4. SEM Micrographs of Fe powders electrodeposited from sulfate electrolyte: morphology of the powder particles (a, c, e); morphology of the surface (b, d, f); j = 2.0 (a, b), 3.5 (c, d) and 5.0 A cm^{-2} (e, f).

The morphologies of the Fe powder particles and of their surfaces deposited from chloride electrolyte at current densities j = 3.6, 4.8 and 6.0 A cm^{-2} are shown in Figs. 5a–5f. In this case, only agglomerates were detected at all the investigated current densities. Some of these agglomerates were spherical (Fig. 5a). The higher magnification microphotographs (Figs. 5b, 5d and 5f) reveal that the top surface of these agglomerates also had cauliflower-like endings. The main characteristic of the top surface of these particles was the presence of crystallites on the cauliflower-like endings. Such a morphology indicates that a second layer of growth of nodules occurred.[19]

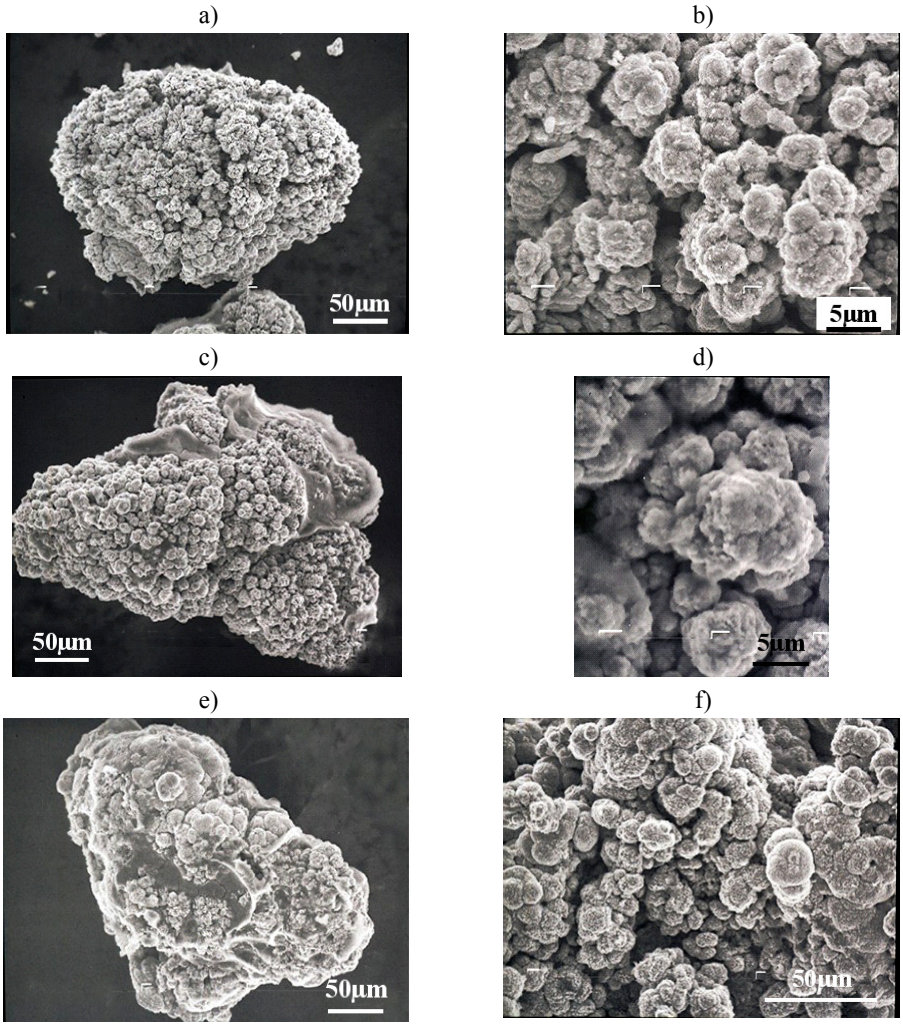

Fig. 5. SEM Micrographs of Fe powders electrodeposited from chloride electrolyte: morphology of powder (a, c, e); morphology of surface (b, d, f); j = 3.6 (a, b), 4.8 (c, d) and 6.0 A cm^{-2} (e, f).

Powders have a high chemical activity because of their large surface area and, hence, readily react with the oxygen in air to form surface oxides.[6,14,20] It is known that corrosion processes occur at the boundary of the surface of the powder particles and the liquid phase. In this way, it is possible to imagine that moisture adsorption can be prevented by the formation of a film on the surface of the powder particles, which could enable their long-term and safe protection. In relation to this, it was necessary to find stabilizers that would enable the creation of hydrophobic adsorption films on the surface of the powder particles, which would be able to protect and stabilize the metal surface from the effect of moisture.[17,20] It was found that benzoic acid, Sap G-30 and benzotriazol were the best stabilizers for copper particles.[17] The assumption is that they stabilize by forming colloidal precipitates in the form of a protective film on the surface of the particles. The X-ray diffractograms of Fe powders deposited from sulfate and chloride electrolytes and stabilized by sodium soap are shown in Fig. 6. Throughout the investigated range of 2θ, the X-ray patterns contain only two characteristic peaks, corresponding to the α-Fe phase with a body-centered cubic (bcc) crystal lattice with (110) and (200) planes. It should be pointed out that reflections of possibly present oxides (FeO, Fe_2O_3 and Fe_3O_4) were not detected in either of the two samples, which proves that the soap solution treatment applied as a method of washing and drying provided good protection of the Fe powders from oxidation.

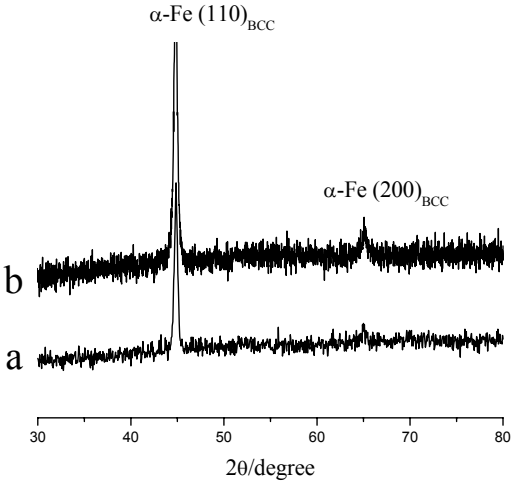

Fig. 6. X-Ray diffractograms of Fe powders electrodeposited from: a) sulfate electrolyte at j = 5.0 A cm^{-2}, and b) chloride electrolyte at j = 6.0 A cm^{-2}.

CONCLUSIONS

The main results obtained in this study can be summarized as follows:

1. Polarization diagrams recorded during the electrochemical deposition of Fe powders were characterized by the presence of two inflexion points, *i.e.*, the

first inflection corresponded to the beginning of metal deposition which is then followed by a rapid rise in the current density, whereas the second inflection characterizes the start of the linear change of the current density with potential.

2. The morphology and composition of the obtained powders depended on the anion presence in the electrolyte. Generally, two types of particles could be distinguished: dendrites (sulfate electrolyte) and agglomerates (chloride electrolyte) at all the investigated current densities.

3. The main characteristic of the top surface of all particles was the presence of crystallites on the cauliflower endings.

4. Cavities, which were the result of bubble formation due to hydrogen evolution, could be found only in the powders electrodeposited from the sulfate electrolytes.

5. The X-ray patterns contained only characteristic peaks corresponding to the α-Fe phase, indicating that the quality of the selected method of stabilization using a soap solution gave good protection from oxidation.

Acknowledgment. This work was financially supported by the Ministry of Science of the Republic of Serbia under the research project "Deposition of ultrafine powders of metals and alloys and nanostructured surfaces by electrochemical techniques" (142032G/2006).

И З В О Д

ЕЛЕКТРОХЕМИЈСКО ТАЛОЖЕЊЕ Fe ПРАХОВА ИЗ КИСЕЛИХ ЕЛЕКТРОЛИТА

ВЕСНА М. МАКСИМОВИЋ[1], ЉУБИЦА Ј. ПАВЛОВИЋ[2], БОРКА М. ЈОВИЋ[3] и МИОМИР Г. ПАВЛОВИЋ[2]

[1]Институт за нуклеарне науке "Винча", п. пр. 522, 11000 Београд, [2]ИХТМ, Центар за електрохемију, Универзитет у Београду, Његошева 12, 11000 Београд и [3]Институт за мултидисциплинарна истраживања, п.пр. 33, 11030 Београд

У овом раду приказани су резултати испитивања поларизационих карактеристика процеса таложења Fe прахова из сулфатних и хлоридних електролита, као и морфологија добијеног праха. Утврђено је да морфологија честица зависи од врсте анјона присутних у електролиту, али не и од примењене густине струје у испитиваном опсегу. Карактеристично за честице које су исталожене из сулфатних електролита је да су оне дендритичне са карфиоластим, кристаличним завршецима и да поседују купасте шупљине. Код Fe прахова исталожених из хлоридних електролита уочени су агломерати. Коришћење раствора сапуна у процесу прања и сушења прахова показао се као добар метод заштите праха од оксидације.

(Примљено 17. децембра 2007, ревидирано 27 фебруара 2008)

REFERENCES

1. R. Piontelli, in *Proceedings of 2nd Meeting of CITCE*, (1950), Milan, Italy, (1951), p. 163
2. S. Tajima, M. Ogata, *Electrochim. Acta* **13** (1968) 1845
3. N. D. Nikolić, Lj. J. Pavlović, M. G. Pavlović, K. I. Popov, *J. Serb. Chem. Soc*. **72** (2007) 1369
4. V. D. Jović, B. M. Jović, V. Maksimović, M. G. Pavlović, *Electrochim. Acta* **52** (2007) 4254
5. V. D. Jović, B. M. Jović, M. G. Pavlović, *Electrochim. Acta* **51** (2006) 5468

6. A. Calusaru, *Electrodeposition of Powders from Solutions*, Elsevier, New York, NY, 1979, p. 363
7. N. Kudryavtsev, V. Petrovna, *Novosti tehniki*, N. K. T. R. **171** (1932) (in Russian)
8. L. Kuzmin, V. Kiseleva, *Zhur. Prikl. Khim.* **22** (1949) 311 (in Russian)
9. C. Hardy, C. Mantell, F. Patent, 814500 (1937)
10. C. Hardy, C. Mantell, US Patent, 2157699 (1938)
11. N. Kurdyavtsev, E. Tereshkovitch, *Zhur. Prikl. Khim.* **21** (1948) 1298 (in Russian)
12. M. Balshin, *NIIMASH* **12** (1935) 5
13. H. Casey, US Patent, 2481079 (1949)
14. I. A.Carlos, C. S.Caruso*, J. Power Sources* **73** (1998) 199
15. M. L. Trudeau, *Nanostruct. Mater.* **12** (1999) 55
16. P. K. Samal, E. Klar, US Patent, 4134800 (1979)
17. M. G. Pavlović, Lj. J. Pavlović, I. D. Doroslovački, N. D. Nikolić, *Hydrometallurgy* **74** (2004) 155
18. F. A. Lowenheim, *Modern Electroplating*, 3rd Ed., Wiley, New York, 1974
19. V. D. Jović, V. Maksimović, M. G. Pavlović, K. I. Popov, *J. Solid State Electrochem.* **10** (2006) 373
20. A. I. Levin, A. V. Pomosov, *Zhur. Prikl. Khim.* **23** (1950) 949 (in Russian).

www.shd.org.rs

Journal of the Serbian Chemical Society

JSCS@tmf.bg.ac.yu • www.shd.org.rs/JSCS

J. Serb. Chem. Soc. 73 (8–9) 871–878 (2008) UDC 546.137–32+543.551:546.11'98+541.135.5
JSCS–3769 *Original scientific paper*

Determination of relative acidity scales for some dipolar aprotic solvents by coulometry using a hydrogen–palladium electrode

RADMILA M. DŽUDOVIĆ[1]*# and LJILJANA N. JAKŠIĆ[2#]

[1]*Faculty of Sciences, University of Kragujevac, Radoja Domanovića 12, P. O. Box 60, 34000 Kragujevac and* [2]*Faculty of Mining and Geology, University of Belgrade, Đušina 7, 11000 Belgrade, Serbia*

(Received 30 July 2007, revised 13 February 2008)

Abstract: A coulometric–potentiometric procedure for the determination of relative acidity scales of acetone, methylethyl ketone, methyl-isobutyl ketone and propylene carbonate is described. The range of the relative acidity scale of a solvent was determined from the difference between the half-neutralization potential of perchloric acid and that of tetrabutylammonium hydroxide. The perchloric acid was generated *in situ* from a hydrogen–palladium electrode in presence of sodium perchlorate or tetrabutylammonium perchlorate as the supporting electrolyte. The electrode pairs glass–SCE and $(H_2/Pd)_{ind}$–SCE were applied for the measurement of the half-neutralization potentials of the acid and base. A wider range of relative acidity scale of the solvents was obtained with the glass–SCE electrode pair and tetrabutylammonium perchlorate as the supporting electrolyte.

Keywords: relative acidity scale; coulometric generation of perchloric acid; hydrogen–palladium electrode; non-aqueous solvents.

INTRODUCTION

The choice of solvent as the medium for acid–base titrations was done on the basis of the thermodynamic constants of the solvent, the dissociation constant of the titrated acid (base), the half-neutralization potential of the titrated acid (base) in the investigated solvent and the relative acidity scale of the solvent.[1]

The autoprotolysis constant, K_S, is one of the basic thermodynamic constants of a solvent, which depends on numerous parameters including the acidity and basicity of the solvent, the relative permeability and polarity of the solvent molecules, *etc*. The K_S value gives information directly relevant to the extent of the acidity scale, pK_S. Solvents with higher pK_S values have a stronger differentiating effect during the titration of multicomponent electrolyte mixtures.

* Corresponding author. E-mail: radadz@kg.ac.yu
# Serbian Chemical Society member.
doi: 10.2298/JSC0809871D

The relative acidity scale of a solvent, E_S, has no physical meaning as does the acidity scale pK_S, which is calculated from the autoprotolysis constant of the solvent. The value of the E_S scale of a solvent is calculated from the difference between the half-neutralization potentials of a strong acid and a strong base in the given solvent. The relative acidity scale defines for every solvent the approximate potential ranges which can be used for potentiometric acid–base titrations under the determined experimental conditions (titrant, electrode pair, *etc*.). Hence, the E_S scale is a practical criterion for the choice of the optimal conditions in potentiometric acid-base titrations in the given solvent. With increasing range of the E_S scale, the possibility of the titration of weak bases (acids) and of differenttiating titrations of multicomponent mixtures of bases (acids) in the solvent is increased.

There are a few data in literature concerning the relative acidity scale of non--aqueous solvents.[2–6] The presented procedures for the evaluation of the E_S scale were based on the determination the difference between the half-neutralization potentials of perchloric acid and tetraethylammonium hydroxide (TEAH) or tetrabutylammonium hydroxide (TBAH) in the given solvent. It was found that the range of the scale depends on the nature of the solvent, the type of the electrode, the nature and concentration of the titrant and the presence of water and other impurities in the solvent.

Although perchloric acid is a strong electrolyte in most non-aqueous solvents, its application as a titrant is connected with some experimental difficulties, such as the instability of the acid in organic solvents, the presence of water, *etc*. It might be expected that an improvement of the procedure of classical titrations with perchloric acid would be obtained by using coulometric titration. With the coulometric titration technique, it is not necessary to prepare a titrant solution as this is generated electrolytically. It was shown[7] that many organic compounds (phenols, thiols, ascorbic acid, esters of gallic acid, *etc*.) and mercury, as well as hydrogen (or deuterium) dissolved in palladium can be successfully applied as anodic depolarizers for the coulometric generation of acids in non-aqueous solvents. The most favorable anodic depolarizer for the coulometric titration of bases as well as for the coulometric determination of protonation constants in non-aqueous solvents is hydrogen dissolved in palladium. The anodic oxidation of hydrogen generates “dry” hydrogen ions, by which means the introduction of a titrant into the solution is avoided, the titrated volume and the ionic strength remain unchanged and the procedure is simplified.

No data have been reported on the application of coulometric titrant generation for determination of the relative acidity scale of solvents.

Employing the possibility of the direct H^+ generation by the electrooxidation of hydrogen dissolved in palladium, in this work a procedure for the coulometric–

–potentiometric determination of the relative acidity scales of some dipolar aprotic solvents was developed.

EXPERIMENTAL

Reagents

All employed chemicals were of analytical grade from Merck or Fluka. Prior to use, acetone (AC), methylethyl ketone (MEK) and methyl-isobutyl ketone (MIBK) were purified by procedures described in the literature.[8] Propylene carbonate (PC) was used without further purification.

Tetrabutylammonium hydroxide (TBAH) in a 2-propanol–methanol mixture (0.10 M) was used. The exact concentration of TBAH was determined coulometrically using a hydrogen–palladium generator electrode.

The liquid organic bases were first dried over fused potassium hydroxide and then distilled under reduced pressure. The concentration of the solutions of the bases were controlled by titrating them with H^+ generated by the oxidation of hydrogen dissolved in palladium.

The supporting electrolyte was 0.10 M sodium perchlorate or 0.10 M tetrabutylammonium perchlorate (TBAP) in the required solvent.

Apparatus

The apparatus for the coulometric–potentiometric determination of relative acidity scales of the solvents is shown in Fig. 1.

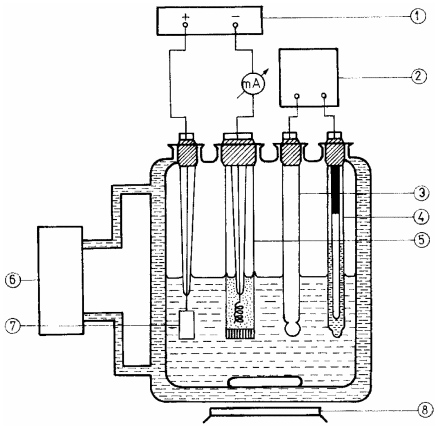

Fig. 1. Schematic diagram of the apparatus for the coulometric–potentiometric determination of the relative acidity scale of solvents: (1) current stabilizer, (2) pH-meter, (3) glass electrode, (4) calomel electrode, (5) Pt-cathode, (6) thermostat, (7) H_2/Pd electrode and (8) magnetic stirrer.

The current source was a voltage–current stabilizer (type STNS, Vinča, Belgrade). The current in the generating circuit was measured with a precise milliampermeter (Iskra, Kranj). The anode and cathode compartments of the electrolytic vessel were separated by a sintered glass disk of porosity 4; the volume of anolyte was 40 ml, and that of the catholyte 10 ml. The potential was measured by means of a pH-meter Radiometer pHM-26. The temperature of the solution was kept constant by circulating thermostated water through the outer glass-mantel of the vessel. The solution was continuously stirred with a magnetic stirrer.

Electrodes

The generator electrode, $(H_2/Pd)_{gen}$, was a palladium plate (1 cm×2 cm×0.5 cm), saturated with hydrogen obtained by electrolyzing a dilute aqueous sulfuric acid solution.

The indicator electrode, $(H_2/Pd)_{ind}$, was made in the form of a palladium spiral wire sealed into a glass tube by means of a platinum wire. The electrode had previously been saturated with hydrogen obtained by the electrolysis of water. The response of $(H_2/Pd)_{ind.}$ electrode in the solvents was investigated from the potential measurements in solutions of coulometrically generated perchloric acid (within the concentration range 0.010 M to 0.0010 M) in sodium perchlorate media. It was found (Fig. 2) that the potential of the $(H_2/Pd)_{ind}$ electrode showed a sub-Nernstian dependence on the logarithm of the concentration of perchloric acid, with a slope of 46 mV in acetone and 44 mV in methylethyl ketone.

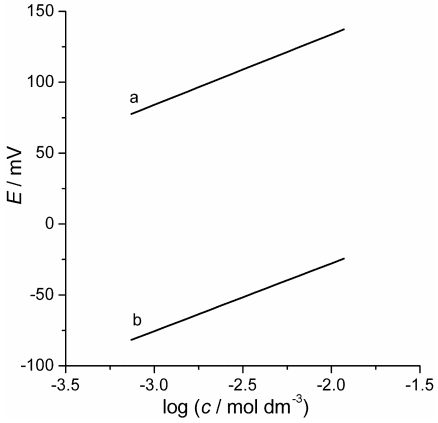

Fig. 2. Plot of the potential of the $(H_2/Pd)_{ind}$ electrode *vs*. logarithm of the concentration of the electrogenerated perchloric acid in (a) acetone and (b) methylethyl ketone.

A glass electrode, type G-202B (Radiometer, Copenhagen), was used. The electrode was conditioned in the required solvent before use.

A modified saturated calomel electrode, type K201 (Radiometer, Copenhagen), with potassium chloride in methanol was used as the reference electrode.

Procedures

Determination of the relative acidity scale. The relative acidity scale of AC, MEK, MIBK and PC were determined from the difference in the half-neutralization potentials of perchloric acid and TBAH. Two electrode pairs, a glass–SCE and a $(H_2/Pd)_{ind}$–SCE, were used for the measurement of the half-neutralization potentials of the acid and base.

Determination of the potential of the half-neutralization of perchloric acid. The supporting electrolyte (sodium perchlorate or TBAP) was poured into the anode (40 ml) and cathode (10 ml) compartments of the electrolytic vessel. The platinum and $(H_2/Pd)_{gen.}$electrodes were immersed into the catholyte and anolyte, respectively. The required amount of hydrogen ions was generated at the $(H_2/Pd)_{gen}$ anode (current of 5.0 mA). The coulometrically obtained perchloric acid was then half-neutralized with a standard solution of TBAH. The potential of half-neutralization of perchloric acid was read 60 min after thermostating (25 °C).

Determination of the potential of half-neutralization of TBAH. The supporting electrolyte was placed into the cathode and anode compartments up to the same level. A suitable volume of a standard solution of TBAH (0.500 ml) was added to the anolyte and then titrated to half neutralization with hydrogen ions generated at the $(H_2/Pd)_{gen}$ anode. The half-neutralization potential of the base was also measured after thermostating the solution.

Coulometric–potentiometric titrations of mixtures of bases in propylene carbonate. The supporting electrolyte was poured into the anode (20 ml) and cathode (5.0 ml) compartments of the electrolytic vessel. The platinum wire was dipped into the catholyte and the $(H_2/Pd)_{gen}$

electrode and the desired electrode couple (glass–SCE or $(H_2/Pd)_{ind.}$–SCE) were placed in the anolyte. A weighed amount of the base being determined was added to the anolyte, the current was switched on; hydrogen ions were generated discontinually and the potentials were read.

RESULTS AND DISCUSSION

The relative acidity scales of acetone, methylethyl ketone, methyl-isobutyl ketone and propylene carbonate were determined by coulometry from the difference between the half-neutralization potentials of solutions of perchloric acid and TBAH of the same concentration in the investigated solvent.

$$E_S = E_{1/2}(HClO_4) - E_{1/2}(TBAH)$$

In order to obtain a half-neutralized solution of perchloric acid, the required amount of acid (1.67×10^{-3} M) was generated *in situ* from the $(H_2/Pd)_{gen}$ electrode and then neutralized to 50 % with a standard solution of TBAH. A half--neutralized solution of TBAH was obtained by titrating a solution of the base (1.67×10^{-3} M) to 50 % with hydrogen ions coulometrically generated at an $(H_2/Pd)_{gen}$ anode. The half-neutralization potentials of perchloric acid and TBAH were measured using both a glass–SCE and a $(H_2/Pd)_{ind}$–SCE electrode pair.

As an example, the calculation of the relative acidity scale of acetone from the experimental data is shown in Table I.

TABLE I. Determination of the relative acidity scale of acetone using a H_2/Pd generator electrode; c(TBAH) = 1.67×10^{-3} M; $c(HClO_4)$ = 1.67×10^{-3} M; supporting electrolyte sodium perchlorate (0.10 M); current 5.0 mA

Electrode pair	Number of determinations	$E_{1/2}(HClO_4)$ / mV	$E_{1/2}$(TBAH) / mV	E_s / mV	S^a / mV
Glass–SCE	6	–470±4	+182±6	652	9
$(H_2/Pd)_{ind}$–SCE	4	–120±7	–418±3	298	10

[a]Standard deviation; the values of the standard deviation represent the accuracy of the measurement of the relative acidity scales of the investigated solvents

The ranges of the relative acidity scales of the investtigated solvents, obtained by the coulometric–potentiometric procedure, are shown in Fig. 3.

As can be seen from Fig. 3, various intervals of the relative acidity scale were obtained for one solvent; the range of the E_S scale depended on the electrode pair and the nature of the employed supporting electrolyte. When a glass––SCE electrode pair was used for measuring the half-neutralization potentials, a wider acidity scale of the solvent was obtained than when a $(H_2/Pd)_{ind}$–SCE electrode couple was applied. Thus, for example, the E_S scale of acetone (in a sodium perchlorate medium) determined with a glass–SCE and a $(H_2/Pd)_{ind}$–SCE electrode pair were about 650 and 300 mV, respectively (Table I). This difference in the relative acidity scale of a solvent can be explained by the sensitivity of the $(H_2/Pd)_{ind}$ electrode being lower than that of a glass electrode in the investigated solvents; the slopes of the potential response of the $(H_2/Pd)_{ind}$ electrode were sub-Nernstian (Fig. 2).

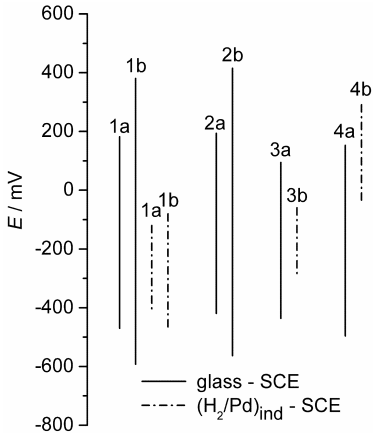

Fig. 3. The relative acidity scale of AC (1), MEK (2), MIBK (3) and PC (4) in (a) sodium perchlorate and (b) TBAP media.

On the basis of this fact, it is to be expected that the highest potential jumps at the end-point would be obtained if a glass electrode were used for the detection of the end-point in the employed solvents. The curves of the coulometric–potentiometric titrations of two-component mixtures of bases in propylene carbonate as the solvent using glass–SCE and $(H_2/Pd)_{ind}$–SCE electrode couples are shown in Fig. 4.

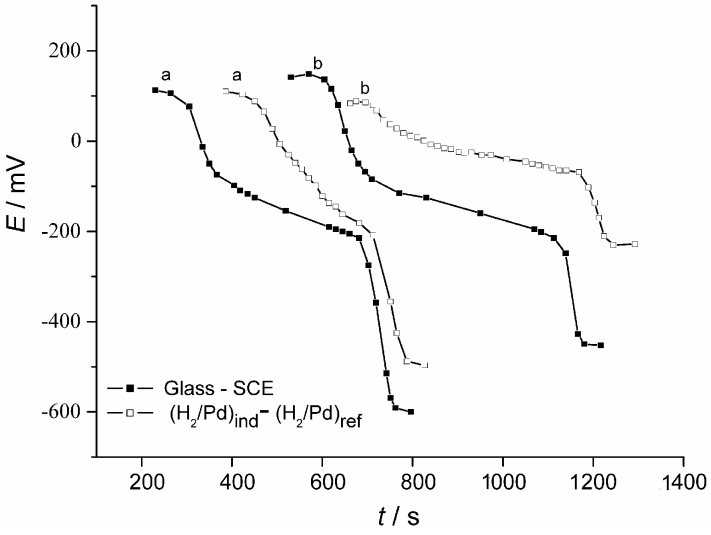

Fig. 4. Coulometric–potentiometric titration curves of mixtures of bases in propylene carbonate: (a) triethylamine + quinoline and (b) triethylamine + 2,2'-bipyridyl.

In the coulometric titration of a mixture of bases, triethylamine + 2,2'-bipyridyl, the potential jumps recorded for the first and second end-point were 60 and 150 mV, respectively, when a glass electrode was used and 30 and 60 mV, respectively, when a $(H_2/Pd)_{ind}$ electrode was used. As in PC, in the other dipolar

aprotic solvents (AC, MEK and MIBK) in accordance with their E_S scales, coulometric–potentiometric titrations of mixtures of bases can be successfully performed using a glass indicator electrode.[9]

The range of a relative acidity scale of a solvent depends on the nature of the supporting electrolyte and also on the presence of water. When TBAP was applied as the supporting electrolyte instead sodium perchlorate, wider E_S scales were obtained. The large influence of the supporting electrolyte on the E_S scales determined using a glass electrode can be explained by specific effects of the cation of the supporting salt on the sensitivity of this electrode.

Water lowered the range of the relative acidity scale in all the investigated solvents. It was found that the addition of small amounts of water (less than 1 %) in the anolyte had a large effect on the relative acidity scale of the solvent. Thus, after the addition of 0.30 % water, the relative acidity scale of acetone was narrowed by 65 mV, whereas after the addition of a further 0.70 % water, the scale was narrowed by an additional 60 mV. In accordance with the influence of water on the E_S scale of the solvent, it is to be expected that the potential jumps at the end-point in the coulometric–potentiometric titrations of bases (acids) will be decreased.

CONCLUSIONS

Based on the presented results, it may be concluded that a generator hydrogen–palladium electrode can be applied for the coulometric–potentiometric determination of relative acidity scales of dipolar aprotic solvents. By applying a hydrogen–palladium generator electrode as a source of H^+, the use of a standard solution of perchloric acid is avoided and the effect of water present in the acid solution is eliminated. A relative acidity scale determined by this method is a practical and useful criterion, which could find application in coulometric–potentiometric acid–base titrimetry in non-aqueous solvents.

Acknowledgement. The authors are grateful to the Ministry of Science of the Republic of Serbia for financial support (Project No. 142060).

ИЗВОД

КУЛОНОМЕТРИЈСКО ОДРЕЂИВАЊЕ РЕЛАТИВНЕ СКАЛЕ КИСЕЛОСТИ НЕКИХ ДИПОЛАРНИХ АПРОТИЧНИХ РАСТВАРАЧА ПРИМЕНОМ ВОДОНИК–ПАЛАДИЈУМОВЕ ЕЛЕКТРОДЕ

РАДМИЛА М. ЏУДОВИЋ[1] и ЉИЉАНА Н. ЈАКШИЋ[2]

[1]*Природно–математички факултет, Универзитет у Крагујевцу, Радоја Домановића 12, 34000 Крагујевац и* [2]*Рударско–геолошки факултет, Универзитет у Београду, Ђушина 7, 11000 Београд*

Приказан је поступак за кулонометријско–потенциометријско одређивање релативних скала киселости ацетона, метилетил кетона, метилизибутил кетона и пропилен-карбоната. Вредност релативне скале киселости растварача одређена је из разлике полу-неутрализационих потенцијала перхлорне киселине и тетрабутиламонијум-хидроксида. Перхлорна киселина је генерисана *in situ* на водоник–паладијумовој електроди у присуству натријум-пер-

хлората или тетрабутиламонијум-перхлората као основног електролита. За мерење полу-неутрализационих потенцијала киселине и базе коришћени су електродни парови стаклена–ЗКЕ и $(H_2/Pd)_{инд}$–ЗКЕ. Применом електродног пара стаклена–ЗКЕ и тетрабутиламонијум-перхлоратног основног електролита добијене су веће вредности за релативне скале киселости испитиваних растварача.

(Примљено 30. јула 2007, ревидирано 13. фебруара 2008)

REFERENCES

1. A. P. Kreshkov, *Analytic Chemistry of Non-Aqueous Solutions*, Khimiya, Moscow, 1982, p. 183 (in Russian)
2. H. B. van der Heijde, E. A. M. F. Dahmen, *Anal. Chim. Acta* **16** (1957) 378
3. H. B. van der Heijde, *Anal. Chim. Acta* **17** (1957) 512
4. N. A. Baranov, N. A. Vlasov, L. P. Potekhina, O. F. Shepotko, *Zh. Anal. Khim.* **25** (1970) 2069
5. A. P. Kreshkov, L. N. Bykova, Z. G. Blagodatskaya, V. D. Arashnikova, *Zh. Anal. Khim.* **23** (1968) 271
6. S. I. Petrov, L. N. Bykova, *Zhur. Anal. Khim.* **25** (1970) 168
7. R. P. Mihajlović, Lj. N. Jakšić, R. M. Džudović, *Anal. Chim. Acta* **557** (2006) 37
8. A. P. Kreshkov, L. N. Bykova, N. A. Kazaryan, *Acid–Base Titrations in Non-Aqueous Solutions,* Khimya, Moscow, 1967, p. 70 (in Russian)
9. R. P. Mihajlović, Lj. N. Jakšić, V. J. Vajgand, *J. Serb. Chem. Soc.* **60** (1995) 141.

Journal of the Serbian Chemical Society
JSCS@tmf.bg.ac.yu • www.shd.org.rs/JSCS
J. Serb. Chem. Soc. 73 (8–9) 879–890 (2008) UDC 615.275:544.4+535.243+543.062:615.1.004.12
JSCS–3770 *Original scientific paper*

Quantitative analysis of ibuprofen in pharmaceuticals and human control serum using kinetic spectrophotometry

SNEŽANA S. MITIĆ[1]*, GORDANA Ž. MILETIĆ[1], ALEKSANDRA N. PAVLOVIĆ[1], BILJANA B. ARSIĆ[1] and VALENTINA V. ŽIVANOVIĆ[2]

[1]*Faculty of Sciences and Mathematics, Department of Chemistry, University of Niš, Višegradska 33, P. O. Box 224, 18000 Niš and* [2]*High Agriculture School, Ćirila i Metodija 1, 18400 Prokuplje, Serbia*

(Received 3 October 2007, revised 25 March 2008)

Abstract: The aim of this work was to develop a new kinetic spectrophotometric method for the determination of ibuprofen in pharmaceutical formulations. Ibuprofen was determined in an acidic ethanolic medium by monitoring the rate of appearance of 1-nitroso-2-naphthol, resulting from the displacement by ibuprofen of Co(III) from the tris(1-nitroso-2-naptholato)cobalt(III) complex. The optimum operating conditions regarding reagent concentrations and temperature were established. The tangent method was adopted for constructing the calibration curve, which was found to be linear over the concentration range 0.21–1.44 and 1.44–2.06 μg ml^{-1}. The optimized conditions yielded a theoretical detection limit of 0.03 μg ml^{-1} based on the 3.3 S_0 criterion. The interference effects of the usual excipients of powdery drugs, foreign ions and amino acids on the reaction rate were studied in order to assess the selectivity of the method. The developed procedure was successfully applied for the rapid determination of ibuprofen in commercial pharmaceutical formulations and human control serum. The unique features of this procedure are that the determination can be performed at room temperature and the analysis time is short. The newly developed method is simple, inexpensive and efficient for use in the analysis of a large number of samples.

Keywords: ibuprofen; kinetic spectrophotometry; validation; pharmaceutical preparation.

INTRODUCTION

Ibuprofen [*RS*-2-(4-isobutylphenyl)propionic acid] (IB) is a non-steroidal anti-inflammatory medication used especially for the relief of the symptoms of arthritis, primary dysmenorrhoea and fever, and as an analgesic, especially where there is an inflammatory component. Ibuprofen was developed by the research arm of the Boots Group. Its side effects are gastrointestinal hemorrhage and ulce-

* Corresponding author. E-mail: mitich_s@yahoo.com
doi: 10.2298/JSC0809879M

ration. Various methods have been used for the determination of ibuprofen in pharmaceutical and biological samples. Until now, chromatographic methods (HPLC, GC, HPTLC, TLC),[1–9] electrophoretic methods,[10–13] spectrophotometric methods[14,15] and titrimetric methods with visual and potentiometric indications[16–18] are the major technique for the determination of ibuprofen.

The aim of this work was the development and validation of a simple, rapid and selective kinetic method for the analysis of ibuprofen in commercial pharmaceutical formulations and human control serum.

EXPERIMENTAL

Apparatus

The reaction rate was monitored spectrophotometrically. The absorbance of the solution was measured at a wavelength of 375 nm, which corresponded to the absorption of 1-nitroso--2-naphthol. The readings were performed on a Perkin-Elmer Lambda 15 UV/Vis spectrophotometer, connected to a thermo-circulating bath.

An Agilent Technologies Model 1200 instrument fitted with a C_{18} (Zorbax 5μm, 250 mm×4.6 mm) analytical column was used for the HPLC analysis.

A Julabo MP-5A model thermostatic bath was used to maintain the reaction temperature at 22.00±0.02 °C.

The pH measurements were made using a Hanna Instruments pH meter.

The solutions were thermostated at 22.00 ± 0.02 °C before the beginning of the reaction.

Reagents

A stock solution (1.0×10^{-3} mol l^{-1}) of ibuprofen was prepared daily in ethanol from pharmaceutical 99.59 % certified products, kindly provided by the Pharmaceutical Laboratory Galenika, a.d., Belgrade, Serbia.

An acetic acid solution (HOAc, 10 mol l^{-1}) was prepared from glacial HOAc (Merck).

A 1-nitroso-2-naphthol solution (1.0×10^{-3} mol l^{-1}) (Merck) was prepared by dissolving a known amount in ethanol.

A potassium bromate solution (0.1 mol l^{-1}) was prepared by dissolving a known amount in water.

A stock cobalt(II) solution (1.7×10^{-3} mol l^{-1}) was prepared by dissolving $CoCl_2\cdot6H_2O$ (Merck) in water. A working solution (1.7×10^{-5} mol l^{-1}) was obtained by diluting the stock cobalt solution with water.

The ionic strength was kept constant at 0.10 by adding an appropriate amount of NaCl solution (1.0 mol l^{-1}).

Analytical grade chemicals and deionized water (MicroMed high purity water system, TKA Wasseraufbereitungssysteme GmbH) were used for the preparation of all solutions.

Procedure

General Procedure. In order to obtain good mechanical and thermal stability, the instruments were run for 10 min before the first measurement. The reaction was performed in a reaction-mixture vessel with four compartments. A solution of 1-nitroso-2-naphthol was placed in one compartment, ibuprofen and acetic acid in the second, $KBrO_3$ in the third, and cobalt(II), electrolyte for ionic strength control and ethanol (total volume 10 ml) in the fourth compartment. The vessel was thermostated at 22.00±0.02 °C and the reaction was initiated by mixing. The reaction solution was put into a cell and the absorbance at 375 nm was measured spectrophotometrically every 30 s over a period of 5−6 min after mixing against the reagent blank prepared similarly.

Procedure for tablets and cream. A total of 20 tablets of each of the two studied pharmaceutical preparations (Ibuprofen, Panfarma, Belgrade, Serbia and Brufen®, Galenika a.d., Belgrade, Serbia) containing IB were weighed and finely powdered using a pestle and mortar. An accurately weighed quantity of the resulting powder, equivalent to 400.0 mg (weight of one tablet) of IB was dissolved in 25.00 ml of ethanol. Then it was centrifuged at 1800 rpm for 10 min and filtered through a 0.45 μm membrane filter (Millipore) directly into a 100.00 ml standard volumetric flask. The residue was washed three times with 15.00 ml of ethanol for complete recovery of the drug. The washings were added to the volumetric flask which was then filled to the mark with the same solvent. 2.50 ml of this solution was made up to 100.00 ml with ethanol to obtain a solution the expected IB concentration of which was 100.0 μg ml^{-1}. For kinetic determination, aliquots of this solution were transferred into vessels. For HPLC determination, aliquots of ibuprofen solution were transferred to a 10.00 ml volumetric flask and evaporated to dryness in a water bath. The residue was reconstituted with mobile phase and 20 μl was transferred into a glass vial for automatic injection into the HPLC system.

In the case of cream (Brufen®, Galenika a.d., Belgrade, Serbia), 4.000 g, which corresponded to 400.0 mg of ibuprofen, was weighed and mixed with 25.00 ml of ethanol. The mixture was stirred intensively for 30 min, centrifuged at 1800 rpm for 10 min and filtered through a 0.45 μm membrane filter (Millipore) directly in a 100.00 ml volumetric flask. The further preparation was the same as in the case of the tablets.

In all cases, it was assumed that the actual content of the tablet and cream corresponded to that reported by the manufacturing laboratories.

Serum sample preparation. Human lyophilized control serum (Lyotrol N, bioMérieux® sa, France) was used. The serum sample was spiked at two concentrations levels. The concentration of IB was chosen to match its normal therapeutic concentration in human serum.[19] To 0.50 ml of serum, the appropriate amount of the stock solution of ibuprofen (10 mg ml^{-1}) and 15 ml of ethanol was added and, after brief vortex mixing, it was centrifuged for 5 min at 3000 rpm to deposit the protein precipitate. The separated supernatant was collected in a 25.00 ml standard volumetric flask and filled up to the mark with the same solvent. The serum sample contained 100.0 μg ml^{-1} ibuprofen. Aliquots of this solution were transferred into vessels. For the kinetic determination, $Fe^{3+}$was masked by adding an appropriate amount of F^- (1.0×10^{-4} g ml^{-1}). For the HPLC determination, aliquots of the ibuprofen solution were transferred to a 10.00 ml volumetric flask and evaporated to dryness in a water bath. The residue was reconstituted with mobile phase and 20 μl was transferred into a glass vial for automatic injection into the HPLC system.

Comparative method. The employed procedures for the comparative methods (HPLC and alkalimetric (NaOH) titration with visual indication (phenolphthalein as the indicator)) are described in the British Pharmacopoeia[17] and US Pharmacopoeia.[18] Ibuprofen was detected and quantified on a 250 mm×4.6 mm Zorbax C_{18} (5 μm) analytical column operating at room temperature. The mobile phase, a mixture of phosphoric acid–acetonitrile–water, 0.5:340:600 v/v, was allowed to equilibrate and diluted to 1000 volumes with water. The eluate was monitored at 214 nm. Injection of the samples (20 μl) was performed using an autosampler. The flow rate of the mobile phase was 2.0 ml min^{-1}.

RESULTS AND DISCUSSIONS

Mechanism of the reaction

According to Kolthoff and Jacobsen,[20] divalent cobalt coordinates with two ligands (1-nitroso-2-naphthol, R(NO)OH), liberating two hydrogen ions for each cobalt ion present:

$$Co^{2+} + 2R(NO)OH \rightarrow Co[R(NO)O]_2 + 2H^+$$

Analyses of the cobalt(II) complex indicated six-coordination, in fact, the cobalt(II) complex corresponded to $Co[R(NO)O]_2 \cdot 2H_2O$. In the present work cobalt(II) was oxidized with $KBrO_3$, whereby tris(1-nitroso-2-naptholato)cobalt(III), $Co[R(NO)O]_3$, was formed.[21] The complex absorbs at 410 nm, while 1-nitroso--2-naphthol absorbs at 370 nm. In acidic medium, the 370 nm band shifts to 375 nm.[22] In the presence of ibuprofen, the absorption band at 410 nm[22] disappeared and appeared at 375 nm (Fig. 1), ibuprofen displacing cobalt(III) from the com-

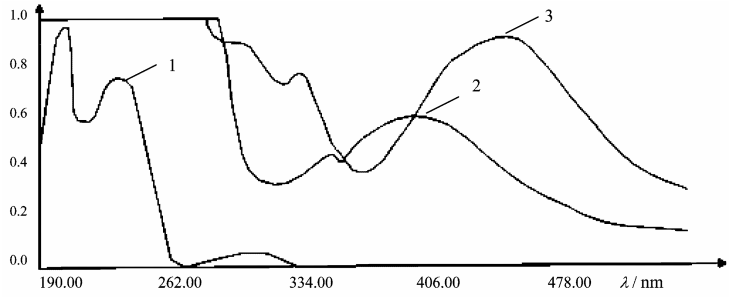

Fig.1. Absorption spectra of: 1) ibuprofen (1.0×10^{-5} mol l^{-1}), 2) 1-nitroso-2-naphthol (1.0×10^{-5} mol l^{-1}) and 3) tris(1-nitroso-2-naphtholato)cobalt(III) complex in ethanolic acetic acid.

plex with 1-nitroso-2-naphthol. The cobalt(III) forms a complex with ibuprofen. Physical studies of cobalt(III) ibuprofenate ($[Co_2(Ibup)_4]^{2+}$), (Ibup = ibuprofenato ion)) showed that in this complex four carboxylate groups are bridging two cobalt atoms (similar to other cobalt(III) carboxylates).[23,24] Ibuprofen was determined by monitoring the rate of appearance of 1-nitroso-2-naphthol in ethanolic acidic medium (Fig. 2):

$$2Co[R(NO)O]_3 + 4IB + 2H^+ \rightarrow [Co_2(Ibup)_4]^{2+} + 6R(NO)OH$$

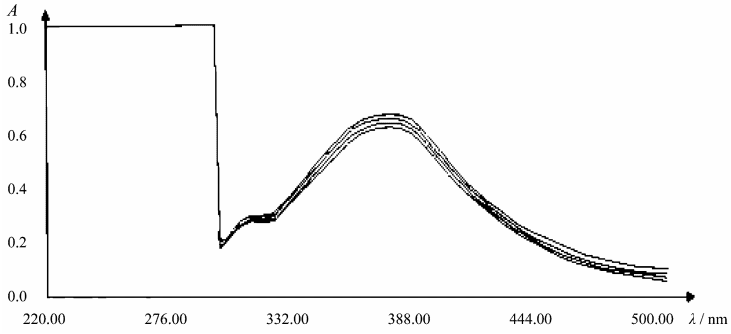

Fig. 2. Repetitative scans of the appearance of 1-nitroso-2-naphthol in ethanolic acetic acid recorded in 2 min intervals in presence of 1.0×10^{-5} mol l^{-1} IB; $c_{R(NO)OH} = 1.0\times10^{-5}$ mol l^{-1}, $c_{CH_3COOH} = 1.0$ mol l^{-1}, $c_{KBrO_3} = 1.0\times10^{-3}$ mol l^{-1}, $c_{Co^{2+}} = 1.7\times10^{-6}$ mol l^{-1}; $t = 22.00\pm0.02$ °C.

Kinetic studies

The tangent method was used for processing of the kinetic data. The rate of the reaction was obtained by measuring the slope of the linear part of the kinetic curves of the absorbance-time plot (slope = dA/dt).

In order to determine the lowest possible determinable concentration of ibuprofen, the working conditions required optimization. Therefore, the dependence of the rate of reactions on the concentration of each of the reactants was determined.

The effect of the concentration of acetic acid (Fig. 3) was studied in the range 1.0−6.0 mol l^{-1}. It can be seen that the reaction rate increased with increasing concentration of acetic acid up to 4.5 mol l^{-1}; beyond this concentration, the rate of the reaction remained constant. For further work a concentration of 5.0 mol l^{-1} was used.

The effect of the concentration of 1-nitroso-2-naphthol on the rate of reaction (Fig. 4) was studied in the range 0.5×10^{-5}–1.1×10^{-5} mol l^{-1}. It can be seen that the reaction rate increased with increasing 1-nitroso-2-naphthol concentration. A concentration of 1.0×10^{-5} mol l^{-1} was chosen as the optimum concentration.

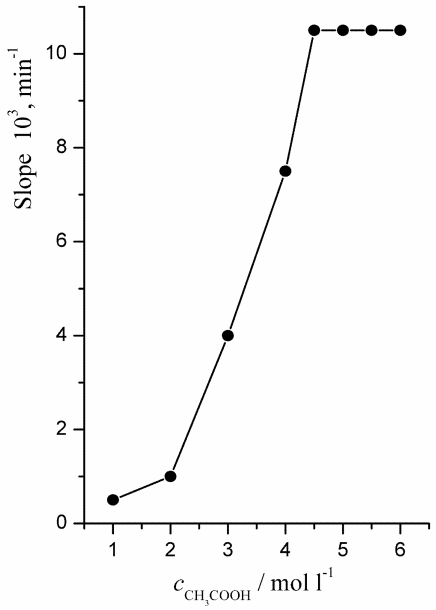

Fig. 3. Dependence of the reaction rate on the acetic acid concentration. Initial concentrations: $c_{R(NO)OH} = 1.0\times10^{-5}$ mol l^{-1}, $c_{KBrO_3} = 1.0\times10^{-3}$ mol l^{-1}, $c_{Co^{2+}} = 1.7\times10^{-6}$ mol l^{-1}; $c_{IB} = 1.0\times10^{-5}$ mol l^{-1}; t = 22.00±0.02 °C.

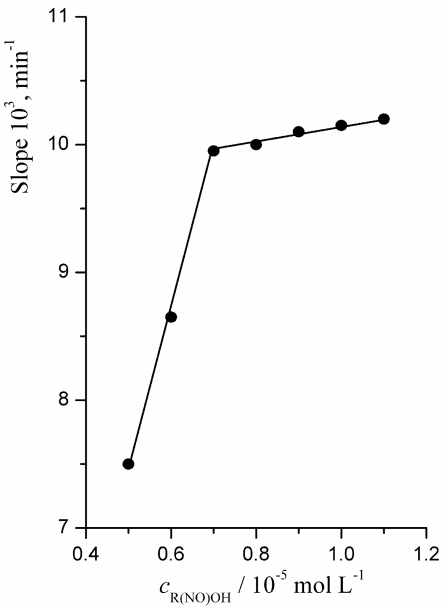

Fig. 4. Dependence of the reaction rate on the 1-nitroso-2-naphthol concentration. Initial concentrations: $c_{CH_3COOH} = 5.0$ mol l^{-1}, $c_{KBrO_3} = 2.0\times10^{-3}$ mol l^{-1}, $c_{Co^{2+}} = 1.7\times10^{-6}$ mol l^{-1}, $c_{IB} = 1.0\times10^{-5}$ mol l^{-1}; t = 22.00±0.02 °C.

The effect of the concentration of $KBrO_3$ (Fig. 5) was studied in the interval of 1.0×10^{-3}–3.0×10^{-3} mol l^{-1}. The reaction rate increased with increasing $KBrO_3$ concentration. For further work, a concentration of 2.5×10^{-3} mol l^{-1} was used.

The correlation between the slope and the Co(II) concentration is given in Fig. 6. The influence of the concentration of Co(II) on the rate of reaction was examined in the range 0.17–4.24×10^{-6} mol l^{-1}. A concentration of 3.4×10^{-5} mol l^{-1} in the final solution was used throughout the experiments.

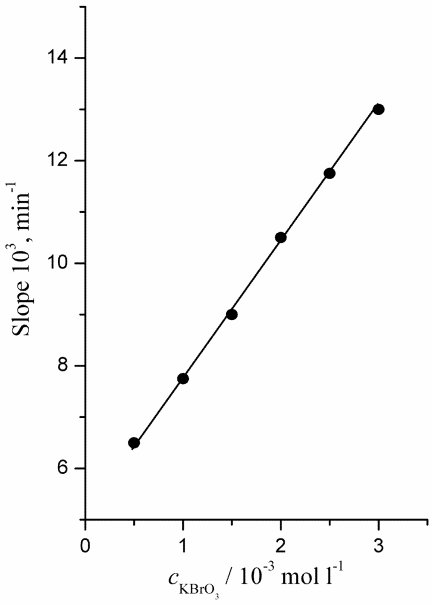

Fig. 5. Dependence of the reaction rate on the $KBrO_3$ concentration. Initial concentrations: c_{CH_3COOH} = 5.0 mol l^{-1}, $c_{R(NO)OH}$ = 1.0×10^{-5} mol l^{-1}, $c_{Co^{2+}}$ = 1.7×10^{-6} mol l^{-1}, c_{IB} = 1.0×10^{-5} mol l^{-1}; t = 22.00±0.02 °C.

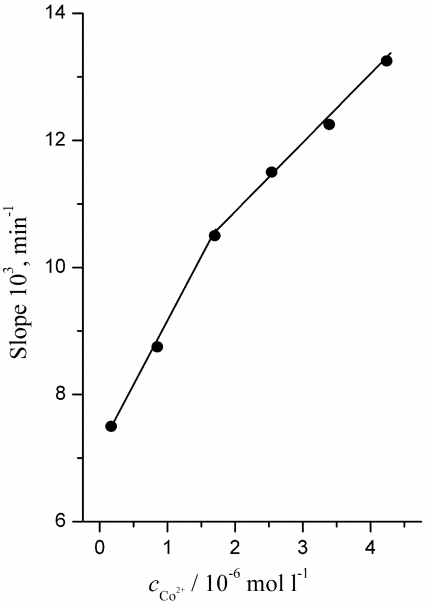

Fig. 6. Dependence of the reaction rate on the cobalt(II) concentration. Initial concentrations: c_{CH_3COOH} = 5.0 mol l^{-1}, $c_{R(NO)OH}$ = 1.0×10^{-5} mol l^{-1}, c_{KBrO_3} = 2.5×10^{-3} mol l^{-1}, c_{IB} = 1.0×10^{-5} mol l^{-1}; t = 22.00±0.02 °C.

The effect of temperature on the reaction rate was studied at 292, 295, 298, 301 and 304 K. The absorbance–time curves obtained at these temperatures indicated the temperature dependence of the reaction rate. The rate for different concentrations of ibuprofen at each temperature was calculated and utilized for plotting the calibration curve. At temperature > 298 K, the linear dynamic range of the determination decreased. The linear dynamic range, regression equation and temperatures are summarized in Table I. The best linearity was obtained at 295 K and hence this temperature was selected as the optimum temperature for the determination process.

The least squares equation ($y = bx + a$, where b and a are the slope and intercept, respectively) for the calibration graph and correlation coefficient, r^2[25]

for the determination of ibuprofen in the concentration range 0.21 to 1.44 μg ml^{-1} under the optimal reaction conditions (c_{CH_3COOH} = 5.0 mol l^{-1}, $c_{R(NO)OH}$ = = 1.0×10^{-5} mol l^{-1}, c_{KBrO_3}= 2.5×10^{-3} mol l^{-1}, $c_{Co^{2+}}$ = 3.4×10^{-6} mol l^{-1}, t = = 22.00±0.02 °C) were calculated:

$$\text{Slope}\times 10^3 = 1.647c_{IB} + 2.645 \qquad r = 0.9989$$

where slope is the slope of the linear part of the kinetic curve of the absorbance–time plot (slope = dA/dt = εl(dc/dt)) and c_{IB} is the ibuprofen concentration expressed in μg ml^{-1}.

TABLE I. Linear dynamic range, regression equation and correlation coefficient at different temperatures

T / K	Linear dynamic range, μg ml^{-1}	Regression equation	Correlation coefficient, r
292	0.41–1.44, n = 5	Slope×10^3 = 1.279c_{IB} + 1.946	0.9986
295	0.21–1.44, n = 6	Slope×10^3 = 1.647c_{IB} + 2.645	0.9989
298	0.21–1.44, n = 6	Slope×10^3 = 3.237c_{IB} + 3.031	0.9985
301	0.21–1.03, n = 4	Slope×10^3 = 2.902c_{IB} + 4.483	0.998
304	0.21–1.03, n = 4	Slope×10^3 = 6.831c_{IB} + 5.095	0.9983

The variance (S_0^2) of the calibration line was evaluated to be 2.566×10^{-4} μg ml^{-1}. The low value of the variance indicates negligible scattering of the experimental data points around the line of regression. The quantitative parameters of the analysis are given in Table II.

TABLE II. Quantitative parameters of the analysis

Calibration range, μg ml^{-1}	0.21–1.44, n = 6
Regression equation	Slope×10^3 = 1.647c_{IB} + 2.645
Slope±SD	(1.647±0.015)×10^{-3}
Intercept±SD	(2.645±0.014)×10^{-3}
Correlation coefficient, r	0.9989
Variance, S_0^2	2.566×10^{-4}
Detection limit, μg ml^{-1}	0.03
Quantification limit, μg ml^{-1}	0.1

The following kinetic equation for the reaction was deduced based on the obtained graphic correlations.

$$\text{Rate} = kc_{R(NO)OH}c_{KBrO_3}c_{Co^{2+}}c_{IB}$$

where k is a constant proportional to the rate constant of the reaction.

The equation is valid for the following concentrations: CH_3COOH, 4.5−6.0 mol l^{-1}; R(NO)OH, 0.7×10^{-5}–1.1×10^{-5} mol l^{-1}; $KBrO_3$, 1.0×10^{-3}–3.0×10^{-3} mol l^{-1}; Co(II), 1.7×10^{-6}–4.24×10^{-6} mol l^{-1} and IB, 0.21−1.44 μg ml^{-1}.

The activation energy for the reaction was calculated from linear regression of Arrhenius plot (log k *vs.* 1/T) and found to be 89.38±0.82 kJ mol^{-1}.

The limits of detection (*LOD*) and quantification (*LOQ*) were evaluated using the following equations:[26–29]

$$LOD = 3.3S_0/b$$
$$LOQ = 10S_0/b$$

where S_0 is the standard deviation of the calibration line and b is the slope. They were found to be 0.030 and 0.10 μg ml^{-1}, respectively.

The precision and accuracy of the system were studied by performing the experiment 5 times for different concentrations of ibuprofen. The results of accuracy and precision of the recommended procedure are presented in Table III.

TABLE III. Accuracy and precision of the determination of ibuprofen

Taken, μg ml^{-1}	Found[a] $x\pm SD$, μg ml^{-1}	RSD[b] / %	$100(x-\mu)/\mu$[c]
0.21	0.22±0.01	3.93	4.76
0.83	0.82±0.02	2.58	–1.2
1.44	1.45±0.02	1.14	0.69

[a]Mean and standard deviation of five determinations at the 95 % confidence level; [b]relative standard deviation; [c]accuracy of the method

Interference studies

To assess the selectivity of the method, the interference of those species accompanying IB in pharmaceutical formulations was studied. The tolerance limits (expressed as the w/w ratios) for the species studied in the determination of 1.65 μg ml^{-1} of IB are given in Table IV. As can be seen, the usual components of powdery drugs (fructose, glucose, lactose, mannitol and sorbitol), the vitamins B_1, B_6 and B_{12}, and Li^+, Na^+ and K^+ do not interfere with the method because the amounts tolerated are much higher than those usually present in pharmaceutical formulations. Binders, such as gelatin, and fillers, such as talc, are insoluble in ethanol, which was used for dissolving the pharmaceutical preparations. Silicon dioxide is also insoluble in ethanol. It should also be noted that higher tolerance levels exist for the presence of the amino acids Ala, Phe, Asp, Met, Tyr, Trp and Ser, the 2-carboxy metabolite of ibuprofen, (2-[4-(2-carboxypropyl)phenyl]propionic acid), and Mn^{2+} and Cd^{2+}. The amino acids His, Arg, Lys and Gly, as well Ca^{2+}, Zn^{2+} and Mg^{2+} interfere with the method. More severe interferences were observed for Fe^{3+} (masked with F^-) and Cu^{2+} ions. No interference was observed when up to 100-fold concentrations of nicotinic acid, citric acid, stearic acid, Si^{4+} and $C_2O_4^{2-}$ were present.

TABLE IV. Effect of foreign species on the determination of 1.65 μg ml^{-1} of ibuprofen

Foreign species	I[a] / %	Tolerance level ($c_{\text{Interferent}}/c_{\text{IB}}$)
Fructose, glucose, lactose, B_1, B_6, B_{12}, Li^+, Na^+, K^+, mannitol, sorbitol	5–10	10^3
Mn^{2+}, Cd^{2+}, Si^{4+}, F^-, $C_2O_4^{2-}$	5–10	10^2
Ala, Phe, Asp, Met, Tyr, Trp, Ser, nicotinic acid, citric acid, stearic acid	< 5	–

TABLE IV. Continued

Foreign species	I^a / %	Tolerance level ($c_{Interferent}/c_{IB}$)
His, Arg, Lys, Gly, Ca^{2+}, Zn^{2+}, Mg^{2+}, 2-[4-(2-carboxypropyl)phenyl] propionic acid	5–10	10
[b]Fe^{3+}, Cu^{2+}	Interference	1

[a]Interference coefficient, $I = (c^0_{IB} - c_{IB})/ c^0_{IB}$ (c^0_{IB} and c_{IB} are the measured concentrations of ibuprofen without and with the interfering species); [b]masked with fluoride ions

Applicability of the proposed method

The proposed method was applied for the determination of ibuprofen in three pharmaceutical formulations using the direct calibration curve. They were treated as described in the Experimental section. As can be seen in Table V, the results obtained for this method are in accordance with the official HPLC method. Also, good recovery was observed in the case of the serum sample (Table VI), indicating that the constituents of the human control serum did not interfere (Fe^{3+} were masked with F^- and the proteins were precipitated) in any way with the detection of ibuprofen. The HPLC chromatograms of the determination of ibuprofen in tablets (1.03 μg ml^{-1}) and the spiked serum (0.52 μg ml^{-1}) are given in Fig. 7. Therefore, the proposed method could be used for the determination of ibuprofen in serum samples. The results of the proposed method were statistically compared with those of the official method using a point hypothesis test.[30,31] Tables V and VI show that the calculated F and *t* values at the 95 % confidence level are less than the theoretical ones, confirming no significant differences between the performance of the proposed and the official method.

TABLE V. Determination of ibuprofen by the kinetic and the official methods (titrimetric method and HPLC)

Pharmaceutical preparation	Taken μg ml^{-1}	IB found by the proposed method[a] $x\pm SD$, μg ml^{-1}	*RSD*[a] %	Recovery[a] %	HPLC[a] $x\pm SD$ μg ml^{-1}	*F* value[b]	*t* value[b]	Titrimetric method[a] $x\pm SD$ μg ml^{-1}
Brufen®[c]	0.83	0.85±0.02	3.16	102.41	0.84±0.03	1.36	0.609	0.86±0.01
Ibuprofen[d]	1.03	1.01±0.03	2.5	98.06	1.02±0.02	1.63	0.687	1.00±0.02
Brufen®[e]	1.44	1.42±0.02	1.32	98.61	1.41±0.01	3.41	1.054	1.39±0.02

[a]Data are based on the average obtained from five determinations; [b]theoretical *F* value ($v_1 = 4$, $v_2 = 4$) and *t* value ($v = 8$) at the 95 % confidence level are 6.39 and 2.306, respectively; [c]tablets (from Galenika a.d., Belgrade, Serbia) containing ibuprofen 400 mg and excipients; [d]tablets (from Panfarma, Belgrade, Serbia) containing ibuprofen 400 mg and excipients; [e]cream (from Galenika a.d., Belgrade, Serbia) containing ibuprofen 1g/100 mg (50 g) and excipients

TABLE VI. Determination of ibuprofen in human control serum by the standard addition method

Proposed method µg ml^{-1}		*RSD*[a] %	Recovery[a] %	HPLC[a] $x\pm SD$, µg ml^{-1}	*F* value[b]	*t* value[b]	Titrimetric method[a] $x\pm SD$, µg ml^{-1}
Added	Found[a] $\bar{x} \pm SD$						
0.31	0.33±0.01	3.92	106.45	0.32±0.02	2.18	1.027	0.35±0.01
0.52	0.50 ±0.02	3.78	96.15	0.51±0.01	2.39	0.861	0.48±0.02

[a]Data are based on the average obtained from five determinations; [b]theoretical *F* value (v_1 = 4, v_2 = 4) and *t* value (v = 8) at the 95 % confidence level are 6.39 and 2.306, respectively

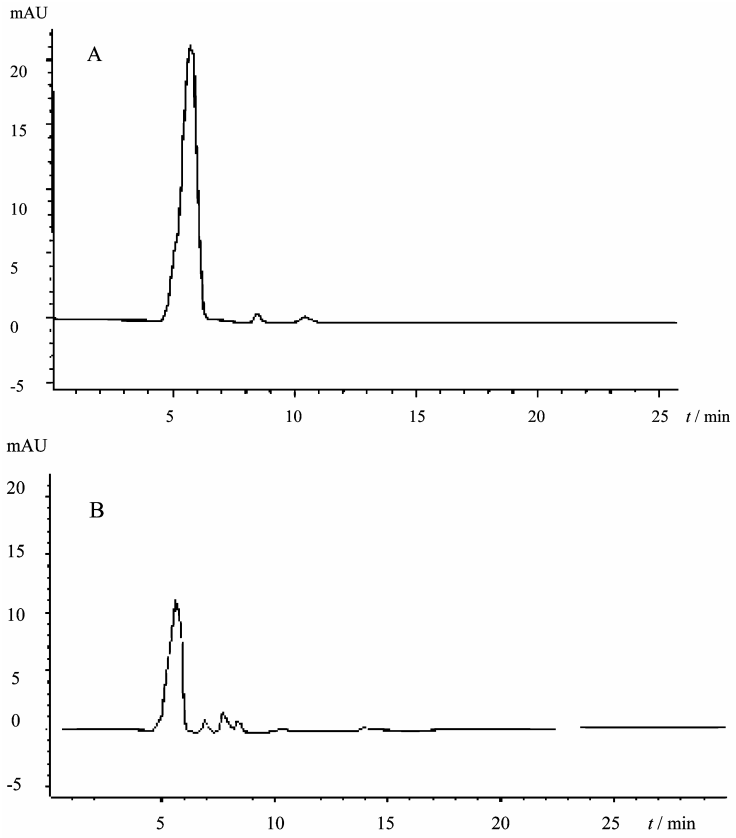

Fig. 7. HPLC chromatograms of: A) ibuprofen tablets (1.03 µg ml^{-1}) and B) serum spiked with 0.52 µg ml^{-1} ibuprofen. Column: C18 (Zorbax, 5µm, 250 mm×4.6 mm). Mobile phase: phosphoric acid–acetonitrile–water, 0.5:340:600 (v/v). Detection: spectrophotometer at 214 nm.

CONCLUSIONS

In conclusion, the proposed kinetic–spectrophotometric method for the determination of ibuprofen in pharmaceutical samples reported in this paper is simple, rapid and inexpensive and is very appropriate for routine quality control

analyses of the active drug in the laboratories of hospitals, the pharmaceutical industries and research institutions. Statistical comparison of the results with the official method showed good agreement and indicated no significant difference in accuracy and precision. The proposed method has also a wider linear dynamic range and lower detection limit in comparison with the spectrophotometric determination of ibuprofen (Table VII).

TABLE VII. Comparison of the proposed kinetic–spectrophotometric method with spectrophotometric determination of ibuprofen

Method	Linear dynamic range, *LOD*	Ref.
Spectrophotometry	100–1300 μg ml^{-1} 62 μg ml^{-1}	14
	6–60 μg ml^{-1}	32
	0.5–3.2 mg ml^{-1}	33
	10–40 μg ml^{-1}	34
	10–500 μg ml^{-1}	35
	0.21–1.44 μg ml^{-1} 1.44–2.06 μg ml^{-1} 0.03 μg ml^{-1}	This work

Acknowledgement. This research was supported by grant number 142015 from the Serbian Ministry of Science. The authors are grateful for the financial support provided by this Ministry.

И З В О Д

ОДРЕЂИВАЊЕ ИБУПРОФЕНА У ФАРМАЦЕУТСКИМ ПРЕПАРАТИМА И ХУМАНОМ КОНТРОЛНОМ СЕРУМУ КОРИШЋЕЊЕМ КИНЕТИЧКЕ СПЕКТРОФОТОМЕТРИЈЕ

СНЕЖАНА С. МИТИЋ[1], ГОРДАНА Ж. МИЛЕТИЋ[1], АЛЕКСАНДРА Н. ПАВЛОВИЋ[1], БИЉАНА Б. АРСИЋ[1] и ВАЛЕНТИНА В. ЖИВАНОВИЋ[2]

[1]*Природно–математички факултет, Одсек за хемију, Универзитет у Нишу, Вишеградска 33, 18000 Ниш и* [2]*Виша пољопривредна школа, Ћирила и Методија 1, 18400 Прокупље*

Циљ рада био је разрада нове кинетичке методе за одређивање ибупрофена у фармацеутским препаратима и хуманом контролном серуму. Ибупрофен је одређиван мерењем брзине појављивања 1-нитрозо-2-нафтола, који настаје услед његовог истискивања из трис-(1-нитрозо-2-нафтолато)кобалт(III) комплекса. Одређени су оптимални услови. Примењена је тангентна метода и добијена калибрациона крива која је линеарна у интервалу концентрације ибупрофена од 0,21–1,44 и 1,44–2,06 μg ml^{-1}. Граница детекције на основу 3,3 S_0 критеријума је 0,03 μg ml^{-1}. Испитан је утицај пуниоца, јона и аминокиселина на брзину реакције. Развијена метода је примењена за одређивање ибупрофена у фармацеутским препаратима и хуманом контролном серуму. Предност методе се огледа у томе што су одређивања врешена на собној температури и у кратком временском интервалу. Нова метода је једноставна и омогућава брзо одређивање ибупрофена у поменутим узорцима.

(Примљено 3. октобра 2007, ревидирано 25. марта 2008)

REFERENCES

1. S. C. Tan, S. H. D. Jackson, C. G. Swift, A. J. Hutt, *Chromatographia* **46** (1997) 23
2. R. Canaparo, E. Muntoni, G. P. Zara, C. Della Pepa, E. Berno, M. Costa, M. Eandi, *Biomed. Chromatogr.* **14** (2000) 219
3. P. Wang, M. Qi, L. Liu, L. Fang, *J. Pharm. Biomed. Anal.* **38** (2005) 714
4. M. Moedar, S. Schrader, M. Winkler, P. Popp, *J. Chromatogr. A* **873** (2000) 95
5. C. Sajeev, P. R. Jadhav, D. RaviShankar, R. N. Saha, *Anal. Chim. Acta* **463** (2002) 207
6. E. G. Jong, J. Kiffers, R. A. A. Maes, *J. Pharm. Biomed. Anal.* **7** (1989) 1617
7. V. V. Dhavse, D. V. Parmar, P. V. Devarajan, *J. Chromatogr. B* **694** (1997) 449
8. M. B. Lippstone, J. Sherma, *J. Planar Chromatogr. Mod. TLC* **8** (1995) 427
9. H. Hopkala, A. Pomykalski, *J. Planar Chromatogr. Mod. TLC* **17** (2004) 383
10. R. Hamoudova, M. Pospisilova, *J. Pharm. Biomed. Anal.* **41** (2006) 1463
11. K. Stubberud, O. Astrom, *J. Chromatogr. A* **826** (1998) 95
12. J. Sadecka, M. Ckart, A. Hercegova, J. Polonsky, I. Skacanii, *J. Pharm. Biomed. Anal.* **25** (2001) 881
13. W. Wei, X. D. Yu, H. X. Ju, *J. Chromatogr. Sci.* **42** (2004) 155
14. I. M. Palabiyik, E. Dinc, F. Onur, *J. Pharm. Biomed. Anal.* **34** (2004) 473
15. D. Ivanović, M. Medenica, S. Marković, G. Mandić, *Arzneim. Forsch. (Drug Res.)* **50** (2000) 1004
16. *European Pharmacopoeia*, 5th Ed., Council of Europe, Strasbourg, 2002
17. *British Pharmacopoeia 98/34/EEC*, The Stationery Office, London, 2005, p. 1024
18. *The United States Pharmacopoeia, USP-27/NF-22*, Authority of the United States Pharmacopoeial Convention, Inc., Rockville, 2004, p. 987
19. The Pharmaceutical Society of Great Britain, *Clarke's isolation and identification of drugs*, The Pharmaceutical Press, London, 1986, p. 678
20. I. M. Kolthoff, E. Jacobsen, *J. Am. Chem. Soc.* **79** (1957) 3677
21. C. M. Callahan, W. C. Fernelius, B. P. Block, *Anal. Chim. Acta* **16** (1957) 101
22. K. K. Chatterjee, *Anal. Chim. Acta* **20** (1959) 423
23. A. L. Abuhijleh, *J. Inorg. Biochem.* **55** (1994) 255
24. M. Kato, Y. Muto, *Coord. Chem. Rev.* **92** (1988) 45
25. J. N. Miller, *Analyst* **116** (1991) 3
26. J. Ermer, *J. Pharm. Biomed. Anal*. **24** (2001) 755
27. D. Perez-Bendito, M. Silva, *Kinetic Methods in Analytical Chemistry*, Ellis Horwood, Chichester, 1988, p. 251
28. H. A. Mottola, *Kinetic Aspects of Analytical Chemistry*, Wiley, New York, 1988, p. 40
29. V. Thomsen, D. Schatzlein, D. Mercuro, *Spectroscopy* **18** (2003) 112
30. C. Hartmann, J. Smeyers-Verbeke, W. Penninckx, Y. V. Heyden, P. Vankeerberghen, D. L. Massart, *Anal Chem.* **67** (1995) 4491
31. D. A. Skoog, D. M. West, F. J. Holler, *Fundamentals of Analytical Chemistry*, Saunders College Publishing, Philadelphia, 1996, p. 51
32. O. I. Teslyuk, S. V. Bel'tyukova, A. V. Yegorova, B. N. Yagodkin, *J. Anal. Chem.* **62** (2007) 330
33. N. A. El Ragehy, M. Abdelkawy, A. El Bazoumy, *Anal. Lett.* **27** (1994) 2127
34. A. K. Sanyal, D. Laha, *J. AOAC Int*. **77** (1994) 1108
35. I. Singhvi, S. C. Chaturvedi, *Asian J. Chem.* **10** (1998) 879.

www.shd.org.rs

Journal of the Serbian Chemical Society

JSCS@tmf.bg.ac.yu • www.shd.org.rs/JSCS

J. Serb. Chem. Soc. 73 (8–9) 891–913 (2008)
JSCS–3771

UDC 546.26+539.24:621.315.59:519.17
Review paper

REVIEW

Carbon nanotubes

SLOBODAN N. MARINKOVIĆ*

Vinča Institute of Nuclear Sciences, P.O. Box 522, Belgrade, Serbia

(Received 14 March, revised 17 May 2008)

Abstract: Nanotubes, the last in the focus of scientists in a series of "all carbon" materials discovered over the last several decades are the most interesting and have the greatest potential. This review aims at presenting in a concise manner the considerable amount of knowledge accumulated since the discovery of this amazing form of solid carbon, particularly during the last 15 years. The topics include methods of synthesis, mathematical description, characterization by Raman spectroscopy, most important properties and applications. Problems related to the determination of CNT properties, as well as difficulties regarding their applications, in particular scaling, which would lead to their utilization, are outlined.

Keywords: carbon nanotubes; single-wall nanotubes; multi-wall nanotubes; intercalation; doping; graphene.

CONTENTS

1. INTRODUCTION
2. SYNTHESIS OF CARBON NANOTUBES
2.1. Arc method
2.2. Laser ablation
2.3. Chemical vapour deposition (CVD)
3. MATHEMATICAL DESCRIPTION OF CARBON NANOTUBES
4. CHARACTERIZATION AND PROPERTIES OF CARBON NANOTUBES
4.1. Raman spectroscopy
4.2. Electronic properties
4.3. Mechanical properties
4.4. Thermal properties
5. APPLICATIONS OF CARBON NANOTUBES
6. CONCLUDING REMARKS

* Correspondence: zmar@ptt.yu
doi: 10.2298/JSC0809891M

1. INTRODUCTION

Carbon is a versatile element and it can form various allotropes, including graphite, diamond and fullerene-like structures. In the well-known layered structure of graphite, there is a large difference in chemical bonding within the layers and between them. The σ-bonds connecting each C atom with its three neighbours within the layers are created by sp^2 hybridization. They are possibly the strongest existing chemical bonds. The remaining fourth, delocalized electron in graphite is responsible for the very weak π-bonds acting between the layers. It also determines the "semimetallic" character of graphite. The difference in the bond strength is reflected in the different bond distances: 0.142 nm between the neighbouring C atoms within the layers, as opposed to 0.335 nm between the layers. Due to the large difference in the bond strength, the layers behave in a rather "independent" way and are termed "graphene" layers.

With the study of C_{60} and C_{70}, it was soon realized that an infinite variety of closed graphitic structures could be formed, each with unique properties. All that was necessary to create such a structure was to have 12 pentagons present to close the hexagonal network (as explained by the Euler theorem). Since C_{70} was already slightly elongated, tubular fullerenes were imagined.

However, carbon nanotubes were discovered long before researchers even imagined that carbon may exist in such a form. It was in 1952 when Radushkevich and Lukyanovich reported the discovery of "worm-like" carbon formations.[1] These were observed during their study of the soot formed by decomposition of CO on iron particles at 600 °C. On the basis of many experiments and TEM images, the authors conclude that the formed product consisted of long filamentary or needle-like carbon crystals with diameters of about 50 nm (the narrowest seen in their TEM images were about 30 nm), probably hollow, growing from iron compound (probably carbide) particles. In other words, the products were carbon nanotubes. The discovered carbon nanotubes (CNTs), as we know today, were in fact multi-walled (MWNTs), but the resolution of their TEM was too low (5–6 nm) to enable the authors to see the arrangement of graphenes in the nanotube walls. It is interesting that the authors also found couples of intertwined nanotubes, resembling at the first sight the DNA double helix structure.

The discovery of nanotubes passed almost unnoticed, like a number of other studies before and after it.[2]

In 1991, researchers at the Naval Research Laboratory first predicted that by simply turning a graphene sheet into a small tube, the structure would at room temperature have a carrier density similar to that of metals and zero band gap, unlike graphite.[3]

Simultaneously, the experimental work of Iijima[4] led to what is wrongly thought today by a majority of researchers to be the first discovery of carbon nanotubes (CNTs), more specifically multiwalled nanotubes (MWNTs). When exa-

mining fullerene soot, Iijima also examined parts of the graphite electrodes of the arc generator and the graphite rod that served as a cathode and found surprisingly regular needle-like structures. A closer examination revealed that each needle consisted of several concentrically arranged seamless graphene tubes, regularly separated by about 0.34 nm spaces, the distance between layers in graphite (Fig. 1). Electron diffraction performed by TEM on individual needles revealed that the tubules seem to consist of rolled up graphene layers. Each tubule appeared to be rolled up in a different fashion, *i.e.*, it exhibited different helicity (instead of "helicity", the term "chirality" is preferred by a number of authors). The different degrees of helicity in each shell are necessary to obtain the best fit between the successive shells in a tube and minimize the interlayer distance.[5] The nanotubes, which could extend in length up to many micrometers, were closed at the end by a half-spherical or faceted cap (the caps consisted of both hexagons and pentagons) and thus resembled extremely elongated, large diameter fullerenes. This paper was the first unambiguous evidence for the possibility of growing carbon nanotubes without the need of any catalyst. It was the work of Iijima that produced a worldwide explosion of research on carbon nanotubes.

The formation of single-wall nanotubes (SWNTs) was first reported in 1993 by two papers submitted independently.[6,7] A sketch of a SWNT with caps at both ends is shown in Fig. 2.

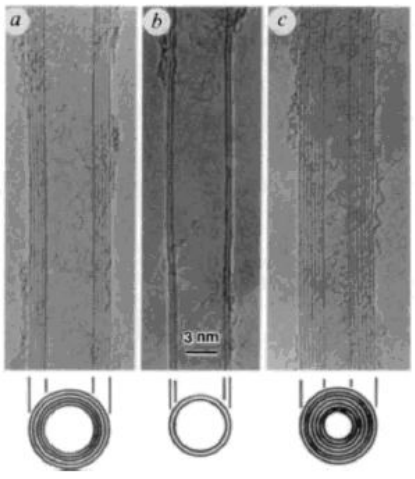

Fig. 1. Electron micrographs of carbon nanotubes. Parallel dark lines correspond to the (002) lattice images of graphite. A cross-section of each nanotube is illustrated: a) a tube consisting of five graphitic sheets, diameter 6.7 nm, b) A two-sheet tube, diameter 5.5 nm and c) A seven-sheet tube, diameter 6.5 nm, which has the smallest hollow diameter (2.2 nm).[4] (Reprinted with permission from Macmillan Publishers Ltd.).

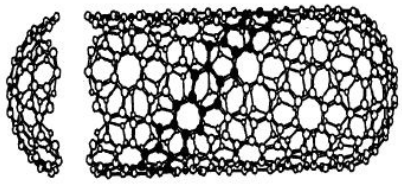

Fig. 2. Sketch of the structure of a single-wall nanotube with caps at both ends. The tube has helicity as indicated by the black coloured carbon atoms forming a screw-like array of hexagons.[8] (Reused with permission. Copyright 2000, American Institute of Physics).

Since the diameter of SWNTs can be as small as 0.4 nm with only 10 atoms around the circumference and the tubes can be only one atom in thickness, the aspect ratio (length-to-diameter) can be very large (>10^4), thus leading to a prototype one-dimensional (1D) system. In addition, depending on their diameter and helicity, CNTs are either one-dimensional metals or semiconductors. Therefore, they can be used to form metal-semiconductor, semiconductor-semiconductor, or metal–metal junctions.

The prospects of using CNTs in electronics and other fields led many researchers to study them, both experimentally and theoretically. In this review, the current knowledge on both pure and doped carbon nanotubes will be presented

2. SYNTHESIS OF CARBON NANOTUBES

Pure carbon nanotubes (CNTs), as well as B- or N-doped CNTs, can be synthesized using conditions far from equilibrium. Other dopants have been far less studied. The effect of substitutional Si atoms has recently been calculated. A number of authors deal with intercalation (insertion between neighbouring graphene layers in MWNTs, or between SWNTs in a bundle) of alkali metals, mainly K,[10–15] Li[10,16,17] and Rb,[13] but other dopants ($FeCl_3$,[12] Ba[18]), as well as La[11] and halogens (I,[19–23] Br[19]) as endohedral dopants (within the nanotube) have also been considered. Monthioux[24] gives an overview of intercalation into SWNTs.

Although there are now several methods for making nanotubes, the carbon arc method remains the most practical for scientific purposes and yields the most highly graphitized tubes, simply because the process uses a very high temperature (4000 K). The significance of properly graphitized CNTs is that only with such materials can one expect to find any correlation between theory and experiment.

2.1. Arc method

CNTs can be grown on the carbon cathode used in the d.c. arc discharge evaporation of carbon in an argon-filled vessel (100 torr).[4] The deposit generated has a hierarchical structure, with nanotubes organized in small bundles, which are themselves organized into 50 μm fibres visible to the eye. The alignment of the nanotubes along the axis of the arc current, the yield of the nanotubes and their structural quality all depend on the conditions of the arc. The most critical parameters are the inert gas pressure, the growth rate, the cooling rate, the stability of the plasma and some other variables difficult to quantify. Nanotube yields of about 60 % of the core material are obtainable under optimal conditions.[25]

The growth mechanism of nanotubes is a complex and fascinating subject. One of the first questions is why elongated structures such as nanotubes (and not balls) form although they are not thermodynamically stable. This seems to be the result of a competition between two types of carbon species present near the cathode surface, namely the anisotropic unidirectional carbon ions accelerated

across the gap, and the thermally evaporated carbon from the cathode with an isotropic velocity distribution. In other words, the introduction of an axis of symmetry in the reaction zone due to the unidirectional carbon species results in elongated structures. Analysis shows that an axis of symmetry always exists in all the methods used to generate nanotubes. For instance, in the catalytic growth of SWNTs, the catalytic particles provide this asymmetry in three dimensions.[5]

The early structures were all multi-wall nanotubes. Single-wall nanotubes with small (≈ 1 nm) and uniform diameters were synthesized simultaneously in 1993 by two research teams using arc-discharge methods with transition metal catalysts.[6,7] Crystalline ropes of SWNTs, with each rope containing tens to hundreds of tubes of approximately the same diameter, were synthesized in this early work. Subsequently, SWNTs have been synthesized by a number of researchers using the arc-discharge method.

The double-walled NT (DWNTs) occupy a somewhat special position because the interactions between the inner and the outer tube are very weak, thus making the possibility of performing studies of the individual constituents of the DWNTs at the single nanotube level. In addition, while retaining very similar morphology and properties as SWNTs, chemical reactivity of DWNTs is significantly different. This is particularly important when functionalization *(i.e.*, grafting of chemical functions at the CNT surface) is required to modify properties of the CNT.

B-doped MWNTs can be produced by arcing either BN/graphite or B/graphite electrodes in an inert atmosphere (*e.g.*, He, N_2). Large quantities of crystalline and long (≤ 100 μm) MWNTs are obtained. They contain 20–30 sheets and usually have ill-formed caps. It has proved difficult to produce B-doped SWNTs using this technique because B may obstruct the growth of the tubules under the extreme conditions.[26]

Arc experiments using pure graphite electrodes in NH_3 indicate that it is difficult to produce N-doped SWNTs and MWNTs, possibly because N_2 molecules are easily created and do not react with carbon. However, Glerup *et al.*[27] have recently demonstrated that it is possible to grow N-doped SWNTs by arcing composite anodes containing graphite, melamine, Ni and Y. The tubes exhibit a low (≤ 1 %) N concentration, and are sometimes corrugated.

2.2. Laser ablation

Pure SWNTs were produced in yields of more than 70 % by condensation of a laser-vaporized carbon–nickel–cobalt mixture.[28]

Zhang *et al.*[29] reported that sandwich-like C-BN nanotubes could be produced by laser vaporization of graphite-BN targets. Evidence for the existence of BC_7N layers within the MWNTs was reported. More recently, Gai *et al.*[30] demonstrated that B-doped SWNTs could be generated using laser vaporization of B-graphite–Co–Ni targets. The authors performed laser ablation experiments in-

side a silica tube placed in a furnace operating at 1100 °C under an Ar atmosphere at ≈ 500 torr. A laser beam (1064 nm, 10 Hz) was used to ablate a target composed of a carbon paste mixed with a Co:Ni catalyst and elemental B. SWNTs were found in the products when the B content in the target material was < 3 at. %, but with no detectable boron was present in the SWNTs. Higher B concentration resulted mostly in a mixture of graphite and metal encapsulated particles, the quantity of SWNTs being low.

Recently, Borowiak-Palen and co-workers[31] reported the production of B-doped SWNTs with higher concentrations of B, in which 15 % of the C atoms were replaced by B. These experiments were conducted by heating B_2O_3 in the presence of pure carbon SWNTs and NH_3 at 1150 °C. Further studies on these samples should be performed because the reported amount of B is too high compared to the solubility of B in graphite and MWNTs (< 2 wt % B).

2.3. Chemical vapour deposition (CVD)

CVD Synthesis of undoped CNTs is relatively easy. Both SWNTs and MWNTs can be grown by decomposing an organic gas over a substrate covered with metal catalyst particles. Nanotubes grow at the sites of the metal catalyst. Their synthesis on a relatively large scale was reported by the catalytic decomposition of hydrocarbons at 1200 °C using a floating catalyst method. The SWNTs were self-organized in rope-like bundles. Thiophene addition was found to promote the growth of the SWNTs and increase the yields of both SWNTs and MWNTs.[32] In a recent work,[33] the activity and lifetime of the catalysts were enhanced by water, thus allowing massive growth of super dense and vertically aligned nanotube "forests" with heights up to 2.5 mm, which could be easily separated from the catalysts, providing nanotube material with carbon purity above 99.98 %. The approach is applicable to other synthesis methods developed for the mass production of SWNTs.

Another approach considered to offer potential for the synthesis of carbon nanotubes (SWNTs in particular) in large quantities at significantly lower cost than that of other methods is the use flames, such as a premixed oxygen–acetylene–argon flame, with $Fe(CO)_5$ vapour as the source of the metallic catalyst.[34]

Various CVD methods have been used to synthesize N-containing CNTs. N-doped MWNTs were produced by: the thermal decomposition of N-containing hydrocarbons over Fe, Co and Ni; the pyrolysis of aminodichlorotriazine over laser-etched Co films at 1050 °C; the pyrolysis of melamine, which resulted in an increased N content (< 7 %) within corrugated tubular structures; the pyrolysis of melamine over laser-etched Fe, resulting in high yields of aligned $C_{13}N_x$ ($x < 1$) nanotubes/nanofibres (< 100 nm outer diameter, < 60 μm long); the pyrolysis of pyridine and methylpyrimidine, resulting in CN_x nanotubes with low N concentrations, which were easily oxidized compared to pure CNTs.[26]

The results showed that it is extremely difficult to generate crystalline and highly ordered structures containing large concentrations of N within a hexagonal carbon network. The degree of perfection strongly depends on the N concentration, the lower the N concentration, the more graphitic and the straighter are the nanotubes.

Of the various means for nanotube synthesis, CVD shows the most promise for industrial scale deposition in terms of its price/unit ratio. In addition, CVD is capable of growing nanotubes directly on a desired substrate, unlike the other mentioned methods. The growth sites are controllable by careful deposition of the catalyst. The CVD technique has the potential for enabling the large-scale production of nanotubes, as well as the growth of nanotubes at specific sites on microfabricated chips or at the tips of scanning probe microscopes. However, a lot of work remains to be done in this area in order to control the B or N content, as well as the nanotube structure.

3. MATHEMATICAL DESCRIPTION OF CARBON NANOTUBES

A SWNT can be mathematically described as a single graphene layer rolled up into a seamless cylinder, one atom thick, usually with a small number (perhaps 10–40) of C atoms around the circumference, and a great length (microns) along the cylinder axis. A carbon nanotube is specified by the chiral vector $\boldsymbol{C}_h$:

$$\boldsymbol{C}_h = n\boldsymbol{a}_1 + m\boldsymbol{a}_2 \quad (1)$$

where (n,m) are the pair of indices that denote the number of unit vectors $n\boldsymbol{a}_1$ and $m\boldsymbol{a}_2$. As shown in Fig. 3, the chiral vector $\boldsymbol{C}_h$ makes an angle θ, the chiral angle, with the so-called zigzag or $\boldsymbol{a}_1$ direction. The vector $\boldsymbol{C}_h$ connects two crystallographically equivalent sites O and A on a two-dimensional graphene sheet where a carbon atom is located on each vertex of the honeycomb structure. The axis of the zigzag nanotube ($m = 0$) corresponds to $\theta = 0°$, whereas the so-called armchair nanotube (for $n = m$) corresponds to $\theta = 30°$ and the nanotube axis for so-called chiral nanotubes (all other CNTs) corresponds to $0 < \theta < 30°$. The seamless cylinder joint of the nanotube is made by joining the line AB' to the parallel line OB in Fig. 3. The nanotube diameter d_t can be written in terms of the integers (n,m) as:

$$d_t = \boldsymbol{C}_h/\pi = a(m^2 + nm + n^2)^{1/2}/\pi \quad (2)$$

where $a = 1.42\times\sqrt{3}$ Å and corresponds to the lattice constant of the graphite sheet (the C–C distance is 1.42 Å).

The chiral angle θ is defined as $\theta = \tan^{-1}[\sqrt{3}m/(m + 2n)]$. Thus, a nanotube can be specified by either its (n,m) indices or equivalently by d_t and θ.

To define the unit cell for a one-dimensional nanotube, the vector OB in Fig. 3 is defined as the shortest repeat distance along the nanotube axis, thereby defining the translation vector $\boldsymbol{T}$:

$$\boldsymbol{T} = t_1\boldsymbol{a}_1 + t_2\boldsymbol{a}_2 \tag{3}$$

where the coefficients t_1 and t_2 are related to (n,m) by:

$$t_1 = (2m + n)/d_R$$
$$t_2 = -(2n + m)/d_R \tag{4}$$

where d_R is the greatest common divisor of $(2m + n, 2n + m)$ and is given by:

$$d_R = \begin{cases} d & \text{if} \quad n - m \text{ is not a multiple of } 3d \\ 3d & \text{if} \quad n - m \text{ is a multiple } 3d, \end{cases} \tag{5}$$

where d is the greatest common divisor of (n,m). The magnitude of the translation vector $\boldsymbol{T} = |\boldsymbol{T}| = \sqrt{3}L/d_R$, where L is the length of the chiral vector $\boldsymbol{C}_h = \pi d_t$ and d_t is the nanotube diameter. The unit cell of the nanotube is defined as the area delineated by the vectors $\boldsymbol{T}$ and $\boldsymbol{C}_h$. The number of hexagons, N, contained within the one-dimensional unit cell of a nanotube is determined by the integers (n,m) and is given by:

$$N = 2(m^2 + n^2 + nm)/dR \tag{6}$$

Thus, assuming 0.142 nm as the value of the C–C distance, $d_t = 1.36$ nm and $N = 20$ are obtained for a (10,10) nanotube.

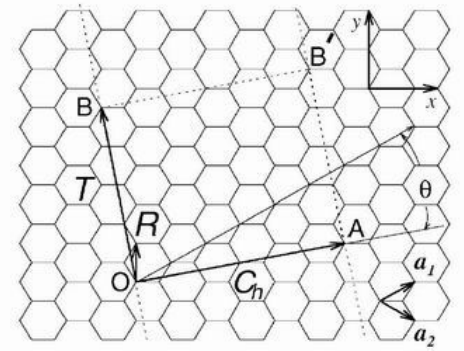

Fig. 3. a) The unrolled honeycomb lattice of a nanotube. When sites O and A, and sites B and B' are connected, a nanotube can be constructed. The vectors OA and OB define the chiral vector $\boldsymbol{C}_h$ and the translational vector $\boldsymbol{T}$ of the nanotube, respectively. The rectangle OAB'B defines the unit cell of the nanotube. The figure is constructed for an $(n,m) = (4,2)$ nanotube.[35] (Reprinted with permission from authors and publisher. Copyright 2004 by Annual Reviews, http://www.annnualreviews.org).

4. CHARACTERIZATION AND PROPERTIES OF CARBON NANOTUBES

The most important methods used to characterize CNTs are Raman spectroscopy, scanning electron microscopy (SEM), transmission electron microscopy (TEM), in particular High Resolution TEM (HRTEM), and scanning tunnelling microscopy (STM). Raman spectroscopy is capable of characterizing CNT samples, but it also provides detailed information on the vibrational modes of SWNTs and reveals a variety of unique phenomena in one-dimensional systems. Only Raman spectroscopy will be considered in this review.

4.1. Raman spectroscopy

The Raman spectra were taken with laser excitation energy E_{laser} = 2.41 eV (514.5 nm wavelength) for a SWNT bundle with diameter distribution of 1.36±0.20 nm (Fig. 4). They exhibit only two dominant features, namely, the radial breathing mode (RBM) out-of-plane vibrations, at 186 cm^{-1}, and the tangential (in-plane vibrations) band in the range from 1520–1620 cm^{-1} (Fig. 4, inset). Because of the strong connection of this tangential band to the corresponding mode in two-dimensional graphite, this higher frequency band for SWNTs is commonly called the G-band. Other lower intensity features, discussed below, also provide important and unique information about SWNTs.

The Raman spectra of SWNTs strongly and non-monotonously depend on the laser excitation energy, E_{laser}, and are associated with a resonance process for this energy with the optical transition energy between van Hove singularities in the valence and conduction bands.[36]

The results of Raman scattering studies on SWNTs[36] reveal not only many of the characteristic normal vibrational modes of a carbon nanotube, but also show that the Raman excitation frequency can be chosen to excite preferentially nanotubes of a particular diameter.

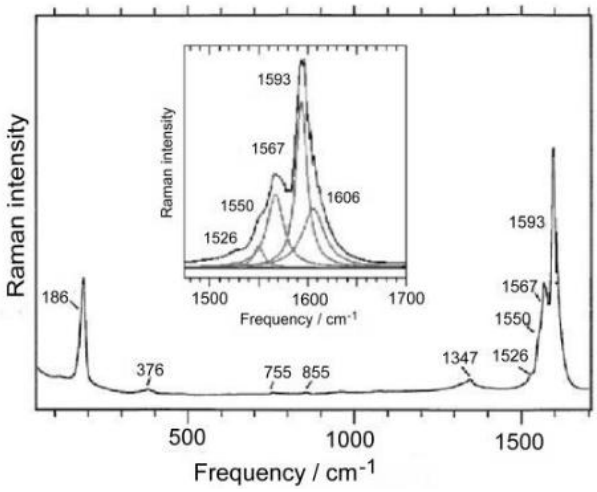

Fig. 4. The Raman spectrum taken with 514.5 nm (2.41 eV) laser excitation of a SWNT bundle sample with a diameter distribution d_t = 1.36±0.20 nm. The inset shows an expanded view of the spectra in the 1480–1700 cm^{-1} range.[36] (Reprinted with permission from AAAS.).

Figure 4 indicates that the G-band for SWNTs consists of two features: one peaking at 1593 cm^{-1} (G^+) and the other at 1567 cm^{-1} (G^-). The G^+ feature is associated with carbon atom in-plane vibrations along the nanotube axis and its frequency, ω_{G^+}, is sensitive to charge transfer from dopant additions to the SWNTs (up-shifts in ω_{G^+} for acceptors and downshifts for donors). In contrast, the G^- feature is associated with in-plane vibrations of carbon atoms along the circumferential direction of the nanotube and its line-shape is highly sensitive to whether the SWNT is metallic or semiconducting.[29] Also the D-band feature in

Fig. 4 with ω_D at 1347 cm^{-1} is commonly found in the Raman spectra of SWNT bundles, stemming from the disorder-induced mode in graphite. Its second harmonic, the G'-band (not shown), occurring at $\approx 2\omega_D$, is associated with a double resonance process.[35] Both the D-band and the G'-band are sensitive to the diameter and helicity of a nanotube.

Jorio[37] stated that the Raman scattering technique could provide complete structural information for 1-D systems, such as carbon nanotubes. Due to the sharp van Hove singularities occurring in carbon nanotubes with diameters less than 2 nm (see Fig. 7), the Raman intensities for the resonance Raman process can be so large that it is possible to observe the Raman spectra from one individual SWNT. The isolated SWNTs were prepared by a chemical vapour deposition method on an oxidized Si substrate containing nanometre-sized iron catalyst particles. The helicity of an (n,m) individual single-wall nanotube can be assigned uniquely by measuring one radial breathing mode frequency ω_{RBM} and using the theory of resonant transitions. A unique helicity assignment can be made for both metallic and semiconducting nanotubes.[37] The differences in the G-band spectra between semiconducting and metallic SWNTs are shown in Fig. 5.

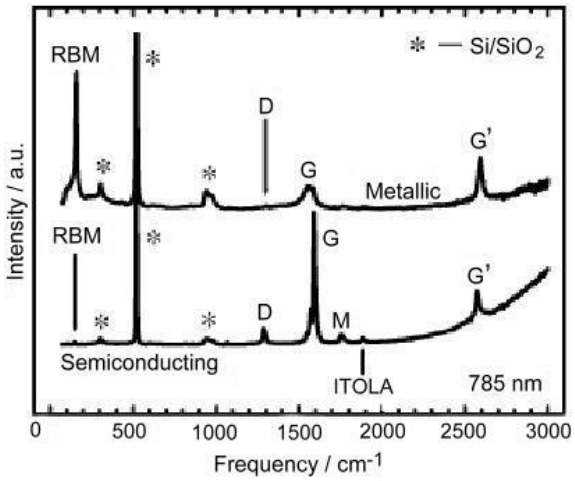

Fig. 5. Raman spectra from a metallic (top) and a semiconducting (bottom) SWNT at the single nanotube level, showing the radial breathing mode (RBM), D-band, G-band, and G'-band features, in addition to weak double resonance features (785 nm (1.58 eV) laser).The silicon substrate provides contributions to the Raman spectra, denoted by ∗.[35] (Reprinted with permission from authors and publicsher. Copyright 2004 by Annual Reviews, http://www.annnualreviews.org).

Measurements on the G-band at the single nanotube level show that this feature is a first-order process, with the frequency ω_{G^+} essentially independent of d_t or chiral angle θ, while ω_{G^-} is only dependent of d_t and not on θ. Such diameter dependent measurements can be done only at the single nanotube level.[37]

Raman spectra of carbon nanotubes, particularly at the single nanotube level, have been particularly rich in information. Due to the simplicity of the geometrical structure of nanotubes, detailed analysis of the Raman spectra has yielded a lot of information about phonon dispersion relations, such as information about their trigonal warping. This information was, in fact, not yet available for two-di-

mensional graphite but could be studied in nanotubes because of their one-dimensionality.[38] Thus, studies on carbon nanotubes are revealing a lot of important information about the electrons and phonons in 2-D graphite through studies at the single nanotube level, where the orientation of the wave vector can be explicitly probed, in contrast to the situation in 2-D graphite, which only allows measurements to be made as a function of the magnitude of the wave vector.[38]

4.2. Electronic properties

The nanometre dimensions of carbon nanotubes together with the unique electronic structure of a two-dimensional graphene sheet make the electronic properties of these one-dimensional carbon nanotube structures highly unusual.

The theory was ahead of experiment as far as the electronic properties of CNTs are concerned. Early theoretical calculations showed that the electronic properties of the carbon nanotubes are very sensitive to their geometric structure.[26] While graphene sheet is a zero-gap semiconductor in which the π-electrons propagate in all directions (2-dimensionally), theory has predicted that carbon nanotubes, where the electrons propagate only along the tube axis, can be either metals or semiconductors with different size energy gaps, depending very sensitively on the diameter and helicity of the tubes, *i.e.*, on the indices (*n*,*m*). The physics behind this sensitivity of the electronic properties of carbon nanotubes to their structure can be understood within the zone-folding picture.

If $n–m = 3j$, where j is an integer, the SWNTs are metallic*. On the other hand, all SWNTs with $n–m = 3j\pm1$ are large-gap (< 1.0 eV for $d_t < 0.7$ nm) semiconductors. Thus, for a uniform distribution of (*n*,*m*) values, there is a one-in-three chance of a SWNT being a metal and a two-in-three chance of it being a semiconductor.

These unique electronic properties arise from the quantum confinement of the electrons normal to the nanotube axis. In the radial direction, the electrons are confined by the monolayer thickness of the graphene sheet (≈ 0.350 nm).

Sufficiently strong hybridization effects between the σ and π states can occur through tube curvature effects in small-diameter nanotubes and these hybridization effects significantly alter their electronic structure. For example, a (5,0) tube, which is predicted to be semiconducting (see above), has been shown to be metallic by *ab initio* calculations.[35] Unusual properties have also been found in ultra-small diameter SWNTs ($d_t \approx 0.4$ nm), produced by confining their synthesis to occur inside zeolite channels.[39] This nanotube is the narrowest attainable that can still remain energetically stable, as predicted by theory. These ultra-small

* Strictly speaking, due to tube curvature effects, a tiny band gap opens up when j is not 0. However, for most experimentally observed carbon nanotubes, the gap would be so small that, for most practical purposes, all the $n–m = 3j$ tubes can be considered as metallic at room temperature because their thermal energy is sufficient to excite electrons from the valence to the conduction band.

diameter SWNTs have been reported to exhibit a variety of unusual properties for an all-carbon system, such as superconductivity.[40] The unit cell for such ultra-small diameter SWNTs is small enough to permit detailed and accurate *ab initio* calculations of their electronic structures.

Carbon nanotubes often have defects, such as pentagons, heptagons, vacancies or dopants, that drastically modify their electronic properties, which are, of course, more complex than those for infinitely long, perfect nanotubes. On the other hand, the introduction of defects into the carbon network is an interesting way to tailor its intrinsic properties to create new potential nanodevices and to propose new potential applications for nanotubes in nano-electronics.

The differences between the doped graphene sheet and CNT have been calculated.[41] Doping of a graphene sheet with 0.5 % B or N provokes a slight increase and shift in the electronic states close to the Fermi level (E_f), B (electron acceptor) in the valence band and N (electron donor) in the conduction band. Thus, density of states (DOS) *vs*. energy curves for a pure (undoped) and doped graphene sheets are quite similar to each other (Fig. 6). However, corresponding curves for doped and undoped nanotubes are quite different (Fig. 7). Because of the quantum confinement in the CNTs, being a consequence of their nanometer dimensions, the resulting number of 1-D conduction and valence bands effectively depends on the standing waves set-up around the circumerence of the nanotube. The spikes are called "van Hove" singularities and are typical of 1-D quantum conduction, which is not present in an infinite graphite crystal.

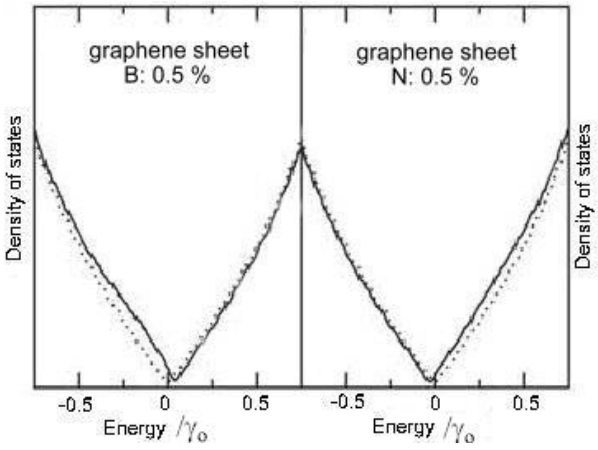

Fig. 6. DOS for doped and undoped graphene sheets (solid and dotted curves, respectively) (Terrones *et al.*[26] on the basis of results of Latil *et al.*[41]) (Reprinted with permission. Copyright Elsevier (2004).).

Little work has been performed on doping SWNTs with either B or N. However, it is believed that these systems should exhibit unusual quantum effects and it should be possible to tailor the band gaps of semiconducting SWNTs when doping at very low concentration levels. It should be pointed out that, in order to observe genuine quantum effects in doped CNTs, the dopants must be present within SWNTs of narrow diameter (< 1–2 nm).[26]

In N-doped SWNTs, N could be present substitutionally (N coordinated to three C atoms in an sp^2-like fashion), or as a pyridine-type N (two coordinated N), which can be incorporated into the SWNT, provided that a C atom is removed from the framework. This type of defect induces localized states below and above the Fermi level. Therefore, substitutional N doping in SWNTs should result in *n*-type conducting behaviour, whereas pyridine-type N may produce either a *p*- or *n*-type conductor, depending on the doping level, the number of N atoms, and the number of removed C atoms within the hexagonal sheet.

In experiments on simultaneous doping of SWNTs, bundles of B- and N-doped single-walled carbon nanotubes (SWNTs) containing up to ≈ 10 at. % B and up to ≈ 2 at. % N were synthesized at high yields under thermochemical treatment of pure carbon SWNT bundles and B_2O_3 in a flowing nitrogen atmosphere.[42]

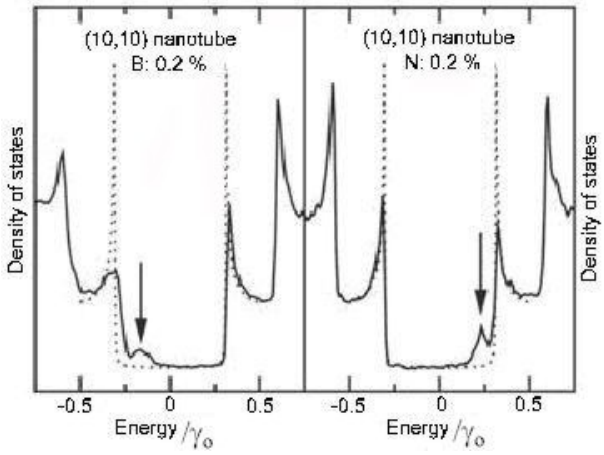

Fig. 7. DOS for doped and undoped metallic CNTs (solid and dotted lines, respectively). Note the peaks in the curves for the doped CNTs (arrows) in the valence band (B) and conduction band (N) (Terrones *et al.*[26] on the basis of results of Latil *et al.*[41]). (Reprinted with permission. Copyright Elsevier (2004).).

The amphoteric character of SWNTs, *i.e.*, their ability to exchange electrons with a dopant atom (or molecule) to form the corresponding positively or negatively charged counterion, has been shown also for the SWNTs exposed to typical electron-donor (potassium, rubidium) and electron-acceptor (iodine, bromine) dopants.[19]

Intercalation of single-wall carbon nanotubes (SWNTs) provides an important tool to modify their electronic band structure. In a particular case of the relatively large iodine ions, the size of SWNTs and the size of iodine are comparable. A commercial material used in the work of Grigorian *et al.*[20] comprised predominantly (6,5) and (7,5) nanotubes with diameters d_t = 0.757 and 0.829 nm, respectively. Taking into account the thickness of the nanotube wall (≈ 0.350 nm), the inner diameters d_{in} were 0.407 and 0.479 nm, respectively. The diameter of the iodine ions (d_I = 0.432 nm) is between these two values. Therefore, larger SWNTs with iodine-filled interiors were found to carry significantly higher charge density as compared to smaller empty ones.[20]

According to recent calculations,[9] silicon substitutional doping of SWNTs can dramatically change the local atomic and electronic structures of the SWNT at the doping site, which results in its preference to form sp^3 bonding, and the band structure of the doped SWNT exhibits a very different characteristic from that of the pristine SWNT. For the (5,5) tube, the metallic band structure can be changed into a doped degenerated semiconducting band structure with a distinct band gap and an unoccupied impurity band above the Fermi level. In addition, due to the formation of sp^3 bonds, the doping silicon atom can improve the local reaction activity of the tube.

4.3. Mechanical properties

Since the carbon–carbon chemical bond in a graphene layer is probably the strongest chemical bond known in nature (the sp^2 bond in graphite is stronger than the sp^3 bond in diamond), carbon nanotubes are expected to have exceptionally good mechanical properties, with significant potential for applications in the reinforcement of composite materials.

Some of the important parameters characterizing the mechanical properties of carbon nanotubes include their elastic constants, Young's modulus, Poisson ratio, response to deformation in the elastic regime, tensile and compressive strains, yield mechanism and strength at failure, toughness, and buckling when bent. One of the unusual features of nanotubes is that they simultaneously combine widely varying length scales: their length can be macroscopic, up to millimetres, whereas their diameters are on the nanoscale.

The manipulation of nanoscale objects is a difficult and challenging task. Nevertheless, a number of direct experimental measurements of the Young's modulus, Y, of nanotubes have appeared in the literature. Calculations show that the Young's modulus of isolated SWNTs does not depend greatly on the nanotube diameter or chiral angle and has a value of approximately 1 TPa, corresponding to the asymptotic limit reported for carbon fibres,[35] whereas Y for MWNTs decreases somewhat with increasing d_t. Despite the very high Young's modulus for carbon nanotubes, atomic force microscopy (AFM) measurements[43] indicate that nanotubes can bend into loops without breaking, testifying to their flexibility, toughness, and capacity for reversible deformation. Small-diameter SWNTs can be elongated by ≈ 30 % before breaking,[41] and values for the breaking strength of 55 GPa have been reported.[44] Tensile strength experiments performed on MWNTs showed that they break at the outermost layer, with the inner layers being pulled out like a sword from its sheath, and somewhat smaller values for the tensile strength were found for MWNTs.[44]

Under bending stress, MWNTs bend by stretching in the outer arc and by compression in the inner arc. For nanotubes with diameters $d_t < 12$ nm, the effective bending modulus was found to have a value of approximately 1 TPa.[45]

However, for MWNTs of larger diameters, the effective bending modulus drops dramatically to values of approximately 100 GPa. From these experiments, it was concluded that MWNTs, although difficult to stretch axially, are easy to bend laterally and they could reversibly withstand large lateral distortions.

Determining the actual strength of nanotubes from simulation is a challenging task. Atomistic calculations indicate that chiral tubes have a lower yield strain than either zigzag or armchair nanotubes,[35] which lowers their mechanical strength.

Concerning doped CNTs, the mechanical properties should not be substantially altered if the dopant concentration is low (*e.g.*, < 0.5 % N).[26]

Hernández and co-workers have calculated the mechanical properties of CN_x and CB_x nanotubes. Their results predict that of all the types of nanotubes considered (pure and doped), pure carbon nanotubes have the highest Young's modulus, approaching those of flat graphene-like sheets. They demonstrated that, although high concentrations of B and/or N within SWNTs lower the Young's modulus, the values still remain in the order of 0.5–0.8 TPa.[46,47]

However, the experimental values are quite different from the theoretical ones. For example, the Young's moduli for pristine and N-doped MWNTs are 0.8–1 TPa and ≈ 30 GPa, respectively. The low values observed for N-doped nanotubes are probably the result of the relatively high N concentration (*e.g.*, 2–5 %) within the tubes, which introduces defects and lowers the mechanical strength.[26]

Recent results showed that CNTs exhibit virtually no fatigue.[48] A 2 mm square block of vertically aligned, multi-walled nanotubes still retains its original structural integrity and properties after being compressed and released more than 500,000 times. The results show that the ability of CNTs to resist wear and tear is similar to the behaviour of muscles, stomach lining, and other soft tissues. This ability, coupled with the strong electrical conductivity of CNTs, suggests that they could be used to create artificial muscles.

4.4. Thermal properties

Although the thermal properties of carbon nanotubes, including their specific heat, thermal conductivity, and thermopower, are quite special, the thermal properties of SWNTs have not been as extensively studied as the electronic, mechanical, or phonon properties of SWNTs, in part because the techniques for making such studies are still under development. The thermal properties of carbon nanotubes display a wide range of behaviours that stem from their relation to the corresponding properties of a two-dimensional graphene layer and from their unique structure and tiny size.[35]

At high temperatures, the specific heat of individual nanotubes should be similar to that of two-dimensional graphene, with the effects of phonon quantization becoming apparent at lower temperatures for SWNTs of small diameter (< 2 nm), where a linear T-dependence of the specific heat is expected. To study

the intrinsic thermal conductivity and thermoelectric power of nanotubes, measurements must be made at the single nanotube level. Such measurements are technically very difficult to realise. Therefore, work in this area is just beginning to appear in the literature.

The thermal conductivity of graphite is generally dominated by phonons and is limited by the small crystallite size within a sample. The apparent long-range crystallinity of nanotubes and the long phonon mean free path led to the speculation that their longitudinal thermal conductivity could possibly exceed the in-plane thermal conductivity of graphite, which, together with diamond, has the highest thermal conductivity of known materials. The reason for the very high thermal conductivity follows from the very high velocity of sound based on kinetic theory arguments and relates to the very high Young's modulus of carbon nanotubes. From the viewpoint of application, it is important that nanotubes have a high thermal conductivity and can conduct heat efficiently, which would prevent structural damage while used as current-carrying wires in micro/nano devices.

Measurements of the temperature-dependent thermal conductivity $\kappa(T)$ for an individual MWNT (14 nm diameter)[49] show very high values of κ (more than 3000 W m K^{-1}), comparable to graphite (in-plane). It is believed that smaller diameter tubes (probably individual SWNTs) will be needed to exhibit thermal conductivities greater than that of graphite. The small diameter of SWNTs causes phonon quantization, which should be observable in the heat capacity and in the thermal conductivity at low T.

The thermal expansion of a SWNT bundle was measured using X-ray diffraction techniques,[50] and the results are consistent with expectations based on graphite. The measurements showed a very small negative thermal expansion along the nanotube axis direction ($-0.15\pm0.20\times10^{-5}$ K^{-1}) but a value of $0.75\pm\pm0.25\times10^{-5}$ K^{-1} was found for the expansion along the of the diameter direction of the SWNT in the temperature range 300–950 K.

Thermopower (TEP) measurements have been of substantial interest in nanotube research. However, most TEP measurements were performed on SWNT bundles with random orientations leading to phenomena dominated by intertube interactions, rather than the intrinsic behaviour of individual SWNTs.

Thermal measurements at the individual nanotube level are expected to have a major impact on the direction of future studies on the thermal properties of nanotubes.

5. APPLICATIONS OF CARBON NANOTUBES

The ultimate electronic device miniaturization would be to use individual molecules as functional devices. Single-wall carbon nanotubes are promising candidates for achieving this. Depending on their diameter and helicity, they are either one-dimensional metals or semiconductors. As already mentioned, they can

therefore be used to form metal–semiconductor, semiconductor–semiconductor, or metal–metal junctions.

Several major steps toward nanotube-based circuitry have been achieved: single-electron transistors employing metallic nanotubes have been demonstrated. An array of field-effect transistors has been made by selectively burning-off metallic nanotubes in SWNT ropes, and several research groups have assembled field-effect transistors based on single nanotubes into logic circuits, which are the building blocks of computers, showing promise for future developments in nanocircuitry.[35]

Intramolecular devices have also been proposed which should display a range of other device functions. For example, by introducing a pentagon and a heptagon into the hexagonal carbon lattice, two tube segments with different atomic and electronic structures can be seamlessly fused together to create intramolecular metal–metal, metal–semiconductor, or semiconductor–semiconductor junctions. Both the existence of such atomic-level structures and investigations of their respective electronic properties have already been carried out experimentally.[51,52]

Joining a semiconducting nanotube to a metallic one, using a pentagon–heptagon pair incorporated in the hexagonal network can be the basis of a nanodiode (or molecular diode) for nano-electronics. An example of such a diode structure is the junction of a semiconducting (8,0) nanotube, which has a 1.2 eV gap in the tight-binding approximation, and a metallic (7,1) tube (although a small curvature-induced gap is present close to the Fermi energy). Nanotube junctions can thus behave as nanoscale metal-metal junctions, metal-semiconductor Schottky barrier junctions, or semiconductor heterojunctions with novel properties, and these different types of junctions can serve as building blocks for nanoscale electronic devices.[35]

A SWNT *p–n* junction diode device has recently been demonstrated.[53] The *p–n* junction was formed along a single nanotube by electrostatic doping using a pair of split gate electrodes. The device can function either as a diode or as an ambipolar field-effect transistor.

An interesting recent development is the employment of the electron beam of a transmission electron microscope to covalently connect crossed SWNTs, which can be useful for device applications. Electron beam welding at elevated temperatures was used to produce molecular junctions of various geometries ("X," "Y," and "T" junctions) and these junctions were found to be stable after the irradiation process. To study the relevance of some of these nanostructures, various models of ideal molecular junctions were generated. The presence of heptagons plays a key role in the topology of nanotube-based molecular junctions. The flexibility of the nanoscale design and the availability of both semiconducting and metallic nanotubes enable a wide variety of configurations. Junctions between semiconducting and metallic nanotubes can act as diodes. Junc-

tions between two crossed nanotubes can act as rectifiers and Y-, T-, or X-junctions and provide more exotic configurations for nanoscale devices.[54]

Another recent publication[55] describes the fabrication of ultrathin, transparent, optically homogeneous, electrically conducting films of pure single-walled carbon nanotubes and the transfer of these films to various substrates, in order to extend the application of CNTs in electronics.

A number of potential applications arise if, instead of undoped CNTs, B- or N-doped nanotubes are used. Theoretical calculations and experimental results[56] have shown that B-doped MWNTs could exhibit enhanced field emission (turn-on voltages of ≈ 1.4 V μm^{-1}) when compared to pristine carbon MWNTs (turn-on voltages of ≈ 3 V μm^{-1}). This phenomenon arises from the preferential presence of B atoms at the nanotube tips, which results in an increased density of states close to the Fermi level. Similarly, Golberg *et al.*[57] demonstrated that N-doped MWNTs are able to emit electrons at relatively low turn-on voltages (2 V μm^{-1}) and high current densities (0.2–0.4 A cm^{-2}). More recently, it was found[26] that individual N-doped MWNTs exhibit excellent field emission properties at 800 K: experimental work functions of 5 eV and emission currents of ≈ 100 nA were obtained at ±10 V. One of the first demonstrated applications was intense electron emitters for large displays, with the metal tips replaced by CNTs. The improvements were a clearer picture, longer life of the emitter and a simpler device, which need neither ultrahigh vacuum nor high temperature (the CNTs emit electrons at room temperature).

Thus, both B- and N-doped CNTs may have great potential as building blocks for stable and intense field-emission sources.

The next application involves the well-known Li^+ batteries (with the Li^+ ions intercalated between the layers in graphite) used for portable computers, mobile telephones, digital cameras, *etc*. If instead of graphite, N-doped CNTs are used, much higher energy storage (480 mA h g^{-1}) will be achieved than in commercial carbon materials used for Li^+ batteries (330 mA h g^{-1}). Interestingly, such nanotubes consist of many short segments with one end closed and the other one open. Upon Li^+ intercalation into the N-doped MWNTs, the graphene layers (the number of which is several tens) expanded and become partly disordered, while after deintercalation, they reorder to a certain degree.[58]

An important application from the ecological viewpoint is for sensors detecting hazardous gases. The N-doped MWNTs have proved more efficient than pure SWNTs or MWNTs, displaying a fast response in the order of milliseconds when exposed to toxic gases and organic solvents, reaching saturation within 2–3 s. Furthermore, while CO and H_2O molecules apparently do not react with the surface of pure carbon SWNTs, if the surface of the tube was doped with a donor or an acceptor, drastic changes in the electronic properties were observed as a result of the binding of the molecules to the doped locations.[26]

An obvious potential application of the CNTs is to reinforce plastic-based composites. The huge strength and modulus values found (see 4.3. Mechanical properties) indicate that composites with CNT reinforcement should have much higher mechanical properties than any other material known. In principle, the preference is to use single-walled tubes for making composites, because the inner layers of multi-walled tubes probably contribute little to the carrying load.

Standard composites with continuous-carbon-fibre reinforcement have excellent stiffness and strength combined with low density, but are expensive to process and are limited to simple shapes, such as sheets and tubes. Short fibre composites, on the other hand, can be moulded, but the fibres become chopped down to a maximum length of about 1 mm during the processing. At this length, the aspect ratio is only about 100, which is not enough to make an extremely strong material. Nanotubes can have aspect ratios of 1,000 or more, and hence, in theory, they should make excellent composites.

However, experiments intended to make strong composites with CNTs have been unsuccessful.[59] The main reason is that highly crystalline CNTs tend to be similar to graphite, and chemically "inert", and it is, therefore, necessary to modify their surface so that efficient tube–matrix interactions can be achieved. The doping with silicon seems to offer a possible solution to this problem,[9] because Si tends to form sp^3 bonds, thus increasing the reactivity of the CNT surface. This, however, remains to be experimentally verified.

The creation of nanotubes containing a few foreign atoms, such as N or B, in the hexagonal network could also circumvent the problem of the non-reactivity of the surface of CNTs. The mechanical properties of the CNTs would not be significantly changed if the dopant concentration were low. Nevertheless, not many experiments have been made so far and much further work is required to solve the problem of fabricating CNT-reinforced plastic matrix composites in a way suitable for commercial production.[26]

Other possible mentioned usages of nanotubes[56] are STM and AFM tips, gas storage devices, actuators, high power electrochemical capacitors, nanothermometers, Fe-filled nanotubes as magnetic storage devices, *etc*. Thus, although a number of early nanotube-based devices have already been demonstrated, the production and integration of nanotube components into reproducible device structures still present many challenges.

Of particular interest is research aimed at merging biotechnology with materials (especially nanomaterials) science. This will allow not only the advantage of improved evolutionary biological components to be taken to generate new smart materials but also to apply today's characterization and fabrication techniques of advanced materials to solving biological problems. Carbon nanotubes functionalized with biological molecules (such as protein peptides and nucleic acids) show great potential for application in bioengineering and nanotechnology.

A fundamental understanding, description, and regulation of such bio-nanosystems will ultimately lead to a new generation of integrated systems combining the unique properties of the carbon nanotube with biological recognition capabilities.[60] A recent article[61] describes a developed multi-step method to covalently link DNA with functionalized MWNTs.

The considerable progress in research concerned with CNTs has further increased their potential in biological and biomedical applications.[62] The recent expansion and availability of chemical modification and bio-functionalization methods have enabled the generation of a new class of bioactive carbon nanotubes which are conjugated with proteins, carbohydrates, or nucleic acids. The final aim is to target and to alter the behaviour of cells at the subcellular or molecular level. Current research topics aim at translating biotechnology modified nanotubes into potential novel therapeutic approaches.

Although the list of potential applications of CNTs is rather impressive, the actual practice restrains it to a few issues. The electronic applications seem to be the most important, but numerous problems must be solved. These involve control of helicity, structure and length, but more fundamental studies are also required, such as growth mechanisms of CNTs. According to some predictions,[63] the scaling of microelectronic devices could lead to the utilization of carbon nanotubes in about ten years. Among the applications already developing are field emission displays, field-effect transistors, atomic-force microscope probe tips, interconnects in advanced CMOS manufacture. Some encouraging data are that a process for fabricating CNTs at room temperature has been developed, and its first commercial appearance has already occurred (in 2007).[64]

6. CONCLUDING REMARKS

With diameters of down to 0.4 nm, only one atom in thickness, and length of up to many microns, carbon nanotubes (CNTs) represent a prototype of a one-dimensional (1-D) system. In addition, depending on their diameter and helicity, CNTs are either 1-D metals or large-gap semiconductors. Due to the unique properties of CNTs, there are great expectations that their practical applications will eventually be developed. In addition, they will be used for further theoretical and experimental studies.

The original difficulties in the synthesis of sufficient quantities of pure and well-characterized CNTs for detailed, systematic experimental investigations have largely been overcome. However, due to experimental difficulties, much remains to be performed in the study of their properties.

B- or N-doped CNTs, SWNTs in particular, should exhibit novel electronic, chemical, and mechanical properties that are not found in their pure carbon counterparts, and are likely to become more useful than undoped material. This is particularly true for low concentrations of the dopants (*e.g.*, < 0.5 %), because in this

case the conductance should be significantly enhanced and the mechanical properties would not be significantly altered. In addition, because of the presence of holes (B-doped tubes) or donors (N-doped tubes), their surface should become more reactive, which would be extremely useful in the development of field-emission sources, nanoelectronics, sensors, and strong composite materials. Unfortunately, efficient routes to dope SWNTs are still awaiting development.

It is worth mentioning that substitutional dopants other than B and N also deserve attention. This is true not only for P (donor), but also for Si, in view of their respective effects in pyrolytic carbon (see for example Ref. 65).

Acknowledgment. The author expresses his thanks to B. Djurašević (Vinča Institute of Nuclear Sciences, Belgrade, Serbia) for his help in providing the necessary literature.

И З В О Д

УГЉЕНИЧНЕ НАНОЦЕВИ

СЛОБОДАН Н. МАРИНКОВИЋ

Институт за нуклеарне науке "Винча", п. пр. 522, 11000 Београд

Иако откривене пре више од пола века, угљеничне наноцеви су доспеле у жижу интересовања научне јавности тек после поновног "открића" 1991. године. Овај до скора непознат, ванредно занимљиви облик елементарног угљеника, надовезује се на низ других угљеничних материјала откривених током последњих деценија, који су у знатној мери омогућили развој високе технологије, али и изменили наш свакодневни живот. У овом прегледу је сажето приказано обимно, мада још недовољно знање о угљеничним наноцевима, стечено у току последњих петнаестак година. Обухваћене су методе синтезе, математички опис, карактеризација Раманском спектроскопијом. Најважнија својства и примене. Наведени су проблеми у вези са одређивањем својстава наноцеви, као и тешкоће везане за њихову примену, нарочито преношење технологије производње на (полу)индустријски ниво.

(Примљено 14. марта, ревидирано 17. маја 2008)

REFERENCES

1. L. V. Radushkevich, V. M. Lukyanovich, *Zhurn. Fizich. Khim*. **26** (1952) 88 (in Russian)
2. M. Monthioux, V. L. Kuznetsov, *Carbon* **44** (2006) 1621
3. J. W. Mintmire, B. I. Dunlap, C. T. White, *Phys. Rev. Lett*. **68** (1992) 631
4. S. Iijima, *Nature* **354** (1991) 56
5. T. W. Ebbesen, *Phys. Today* **49** (1996) 26
6. S. lijima, T. Ichihashi, *Nature* **363** (1993) 603
7. D.S. Bethune, C.H. Klang, M.S. deVries, G. Gorman, R. Savoy, J. Vazquez, R. Beyers, *Nature* **363** (1993) 605
8. W. Krätschmer, in *Fullerenes and Nanotubes – An Introduction*, Hans Kuzmany, Ed., *Conference Proceeding* **544** (2000) 3, American Institute of Physics, Melville, NY, USA
9. C. X. Song, Z. Yueyuan, L. Mingwen, L. Xiangdong, H. Feng, Z. Boda, B. Hongyu Zhang, *Phys. Lett. A* **358** (2006) 166
10. P. Chen, X. Wu, J. Lin, K. L. Tan, *Science* **285** (1999) 91

11. S. Eisebitt, A. Karl, A. Zimina, R. Scherer, M. Freiwald, W. Eberhardt, F. Hauke, A. Hirsch, Y. Achiba, *AIP Conf. Proc*. **544** (2000) 380
12. X. Liu, T. Pichler, M. Knupfer, M. S. Golden, J. Fink, H. Kataura, *AIP Conf. Proc*. **633** (2002) 267
13. N. M. Nemes, J. E. Fischer, K. Kamaras, D. B. Tanner, A. G. Rinzler, *AIP Conf. Proc.* **633** (2002) 259
14. H. Rauf, T. Pichler, F. Simon, H. Kuzmany, *AIP Conf. Proc*. **723** (2004) 213
15. T. Pichler, H. Rauf, M. Knupfer, J. Fink, H. Kataura, *Synth. Met.* **153** (2005) 333
16. P. Petit, E. Jouguelet, C. Mathis, P. Bernier, *AIP Conf. Proc*. **544** (2000) 395
17. L. Petaccia, A. Goldoni, S. Lizzit, R. Larciprete, *J. El. Spectr. Relat. Phenom*. **144–147** (2005) 793
18. X. Liu, T. Pichler, M. Knupfer, J. Fink, *AIP Conf. Proc*. **723** (2004) 205
19. A. M. Rao, P. C. Eklund, S. Bandow, A. Thess, R. E. Smalley, *Nature* **388** (1997) 257
20. L. Grigorian,, S. Colbern, I. O. Maciel, M. A. Pimenta, F. Plentz, A. Jorio, *Nanotechnology* **18** (2007) 435705
21. X. Fan, E. C. Dickey, P. C. Eklund, K. A. Williams, L. Grigorian, R. Buczko, S. T. Pantelides, S. J. Pennycook, *Phys. Rev. Lett.* **84** (2000) 4621
22. L. Grigorian, K. A. Williams, S. Fang, G. U. Sumanasekera, A. L. Loper, E. C. Dickey, S. J. Pennycook, P. C. Eklund, *Phys. Rev. Lett.* **80** (1998) 5560
23. N. Bendiab, R. Almairac, S. Rols, R. Aznar, J.-L. Sauvajol, I. Mirebeau, *Phys. Rev. B* **69** (2004) 195415
24. M. Monthioux, *Carbon* **40** (2002) 1809
25. T. W. Ebbesen, P. M. Ajayan, *Nature* **358** (1992) 220
26. M. Terrones, A. Jorio, M. Endo, A. M. Rao, Y. A. Kim, T. Hayashi, H. Terrones, J.-C. Charlier, G. Dresselhaus, M. S. Dresselhaus, *Mater. Today* **7(10)** (2004) 30
27. M. Glerup, J. Steinmetz, D. Samaille, O. Stephan, S. Enouz, A. Loiseau, S. Roth, P. Bernier, *Chem. Phys. Lett.* **387** (2004) 193
28. A. Thess, R. Lee, *Science* **273** (1996) 483
29. Y. Zhang, H. Gu, K. Suenaga, S. Iijima, *Chem. Phys. Lett*. **279** (1997) 264
30. P. L. Gai, O. Stephan, K. McGuire, A. M. Rao, M. S. Dresselhaus, G. Dresselhaus, C. Colliex, *J. Mater. Chem*. **14** (2004) 669
31. E. Borowiak-Palen, T. Pichler, G. G. Fuentes, A. Graff, R. J. Kalenczuk, M. Knupfer, J. Fink, *Chem. Phys. Lett*. **378** (2003) 516
32. R. Saito, M. Fujita, G. Dresselhaus, M. S. Dresselhaus, *Appl. Phys. Lett.* **60** (1992) 2204
33. K. Hata, D. N. Futaba, K. Mizuno, T. Namai, M. Yumura, S. Iijima, *Science* **306** (2004) 1362
34. M. J. Height, J. B. Howard, J. W. Tester, J. B. Vander Sande, *Carbon* **42** (2004) 2295
35. M. S. Dresselhaus, G. Dresselhaus, A. Jorio, *Annu. Rev. Mater. Res*. **34** (2004) 247
36. A. M. Rao, E. Richter, S. Bandow, B. Chase, P. C. Eklund, K. A. Williams, S. Fang, K. R. Subbaswamy, M. Menon, A. Thess, R. E. Smalley, G. Dresselhaus, M. S. Dresselhaus, *Science* **275** (1997) 187
37. A. Jorio, R. Saito, J. H. Hafner, C. M. Lieber, M. Hunter, T. McClure, G. Dresselhaus, M. S. Dresselhaus, *Phys. Rev. Lett*. **86** (2001) 1118
38. Ge. G. Samsonidze, R. Saito, A. Jorio, A. G. Souza Filho, A. Grüneis, M. A. Pimenta, G. Dresselhaus, M. S. Dresselhaus, *Phys. Rev. Lett*. **90** (2003) 027403
39. N. Wang, Z. K. Tang, G. D. Li, J. S. Chen, *Nature* **408** (2000) 50

40. Z. K. Tang, L. Zhang, N. Wang, X. X. Zhang, G. H. Wen, G. D. Li, J. N. Wang, C. T. Chan, P. Sheng, *Science* **292** (2001) 2462
41. S. Latil, S. Roche, D. Mayou, J.-C. Charlier, *Phys. Rev. Lett.* **92** (2004) 256805
42. D. Golberg, Y. Bando, L. Bourgeois, K. Kurashima, T. Sato, *Carbon* **38** (2000) 2017
43. M. R. Falvo, G. J. Clary, R. M. Taylor, V. Chi, F. P. Brooks Jr., S. Washburn, R. Superfine, *Nature* **389** (1997) 582
44. M.-F. Yu, B. S. Files, S. Arepalli, R. S. Ruoff, *Phys. Rev. Lett*. **84** (2000) 5552
45. P. Poncharal, Z. L. Wang, D. Ugarte, W. A. de Heer, *Science* **283** (1999) 1513
46. E. Hernández, C. Goze, P. Bernier, A. Rubio, *Phys. Rev. Lett*. **80** (1998) 4502
47. E. Hernández, C. Goze, P. Bernier, A. Rubio, *Appl. Phys*. *A* **68** (1999) 287
48. C. Reinhold, *Mater. Today* **10(9)** (2007) 10
49. J. P. Small, L. Shi, P. Kim, *Solid State Commun*. **127** (2003) 181
50. Y. Maniwa, R. Fujiwara, H. Kira, H. Tou, H. Kataura, S. Suzuki, Y. Achiba, E. Nishibori, M. Takata, M. Sakata, A. Fujiwara, H. Suematsu, *Phys. Rev*. *B* **64** (2001) 241402
51. Z. Yao, H. W. Ch. Postma, L. Balents, C. Dekker, *Nature* **402** (1999) 273
52. M. Ouyang, J.-L. Huang, C. L. Cheung, C. M. Lieber, *Science* **292** (2001) 702
53. J. U. Lee, P. P. Gipp, C. M. Heller, *Appl. Phys. Lett***. 85** (2004) 145
54. M. Terrones, F. Banhart, N. Grobert, J.-C. Charlier, H. Terrones, P. M. Ajayan, *Phys. Rev. Lett*. **89** (2002) 075505
55. Z. Wu, Z. Chen, X. Du, J. M. Logan, J. Sippel, M. Nikolou, K. Kamaras, J. R. Reynolds, D. B. Tanner, A. F. Hebard, A. G. Rinzler, *Science* **305** (2004) 1273
56. J.-C. Charlier, M. Terrones, M. Baxendale, V. Meunier, T. Zacharia, N. L. Rupesinghe, W. K. Hsu, N. Grobert, H. Terrones, G. A. J. Amaratunga, *Nano Lett.* **2** (2002) 1191
57. D. Golberg, P. S. Dorozhkin, Y. Bando, Z.-C. Dong, C. C. Tang, Y. Nemura, N. Grobert, M. Reyes-Reyes, H. Terrones, M. Terrones, *Appl. Phys*., *A* **76** (2003) 499
58. D. Y. Zhong, G. Y. Zhang, S. Liu, E. G. Wang, Q. Wang, H. Li, X. J. Huang, *Appl. Phys. Lett*. **79** (2001) 3500
59. P. Calvert, *Nature* **399** (1999) 210
60. H. Gao, Y. Kong, *Annu. Rev. Mater. Res*. **34** (2004) 123
61. W. Chen, C. H. Tzang, J. Tang, M. Yang, S. T. Lee, *Appl. Phys. Lett*. **86** (2005) 103114
62. W. Yang, P. Thordarson, J. J. Gooding, S. P. Ringer, F. Braet, *Nanotechnology* **18** (2007) 412001
63. J. Robertson, *Mater. Today* **10(1–2)** (2007) 36
64. T. Cheyney, *Small Times,* September 2007
65. S. N. Marinković, in *Chemistry and Physics of Carbon*, Vol. 19, P. A. Thrower, Ed., Marcel Dekker, N.Y., 1984, pp. 1–64.

www.shd.org.rs

Journal of the Serbian Chemical Society

JSCS@tmf.bg.ac.yu • www.shd.org.rs/JSCS

J. Serb. Chem. Soc. *73* (8–9) 915–921 (2008)
JSCS–3772

UDC 678.744+66.095.26:541.131:536.7
Short communication

SHORT COMMUNICATION

The thermal stability of poly(methyl methacrylate) prepared by RAFT polymerisation

LYNNE KATSIKAS[1#], MILENA AVRAMOVIĆ[1#], RUBÉN DARÍO BETANCOURT CORTÉS[1], MILOŠ MILOVANOVIĆ[2#], MELINA T. KALAGASIDIS-KRUŠIĆ[1] and IVANKA G. POPOVIĆ[1*#]

[1]*Faculty of Technology and Metallurgy, University of Belgrade, Belgrade and* [2]*Institute of Chemistry, Technology and Metallurgy, University of Belgrade, Belgrade, Serbia*

(Received 10 June 2008)

Abstract: Poly(methyl methacrylate), PMMA, was prepared by reversible addition–fragmentation chain transfer, RAFT, polymerisation using 2-(2-cyanopropyl)-dithiobenzoate, CPDB, as the RAFT agent. The thermal stability of the resulting polymer approached that of anionically prepared PMMA, as determined by thermogravimetry. This was the consequence of the RAFT prepared polymer having no head-to-head links and no chain end double bonds, which are responsible for the relatively low thermal stability of radically prepared PMMA.

Keywords: thermogravimetry; stability; RAFT; PMMA.

INTRODUCTION

The controlled (living) radical polymerisation, CLRP, of a wide variety of monomers has received considerable interest in recent years as the resulting polymers have very narrow molar mass distributions (approaching those of ionically prepared polymers but with less stringent polymerization conditions) and, due to the living nature of the polymerisations, copolymers of well defined structure are readily obtainable. The four distinct mechanisms usually employed to date for controlling radical polymerizations are nitroxide-mediated polymerisation, NMP,[1] atom transfer radical polymerisation, ATRP,[2] reversible addition–fragmentation chain transfer polymerisation, RAFT[3] and interchange of xanthates, MADIX.[4]

RAFT Polymerisation is the most recently developed of these methods and has evolved as one of the most versatile of the CLRP techniques, the other being MADIX, because of its high tolerance to a wide variety of monomers and the mild conditions required.

* Corresponding author. E-mail: ivanka@tmf.bg.ac.yu
# Serbian Chemical Society member.
doi: 10.2298/JSC0809915K

As can be seen from Scheme 1, classical radical–radical termination does not occur in RAFT polymerisations, the isolated polymer is dormant with the RAFT agent attached to the ends of the chains. Thus, thermally weak links, *i.e.*, head-to--head bonds and chain end unsaturation, present in conventional radically prepared polymers due to termination by radical–radical coupling and disproportiation, respectively, should be absent in RAFT prepared polymers. Then, if the thermal stability of a polymer is governed by such weak links, the RAFT prepared polymers should be more stable than the conventionally prepared polymers.

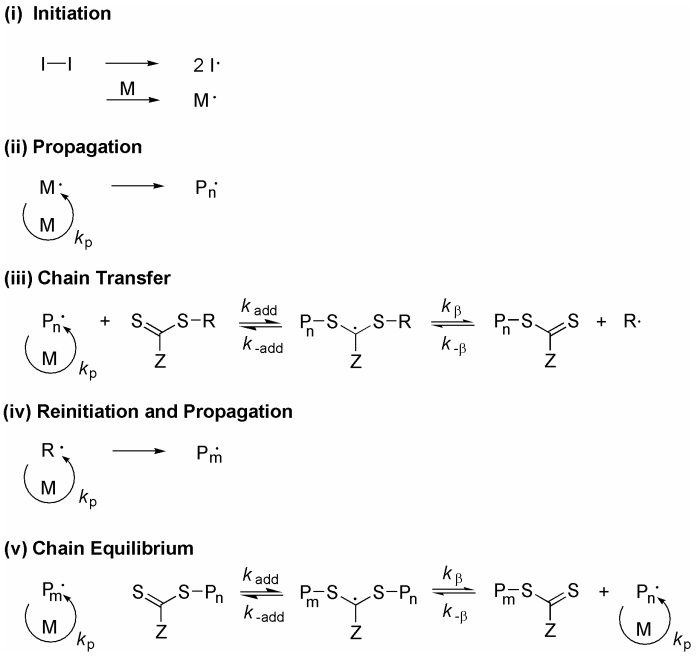

Scheme 1.

Radically prepared poly(methyl methacrylate) (PMMA) is known to thermally degrade by depolymerisation to yield almost exclusively monomer.[5] In spite of this, free radically prepared PMMA degrades in three distinct temperature regions depending on the mode of initiation of depolymerisation. Thus, in order of increasing temperature, depolymerisation of PMMA is initiated by scission of head-to-head bonds, scission of the β-bond to chain end unsaturation and main chain scission.[6] On the other hand, anionically prepared PMMA has no weak links arising during termination and hence only main chain scission initiates thermal depolymerisation.

The aim of this study was to determine the thermal stability of PMMA prepared by the RAFT mechanism. To the best of our knowledge this is the first purpose designed study of the thermal stability of a polymer prepared by the RAFT mechanism.

EXPERIMENTAL

Methyl methacrylate (Fluka) was distilled under reduced pressure after removal of the inhibitor with a 5.0 % aqueous NaOH solution. Azobis(isobutyronitrile), AIBN, (Aldrich), employed as the initiator, was recrystalised from methanol. Benzene, thiophene free, (Fluka) was distilled before use.

The RAFT agent, 2-(2-cyanopropyl)-dithiobenzoate (CPDB), was prepared by a method described in the literature.[7] It should be mentioned here that the yields of the RAFT agent were extremely low when a chromatographically pure substance was obtained. The structure of the RAFT agent was confirmed by ^{13}C-NMR spectroscopy using a Varian-Gemini-200 (200 MHz) instrument.

The RAFT polymerisation was performed in an ampoule containing MMA 30 ml (0.28 mol), benzene 10 ml (0.11 mol), AIBN 40 mg (0.24 mmol) and CPDB 104 mg (0.470 mmol). The ampule was bubbled with N_2 for 15 min and sealed under vacuum and placed in a water bath at 60 °C. After 16 h, the reaction mixture was poured into methanol containing 5.0 % water. The polymer sample was reprecipitated from a benzene solution into methanol containing 5.0 % water and dried to constant mass at room temperature under vacuum. The percent conversion was determined gravimetrically.

The RAFT agent was removed from the PMMA samples by dissolving 0.50 g of the polymer in 40 ml toluene. AIBN (10 g) was added to this solution and, after removal of oxygen, the solution was heated at 80 °C for 3 h.[8] The polymer was precipitated into methanol containing 5.0 % water and dried to constant mass at room temperature under vacuum.

The conventional radical polymerisation of MMA was performed in an ampoule containing MMA and AIBN at a molar ratio of MMA:AIBN of 25. The ampoule was bubbled with nitrogen and sealed under vacuum. The polymerisation lasted 15 min at 60 °C. The anionically prepared sample was obtained from PSS Polymer Standards Service GmbH, Mainz, Germany.

The number and weight average molar masses, M_n and M_w, respectively, and the polydispersity index, *PD*, of the obtained polymers and the polymer standard were determined at 30 °C by gel permeation chromatography, GPC, using a Waters instrument fitted with four analytical columns (Waters HR 2, HR 3, HR 4 and HR 5E) and a refractive index detector. Chloroform was used as the solvent at a flow rate of 1.0 ml min^{-1}. The obtained chromatograms were analysed with Waters Breeze software using a calibration curve of narrow molar mass distribution PMMA standards (PSS Polymer Standards Service GmbH, Mainz, Germany).

Non-isothermal, non-oxidative thermogravimetry, TG, and differential TG, DTG, was performed using a Perkin Elmer TGS-2 instrument in the temperature range 0–600 °C at heating rates of 2.5, 10, 20 and 40 °C min^{-1}, under a dynamic nitrogen flow (flow rate 26 ml min^{-1}).

RESULTS AND DISCUSSION

The ^{13}C-NMR spectrum and the numbering of the C atoms of the prepared CPDE are shown in Fig. 1, from which it can be seen that all the expected peaks were present. No additional peaks were found in the spectrum, confirming that the sample was pure.

The polymer obtained after the RAFT polymerisation was pink due to the attachment of CPDB to the chain ends and had a weight average molar mass, M_w, of 3.59 kg mol^{-1} and a polydispersity index, *PD*, of 1.19. After removal of the RAFT agent, the polymer was the normal white colour of precipitated PMMA.

The M_W of the polymer after removal of the RAFT agent remained unchanged and the *PD* decreased to 1.15.

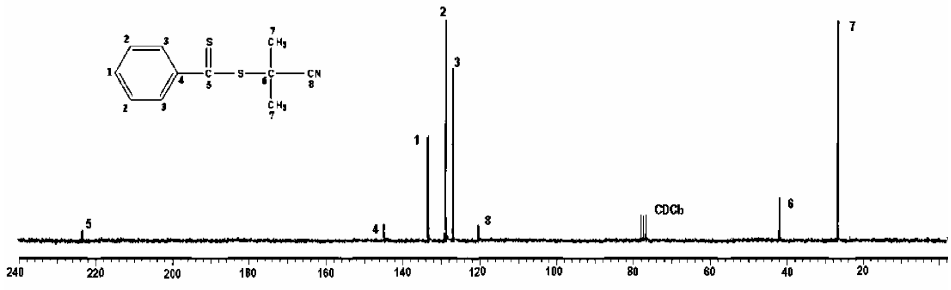

Fig. 1. ^{13}C-NMR Spectrum of CPDB (inset structure of CPDB with C atoms numbered).

The TG curves of the RAFT prepared PMMA sample at heating rates of 2.5, 10, 20 and 40 °C min^{-1} both before and after removal of the RAFT agent are shown in Figs. 2a and 2b, respectively. In both cases, the curves recorded at different heating rates run completely parallel to one another, showing that only one degradation mechanism was operative.

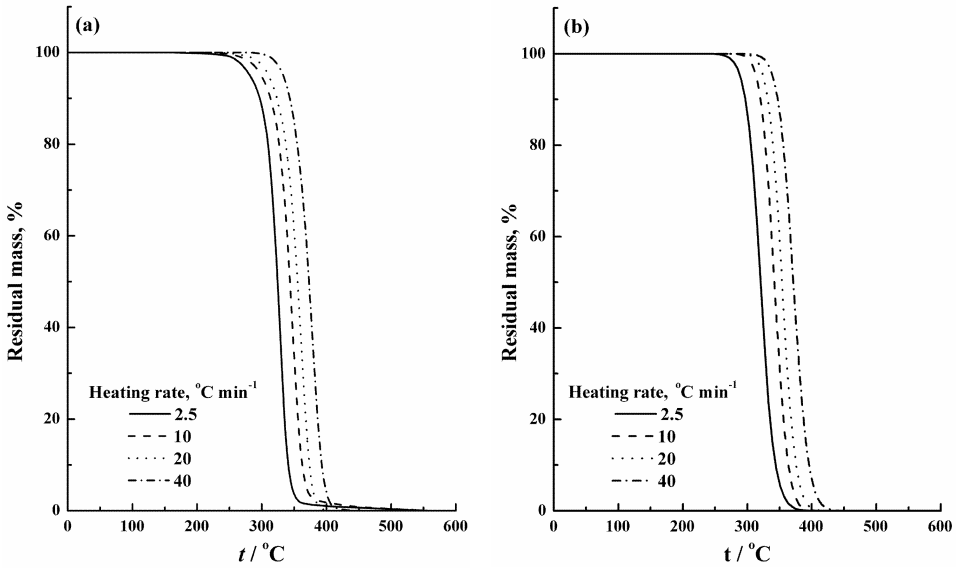

Fig. 2. TG Curves recorded at 2.5, 10, 20 and 40 °C min^{-1} of the polymer obtained after 16 h RAFT polymerisation both before (a) and after (b) removal of the RAFT agent.

In order to compare the TG curves of the examined polymers, the TG curves of each polymer recorded at 10 °C min^{-1} are presented in Fig. 3, together with those of an anionically and conventional radically prepared PMMA samples of weight average molar mass 5.25 kg mol^{-1} (*PD* 1.04) and 4.46 kg mol^{-1} (*PD* 1.67), respectively, for comparison.

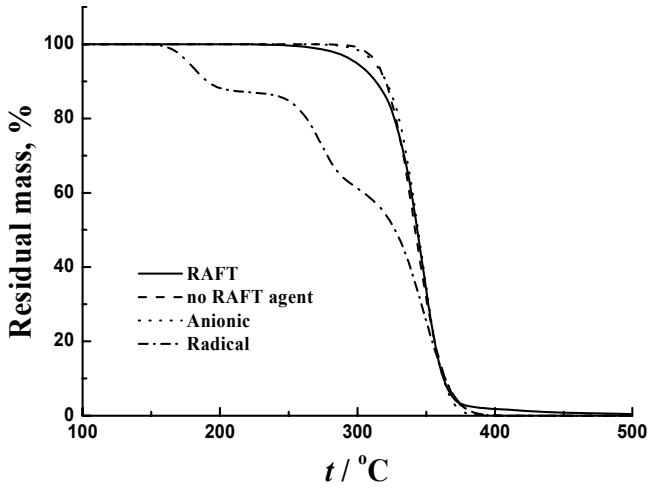

Fig. 3. TG curves recorded at a heating rate of 10 °C min^{-1} of the polymer before and after the removal of the RAFT agent with the curves of an anionically and a conventional radically prepared polymer. The molar masses of the polymers were all comparable.

It is immediately visible that the RAFT prepared samples, both before and after removal of the RAFT agent, were considerably more stable than the radically prepared sample. Before removal of the RAFT agent, the polymer was less stable than after. This is probably due to the thermal degradation of the RAFT agent at the ends of the polymer chains. The mass loss commences slightly earlier with the PMMA with the RAFT agent still attached than after it had been removed and there is a high temperature tail visible on the TG curve. It would appear that the degradation of CPDB occurs in the same temperature range as main chain scission when it is attached to the end of the polymer chains. Thermal treatment has been used to remove the RAFT agent from polymers[9,10] but not CPDB, which appears to be too stable for this method to be applicable. Most significantly, the TG curves of the RAFT prepared sample after removal of the RAFT agent and of the anionically prepared sample almost overlap. This means that the cyano-isopropyl groups from AIBN, which replaced the RAFT agent at the chain ends, did not initiate depolymerisation.

The characteristic mass loss temperatures, *i.e.*, the temperatures corresponding to 5, 10, 50 and 90 %, $T_{5\%}$, $T_{10\%}$, $T_{20\%}$, $T_{50\%}$ and $T_{90\%}$, respectively, for a heating rate of 10 °C min^{-1} are given in Table I. Again the similarity between the RAFT prepared PMMA after removal of the attached CPDB and the anionically prepared PMMA can be clearly seen.

These differences and similarities are even more visible in the DTG curves of the four polymers, shown in Fig. 4. Thus the DTG peaks at approximately 181 and 274 °C on the curve of the conventional radically polymerised PMMA arise

from depolymerisation initiated by the scission of the head-to-head bonds formed during chain termination by combination and from depolymerisation initiated by scission of the β-bond to the chain end vinylidene bonds formed during chain termination by disproportiation, respectively. The amount of degradation initiated by such weak links decreases as the molar mass of the polymer increases because their concentration in the polymer decreases. These weak bonds were obviously absent in the RAFT- and anionically-prepared polymers as only the DTG peak corresponding to main chain scission was present.

TABLE I. The temperatures of 5, 10, 20, 50 and 90 % mass loss for the examined PMMA samples

Synthesis method	$T_{5\%}$ / °C	$T_{10\%}$ / °C	$T_{20\%}$ / °C	$T_{50\%}$ / °C	$T_{90\%}$ / °C
RAFT	298	312	327	342	363
RAFT removed	314	321	328	343	363
Anionic	311	321	330	345	363
Radical	176	191	263	328	363

As the RAFT mechanism is applicable under less stringent conditions than are required for anionic polymerisation, industrial samples of PMMA with improved thermal stability could be readily prepared using this method.

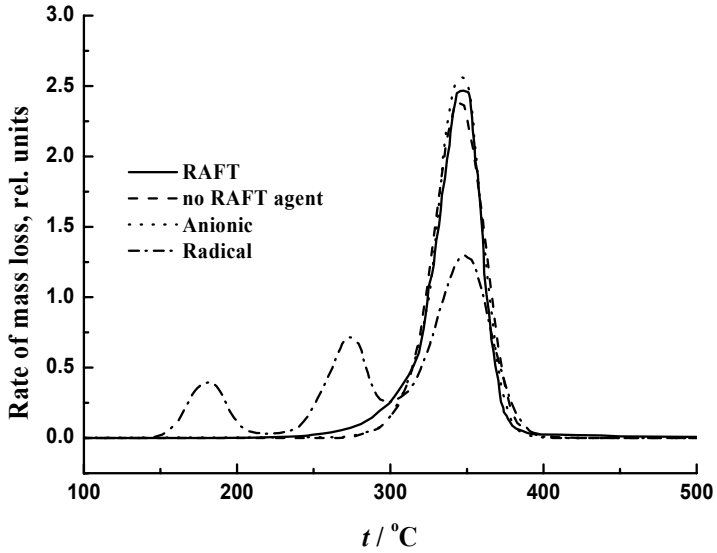

Fig. 4. The corresponding DTG curves of the TG curves shown in Fig. 3.

CONCLUSIONS

In conclusion, not only did the RAFT prepared PMMA have a narrow molar mass distribution, approaching that of anionically prepared PMMA, but also a significantly greater thermal stability than conventional radically prepared polymers. It is to be expected that any polymer which can be successfully prepared

under controlled conditions and the thermal stability of which depends on the presence of weak bonds originating from radical–radical termination during its polymerisation, would also exhibit such an increase in thermal stability when prepared by the RAFT mechanism.

Acknowledgement. This study was financially supported by the Ministry of Science of the Republic of Serbia under contract No. 142023.

И З В О Д

ТЕРМИЧКА СТАБИЛНОСТ ПОЛИ(МЕТИЛ МЕТАКРИЛАТА) СИНТЕТИСАНОГ RAFT ПОЛИМЕРИЗАЦИЈОМ

LYNNE KATSIKAS[1], МИЛЕНА АВРАМОВИЋ[1], RUBÉN DARÍO BETANCOURT CORTÉS[1], МИЛОШ МИЛОВАНОВИЋ[2] , МЕЛИНА Т. КАЛАГАСИДИС-КРУШИЋ[1] и ИВАНКА Г. ПОПОВИЋ[1]

[1]Технолошко–металуршки факултет, Универзитет у Београду, Београд и [2]Институт за хемију, технологију и металургију, Универзитет у Београду, Београд

Поли(метил метакрилат), PMMA, је синтетисан контролисаном радикалном RAFT полимеризацијом, односно реверзибилном адиционо-фрагментационом трансфер полимеризацијом, у присуству 2-(2-цијанопропил)-дитиобензоата, CPDB, као RAFT агенса. Термичка стабилност PMMA синтетисаног RAFT полимеризацијом је слична полимеру добијеном анјонском полимеризацијом, што је показала термогравиметријска анализа. PMMA синтетисан RAFT полимеризацијом показује знатно бољу термичку стабилност у односу на PMMA синтетисан полимеризацијом преко слободних радикала, због одсуства термички лабилних веза глава–глава остатака мономера у полимерном ланцу, као и двоструких веза на крајевима ланаца.

(Примљено 10. јуна 2008)

REFERENCES

1. C. J. Hawker, A. W. Bosman, E. Harth, *Chem. Rev.* **101** (2001) 3661
2. K. Matyjaszewski J. Xia, *Chem. Rev.* **101** (2001) 2921
3. G. Moad, E. Rizzardo, S. H. Thang, *Aust. J. Chem.* **58** (2005) 379
4. S. Perrier, P. Takolpuckdee, *J. Polym. Sci., A* **43** (2005) 5347
5. N. Grassie, *Pure Appl. Chem.* **30** (1972) 119
6. T. Kashiwagi, A. Inabi, J. E. Brown, K. Hatada, T. Kitayama, E. Masuda, *Macromolecules* **19** (1986) 2160
7. S. Perrier, C. Barner-Kowollik, J. F. Quinn, P. Vana, T. P. Davis, *Macromolecules* **35S** (2002) 30
8. S. Perrier, P. Takolpuckdee, C. A. Mars, *Macromolecules* **38** (2005) 2033
9. A. Postma, T. P. Davis, G. Moad, M. S. O'Shea, *Macromolecules* **38** (2005) 5371
10. J. Xu, J. He, W. Tang, Y. Yang, *Macromolecules* **39** (2006) 3753.

www.shd.org.rs

Journal of the Serbian Chemical Society

JSCS@tmf.bg.ac.yu • www.shd.org.rs/JSCS

J. Serb. Chem. Soc. 73 (8–9) 923–934 (2008)
JSCS–3773

UDC 504.55.054:549.25:613.001.24(497.11)
Original scientific paper

Potential health risk assessment for soil heavy metal contamination in the central zone of Belgrade (Serbia)

IVAN GRŽETIĆ*# and RABIA H. AHMED GHARIANI

University of Belgrade – Faculty of Chemistry, Studentski trg 16, 11000 Belgrade, Serbia

(Received 17 March, revised 14 May 2008)

Abstract: An investigation of the soil quality in the centre of Belgrade was performed to define how seriously the soil is polluted. On the basis of the heavy metal content (Zn, Cd, Pb, Co, Ni, Cu, Cr and Mn), the potential health risk assessment calculated for a lifetime of exposure (ingestion and inhalation), based on the USEPA model, was determined as the cumulative carcinogenic and non-carcinogenic risk for children and adults. The study proved that soil contamination in Belgrade is not insignificant; risk assessment indicated that the carcinogenic risk is completely insignificant but the cumulative non-carcinogenic risk tends to became significant, mainly for children, since it approaches unacceptable values. There is no particularly dangerous single heavy metal, but their cumulative effect, expressed as Child Soil Ingestion Hazardous Index, is for concern.

Keywords: health risk assessment; soil pollution; heavy metals; Belgrade.

INTRODUCTION

The city of Belgrade, capital of Serbia, is a conglomeration of 17 municipalities, 10 of which belong to the inner and 7 to the greater area. The latter have suburban and rural features. Belgrade is situated in South–Eastern Europe, on the Balkan Peninsula. It is located on the confluence of two rivers, the Danube and the Sava. They surround the city on three sides. The city has the coordinates 44°49'14'' of the northern geographical latitude and 20°27'44''of the eastern geographical longitude. Its height above sea level is 116.75 m, with the highest point within the city 248.6 m and the lowest 75.3 m above sea level. Belgrade has a circumference of 427 km, an area of 322,268 ha and a total population of 1,602,226 inhabitants.

The investigation of the soil quality in the centre of Belgrade had a special goal, *i.e.*, to define how seriously the soil is polluted and to determine its poten-

* Corresponding author. E-mail: grzetic@chem.bg.ac.yu
# Serbian Chemical Society member.
doi: 10.2298/JSC0809923G

tial health risk as a cumulative carcinogenic and non-carcinogenic risk for children and adults.

The whole procedure was based on the sampling of soil in the central (urban) area of Belgrade, its investigation by atomic absorption spectroscopy on heavy metals, *i.e.*, Zn, Cd, Pb, Co, Ni, Cu, Cr and Mn, and the calculation of potential health risk on the basis of the US Environmental Protection Agency health risk assessment model.[1]

EXPERIMENTAL

Sampling sites

The surface soil samples (0–5 cm) were collected at 16 locations near major and minor roads and 4 samples from park areas (Fig. 1).

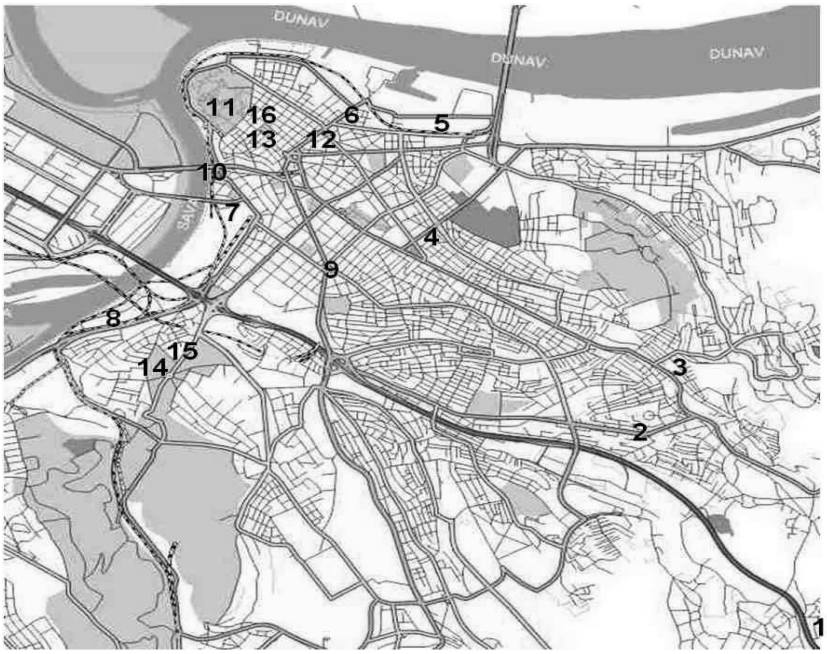

Fig. 1. Belgrade sampling sites: 1. pay toll ramp at the highway to Niš, 2. Ustanička Street, 3. Milana Rakića Street, 4. Ruzveltova Street, 5. Dunav Railway Station, 6. Francuska Street, lower, 7. Intercity bus station, 8. Belgrade Fair, 9. Slavija Square, 10. Brankov Bridge, 11. Kalemegdan Park, 12. Francuska Street, upper, 13. Student Park, 14. Park near Vojvode Putnika, 15. Boulevard Vojvode Putnika and 16. Rige od Fere Street.

Methods

Metal extraction was performed in several steps (sequential extraction procedure)[2] and the obtained sum of each metal were taken as the final concentration of the available metal from the soil.

Metal determination in the extracts was performed by atomic absorption spectroscopy, using a "Perkin Elmer 2380" instrument.

Health risk assessment

Health risk assessment models were developed basically in Europe[3] and in the United States.[1,4] The European model is still under development and is not as straightforward as the American model. Therefore, it was decided to apply the American model developed by USEPA. This model has been developed in all details and is fully available through Risk Assessment Information System (RAIS) (http://rais.ornl.gov/) and is supported by the Toxicological profiles developed and gathered by the USEPA Integrated Risk Information System (IRIS) (http://cfpub.epa.gov/ncea/iris/index.cfm) and by the US Agency for Toxic Substances and Disease Registry – Toxicological profiles (ATSDR) (http://www.atsdr.cdc.gov/toxfaq.html).

The risk assessment is a multi-step procedure that comprise (1) data collection (gathering and analyzing the site data relevant to human health), (2) exposure assessment (estimation of the magnitude of actual and/or potential human exposures), (3) toxicity assessment (determination of adverse health effects associated with exposure to different chemicals) and (4) risk characterization (summarizes and combines the outputs of the calculations of exposure and toxicity assessments).[5]

In the present case, Cd, Cr, Co, Cu, Pb, Mn, Ni and Zn were identified as potential hazardous agents in the soil at different locations in Belgrade which are relevant to human health (Fig. 1).

In the case of exposure assessment, a specific approach characteristic for human exposure to soil in residential urban areas was applied, taking particularly care of the different exposure rates for children and adults[6] (usually expressed as exposure factors, USEPA). In addition, the magnitude of exposure and, consequently, the intake or dose (consumed or inhaled amount) of contaminated soil is almost always different for different individuals. Therefore, a very useful and valuable approximation was made, *i.e.*, the risk was calculated for the lifetime exposure, the total exposure to a substance that a human would receive in a lifetime – usually assumed to be 70 years. All other parameter that may be site characteristic were taken to be constant through the whole calculating procedure for all elements and all sites, since their importance becomes less significant in case of the lifetime exposure approximation.

RESULTS AND DISCUSSION

Total contents of heavy metals in the soil of Belgrade are presented in Table I. Most of the data does not need further comments but additional argumentation is required in the case of Cr. The presence of Cr(VI) in natural environments requires a rather high redox potential, over 700 mV for a pH of around 5.0, but a redox potential of 400 mV for pH 7.0 to 8.0 is sufficient for Cr(VI) to dominate in the system.[7] The redox potential in soil usually varies from a minimum of –550 to maximum of 700 mV, but aerated soil most frequently has a redox potential up to 400 mV.[8] Therefore, it is assumed that Cr(VI) in the streets of Belgrade was the dominating chromium species since the measured soil pH was around 7.8.[9]

Plain data on the metal content of soil is sometimes insufficient to describe the full risk that arises from the exposure of humans, both children and adults, to different heavy metals from soil, particularly in the case when more details on human health risk are required.

Following the toxicological profiles of all the investigated elements,[10–12] it can be seen that most of the heavy metals have adverse health effects on humans,

so-called toxicological effects, but some of the metals are additionally carcinogenic. For example, the investigated Co, Cr and Cd, induce both non-carcinogenic and carcinogenic risk, while Zn, Ni, Mn and Cu (Table II) induce only non-carcinogenic risk. Lead is a specific element, since there are no published data for this metal yet which are relevant for risk assessment calculations, although there is no doubt that Pb is a toxic element. A comprehensive and up-to-date literature overview on lead toxicity is collected in the ATSDR toxicological profile for lead.[13] Even so the available evidence is considered to be inadequate to contradict or demonstrate any potential carcinogenicity from lead exposure for humans.

TABLE I. Total content of heavy metals in the soil of Belgrade (mg/kg)

Sampling site	Cd	Cr	Co	Cu	Pb	Mn	Ni	Zn
Pay toll ramp at highway to Niš (1)	13.41	159.96	38.91	48.61	148.79	644.50	360.95	272.50
Ustanička Street (2)	17.75	59.21	34.20	88.65	443.80	658.70	115.66	259.25
Milana Rakića Street (3)	10.18	43.15	22.70	65.90	635.07	409.71	89.95	200.13
Ruzveltova Street (4)	9.64	65.82	15.24	314.80	321.54	393.82	57.65	247.69
Dunav Railway station (5)	5.18	81.99	12.03	101.54	204.76	422.70	119.66	358.43
Francuska Street lower (6)	9.06	55.92	13.33	56.41	51.35	845.63	107.17	132.63
Intercity bus station (7)	7.79	66.83	28.24	60.09	85.10	810.42	85.83	140.41
Belgrade Fair (8)	9.75	56.81	26.25	79.85	262.22	537.55	97.66	216.95
Slavija Square (9)	11.30	71.65	18.57	255.19	243.58	666.63	106.04	296.18
Brankov Bridge (10)	7.76	57.67	18.45	119.87	285.80	413.16	211.36	734.16
Kalemegdan Park (11)	9.12	49.65	22.41	90.95	262.94	787.57	109.14	201.58
Francuska Street upper (12)	5.22	67.39	28.83	131.68	180.78	667.61	119.83	309.25
Student Park (13)	5.34	59.58	27.12	107.32	180.03	763.57	108.71	192.34
Park near Vojvode Putnika (14)	8.60	64.08	34.22	118.63	46.51	1020.08	84.06	195.11
Boulevard Vojvode Putnika (15)	4.01	92.91	27.45	134.95	1847.64	561.62	84.56	260.51
Rige od Fere Street (16)	8.32	71.01	41.57	182.26	401.06	665.52	120.42	276.72
Minimum concentration	4.01	43.15	12.03	48.61	46.51	393.82	57.65	132.63
Maximum concentration	17.75	159.96	41.57	314.80	1847.64	1020.08	360.95	734.16
Median concentration	8.83	64.95	26.69	104.43	252.90	662.11	107.94	253.47
Geometric mean	8.32	66.95	24.08	106.69	230.83	617.74	112.24	246.51
Arithmetic mean	8.90	70.23	25.59	122.29	350.06	641.80	123.67	268.37

Exposure of humans to soil actually is through dust exposure that comprises inhalation and/or oral exposure (ingestion). For such exposition, the most recent EPA guidance recommends daily rates of 200 mg/day for children and 100 mg/day for adults.[6,14]

Risk characterization relevant for the present investigation comprises calculations of carcinogenic and non-carcinogenic risk for ingestion and inhalation of soil. Sometimes dermal exposure to soil is included as well, but since these risks are about 100 times smaller then the risk that arises from ingestion and inhalation, it was omitted here.

TABLE II. Some toxicological characteristics of the investigated elements[10,12]

Characteristic	Cd	Cr	Co	Cu	Pb	Mn	Ni	Zn
Minimal risk level (*MRL*)[a] oral (mg/kg/day)	0.0002		0.01	0.01		?		
Minimal risk level (*MRL*) inhalation (mg/m^3)		0.00004	0.0001				0.00004	0.0002
RAIS oral chronic reference dose (mg/kg/day) (*RfD*)	0.001	0.003	0.02	0.04	0.3	0.046	0.14	0.02
RAIS dermal chronic reference dose (mg/kg/day)	0.00001	0.0075	0.016	0.012		0.04	0.0056	0.0054
Cancer EPA weight-of-evidence classification[b]	B1	Cr(VI)A Cr(III) D	B2 (B1?)	D	B2	B2	B2	B2
Inhalation Unit Risk[c] (mg/m^3)$^{-1}$	1.8	1.2	2.8			?		0.48

[a]Minimal risk level (MRL): an estimate of the daily human exposure to a hazardous substance that is likely to be without an appreciable risk of adverse non-cancer health effects over a specified route and duration of exposure; [b]cancer EPA weight-of-evidence classification: A – human carcinogen, B1 – probable human carcinogen, B2 – probable human carcinogen, C – possible human carcinogen, D – not classifiable as to human carcinogenicity, E – good evidence for absence of carcinogenicity; [c]Unit risk: excess lifetime cancer risk per unit concentration of the substance in the medium where human contact occurs (1 μg/l in water or 1 μg/m^3 in air), usually expressed in units of proportion (of a population).

Basic formulas and values used for the calculation of ingestion and inhalation of soil are presented in Table III.

TABLE III. Calculation of carcinogenic and non-carcinogenic risk for ingestion and inhalation of soil[1,15]

CDI, chronic daily intake for carcinogenic risk (ingestion of soil)

Carcinogenic: CDI (mg/kg/day) = $CS \times IF \times EF / AT$,

where $IF = \frac{IR_{\text{Adult}} \times ED_{\text{Adult}}}{BW_{\text{Adult}}} + \frac{IR_{\text{Child}} \times ED_{\text{Child}}}{BW_{\text{Child}}}$

Non-carcinogenic: CDI (mg/kg/day) = $CS \times IN \times EF \times ED / BW \times AT$

CDI, chronic daily intake (inhalation of soil dust) for carcinogenic and non-carcinogenic risk

$$CDI(\text{mg}/\text{m}^3) = \frac{CS \times IF \times EF\left(\frac{1}{PEF} + \frac{1}{VF}\right)\left(ET_{\text{Outdoor}} + \left(ET_{\text{Indoor}} DF_{\text{Indoor}}\right)\right)}{AT}$$

Variable	Value used
AT – averaging time for non-carcinogens	365 days/year/$ED_{\text{Chhild or adult}}$
AT – averaging time for carcinogens	365 days/year/70 years
BW_{Adult} – body weight adult	70 kg
BW_{Child} – body weight child	15 kg
CS – concentration in soil or sediment	Chemical specific (mg/kg)
EF – exposure frequency	350 days/year
ET_{Indoor} = Exposure time indoor	0.683
ET_{Outdoor} = Exposure time outdoor	0.073
DF – dilution factor indoor	0.4

TABLE III. Continued

Variable	Value used
IN – inhalation rate	20 m^3/day
PEF – particulate emission factor, climate specific[15]	m^3/kg
VF – volatilization factor, chemical specific[15]	m^3/kg
IF – intake factor	–
IR_{Adult} – ingestion rate adult	0.0001 kg/day
IR_{Child} – ingestion rate child	0.0002 kg/day
ED_{Child} – exposure duration child	6 years
ED_{Adult} – exposure duration adult	24 years (for general case: 30 years)

For carcinogens, the risks are estimated as the incremental probability of an individual developing cancer over a lifetime as a result of exposure to the potential carcinogen. The basic equation for calculating the excess lifetime cancer risk is:

$$\text{Risk} = CDI \times SF \tag{1}$$

where "Risk" is a unitless probability of an individual developing cancer over a lifetime; *CDI* is the chronic daily intake or dose (mg/kg/day); *SF* is the slope factor, expressed in $(\text{mg/kg/day})^{-1}$. It converts the estimated daily intake averaged over a lifetime of exposure directly to incremental risk of an individual developing cancer.

The basic equation for calculating systemic toxicity or non-carcinogenic hazard for a single substance/element is expressed as the hazard quotient:

$$\text{Non-cancer hazard quotient} = CDI/RfD \tag{2}$$

where the non-cancer hazard quotient is a unitless number that is not expressed as the probability of an individual suffering an adverse effect. As a rule, the greater is the value of *CDI*/*RfD* above unity, the greater is the level of concern, since *CDI* is greater than *RfD*. It is also the ratio of a single substance exposure level over a specified time period to a reference dose for that substance derived from a similar exposure period. *CDI* is the chronic daily intake of a toxicant expressed in mg/kg/day and *RfD* is the chronic reference dose for the toxicant expressed in mg/kg/day. It is a mg/kg/day of the daily exposure level for the human population, including sensitive subpopulations, which is likely to be without an appreciable risk of deleterious effects during a lifetime.

All risks are cumulative, hence it is possible to calculate the cumulative cancer risk expressed as the total cancer risk, or non-carcinogenic hazard expressed as the hazard index.

The cancer risk equation which describes estimates of incremental individual lifetime cancer risk for the simultaneous exposure to several carcinogens is as follows:

$$\text{Total cancer risk} = \sum_{k=1}^{n} CDI_k SF_k \tag{3}$$

where CDI_k is the chronic daily intake or dose (mg/kg/day) for substance k, SF_k is the slope factor, expressed in $(mg/kg/day)^{-1}$, for substance k and $CDI_k \times SF_k$ is the risk estimate for the k^{th} substance.

For each chronic non-carcinogenic exposure, the separate chronic hazard index (*HI*) should first be calculated from the ratios of the chronic daily intake (*CDI*) to the chronic reference dose (*RfD*) for the individual chemicals and then the obtained results summed as described in the equation:

$$\text{Chronic hazard index} = \sum_{k=1}^{n} CDI_k / RfD_k \tag{4}$$

where the hazard index is a unitless number that is not expressed as the probability of an individual* suffering an adverse effect. As a rule, the greater is the value of *E*/*RfD* above unity, the greater is the level of concern. It is the sum of more than one hazard quotient for multiple substances and/or multiple exposure pathways, CDI_k is the chronic daily intake of the k^{th} toxicant in mg mg/kg/day and RfD_k is the chronic reference dose for the k^{th} toxicant in mg/kg/day.

By incorporation of the obtained measured data (Table I) into the above described formulas (Table III), values for the non-carcinogenic hazard index and carcinogenic lifetime risk for individual elements, the cumulative risk for different exposure pathways for individual elements and the cumulative risk for all elements were obtained (Table IV).

The investigations show that the measured soil concentrations of all the investigated element generates no significant carcinogenic lifetime risk due to ingestion and/or inhalation of soil. No matter how small the probability is, a carcinogenic risk exists and varies from the maximum value of 2×10^{-7} in case of Cr(VI) to the minimum value of 7×10^{-10} for Cd (Table IV). According to data obtained from Belgrade Public Health Institute,[16] the real cancer occurrence in Belgrade for 2006 was around 4×10^{-3}. This is a very high value in comparison to the results obtained in this study. Hence, the risk that evolves due to exposure to heavy metals in soil contributes so little to the total cancer risks that it is completely insignificant.

On the other hand, the non-carcinogenic risk, expressed as the hazardous index, is not so benevolent; the cumulative index is close to one or even exceeds that value, particularly in cases of the exposure of children (Table IV). Generally speaking, the hazardous index (*HI*) for the ingestion of soil by children is some

* Simultaneous exposures to several chemicals could result in an adverse health effect. The magnitude of the adverse effect will be proportional to the sum of the ratios of the subthreshold exposures to acceptable exposures. While any single chemical with an exposure level greater than the toxicity value will cause the hazard index to exceed unity, for multiple chemical exposures, the hazard index can also exceed unity even if no single hazard quotient exceeds unit.[1]

10 times greater in comparison to the corresponding results obtained for adults. From the point of view of *HI*, there is no particularly dangerous single heavy metal, but their cumulative effect is for concern (Table IV), since the cumulative risk for the median values was 0.7 and cumulative risk for the maximum values was 1.6. This is an alarming value for toxicologists since it indicates that the heath of children is endangered, but what kind of health effects could evolve from cumulative effects of heavy metals in soil and their influence on children was not the in the scope of this investigation.

For cadmium, the most serious chronic effect of oral exposure is renal toxicity. Renal *NOAEL** for Cd is 0.0021 mg/kg/day.[17] *MRL* for Cd is 0.0002 mg/kg/day (Table II). Since the minimum calculated value of the non-carcinogenic *CDI* for Cd for child ingestion of soil is 0.0002 mg/kg/day and that for the median value 0.0001 mg/kg/day, it could be concluded that there is no potential non-carcinogenic risk that could be eventually caused by Cd for children who are exposed to soil dust on the streets of Belgrade.

Chromium risk analysis predicts that the current occupational standards for hexavalent chromium permit a lifetime excess risk of dying of lung cancer that exceeds 1 in 10 for Cr concentrations in air of 1 mg/m^3.[18] The calculated risk in the case of Belgrade soil and soil dust is very small (2×10^{-7}), hence there is no respective cancer risk. Corresponding toxicological effects can arise when a daily intake is above the *RfD* of Cr or 0.003 mg/kg/day. The present calculations revealed that the daily intake is very near to the value of child non-carcinogenic *CDI* (0.00084 mg/kg/day for Cr median and 0.002 mg/kg/day for Cr maximum value), hence a child non-carcinogenic hazard is possible.

Cobalt is an essential element for humans and its dietary allowance is 0.1 μg. The average daily intake of cobalt from food is estimated to be 5 to 40 μg/day.[19] None of cobalt concentrations measured in Belgrade soil should provoke any concern since the adult and child ingestion of soil non-carcinogenic *CDI*s (0.036 μg/kg/day and 0.34 μg /kg/day, respectively) are sufficiently small in comparison with average daily intake of cobalt from food.

Copper in the soil surface, or aerated soil, is usually present as Cu(II). Although most copper salts occur in two valence states, *i.e.*, Cu(I) or Cu(II) ions, the biological availability and toxicity of copper is most likely associated with the divalent state.[20] Adult and child ingestion of soil non-carcinogenic *CDI*s for Cu (0.0013 mg/kg/day and 0.00014 mg/kg/day, respectively) are smaller then oral chronic *RfD* (0.04 mg/kg/day), hence copper generates risk neither for children nor for adults.

* *NOAEL* (No-Observed-Adverse-Effect Level): the dose of a chemical at which there were no statistically or biologically significant increases in the frequency or severity of adverse effects seen between the exposed population and an appropriate control. Effects may be produced at this dose, but they are not considered to be adverse.

Table IV. Non-carcinogenic hazard index and carcinogenic lifetime risk for individual elements, cumulative risk for different exposure pathways for individual elements and cumulative risk for all elements

Element	Risk					
	Non-carcinogenic risk	Non-carcinogenic risk	Non-carcinogenic risk	Cumulative non-carcinogenic risk	Carcinogenic risk	Cumulative carcinogenic risk
	Type of risk					
	Child ingestion of soil, *HI*	Adult ingestion of soil, *HI*	Adult inhalation of soil particulates, *HI*	Adult total soil *HI* for a single element	Inhalation of soil particulates risk ($\times 10^7$)	Total soil risk for a single element ($\times 10^7$)
Cd minimum	0.0511	0.0055	0.0000	0.0055	0.008	0.008
Cd maximum	0.2270	0.0243	0.0000	0.0243	0.034	0.034
Cd median	0.1130	0.0121	0.0000	0.0121	0.017	0.017
Cr(VI) minimum	0.1840	0.0197	0.0001	0.0198	0.542	0.542
Cr(VI) maximum	0.6820	0.0730	0.0004	0.0734	2.010	2.010
Cr(VI) median	0.2770	0.0297	0.0002	0.0299	0.816	0.816
Co minimum	0.0077	0.0008	0.0001	0.0010	0.035	0.035
Co maximum	0.0266	0.0029	0.0005	0.0034	0.122	0.122
Co median	0.0171	0.0018	0.0003	0.0022	0.078	0.078
Cu minimum	0.0155	0.0017	0.0000	0.0017	–	–
Cu maximum	0.1010	0.0108	0.0000	0.0108	–	–
Cu median	0.0334	0.0036	0.0000	0.0036	–	–
Mn minimum	0.1090	0.0117	0.0019	0.0136	–	–
Mn maximum	0.2840	0.0304	0.0050	0.0354	–	–
Mn median	0.1840	0.0197	0.0032	0.0229	–	–
Ni minimum	0.0369	0.0040	0.0000	0.0040	–	–
Ni maximum	0.2310	0.0247	0.0000	0.0247	–	–
Ni median	0.0690	0.0074	0.0000	0.0074	–	–
Zn minimum	0.0057	0.0006	0.0000	0.0006	–	–
Zn maximum	0.0313	0.0034	0.0000	0.0034	–	–
Zn median	0.0108	0.0012	0.0000	0.0012	–	–
Cumulative soil risk for all elements – risk is additive						
Cumulative risk for min. values	0.4098	0.0439	0.0022	0.0461	0.585	0.585
Cumulative risk for max. values	1.5829	0.1694	0.0059	0.1753	2.166	2.1666
Cumulative risk for median values	0.7043	0.0755	0.0037	0.0792	0.911	0.911

The case of manganese is rather complex. The origin of manganese on Belgrade streets is twofold. Some of it is a natural part of soil but additionally it is brought there by traffic, since in Serbia “unleaded” gasoline is produced with MMT (methylcyclopentadienyl manganese tricarbonyl) additive. Manganese can bring forth a variety of serious toxic responses upon prolonged exposure to ele-

vated concentrations, either orally or by inhalation. The central nervous system is the primary target. Initial symptoms are headache, insomnia, disorientation, anxiety, lethargy and memory loss. This combination of symptoms is a disease called "manganism", and these symptoms progress with continued exposure and eventually include motor disturbances, tremors, and difficulty in walking, symptoms similar to those seen with Parkinsonism.[21,22] However, manganese is also an essential trace element and is necessary for good health; the recommended dietary allowance for an adult human is 2–5 mg/day.[11] The present calculations for adult and child ingestion of soil non-carcinogenic *CDI*s for Mn (0.008 and 0.0009 mg/kg/day, respectively) show that these concentrations still do not exceed the chronic *RfD* for Mn (0.04 mg/kg/day) (Table II). However, since the contribution of traffic to the Mn content in Belgrade soil is not negligible, further monitoring of Mn is necessary.

Nickel is a probable human carcinogen, only some industrial Ni compounds exhibit carcinogenic effects, but many others do not. The most common adverse health effect of nickel in humans is an allergic reaction.[11] The present results showed that the current concentrations of Ni in Belgrade soil are below any alerting values.

Zinc is an essential element with a recommended daily allowances ranging from 5 mg for infants to 15 mg for adults. Too little zinc can cause health problems, but too much zinc is also harmful. Harmful health effects generally begin at levels in the 100 to 250 mg/day range.[11] The present results showed that the current concentrations of Zn in Belgrade soil are below any alerting values.

The presence of lead in Belgrade streets and soil is exclusively related to traffic and use of leaded gasoline.[23] Serbia is one among a few countries in Europe that have not ceased to produce and use leaded gasoline. Lead can affect almost every organ and system in the human body. Evidence shows that lead is a multi-target toxicant, causing effects in the gastrointestinal tract, hematopoietic system, cardiovascular system, central and peripheral nervous systems, kidneys, immune system and reproductive system. The most sensitive systems are the central nervous system, particularly in children, and the cardiovascular system. Irreversible brain damage occurs at blood Pb levels greater than or equal to 100 μg/dl in adults and at 80–100 μg/dl in children.[11] Pb blood levels over 4.62 μg/dl in children are associated with higher resting blood pressure.[24] Assuming the worst case scenario, for children with daily soil intake rates of 200 mg/day and maximal concentration of Pb of 1847.64 mg/kg in the soil, the calculated chronic daily intake for non-carcinogenic risk or *CDI* is 0.024 mg/kg/day. Hence, for a 15 kg child, the *CDI* is 0.36 mg/day (360 μg/day), and if all that Pb would enter into the blood, which is not the case, the child should have serious health problems.

CONCLUSION

This study has proven that soil contamination in Belgrade is not unimportant; risk assessment, calculated for a lifetime exposure, indicated that the carcinogenic risk is completely insignificant but the non-carcinogenic risk tends to became significant, mainly for children, since it approaches values which could be unacceptable. There is no particularly dangerous single heavy metal, but their cumulative effect, expressed as the child soil ingestion hazardous index, is for concern. Similar, but still rare literature data, describe urban soils that contain heavy metals.[25–27] They report evident corresponding non-carcinogenic hazard index which is around or above one, but they do not report carcinogenic lifetime risk for any individual element.

The investigation that remains, which was not in the scope of this study, is research by biomedical experts which should reveal the exact adverse effects that heavy metal contamination of soil might induce in humans, particularly among individuals in vulnerable populations, such as children.

Acknowledgements. This project was partly financed by the Ministry of Science of the Republic of Serbia (project no. 146008), and partly by a "Yugoimport SDPR" grant, which is gratefully acknowledged.

ИЗВОД

ПРОЦЕНА ПОТЕНЦИЈАЛНОГ РИЗИКА ПО ЗДРАВЉЕ ЉУДИ УСЛЕД ПРИСУСТВА ТЕШКИХ МЕТАЛА У ЗЕМЉИШТУ ЦЕНТРАЛНЕ ЗОНЕ БЕОГРАДА

ИВАН ГРЖЕТИЋ и RABIA H. AHMED GHARIANI

Универзитет у Београду – Хемијски факултет, Студентски трг 16, 11000 Београд

Испитивање земљишта централне зоне Београда рађено је са циљем да се одреди ниво његове загађености тешким металима. Полазећи од садржаја тешких метала (Zn, Cd, Pb, Co, Ni, Cu, Cr и Mn) процењен је кумулативни потенцијални канцерогени и неканцерогени здравствени ризик (за ингестију и инхалацију) за животни век човека, деце и одраслих, полазећи од модела који је развила америчка агенција за заштиту животне средине. Истраживања показују да загађење земљишта у Београду није занемарљиво иако процена канцерогеног ризика указује да је он занемарљив, али да неканцерогени ризик постаје значајан, посебно у случају деце. За сада не постоји одређени тешки метал који се може идентификовати као опасан, али кумулативни ефекат свих испитиваних метала исказан кроз ингестиони хазардни индекс за децу постаје забрињавајући пошто се приближава вредностима које се сматрају неповољним.

(Примљено 17. марта, ревидирано 14. маја 2008)

REFERENCES

1. USEPA, United States Environmental Protection Agency, 1989, EPA/540/1-89/002
2. S. Sakan, I. Gržetić, D. Djordjević, *Environ. Sci. Pollut. Res. Int*. **14** (2007) 229
3. ECB, European Chemicals Bureau (ECB), European Commission – Joint Research Centre, (2003) EUR 20418 EN/1

4. USEPA, United States Environmental Protection Agency, *Risk*, 1991, OSWER Directive 9285.7-01B
5. I, Gržetić, *Inpharm.* **5** (2001) 15
6. USEPA, United States Environmental Protection Agency (1997) EPA/600/P-95/002Fa
7. NIAIST, National Institute of Advanced Industrial Science and Technology, Geological Survey of Japan, Open File Report, 2005, No. 419
8. M. Vorenhout, G. H. van der Geest, D. van Marum, K. Wattel, H. J. P. Eijsackers, *J. Environ. Qual.* **33** (2004) 1177
9. I. Gržetić, R. H. A. Ghariani, M. Antić, S. Nikolić, S. Mandić, 2008, unpublished results
10. IRIS, Integrated Risk Information System, United States Environmental Protection Agency, 2007, http://cfpub.epa.gov/ncea/iris/index.cfm (accessed 19 January 2008)
11. RAIS, The Risk Assessment Information System, 2007, http://rais.ornl.gov/tox/ /rap_toxp.shtml ((accessed 15 January 2008)
12. ATSDR, US Agency for Toxic Substances and Disease Registry, 2007 http://www.atsdr.cdc.gov/mrls/ (accessed 19 January 2008)
13. ATSDR Pb, US Agency for Toxic Substances and Disease Registry, 2007, http://www.atsdr.cdc.gov/toxprofiles/tp13.html (accessed 19 January 2008)
14. USEPA, United States Environmental Protection Agency, 1996, EPA/540/R-96/018
15. USEPA, United States Environmental Protection Agency, 2002, OSWER 9355.4-24
16. BPHI, Belgrade Public Health Institute, 2006, http://www.zdravlje.org.yu/statistika/2006/ /index.html (accessed 16 January 2008)
17. K. Nogawa, R. Honda, T. Kido, I. Tsuritani, Y. Yamada, M. Ishizaki, H. Yamaha, *Environ. Res.* **48** (1989) 7
18. R. M. Park, J. F. Bena, L. T. Stayner, H. J. Gibb, P. S. Lees, *Risk Anal*. **24** (2004) 1099
19. ATSDR Co, US Agency for Toxic Substances and Disease Registry, 2004, http:// //www.atsdr.cdc.gov/toxprofiles/tp33.html (accessed 19 January 2008)
20. ATSDR Cu, US Agency for Toxic Substances and Disease Registry, 2004, http:// //www.atsdr.cdc.gov/toxprofiles/tp132.html (accessed 20 January 2008)
21. D. B. Calne, N. S. Chu, C. C. Huang, C.-S. Lu, W. Olanow, *Neurology* **44** (1994) 1583
22. N. S. Chu, F. H. Hochberg, D. B. Calne, C. Olanow, in: *Handbook of Neurotoxicology of manganese*, L. Chang, R. Dyyer, (Eds.), New York, NY, Marcel Dekker Inc., 1995, p. 91
23. I. Grzetic, *J. Environ. Prot. Ecol.* **4** (2003) 761
24. B. B. Gump, P. Stewart, J. Reihman, E. Lonky, T. Darvill, K. A. Matthews, P. J. Parsons *Neurotoxicol. Teratol.* **27** (2005) 655
25. K.-P. Chao, C.-T. Tsai, J. H. C. Wang, S.-T. Lin, C.-F. Chiang, *Pract. Period. Hazard. Toxic Radioactive Waste Mgmt.* **9** (2005)167
26. S.-W. Lee, B.-T. Lee, J.-Y. Kim, K.-W. Kim, J.-S. Lee, *Environ. Monit. Assess* **119** (2006), 233
27. E. J. Petersen, A. A. Jennings, J. Ma, *J. Environ. Eng.* **132** (2006) 392.

J. Serb. Chem. Soc. 73 (8–9) 935 (2008)

Errata (printed version only)

1. Issue No. 7 (2008), Vol. **73**, page 737:

– Line 10 from the top ("**Error! Objects cannot be created from editing field codes.**") should be replaced by following Scheme:

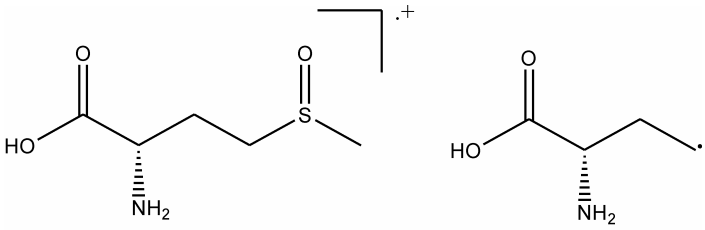

2. Issue No. 7 (2008), Vol. **73**, page 743:

– Line 3 from the top ("**Error! Objects cannot be created from editing field codes.**") should be replaced by following Scheme:

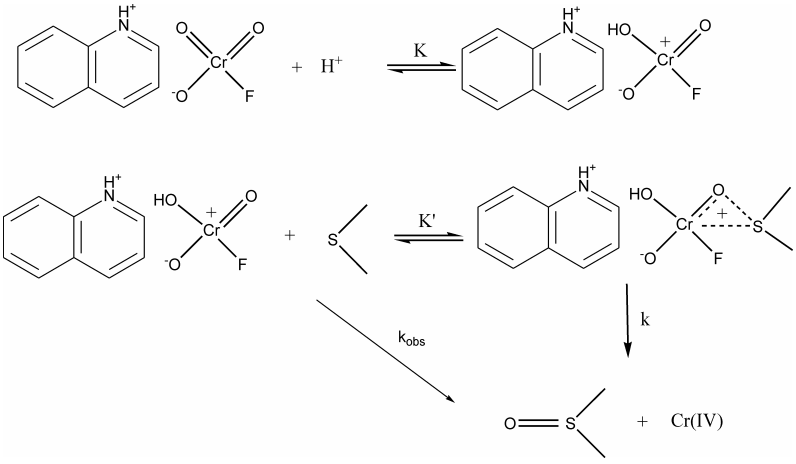

3. Issue No. 7 (2008), Vol. **73**, page 767:

– Lines 3–5 from the bottom should read:

…the β-diketone influence the ν(C⋯⋯C) and ν(C⋯⋯O) band frequencies, due to different resonance and inductive effects along…